Helmholtz-Zentrum Dresden-Rossendorf (HZDR)

An updated status and trends in actinide metal-organic frameworks (An-MOFs): from synthesis to application

Lyu, K.; Fichter, S.; Gu, M.; März, J.; Schmidt, M.;

An updated status and trends in actinide metal-organic frameworks (An-MOFs): from synthesis to application

Kai Lv [a, b, *], Sebastian Fichter [b], Mei Gu [a], Juliane März [b], Moritz Schmidt [b, *]

a) Radiochemistry Lab, Institute of Nuclear Physics and Chemistry, China Academy of Engineering Physics, 621900 Mianyang, Sichuan, China
b) Helmholtz-Zentrum Dresden-Rossendorf (HZDR), Institute of Resource Ecology, Bautzner Landstraβe 400, 01328 Dresden, Germany

* Corresponding author
E-mail address: lvkai@caep.cn (Kai Lv), moritz.schmidt@hzdr.de (Moritz Schmidt)

Contents

Abstract

Actinide metal-organic frameworks (An-MOFs) consisting of actinide nodes and organic linkers represent an underexplored category of coordination polymers due to challenges in their synthetic and characterization. The unparalleled coordination chemistry of actinide elements confers a huge opportunity to explore the rational design, chemical reactivity, and versatile properties of An-MOFs as one of the most intriguing class of metal-organic frameworks (MOFs). Significant advances in this "juvenile" MOF research field have been witnessed in recent years and progress in the An-MOFs area since 2003 has been reviewed

from the aspects of the synthesis, structure, and applications. The preparative handling and synthetic strategies implemented in constructing An-MOFs are illustrated. Their structure motifs are then classified and expounded by actinide building blocks and organic linkers. The modularity, topology, and porosity of An-MOFs are specified to highlight a great potential to tune their electronic structures and ensuing properties. Ultimately, applications of An-MOFs as selective adsorbents, heterogenous catalysts, luminescent sensors, conducting, and semiconducting materials, and nuclear targets are underlined. This updated review is envisaged to guide in-depth investigation of largely elusive transuranium MOFs and the development of thorium or uranium-based MOFs towards practical applications.

Keywords

Actinide coordination chemistry, Metal-Organic Frameworks, Actinide MOF, Transuranium elements, Uranium and Thorium, Properties and Applications

Introduction

The discovery and fundamental understanding of actinide elements have been forging ahead as scientists progressively unveil the solar planets naming actinides. Since the synthesis of transuranium elements in the early 1940s, research turned towards nuclear weapon-related manufacturing and testing projects, in which metallic character, chemical properties, and ensuing separation and purifications were primarily explored. The development of nuclear energy for civil utilization as well as military applications during the Cold War, contributed to the growth of actinide chemistry until the Chernobyl disaster led to a decline of the still young field of actinide chemistry. The renaissance of actinide chemistry not only roots in the extraordinary electronic structure of actinide elements, enabling a vast array of bonding and reactivity[1], but also originates from a pressing demand for intensifying the capabilities in weapon security, energy production, radioecological mitigation, and beyond. Nowadays, U- or Pu-based fission energy is the most prominent driving force for the development of actinide chemistry. In this field, the nuclear fuel cycle ranges from the extraction of uranium from solid or liquid ores to the recycling of uranium and plutonium, or the removal of minor actinide. The safe and efficient management of ever-increasing amounts of radioactive waste is a prerequisite of nuclear power generation. Besides seeking for a suitable matrix to immobilize residual actinides, it involves the migration pathways of actinides in the environment as consequences of the waste container or barrier breach. One emerging application of actinide chemistry is alpha radiopharmaceutical therapy (α-RPT) due to the high linear energy transfer of actinide with minimal toxicity. However, it remains as a challenge to develop efficient chelators for actinide and its daughter isotopes[2,3]. Therefore, in-depth knowledge of actinide binding modes, thermodynamic and kinetic reactivity with inorganic or

organic ligands in both solution and solid-state is required. Actinide coordination chemistry contributes to the precise control of actinide-bearing species, reliable prediction of chemical activity, and highly efficient actinide separation in complicated systems. While actinide coordination chemistry shares some general concepts with the extensively studied transition metal, and lanthanide coordination chemistry, it demonstrates unparalleled characteristics such as large coordination numbers, diverse coordination geometries, and multiple accessible oxidation states that portends a vast opportunity of exploring the rational design and chemical properties of actinide complexes and coordination polymers.

Most efforts in actinide coordination chemistry have been devoted to the structural bonding and chemical reactivity of uranium and thorium complexes in the past few decades, as illustrated by several reviews of actinide complexes[4,5]. In contrast to molecular actinide complexes, actinide coordination polymers represent a remarkable category of materials where unique structural motifs in higher-dimensions and chemical properties can be pursued. An-MOFs, as a subclass of actinide coordination polymers, can be defined as coordination networks with organic ligands containing potential voids according to IUPAC terminology of MOFs[6]. While the porosity of some An-MOFs has been proven, the presumed voids in a considerable number of An-MOFs have yet to be verified. Besides, a few one-dimensional actinide coordination polymers do not have cross-links, loops, or spiro-links between chains and cannot be rigidly classified as An-MOFs. However, it is the coordination modes and resulting properties of these supramolecular frameworks that should matter rather than which exact category they fall into. Hence, actinide-organic frameworks alongside with actinide supramolecular frameworks will be covered in this review and hereafter collectively referred to as An-MOFs. For clarity, we name An-MOFs by placing actinide prior to the acronym of linkers except for named frameworks.

An burgeoning growth of design principles, synthetic methodology, comprehensive characterization, and myriad applications of MOFs based on transition metals and lanthanoids have been developed in recent decades[7–13]. In contrast, An-MOFs represent an underdeveloped area where rational design, construction of topology, and functionality are relatively poorly understood. By far the most noticeable progress has been made for Th- and U-MOFs due to the relatively large natural abundances, low specific activity, and intermediate chemical toxicity of thorium and uranium. Transuranium metal-organic frameworks (TRU-MOFs) remain extremely rare due to the scarcity of TRU elements and the limitations associated with their handling. The growing number of An-MOFs will enable the construction of a versatile platform for inquiring about divergence and convergence between Th, U, and TRU coordination chemistry as well as interrogating fundamental covalency for challenging actinide separations. Moreover, An-MOFs has been proposed as one of the hierarchical nuclear waste forms as alternatives to vitreous and cementitious waste forms[14]. Compared with pyrochlore[15], perovskite[16], fluoride[17], surface-functionalized nanoparticles[18], and hierarchically porous silica[19], An-MOFs are expected to homogenously immobilize a large amount of actinide and volatile radionuclides, thus reducing financial cost of nuclear waste management. An-MOFs also demonstrate

their utility in isolating pure actinide species by the assembly of actinide cores or clusters with capping ligands or counterions into periodic MOF matrices, offering a unique structure perspective of actinide hydrolysis chemistry. It is also notable that An-MOFs represent a rising category of multifunctional materials since they possess unique chemical or physical properties and high chemical, thermal, and radiolytic stability under harsh conditions as a result of their high-charge-density and strong coordination field.

U(VI)-based coordination polymers were reviewed by Cahill in 2007[20,21]. In 2011, Chen generalized the extended structures and physicochemical properties of U(VI)-MOFs[22]. Since carboxylate and phosphonate ligands are the predominant linkers in An-MOFs, Loiseau, and Sun made comprehensive reviews of uranium carboxylate and uranium phosphonate chemistry in 2014[4]and 2015[23], respectively. Thuéry summarized the structural chemistry of heterometallic uranyl-containing coordination polymers in 2017[24] while Cahill outlined a few actinide supramolecular assembly in 2018[25]. Meanwhile, Shustova presented a seminal overview of the structural motifs of Th-, U-MOFs, and MOFs for radionuclide immobilization[26]. Recently, Zhang recorded the structure and functionality of An-MOFs prepared by the Farha group[27] meanwhile the Zhou group summarized MOFs based on group 3 and 4 metals, including several Th-, Np-, and Pu-MOFs[28]. The Park group discussed the coordination environments and chemical behaviors of a portion of An-MOFs, focusing their implications for nuclear industry[29].

The rapid growth of An-MOF research in the most recent three years indicates that a timely update of An-MOFs is indispensable. The theoretical modeling of the electronic structures of Th-, U-MOFs has been newly reviewed[30], and will thus be beyond the scope of our manuscript. Since previous overview articles focused on the structural aspects of a part of U-MOFs[4] and heterometallic Th- and U-MOFs[24], we will provide an up-to-date generalization of U-MOFs approximately since 2014 and heterometallic An-MOFs since 2017. To gain a complete and clear picture of Th-, Np-, Pu-, Am- and Cf-MOFs, we will cover these An-MOFs since 2003 (publication of TOF-1). We will analyze the building blocks and framework motifs of each An-MOF besides elaborating their traditional and emergent properties as well as multitudinous applications (Fig.1).
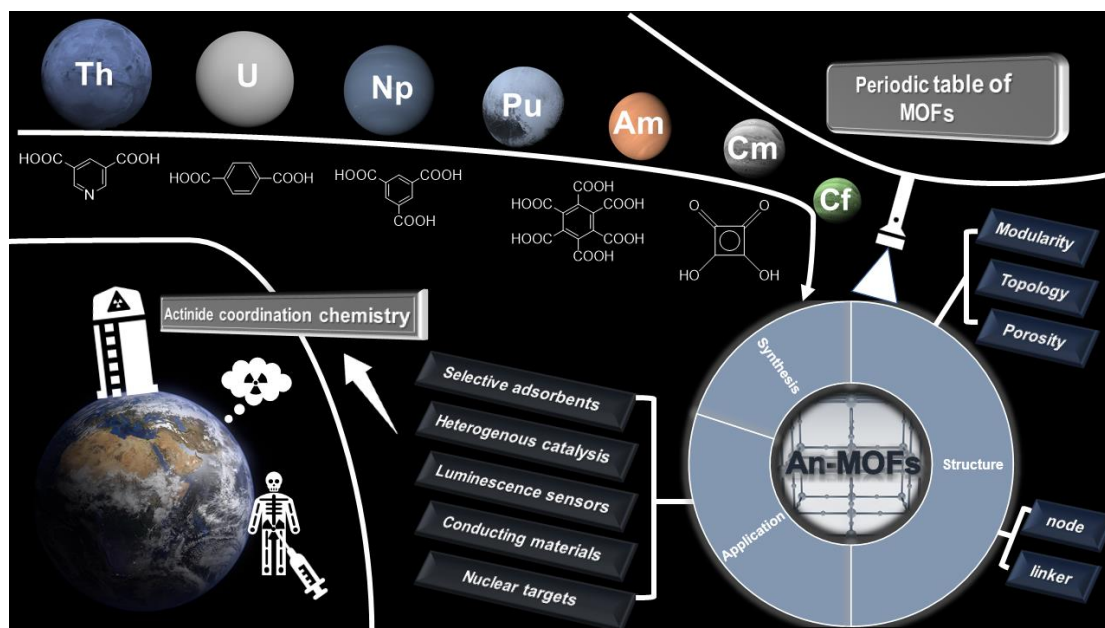
Figure 1. Sketch of An-MOFs covered in this review.

2. Synthesis of An-MOFs

2.1 Handling of An-MOFs

2.1.1 Actinide precursors

The choice of actinide precursor for An-MOFs syntheses is a balance between accessibility and reaction utility. Commercially available $Th(NO_3)_4 \cdot xH_2O$ (x = 0-6) as a stable precursor can be converted to $ThCl_4 \cdot 4H_2O$ for the construction of Th-MOFs. ThO_2 was once used as a thorium precursor that was dissolved in hydrothermal HF[31]. Starting with $ThCl_4 \cdot 4H_2O$, anhydrous thorium tetrachloride complexes including $ThCl_4(DME)_2$ (DME = dimethoxyethane), $ThCl_4(1,4\text{-dioxane})_2$, and $ThCl_4(THF)_{3.5}$ (THF = tetrahydrofuran) are accessible in lab-scale and used for thorium organometallic chemistry[32] (Fig.2a). Currently, purchasable uranyl precursors include $UO_2(NO_3)_2 \cdot 6H_2O$, $UO_2(CH_3COO)_2 \cdot xH_2O$ (x = 0, 2), $Zn(UO_2)_2(CH_3COO)_6 \cdot 7H_2O$, $UO_2SO_4 \cdot 3H_2O$, $UO_2Cl_2 \cdot 3H_2O$, and $UO_2(CHOO)_2 \cdot H_2O$ and the first three has been widely used for the synthesis of U(VI)-MOFs. Uranyl nitrate can be freshly prepared by dissolving UO_2 in concentrated HNO_3 and adjusting the pH to ~ 2.5 by concentrated $NH_3 \cdot H_2O$[33]. To slowly release uranyl ions from a precursor, uranyl zinc acetate has been adopted for the synthesis of U(VI)-MOFs that cannot be obtained from uranyl nitrate. This precursor also acts as a zinc source for heterometallic An-MOFs[34]. Uranyl sulfate is almost exclusively used for rotaxane-based U(VI)-MOFs due to sulfate's relatively strong binding to UO_2^{2+}[35]. $UO_2Cl_2 \cdot 3H_2O$ was recently used as a uranyl precursor that offers Cl^- counterions and

coordinating water in the resulting framework[36]. As for U(IV)-MOFs, UCl_4 is generally utilized as a lab-made precursor. UCl_3 was intended as a precursor for U(III)-MOFs, however in-situ conversion into U(IV) occurred due to traces of oxygen in starting reactants[37]. $U(SO_4)_2 \cdot 4H_2O$ was recently used as a less reactive precursor probably due to its reduced tendency to hydrolyze while the sulfate ions can act as an auxiliary bidentate ligand[38]. It can be freshly prepared by photoreduction of uranyl sulfate in the presence of ethanol. Such photoreduction in a mixed solvent under ambient sunlight allowed the in-situ formation of the precursor without a need to exclude air and moisture during the synthetic procedure[39], which did however take one year. As an alternative to UCl_4, UI_4(1,2-dioxane)$_2$ was obtained in high yield by reacting uranium turnings (mixed uranium oxides) with a 1,4-dioxane solution of iodine at room-temperature[40]. By heating UO_2 with $AlCl_3$ in an ampoule, a facile synthesis of pure UCl_4 was achieved in a large batch, which is also used to prepare UBr_4 and UI_4 [41](Fig. 2b).

Starting from $^{237}NpO_2$, syntheses of neptunium precursors of a single oxidation state is compiled (Fig.2c). Solid NpO_2OH was prepared by precipitation of NpO_2^+ [42], and NpO_2^{2+} nitrate solution could be directly used as a precursor[43]. In the case of Np precursors of mixed valency, in-situ reduction is a common reaction in aqueous hydrothermal systems even in the presence of certain oxidation agents, driven by the formation of highly insoluble Np(IV) products[44,45]. However, $NpCl_4$ precursor could be oxidized to Np(V) in the presence of mellitic acid, which was ascribed to the stabilization of Np(V) species in solid frameworks[46], revealing the valency complexity in Np-MOFs induced by in-situ redox chemistry of Np.

Similarly, freshly prepared Pu(VI) nitrate from $^{242}PuO_2$ was used as a precursor and driven to the least soluble Pu(IV) phosphonate[47]. $^{242}PuO_2$ can convert to $Pu(OH)_4$ that subsequently transforms to $PuCl_4$[48]. The $PuBr_3$ precursor was obtained by reducing $Pu(OH)_4$ or starting with $PuCl_3$ in mixed-valent Pu-MOFs. Upon gentle heating under the N_2 stream, a forest green solution of Pu^{4+} reduced to a violet Pu^{3+} solution and formed a purple-black $PuBr_3$ hydrate residue after complete evaporation[49]. By treating a $^{239}Pu(IV)$ stock solution with HNO_3 in a proper dry down timing, an exploratory synthesis of Pu-UiO-66 was demonstrated. The failure in the formation of suitable single-crystals implied an elusive grapple between the controlled hydrolysis to hexanuclear clusters and uncontrolled polymerization, which thwarted synthetic efforts for Pu(IV)[50]. PuO_2^{2+} nitrate solution was recently utilized to successfully prepare one Pu(VI)-MOF[43] (Fig.2d).

In the preparation of Am precursors, $^{243}AmO_2$ was first converted into $AmCl_3$ that could also be obtained via $Am(OH)_3$[51] (Fig.2e). Subsequently, $AmCl_3$ residue was transformed into an $Am(NO_3)_3$ stock solution by repeated acid digestion and dry-down[52]. This hydrated $AmCl_3$ can be converted into $AmCl(\mu-Cl)_2(THF)_2$ as useful synthons for organometallic americium chemistry[53]. $^{249}CfCl_3$ precursor was produced from $Cf(OH)_3$ solid or $CfCl_3$ stock solution(Fig.2f), the latter route of which was used to prepare $^{248}CmCl_3$ precursor[54].

It is of great significance to gain actinide precursors of specific oxidation states from raw materials and keep valences for the entire duration of an experiment. Besides

actinide chloride, nitrate, hydroxide, or organic complexes as precursors by the aforementioned chemical reactions, actinide precursors can be prepared by electrochemical oxidation or reduction on chemically modified electrodes as was demonstrated by electrochemical oxidation of ^{243}Am(III)[55,56].

a

$ThCl_4(H_2O)_4$ → (Me$_3$SiCl, HCl/Et$_2$O, 1,4-dioxane; 403 K, 24 h) → $ThCl_4$(1,4-dioxane)$_2$

^{232}Th(NO$_3$)$_4$(H$_2$O)$_5$ → (HCl, 373K, 6h) → $ThCl_4(H_2O)_4$

$ThCl_4(H_2O)_4$ → (DME, 363 K, 12 h) → $ThCl_4$(DME)$_2$

$ThCl_4$(1,4-dioxane)$_2$ → (THF, RT, 10 min) → $ThCl_4$(THF)$_{3.5}$

$ThCl_4$(THF)$_{3.5}$ → (DME, RT, 10 min) → $ThCl_4$(DME)$_2$

b

^{238}UO$_2$ → (I$_2$, 1,4-dioxane, RT, 5 d) → UI$_4$(1,4-dioxane)$_2$

^{238}UO$_2$ → (AlCl$_3$, 623 K, 1 d) → UCl$_4$

^{238}UO$_3$ → (C$_3$Cl$_6$, N$_2$, 443 K) → UCl$_4$ → (Zn metal, Ar, 773-1073 K) → UCl$_3$

c

^{237}NpO$_2$ → (8M HNO$_3$, 473 K, 3 d) → NpO$_2$(NO$_3$)$_2$ (residue) → (C$_3$Cl$_6$, 473 K, 1 d) → NpCl$_4$

NpO$_2$(NO$_3$)$_2$ (residue) → (H$_2$O, O$_3$, RT, 5 h) → NpO$_2$(NO$_3$)$_2$ (aq) → (NaNO$_3$, NH$_4$OH) → NpO$_2$OH

d

^{242}PuO$_2$ → (HNO$_3$, HF / NaOH) → Pu(OH)$_4$ → (8M HBr, N$_2$) → PuBr$_3$ ← (8M HBr, 403 K, 1 h) ← PuCl$_3$

^{242}PuO$_2$ → (8M HNO$_3$, 473 K, 3 d) → PuO$_2$(NO$_3$)$_2$ (residue) → (H$_2$O, O$_3$, RT, 5 h) → PuO$_2$(NO$_3$)$_2$ (aq)

Pu(OH)$_4$ → (12 M HCl, Ar) → PuCl$_4$

e

^{243}AmO$_2$ → (6M HCl, 473 K, 1 h) → AmCl$_3$ → (5M HNO$_3$) → Am(NO$_3$)$_3$

^{243}Am(OH)$_3$ → (12M HCl, 398 K) → AmCl$_3$

AmCl$_3$ → (Me$_3$SiCl, THF) → AmCl$_3$(THF)$_2$

f

^{249}Cf(OH)$_3$ → (12M HCl, 398 K) → CfCl$_3$ ← (12M HCl) ← Cf$_2$(CO$_3$)$_3$ ← (2M (NH$_4$)$_3$CO$_3$) ← ^{249}CfCl$_3$ (aq)
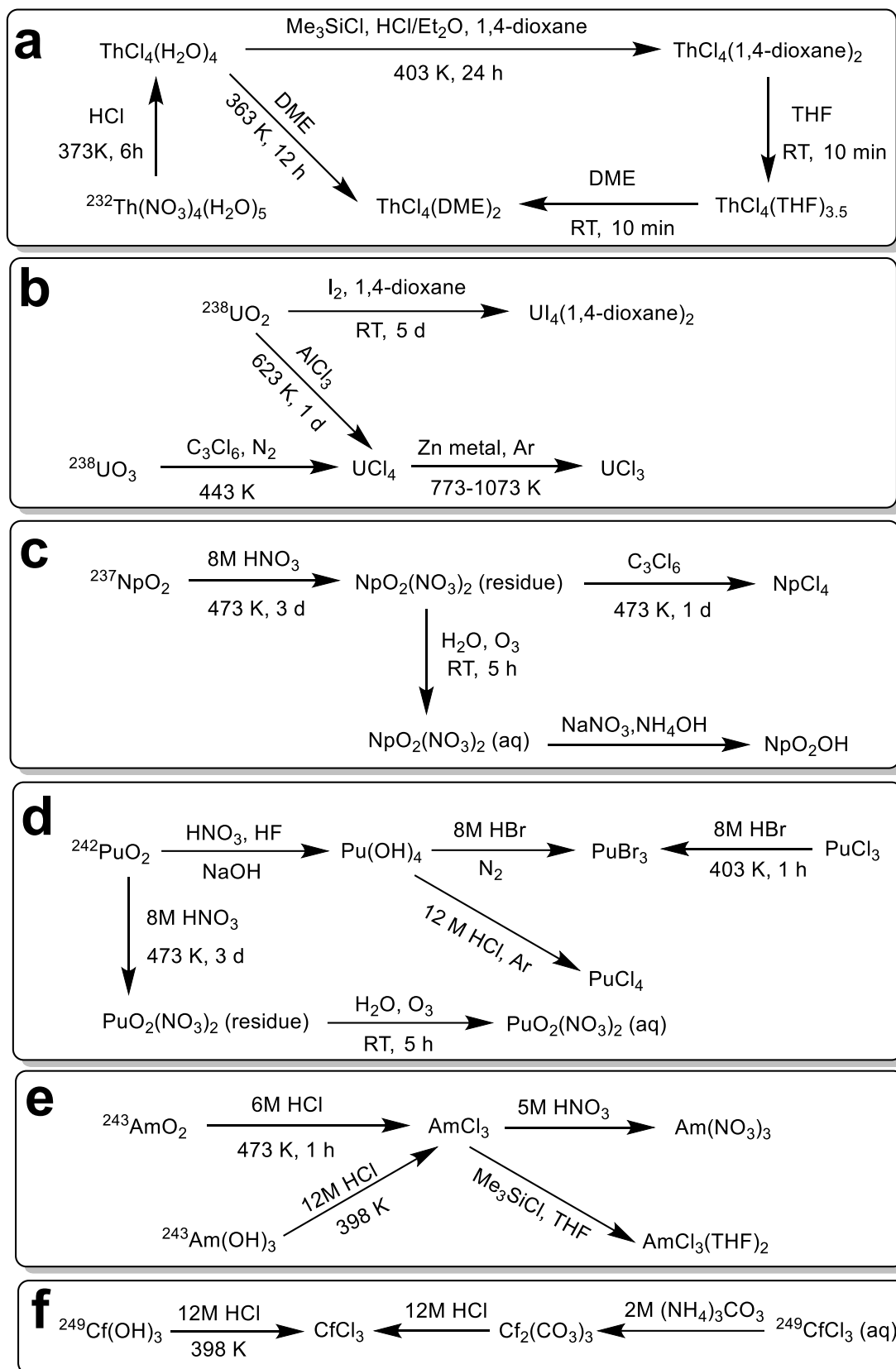
Figure 2. Chemical synthesis routes for actinide precursors of An-MOFs: (a) Th(IV); (b) U(III), U(IV); (c) Np(IV), Np(V) and Np(VI); (d) Pu(III), Pu(IV) and Pu(VI); (e) Am(III); (f) Cf(III).

2.1.2 Constrains in actinide handling

Even though thorium and uranium precursors are of low radioactivity, it is a prerequisite to prepare Th- and U-MOFs in fume hoods or negative pressure gloveboxes in licensed radiochemistry labs due to their intrinsic chemotoxicity, and radiotoxicity. Since TRU-MOFs pose a significant health risk to synthetic scientists, experimental yields or physicochemical characterization would require significant handling and these aspects are currently far from clear due to lack of sufficient amount of TRU-MOFs. To minimize personal irradiation dose throughout any syntheses, it is of utmost importance to minimize time spent handling radioactivity, maximize operational distance, and use appropriate shielding. Besides, before conducting chemistry with radiolytically challenging TRU isotopes, the potential use of nonradioactive lanthanide or natural thorium or uranium as starters to optimize synthetic conditions and reaction scales as well as to provide necessary benchmarks for structural comparisons is often worthwhile. Such a preemptive search for surrogate frameworks and "dummy runs" with low or without radioactivity is imperative considering the scarcity of TRU precursors [52].

Upon completion of experimental work, the An-MOFs, particularly TRU-MOFs are worthwhile to recycle (Fig.3). First, An-MOFs will be dissolved according to their chemical stabilities and converted into a crude solution. Second, by cost-effective chemical separation such as extraction chromatography, an actinide stock solution can be isolated from byproducts. Third, after evaporating the stock solution to dryness, the resulting actinide residue can be transformed into a solid-state precursor by subsequent chemical reactions. The pure stock solution can also be used directly as a solution-state precursor or quantitatively diluted into actinide isotope tracers for radioanalytical applications. Last but not least, one key issue about handling An-MOFs is the strict surveillance of actinide materials, particularly U and Pu materials of high proliferation concern. The ^{237}Np associated with the nuclear fuel cycle, or defense applications should be included here as alternative nuclear materials[57]. Indeed, actinide-bearing materials throughout An-MOFs syntheses need to be monitored by non-destructive radioanalytical techniques and the composition of actinide waste generated from de novo synthesis or recycling of An-MOFs should be recorded for subsequent industrial waste disposal.
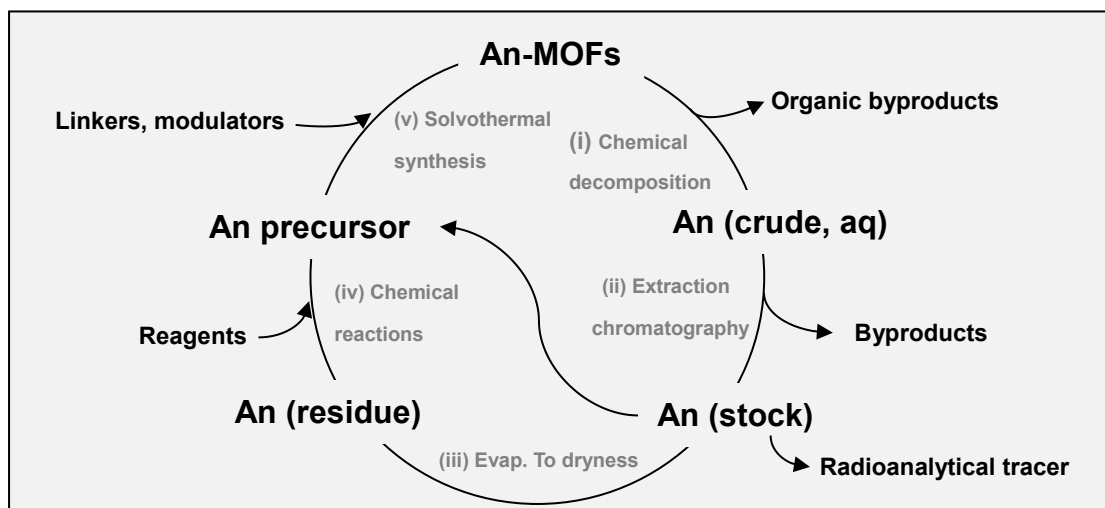
Figure 3. Schematic showing of 'cradle to grave' recycle of An-MOFs.

2.2 Synthetic strategies

Current synthetic methodologies established for transition metal, and lanthanide based MOFs apply for An-MOFs. Solvo-hydrothermal syntheses, as a general pathway to a diversity of crystalline An-MOFs, are undoubtedly complicated since subtle changes to pH, solvent, temperature, reaction duration, and precursor composition may lead to the stabilization of one structural motif over another. In-situ hydrolysis of ligand precursors occasionally occurs with or without metal ions under mild conditions, or radiolysis-assisted conversion[51]. The resulting ligands (e.g. oxalic acid) will complicate the little-known thermodynamic and kinetic equilibria of actinide-ligand reactions. Numerous instances where it does not provide a crystalline An-MOF are not reported. An-MOF syntheses still proceed empirically and herein the respective role of synthetic factors for An-MOFs are briefly discussed.

The first factor is solution acidity. Upon elevation of solution pH, actinide species undergo hydrolysis reactions, eventually giving rise to the formation of oxo/hydroxo bridges between metal cations. Meanwhile, organic linkers such as weak carboxylic acid tend to be deprotonated. The nucleophilic aquo-hydroxo actinide entities can initiate inorganic polymerization and tend to form large oligomers that are competitively stabilized by deprotonated ligands. The solvent composition has an unclear yet pivotal role in shaping An-MOFs. The addition of H_2O into the commonly used DMF (N, N-dimethylformamide) favors the olation/oxolation condensation and the stabilization of actinide clusters while DMF will decompose into dimethylamine that facilitates ligands deprotonation as well as balance the negative charge of cationic frameworks. An excess of H_2O, however, might lead directly to the formation of dense actinide oxides. NMP (N-methyl-2-pyrrolidone), CH_3CN, and DEF (N, N-diethylformamide) with good hydrolytic stability and ligand solubility can be used as alternative solvents for DMF. As the reaction temperature elevates and duration prolongs, actinide precursors are inclined to hydrolyze, which is beneficial for nucleation. One representative example is that the kinetically favored tetranuclear

cluster in Th-NU-1011 transformed into a thermodynamically stable hexanuclear cluster in Th-NU-1008 as reaction time became longer[58]. However, the effect of temperature and duration on the nucleation and crystal growth of An-MOFs appears to be poorly understood due to the paucity of relevant thermochemical data. The molar ratio of actinide precursor to organic ligand not only determines the unsaturated states and connectivity of actinide nodes, but also leads to frameworks of different charge, dimensionality, or morphology. It is critical to tune the size and shape of An-MOFs upon varying aforementioned synthetic factors without significant alteration of their designed physicochemical properties, which, however, remains a daunting challenge. A composition diagram of the actinide-ligand system in single or mixed solvents as a function of pH, temperature, duration, and precursor ratio[59–63] is recommended to unveil the synthesis-structure relationship of An-MOFs.

Direct approaches to An-MOF syntheses, most notably solvo-hydrothermal methods, are effective for producing porous frameworks with contingent functionality. To install desired functionalities where one-pot direct routes are not feasible, postsynthetic modification (PSM) has recently become instrumental in preparing heterometallic An-MOFs[64,65]. Even though An-MOFs can be prepared by one-pot synthesis or PSM, the reactions are usually carried out over long time periods or via high energy-input. As an alternative to thermal energy input, both microwave- or ultrasonic-assisted synthetic methods demonstrate their utility in the preparation of Th-MOFs on a large and controllable scale[66,67].

2.2.1 Modulated synthesis

Owing to the strong Lewis acidity of actinide cations and correspondingly high tendency to coordinate with organic ligands, bulk polycrystalline or amorphous precipitates via fast nucleation were often encountered in An(IV)-MOFs. Slow diffusion methods at room temperature have been adopted for several U-MOFs[38,39], but it took weeks or even months to obtain single-crystals. By introducing certain types of species with similar chemical functionality as linkers, the coordination equilibrium between actinide precursor and organic ligands can be regulated, thus ameliorating the crystallization kinetics of single crystals. This utilization of modulators can not only control the number of defect sites, but also determines the particle morphology, and kinetic transformation of topology by tuning the modulator type and concentration, leading to the anisotropic, reproducible growth of high-quality MOFs[68,69] with structural diversity, exemplified by the formation of NU-1008/NU-902[70], NU-500/NU-600/NU-906/NU-1008[71]. Generally speaking, modulators including inorganic or organic acids, N-donor bases, alkylamine, and ionic liquids have been applied for An-MOFs and have multiple roles as: (1) pH modulator to adjust the system's pH and control deprotonation of linkers; (2) coordination modulator to reversibly bind to actinides; (3) templating or structure-directing agent to induce desired framework characteristics (e.g. porosity, chirality). The experimental or calculated pK_a behind each modulator (Table S1) can be used as a reference for roughly estimating the conjugated basicity at a specific solution pH as

well as accounting for coordinative competitions between modulators and linkers. Hydrofluoric acid has long been used in developing Th-MOFs as a mineralizing agent due to the strong affinity of F^- towards thorium while also adjusting solution pH[72–74]. It was also repeatedly used in the preparation of uranyl phosphonate frameworks[75,76]. In the presence of HF, An-MOFs have a strong tendency to form fluoride-sharing multinuclear secondary building units (SBUs). Even though HF proves to be reliable in preparing An-MOFs single crystals, its corrosive nature causes operation risk and expectedly disables the coordination of relatively weak N-donor linkers[72]. Hence, it has been gradually replaced by strong inorganic acids such as HCl, and HNO_3, which can adjust solution acidity to control crystallization kinetics. For instance, the addition of increasing equivalents of HNO_3 resulted in Th-SINAP-10 products from powder to intergrown polycrystalline, and eventually to large octahedral single crystals[77] (Fig.4a). Compared to HNO_3, HCl is a less-exploited non-oxidizing modulator but it recently extended its utility in Th- and U-MOFs syntheses[60-63]. As a weak acid, H_3BO_3 is a mineralizing agent to promote the growth of high-quality single crystals of U-MOFs[81,82]. Inorganic bases including NH_4Cl[83], NH_4OH[33,84], and NaOH[85–87] have been used to adjust solution pH as well as offering a counter cation or acting as Na^+ precursor for heterometallic An-MOFs.

Organic acids such as trifluoroacetic acid (TFA), oxalic acid, formic acid, benzoic acid, and acetic acid play a significant role in slowing down the reaction between actinide cores/clusters and organic linkers. While TFA is frequently used as a strong acid modulator in organic solvents, the exclusion of TFA in any syntheses of Pu-UiO-66 was emphasized, because synthetic attempts in the presence of TFA precipitated. The decomposition of TFA into HF upon heating or ultrasonic treatment might contribute to the formation of the plutonium fluoride precipitate[50]. The strong planar complexation ability of $C_2O_4^{2-}$ enables its use as an auxiliary bridging ligand to tune framework motifs[88]. Formic acid has been widely used as the simplest monocarboxylic acid modulator to control the crystal growth of MOFs as well as a model ligand to gives rise to An-MOFs. By varying precursor composition and solvent mixture, the thermodynamic competition between $HCOO^-$, OH^-, H_2O, and DMF for the coordination with Th^{4+} led to six Th-MOFs with different SBUs and topologies[89]. Benzoic acid was indispensable for the construction of certain An-MOFs[58]while 2-fluorobenzoic acid was recently used as a modulator for Ce(IV)-MOFs[90] and could be transferred to prepare An(IV)-MOFs. Acetic acid was demonstrated as a weak acid modulator for a tetra(4-carboxyphenyl)porphyrin based U-MOF due to their similar pK_a values[91]. Occasionally, the combination of strong acids with weak ones as mixed modulator contributes to the development of single-crystal An-MOFs. For example, without HNO_3, only microcrystalline Th-SINAP-7 was produced due to fast nucleation even in the presence of HCOOH, while large crystals emerged in the presence of HNO_3[92].

Generally, N-donor ligands can serve as temporary organic templates as well as to deprotonate carboxylate groups due to the weakly alkaline nature. Pyrazine and H_2O assisted in constructing a 3D uranyl-bearing supramolecular framework via hydrogen

bonds[93]. Such a templating role was also found for piperazine, which also acts as charge-balancing species in uranyl-organic nanotube[94]. Weakly basic ligands including bipyridine, terpyridine, and phenanthroline have been used as modulators for Th-, U-, and Am-MOFs, among which 2,2-bipyridine (2,2-bipy)[95], 4,4-bipyridine (4,4-bipy)[96], and 1,10-phenanthroline (1,10-phen)[97] are most frequently used. While 2,2-bipy and 4,4-bipy normally do not connect with actinides in the presence of carboxylate ligands due to their lower binding affinity, they act as charge balancing molecule or induce hydrogen bonding and π-π interaction, which contribute to stabilizing An-MOFs. Compared to bipyridine, the shorter distance of two adjacent nitrogen atoms in 1,10-phen enables its higher affinity for the actinides, while its structural rigidity readily provides steric hindrance at the actinide center, as well as generating additional node connectivity. It can also serve as a capping ligand to regulate the rate of framework extension and crystal growth. The inclusion of 1,10-phen was necessary for the preparation of GWMOF-13 single-crystals, where otherwise only microcrystalline fine powder is produced[98]. Mostly, these three aza-aromatic ligands were added along with different labile metal ions to generate free metal complexes inside certain heterometallic An-MOFs[99–101]. Other bi-, and terpyridine derivatives such as 4,4'-bipyridine-N,N'-dioxide[102], 4,4'-vinylenedipyridine, 4,4'-trimethylenedipyridine[103], 5,5′-dimethyl-2,2′-dipyridyl[100] and 2,2':6',2''-terpyridine[104] were used as coligands, charge compensators or space-filling templates in a few U-MOFs.
1,4-diaminobutane[105]as a secondary amine, trimethylamine[106] and triethylamine[107] as tertiary amines, and urea[108] have sporadically been reported as soft bases in the synthesis of An-MOFs. The quaternary ammonium salts including tetramethylammonium bromide[109], tetraethylammonium hydroxide[110], tetrapropylammonium hydroxide[108], tetrabutylammonium hydroxide[111], and benzyltriethylammonium hydroxide[112] were adopted to act as positively charged counterions that induces electrostatic attraction and van-der-Waals interaction with anionic U-MOFs. Likewise, due to bulky phosphonium cations stopping oligomerization, methyltriphenylphosphonium bromide[113] and tetraphenylphosphonium bromide (TPPB)[114] were used to induce structural variety in certain U-MOFs. It is noted that TPPB, as a useful phase-transfer catalyst, allowed Th- and U-MOFs bearing TPPB to remove TcO_4^- from radioactive waste streams. A few imidazole ligands such as 1,4-di(1H-imidazole-1-yl)benzene, 1,1-(1,4-butanediyl)bis(imidazole), 4,4'-bis(1-imidazolyl)biphenyl, 1-biphenyl-4-yl-1H-imidazole were adopted as pillar-like coligands as well as space-filling templates for U- and Th-MOFs. Three thermostable, nonvolatile task-specific imidazole-based ionic liquids, namely 1-octyl-3-methylimidazolium chloride[115], 1-butyl-2,3-dimethylimidazolium chloride, 1-butyl-1-methylpyrrolidinium bromide, 1-butyl-3-methylimidazolium tetrafluoroborate[76], and 1-allyl-3-methylimidazolium chloride[116] were used as templates and ionothermal solvent for some U- and Th-MOFs syntheses. As both a water-soluble strong base and ionic liquid, guanidinium salts[78,117] were useful in the preparation of Th-MOFs. Different ratios of modulator to solvent may result in single crystals or mixed phases of An-MOFs. For

instance, increasing the starting water concentration can accelerate the olation and oxolation reactions while a high concentration of benzoic acid lowers the initial pH that inhibits metal hydrolysis, as encountered in the preparation of some Th-MOFs[58].
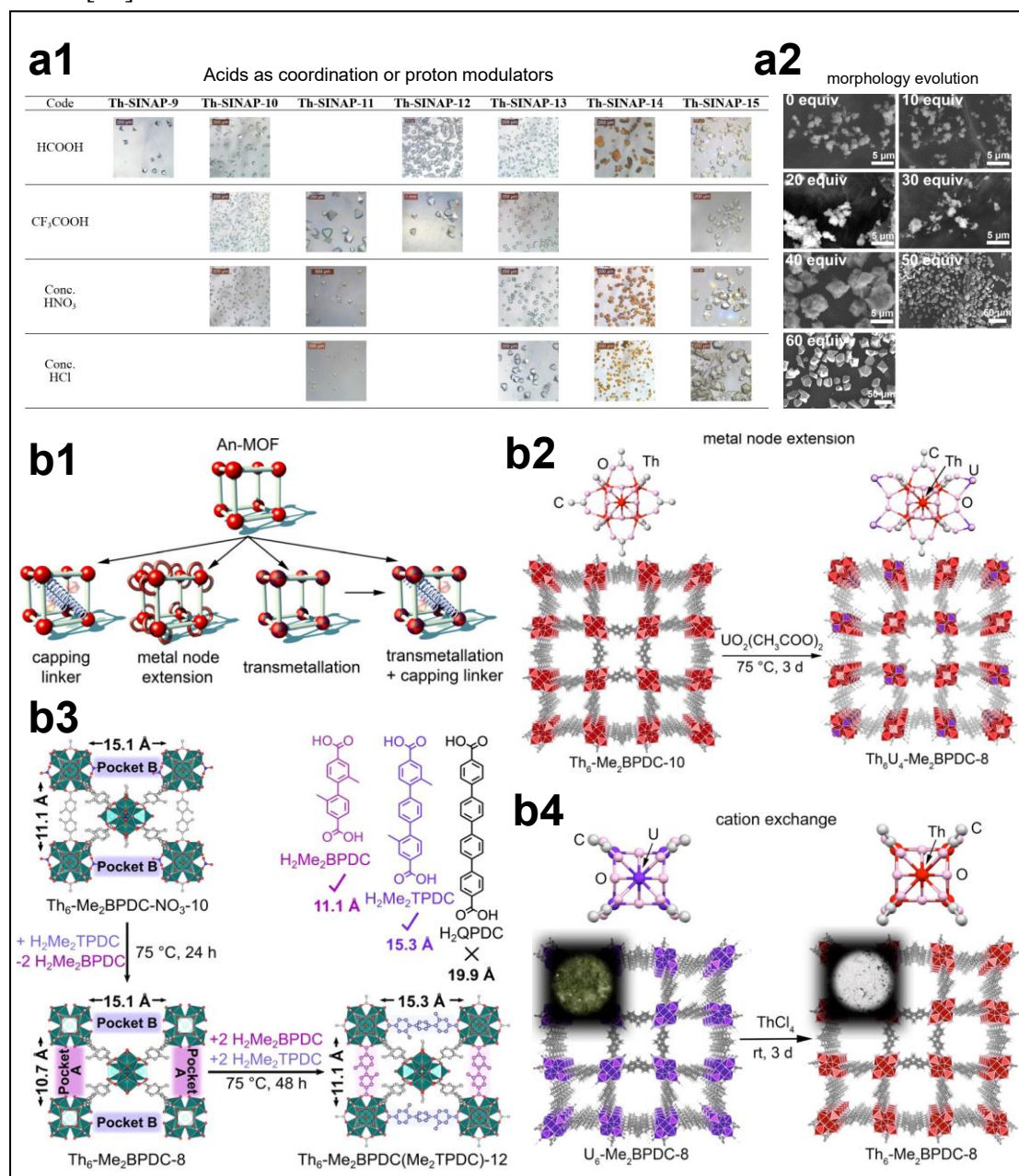

Figure 4. Synthetic strategies of An-MOFs: (a1) Performance of HCOOH, TFA, concentrated HNO₃, and HCl as modulators for Th-SINAP-(9-15). (a2) SEM images of Th-SINAP-10 in the presence of 0, 10, 20, 30, 40, 50, and 60 equivalents of concentrated HNO₃ (Reproduced from ref. [77] with permission from The Royal Society of Chemistry, Copyright 2020); (b1) actinide node engineering including capping linker installation, metal exchange, and node extension. (b2) metal node extension. (b3) sequential linker installation. (b4) cation exchange. (Reproduced from ref. [64,65] with permission from the American Chemical Society, Copyright 2017, 2019).

2.2.2 Mixed-linker synthesis

The advances of mixed-linker strategy for multifunctional MOFs, particularly for Zr-MOFs have been reviewed by Zhou's group and mixed-linker MOFs are generally categorized into pre-designed or existing (i) pillared-layer, (ii) cage-directed, (iii) metal-organic cluster, or (iv) templated framework that connected to a secondary linker[118]. By adopting a mixed-linker strategy, it is feasible that different functional groups can be placed at the desired positions of MOFs as well as to create structural defects while preserving framework integrity, thus exhibiting two complementary or contradictory properties within pore environments.

Layer motifs are frequently encountered in U(VI)-MOFs due to preferred coordination in the equatorial plane of uranyl, which makes them suitable platform for pillared-layer U(VI)-MOFs. The uranyl organophosphinate layers are joined by rigid imidazole coligands to form a 3D framework, however, the accessible tunability of which was not comparable to 2D U(VI)-MOFs bearing only organophosphinate linker[119]. Since electronegative imidazole induced equatorial plane bending of uranyl, this incurvation geometry results in a 3D framework regarded as a uranyl-dicarboxylate layer interpenetrated by another layer composed of uranyl and coligands. Besides imidazole, pyridine ligands such as 4,4'-trimethylenedipyridine can act as pillars cross-linking uranyl-dicarboxylate layers to form 3D frameworks[103]. Planar oxalate tends to coordinate with uranyl ions to form an infinite uranyl-oxalate chain that is bridged by a second ligand to form multidimensional frameworks, which can be classified as predesigned metal-organic clusters [109]. Templated 2D frameworks can be observed in U-BCBP-1, in which adjoining uranyl ions are connected by two sequences of BDC to form a wave-shaped 2D layer. Rather than pillaring, the second BCBP, as isoreticular with BDC, connects interphase dinuclear motifs to generate a double-layered 2D structure[83]. Similarly, in U-BDC-CB[6], the uranyl-terephthalate layers are held together by an array of $Na_2(CB5)_2$ as templates[120]. Since the Th_6 cluster of NU-905 has unsaturated metal sites, by intentionally introducing a size-matching photosensitizer ligand into the framework as a capping agent, it enhances the photocatalytic properties of NU-905[121]. Th-IHEP-5 has been very recently reported as a templated mixed-linker Th-MOF by using 2,2′-bipyridine-5,5′-dicarboxylic acid. Compared with pristine NU-905, the expected superior photocatalytic behavior of Th-IHEP-5 implies the success of this synthetic methodology for the target applications[122]. Few trials in mixed-linker strategy have demonstrated the roles of auxiliary linkers as templating or complexing agents[123] that shape periodic motifs and properties of functional An-MOFs.

2.2.3 Postsynthetic modification

PSM is evolving as a viable strategy for delicately altering either metal nodes, organic linkers, or both and four general strategies hold great promise in introducing

functionality into An-MOFs: (1) solvent-assisted ligand incorporation (SALI) equivalent to capping linker installation, (2) metal node extension including solvothermal deposition and atomic layer deposition, (3) cation exchange (or transmetallation) at actinide nodes, (4) solvent-assisted ligand exchange (SALE). The former three are node-centric PSM techniques while the last one is linker-centric [124]. Each PSM method and combinations were demonstrated by the Shustova group in order to homogenously immobilize actinides through covalent bond formation within heterometallic An-MOFs[26,64,65] (Fig.4b).

Due to the presence of labile nitrate groups coordinated to the equatorial position of unsaturated thorium nodes, heating of Th_6-Me_2BPDC-NO_3-10 in a solution of H_2Me_2TPDC linker resulted in the formation of Th_6-Me_2BPDC-8, which subsequently transformed into Th_6-$Me_2BPDC(Me_2TPDC)$-12 in the presence of two capping linkers. Moreover, as the $BPDC^{2-}$ replaced Me_2BPDC^{2-} in Th_6-Me_2BPDC-NO_3-10, it produced a 10-coordinate Th_6-$BPDC$-10, which cannot be directly synthesized. The transformational capping linker installation revealed its great potential to precisely tune the degree of actinide node saturation together with the control of the molar ratio of actinide salts to linker. Heating Th_6-Me_2BPDC-10 in the presence of $ThCl_4$ and H_2TPDC-NH_2 led to simultaneous capping linker installation and guest incorporation inside the framework.

Thermal treatment of parent compound Th_6-Me_2BPDC-10 in the presence of $UO_2(CH_3COO)_2$ at 75 °C for 3 days resulted in the formation of Th_6U_4-Me_2BPDC-8, in which thorium-based metal nodes are extended with UO_2^{2+}. Due to the interaction between UO_2^{2+} and labile hydroxyl or aqua groups in the Zr_6 node, uranyl can be grafted on NU-1000. The unsaturated nodes of Zr_6-Me_2BPDC-8 can incorporate uranyl to form $Zr_6U_{0.87}$-Me_2BPDC-8, which was used as a precursor for sequential capping linker installation and guest uranyl inclusion.

Transmetallation in An-MOFs was successful by soaking U_6-Me_2BPDC-8 in a solution containing $ThCl_4$ at 25 °C for 3 days. Further capping linker installation of this transmetallated U-MOF in the presence of SDC and $ThCl_4$ at 75 °C for 24 h resulted in a $Th_{5.65}U_{0.35}$-$Me_2BPDC(SDC)$. Both Zr-to-An and Th-to-U substitutions were not successful probably due to the differences in metal node stability and unfavorable transmetallation energy compared to the molecular complexes. U_6-Me_2BPDC-8 can transform into $U_{1.23}Th_{4.77}$-Me_2BPDC-8 under different transmetallation conditions, which is used as a precursor for subsequent Co node extension. Very recently, a spiropyran-based linker, namely 4,4'-(1',3',3'-trimethyl-6-nitrospiro[chromene-2,2'-indoline]-4',7'-diyl)dibenzoic acid (TNDA) has been installed on the unsaturated metal nodes of Th_6-Me_2BPDC-8 and $U_{1.23}Th_{4.77}$-Me_2BPDC-8, enabling the dynamic control of electronic behavior of these photoresponsive An-MOFs[125]. The amount of installed linker can be determined by acidic digestion of samples and subsequent ^{1}H NMR spectroscopic analysis. It is noted that the relatively robust Th_6-Me_2BPDC-8 and Th_6-Me_2BPDC-NO_3-10, possessing the same metal node arrangement as their Zr-analog, revealed structural crystalline-to-amorphous-to-crystalline changes upon exposure to different solvents due to the degree of metal node saturation. This solvent-induced structural memory

effect should be taken into consideration when preparing seemingly stable yet flexible An-MOFs.

2.2.4 Microwave-, ultrasonic-assisted synthesis

The high-intensity ultrasound methods enable tunable sonochemical syntheses of MOF meanwhile reverse micelle in organic solvents serves as MOF nanoreactors. The ultrasound-assisted reverse micelle (UARM) can be integrated to accelerate MOF syntheses as well as enhance certain physicochemical properties. Afzali and coworkers prepared one type of Th-MOF, namely Th-2,6-PDC via UARM[66]. In the typical UARM experiment, thorium nitrate and 2,6-pyridinedicarboxylic acid in H_2O were prepared and added to a mixture of sodium dodecyl sulfate and n-hexane. The resulting mixture was stirred at 85°C for 1 hour and entered into the ultrasound bath under various synthetic parameters including surfactant content, ultrasound duration, power, and temperature. Analysis of variance and response surface methodology was used to develop Th-2,6-PDC with high thermal stability, large surface area, and low mean particle size. By replacing ultrasonic with microwave heating, the microwave-assisted reverse micelle (MARM) method was developed and optimized in terms of solvent, surfactant, microwave irradiation power, and duration[67]. In both methods, after centrifuging, silver crystals of Th-2,6-PDC were washed by H_2O and dried under vacuum at 30 °C. The resulting optimal samples are assumed to have larger surface areas and more accessible mesopores compared to pyridinecarboxylate-based Th-MOFs. These methods can be considered as an efficient strategy for producing An-MOFs on a large lab-scale.

3. Structural analysis of An-MOFs
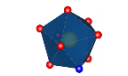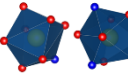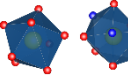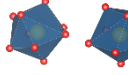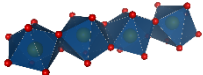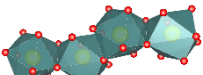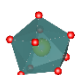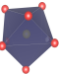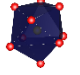
3.1 Metal core/cluster

The nuclearity of actinide centers in An-MOFs stems from the elusive competition between actinide hydrolysis-condensation, An-modulator, and An-ligand coordination under reaction conditions. Therefore, rather than a fine control, the serendipitous formation of actinide nodes is likely to occur. Nonetheless, architecture tuning is vital to the topology and reactivity of resulting An-MOFs. We classify An-based primary building units (PBUs) and/or secondary building units (SBUs) based on the oxidation states and coordination number (CN) of actinide centers besides. The coordination environment of actinides in An-MOFs as well as the main group or transition metal building blocks in heterometallic An-MOFs will be elaborated as the metal cluster arrangement varies in the coordinating modes of stabilizing ligands or terminal solvent molecules.

3.1.1 An(III) core/cluster

The use of trivalent TRU precursor inhibits an expansion of An(III)-MOFs due to the synthetic challenges. However, similarities and discrepancies in terms of core/cluster can be drawn from the limited number of An(III)-MOFs and trivalent lanthanide MOF (Ln(III)-MOFs) analogues. The actinide CN mainly being nine yields distorted capped square antiprismatic PBUs and edge-sharing chain-like SBUs (Table 1), analogue to Ln(III)-MOFs.

Table 1 Summary of structural aspects of An(III)-MOFs

An-MOFs	An (III) core/cluster [b]	Ligand [c]	PBU Coordination [d]	Ref.
Pu^{III}-1		2,6-PDC	[PuO$_8$N]: 2 η^1, 1 "NO$_2$", 4 H$_2$O	[49]
Pu$^{III, IV}$-3 [a]			[Pu^{III}O$_7$N]: 4 η^1, 1 "NO$_2$", 1 H$_2$O, [Pu^{IV}O$_6$N$_3$]: 3 "NO$_2$"	
Pu$^{III, IV}$-4 [a]			[Pu^{III}O$_8$]: 4 η^1, 4 H$_2$O, [Pu^{IV}O$_6$N$_3$]: 3 "NO$_2$"	
Pu-1α		MEL	[PuO$_9$]: 3 η^1, 1 η^2, 4 H$_2$O; 2 η^1, 1 η^2, 5 H$_2$O	[48]
Pu-1β			[PuO$_9$]: 2 η^1, 1 η^2, 5 H$_2$O	
PuC1P2	chain	C1P2	[PuO$_8$]: 4 η^1, 2 η^2	[126]
Am-GWMOF-6	chain	C6	[AmO$_9$]: 4 η^1, 2 η^2, 1 H$_2$O	[52]
Am1		Squarate	[AmO$_9$]: 3 η^1, 2 η^2, 2 H$_2$O	[51]
Am2			[AmO$_9$]: 3 η^1, 1 η^2, 2 H$_2$O, 1 η^2-C$_2$O$_4^{2-}$	
1-Am		MEL	[AmO$_9$]: 1 η^1, 2 η^2, 4 H$_2$O	[127]
Cm-2		MEL	[CmO$_9$]: 1 η^1, 2 η^2, 4 H$_2$O	[54]
Cf-1		MEL	[CfO$_8$]: 3 η^1, 5 H$_2$O	[128]
Cf1		Squarate	[CfO$_9$]: 3 η^1, 2 η^2, 2 H$_2$O	[51]
Cf2			[CfO$_9$]: 3 η^1, 1 η^2, 2 H$_2$O, 1 η^2-C$_2$O$_4^{2-}$	

(a) These compounds are of mixed valences; (b) The PBU composition is illustrated in the square bracket embedded with its schematic representation; (c) Linkers are abbreviated as: **2,6-PDC** = 2,6-pyridinedicarboxylic acid or dipicolinic acid (**DPA**); **MEL** = Mellitic acid; **C1P2** = methylenediphosphonate; **C6** = Adipic acid; (d) The η^1, η^2 refer to monodentate, bidentate carboxylate or phosphonate groups while "NO$_2$" means one nitrogen and two oxygen atoms from one linker. The η^2-C$_2$O$_4^{2-}$ is the bidentate oxalate offering two oxygen atoms to the PBU. Such description of PBU coordination environment is adopted hereafter.
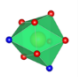
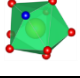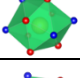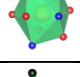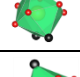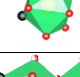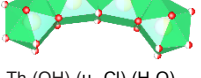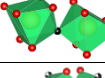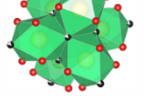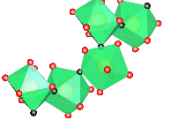However, mixed-valency clusters can only be observed in An (III)-MOFs. Despite of Pu(III) precursors, in Pu$^{III, IV}$-3 and Pu$^{III, IV}$-4, the CN of Pu^{3+}, Pu^{4+} is eight, nine, defining a distorted bicapped, tricapped trigonal prismatic PBU, respectively[49].
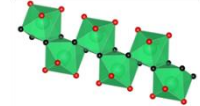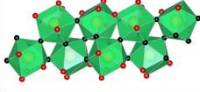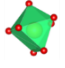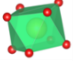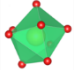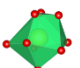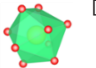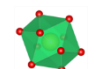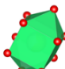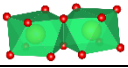
Moreover, Pu-1α has two unique Pu(III) PBUs of distorted monocapped square antiprismatic and muffin geometry, the latter of which dominates Pu-1β[48]. Compared with a large variety of polynuclear Ln(III) clusters[28], current building blocks in An(III)-MOFs are limited to monomer and chain-like SBUs. Novel An(III) oligomers will hopefully fill the gap between An(III)-MOFs and Ln(III)-MOFs.
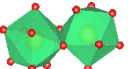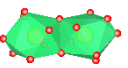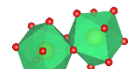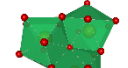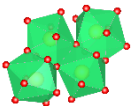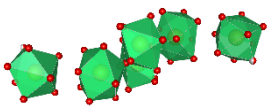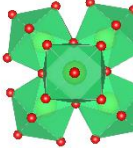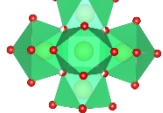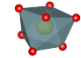
3.1.2 An(IV) core/cluster
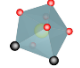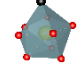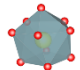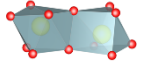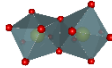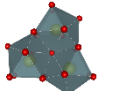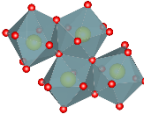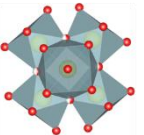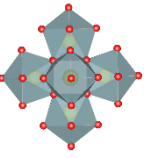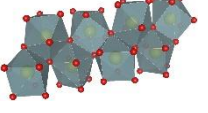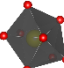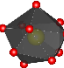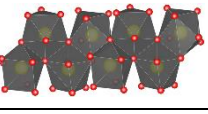
Tetravalent Th, U, Np, Pu based MOFs represent the most diverse category of An-MOFs, which can be used to seek out periodic trends in the structural divergence and convergence. They possess nitrogen-, chloride-, fluoride-containing or pure oxygen-bearing building blocks in the form of monomer, dimer, trimer, tetramer, hexamer and infinite chain (Table 2).
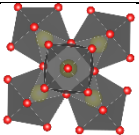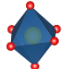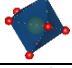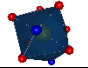
Table 2 Summary of structural aspects of An(IV)-MOFs

An-MOFs	An(IV) core/cluster	Ligand [a]	PBU Coordination [b]	Ref.
Th-2,3-PDC		2,3-PDC	2 η^1, 2 "NO", 3 H_2O	[129]
Th-2,3-PZDC	[ThO$_7$N$_2$]	2,3-PZDC	2 η^1, 2 "NO", 3 H_2O	[129]
Th-2,4-PDC		2,4-PDC	4 η^1, 2 "NO", 1 H_2O	[129]
Th-EDTA		EDTA	2 η^1, 1 "N$_2$O$_4$", 1 H_2O	[130]
Th-3,5-PYC	[ThO$_8$N]	3,5-PYC	5 η^1, 1 "NO", 2 H_2O	[131]
Th-NTA		NTA	4 η^1, 1 "NO$_3$", 1 H_2O	[130]
Th-2,5-PZDC		2,5-PZDC	[ThO$_6$N$_4$]: 4 "NO", 2 H_2O	[129]
Th-2,5-PDC		2,5-PDC	[ThO$_7$N$_3$]: 1 η^1, 3 "NO", 3 H_2O	[129]
Th-BTB		BTB	[ThO$_6$Cl$_3$]: 3 η^2, 3 Cl$^-$	[116]
Th-TPO-2		TPO	[ThO$_7$Cl$_2$]: 1 η^1, 3 η^2, 2 Cl$^-$	[132]
Th-Q[10]	Th$_4$(OH)$_8$(μ_2-Cl)$_2$(H_2O)$_{17}$	Q[10]	[ThO$_8$Cl$_2$]: 2 C=O, 1 μ_2-Cl, 6 H_2O	[133]
Th-BBP-1	Th$_2$O$_{12}$F	BBP	[ThO$_6$F]: 6 η^1, μ_2-F	[31]
TOF-3	Th$_6$F$_6$(μ_3-F)$_8$(COO)$_{12}$	ADA	[ThO$_4$F$_5$]: 4 η^1, 4 μ_3-F, 1 F$^-$	[74]
TOF-2	chain	BTC	[ThO$_6$F$_2$]: 6 η^1, 2 μ_2-F	[73]

Th-4-CPP	chain	4-CPP	[ThO$_4$F$_4$]: 4 η^1, 4 μ$_2$-F		[134]
TOF-1	chain	3,5-PDC	[ThO$_4$F$_5$]: 3 η^1, 5 μ$_2$-F, 1 H$_2$O		[72]
Th-BBP-2		BBP	[ThO$_7$]: 7 η^1		[31]
Th-BDC-2	[ThO$_8$]	BDC	4 η^2		[61]
Th-2,6-NDC		2,6-NDC	4 η^2		[135]
GWMOF-13		OBA	8 η^1		[98]
Th-BDC-4		BDC	8 η^1		[136]
Th-BA		BA	8 η^1		[137]
Th-BTC-5	[ThO$_8$]	BTC	8 η^1		[62]
Th-3-FA		3-FA	8 η^1		[63]
Th-2,5-FDC-2		2,5-FDC	6 η^1, 2 H$_2$O		[63]
Th-BTC-2	[ThO$_9$]	BTC	4 η^1, 2 η^2, 1 DMF		[62]
Th-BTC-3		BTC	4 η^1, 2 η^2, 1 DMF		[62]
Th-BTC-4		BTC	3 η^1, 1 η^2, 2 DMF, 1 η^2-NO$_3^-$		[62]
Th-SINAP-4		HCOOH	9 η^1		[89]
Th-SINAP-5		HCOOH	9 η^1		[89]
Th-M3,4-PYC		M3,4-PYC	4 η^1, 5 H$_2$O		[138]
Th-PAT		PAT	3 η^1, 1 η^2, 1 η^2-C$_2$O$_4^{2-}$, 2 H$_2$O		[105]
Th-SINAP-6	[ThO$_9$]	HCOOH	8 η^1, 1 DMF		[89]
Th-2-SB		2-SB	2 η^1, 2 η^2, 3 H$_2$O		[139]
Th-NTB	[ThO$_{10}$]	NTB	3 η^1, 3 η^2, 1 H$_2$O		[116]
ECUT-36		NTB	3 η^1, 3 η^2, 1 H$_2$O		[140]
Th-BDC-1		BDC	4 η^2, 2 DMF		[61]
Th-L$_{135}$		L$_{135}$	2 η^1, 1 η^2, 6 DMF		[141]
Th-IDA	[ThO$_{10}$]	IDA	2 η^1, 2 η^2, 2 η^2-C$_2$O$_4^{2-}$		[130]
Th-OA-(2,3)		OA	5 η^2-C$_2$O$_4^{2-}$		[142]
Th-TEDGA-OA		TEDGA, OA	2 η^3, 2 η^2-C$_2$O$_4^{2-}$		[143]
SCU-11		MTB	4 η^1, 2 η^2, 2 H$_2$O		[144]
Th-BCPBA	Th$_2$O$_{14}$	BCPBA	[ThO$_8$]: 6 η^1, 2 μ$_2$-OH		[136]
Th-M4,5-PYC	Th$_2$O$_{16}$	M4,5-PYC	[ThO$_9$]: 1 η^1, 2 μ$_2$-OH, 6 H$_2$O		[138]
Th-BTC-6	Th$_2$O$_{16}$	BTC	[ThO$_9$]: 4 η^1, 1 η^2, 2 μ$_2$-OH, 1 H$_2$O		[62]
Th-TPO-1	Th$_2$O$_{18}$	TPO	[ThO$_{10}$]: 3 η^1, 2 η^2, 2 μ$_2$-O, 1 H$_2$O		[132]
Th-BTC-1	Th$_3$O$_{21}$	BTC	[ThO$_{10}$]: 2 η^1, 3 η^2, 1 μ$_3$-O, 1 H$_2$O		[62]
SCU-8		BPTC			[117]

Name	Structure	Ligand	Coordination	Ref.
Th-NU-1011	$Th_4O_2(OH)_4(H_2O)_4(DMF)_2$	TCPB-Br$_2$	[ThO$_8$]: 4 η^1, 1 μ_3-O, 1 H$_2$O, 2 OH; [ThO$_9$]: 4 η^1, 2 μ_3-O, 1 H$_2$O, 2 DMF	[58]
Th-IHEP-5	$Th_6O_2(CO_2)_{10}(DMF)_4(H_2O)_2$	TCPP, 2,5-BPYDC	[ThO$_9$]: 6 η^1, 2 μ_3-O, 1 DMF; [ThO$_8$]: 6 η^1, 2 μ_3-O	[122]
Th-IHEP-6		TCPP, BPDC	[ThO$_9$]: 6 η^1, 2 μ_3-O, 1 DMF; [ThO$_8$]: 6 η^1, 2 μ_3-O	[122]
NU-905	$Th_6O_2(HCO_2)_4(H_2O)_6$	TCPP	[ThO$_9$]: 6 η^1, 1 μ_3-O, 1 H$_2$O, 1 HCOOH; [ThO$_8$]: 6 η^1, 1 H$_2$O, 1 HCOOH	[121]
Th-TATAB	I:$Th_6O_4(OH)_4(H_2O)_6(HCO_2)_8(CO_2)_4$	TATAB	[ThO$_9$]: 2 η^1, 2 HCOOH, 4 μ_3-O, 1 H$_2$O	[145]
Th-TTHA	II:$Th_6O_4(OH)_4(H_2O)_6(HCO_2)_4(CO_2)_8$	TTHA	2 η^1, 2 HCOOH, 4 μ_3-O, 1 H$_2$O	[146]
Th-TCI		TCI	4 η^1, 4 μ_3-O, 1 H$_2$O	[147]
Th-BDC-3	$Th_6O_4(OH)_4(H_2O)_6(CO_2)_{12}$	BDC	4 η^1, 4 μ_3-O, 1 H$_2$O	[61]
Th-SINAP-1	$Th_6O_4(OH)_4(H_2O)_6(HCO_2)_{12}$	HCOOH	[ThO$_9$]: 4 μ_2-HCOO$^-$, 2 μ_3-O, 2 μ_3-OH, 1 H$_2$O; [ThO$_9$]': 5 μ_2-HCOO$^-$, 2 μ_3-O, 2 μ_3-OH	[89]
Th-SINAP-7	$Th_6O_4(OH)_4(H_2O)_6(CO_2)_{12}$	1,4-NDC	[ThO$_9$]: 4 η^1, 4 μ_3-O, 1 H$_2$O	[92]
Th-SINAP-8		2,6-NDC		[92]
Th-SINAP-9		FA		[77]
Th-SINAP-10		BDC		[77]
Th-SINAP-11		4-CCN		[77]
Th-SINAP-12		PEDA		[77]
Th-SINAP-13		BPDC		[77]
Th-SINAP-14		ABDC		[77]
Th-SINAP-15		SDC		[77]
Th-NU-1008	$Th_6O_4(OH)_4(H_2O)_6(HCO_2)_4(CO_2)_8$ $Th_6O_4(OH)_4(H_2O)_6(CO_2)_{12}$	TCPB-Br$_2$	[ThO$_9$]: 4 η^1, 4 μ_3-O, 1 H$_2$O, 1 HCOOH; [ThO$_9$]': 2 η^1, 4 μ_3-O, 1 H$_2$O, 2 HCOOH	[58]
TOF-16		2,5-BNDC	4 η^1, 4 μ_3-O, 1 H$_2$O	[79]
Th-UiO-66-R	$Th_6O_4(OH)_4(DMF)_6(CO_2)_{12}$	BDC-R	4 η^1, 4 μ_3-O, 1 H$_2$O	[148]
Th$_6$-BPDC-12		BPDC	4 η^1, 4 μ_3-O, 1 DMF	[65]
Th-SINAP-2	$Th_6O_4(OH)_4(DMF)_2(HCO_2)_{12}$	HCOOH	[ThO$_8$]: 4 μ_2-HCOO$^-$, 2 μ_3-O, 2 μ_3-OH; [ThO$_9$]: 4 μ_2-HCOO$^-$, 2 μ_3-O, 2 μ_3-OH, 1 DMF	[89]
Th$_6$-Me$_2$BPDC-8		BPDC-Me$_2$	[ThO$_8$]: 2 η^1, 4 μ_3-O, 2 OH; [ThO$_9$]: 4 η^1, 4 μ_3-O, 1 OH	[65]
Th$_6$-Me$_2$BPDC-NO$_3$-10	$Th_6O_4(OH)_{14}(CO_2)_8$ $Th_6O_4(OH)_6(NO_3)_2(CO_2)_{10}$	BPDC-Me$_2$	[ThO$_9$]: 4 η^1, 4 μ_3-O, 1 OH; [ThO$_8$]: 2 η^1, 4 μ_3-O, 1 η^1-NO$_3^-$	[65]
U4-3, U4-4		C1P2	[UO$_7$]: 6 η^1, 1 H$_2$O	[111]
U4-BTC-2	[UO$_8$]	BTC	4 η^1, 2 η^2	[149]
U4-BDC-6		BDC	8 η^1	[150]
U4-2-H$_2$O		C1P2	4 η^2	[111]
U46-2		C1P2	4 η^1, 2 H$_2$O	[111]

U4-2-FA-1		2-FA	$[UO_6Cl_2]$: 4 η^1, 2 H_2O, 2 Cl^-	[60]
U4-BDC-(3,4)		BDC	$[UO_8Cl]$: 6 η^1, 2 DMF, 1 Cl^-	[59]
U4-BDC-5	$[UO_{10}]$	BDC	4 η^2, 2 DMF	[59]
U4-Cl$_2$DHBQ		Cl$_2$DHBQ	4 η^2, 2 H_2O	[38]
U4-5	U_2O_{12}	C1P2	$[UO_7]$: 3 η^1, 2 η^2	[111]
U4-MEL	U_2O_{14}	MEL	$[UO_8]$: 5 η^1, 2 μ_2-OH, 1 H_2O	[46]
U4-BTC-1	U_3O_{22}	BTC	$[UO_8]$: 6 η^1, 1 μ_3-O, 1 H_2O	[37]
U4-BDC-2	$U_4O_2(CO_2)_4(HCO_2)_6$	BDC	$[UO_8]$: 4 η^1, 2 HCOOH, 2 μ_3-O $[UO_9]$: 6 η^1, 1 HCOOH, 1 μ_3-O	[151]
U4-FA-2	$U_6O_4(OH)_4(H_2O)_2(HCO_2)_4(CO_2)_8$	FA	$[UO_8]$: 3 η^1, 1 HCOOH, 4 μ_3-O; $[UO_9]$: 4 η^1, 1 H_2O, 4 μ_3-O	[151]
U$_6$-Me$_2$BPDC-8	$U_6O_4(OH)_{14}(CO_2)_8$	BPDC-Me$_2$	$[UO_8]$: 2 η^1, 4 μ_3-O, 2 OH; $[UO_9]$: 4 η^1, 4 μ_3-O, 1 OH	[65]
U$_6$-Me$_2$BPDC-TFA-10	$U_6O_4(OH)_6(TFA)_4(CO_2)_{10}$	BPDC-Me$_2$	$[UO_9]$: 4 η^1, 4 μ_3-O, 1 OH; $[UO_8]$: 2 η^1, 4 μ_3-O, 1 η^2-TFA	[65]
U4-BPDC	$U_6O_4(OH)_4(H_2O)_6(CO_2)_{12}$	BPDC	$[UO_9]$: 4 η^1, 4 μ_3-O, 1 H_2O	[152]
U4-NDC		2,6-NDC		[152]
U4-BDC-1		BDC		[152]
U4-FA-1		FA		[152]
U4-C5	$U_6O_4(OH)_4(NO_3)_6(CO_2)_6$	C5	$[UO_9]$: 3 η^1, 4 μ_3-O, 1 η^2-NO$_3^-$	[39]
U4-1,2-BDC	chain	1,2-BDC	$[UO_8]$: 4 η^1, 3 μ_3-O, 1 H_2O	[46]
Np-MeP-1		MeP	$[NpO_8]$: 5 η^1, 1 H_2O, 1 η^2-NO$_3^-$	[44]
NpC1P2-1		C1P2	$[NpO_8]$: 6 η^1, 2 H_2O	[45]
Np-BDC-1		BDC	$[NpO_{10}]$: 4 η^2, 2 DMF	[153]
Np-1,2-BDC	chain	1,2-BDC	$[NpO_8]$: 4 η^1, 3 μ_3-O, 1 H_2O	[46]
Np-BDC-2		BDC	$[NpO_9]$: 4 η^1, 4 μ_3-O, 1 H_2O	[153]
Np-BPDC		BPDC		[153]
Np-BPDC-NH$_2$		BPDC-NH$_2$		[153]

Np-TPDC-NH$_2$	Np$_6$O$_4$(OH)$_4$(H$_2$O)$_6$(CO$_2$)$_{12}$	TPDC-NH$_2$		[153]
Pu-1		MeP	[PuO$_6$]: 6 η^1	[47]
Pu-2		MeP	[PuO$_7$]: 6 η^1, 1 H$_2$O	[47]
Pu^{IV}-2		2,6-PDC	[PuO$_7$N$_2$]: 2 "NO$_2$", 3 H$_2$O	[49]

(a) Linkers are abbreviated as: **2,3-PDC** = 2,3-pyridinedicarboxylic acid; **2,3-PZDC** = 2,3-pyrazinecardiboyxlic acid; **2,4-PDC** = 2,4-pyridinedicarboxylic acid; **EDTA** = Ethylenediaminetetraacetic acid; **3,5-PYC** = 3,5-pyrazoledicarboxylic acid; **NTA** = nitrilotriacylic acid; **2,5-PZDC** = 2,5-pyrazinecardiboyxlic acid; **2,5-PDC** = 2,5-pyridinedicarboxylic acid; **BTB** = 1,3,5-tris(4-carboxyphenyl)benzene; **TPO** = tris-(4-carboxylphenyl)phosphine oxide; **Q[10]** = Cucurbit[10]uril; **BBP** = 1,4-benzenebisphosphonic acid; **ADA** = 1,3-adamantanediacetic acid; **BTC** = 1,3,5-benzenetricarboxylic acid; **4-CPP** = 4-carboxyphenylphosphonic acid; **3,5-PDC** = 3,5-pyridinedicarboxylic acid; **BDC** = 1,4- benzenedicarboxylic acid; **BA** = Benzoic acid; **3-FA** = 3-furoic acid; **2,5-FDC** = 2,5-furandicarboxylate; **M3,4-PYC** = 1-methyl-3,4-pyrazoledicarboxylic acid; **PAT** = phosphonoacetic acid; **2-SB** = 2-sulfocarboxylbenzoic acid; **NTB** = 4,4',4'-nitrilotribenzoic acid; **L$_{135}$** = 5-(1,8-naphthalimido)-isophthalate acid; **IDA** = iminodiacetic acid; **OA** = Oxalic acid; **TEDGA** = tetraethyldiglycolamide; **MTB** = tetrakis(4-carboxyphenyl)methane; **BCPBA** = 3,5-bis (4-carboxylphenoxy)benzoic acid; **M4,5-PYC** = 1-methyl-4,5-pyrazoledicarboxylic acid; **BPTC** = [1,1'-biphenyl]-3,4',5-tricarboxylicacid; **TCPB-Br$_2$** = 1,4-dibromo-2,3,5,6-tetrakis(4-carboxyphenyl) benzene; **TCPP** = meso-tetra(4-carboxyphenyl) porphine; **2,5-BPYDC** = 2,2'-bipyridine-5, 5'-dicarboxylic acid; **BPDC** = biphenyl-4,4'-dicarboxylic acid; **TATAB** = 4,4',4"-s-triazine-1,3,5-triyltri-p-aminobenzoate; **TTHA** = 1,3,5-triazine-2,4,6-triamine hexaacetic acid; **TCI** = tris (2-carboxyethyl) isocyanurate; **1,4-NDC** = 1,4-naphtalenedicarboxylic acid; **2,6-NDC** = 2,6-naphtalenedicarboxylic acid; **FA** = fumaric acid; **4-CCN** = 4-carboxycinnamic acid; **PEDA** = 1,4-phenylenediacrylic acid; **ABDC** = 4,4'-azobisbenzoic acid; **SDC** = 4,4'-stilbenedicarboxylic acid; **2,5-BNDC** = 2,2'-dihydroxy-[1,1'-binaphthalene]-5,5'-dicarboxylic acid; **BDC-R** = substituted 1,4- benzenedicarboxylic acid (R = H, NH$_2$, (NH$_2$)$_2$, OH, CH$_3$, OCH$_3$, (OCH$_3$)$_2$, NO$_2$, Cl, Br, Cl$_2$, Br$_2$, and (CF$_3$)$_2$); **BPDC-Me$_2$** = 2,2'-dimethylbiphenyl-4,4'-dicarboxylate; **2-FA** = 3-furoic acid; **Cl$_2$DHBQ** = 2,5-dichloro-3,6-dihydroxybenzoquinone; **C5** = glutaric acid; **1,2-BDC** = 1,2-benzenedicarboxylic acid; **MeP** = methylphosphonate; **BPDC-NH$_2$** = 2-amino-(1,1'-biphenyl)-4,4'-dicarboxylic acid; (b) The "NO", "N$_2$O$_4$", "NO$_3$" mean one nitrogen and one oxygen atom, two nitrogen and four oxygen atoms, one nitrogen and three oxygen atoms from one linker, respectively. The η^2-NO$_3^-$, η^2-TFA are bidentate ligands offering two oxygens to one PBU while μ_2-HCOO$^-$ is the bridging formate, carboxylate group with two oxygen atoms at two PBUs.

The nitrogen-bearing Th(IV), Pu(IV) PBUs (CN = 9, 10) are observed with N, O-donor ligands, especially where coordinating nitrogen atoms and carboxylate groups are in neighboring positions. The chloride tends to enter the coordination sphere of Th(IV), U(IV) when using chloride-containing ionic liquid or hydrochloric acid as synthetic modulator. For instance, the chloride ion bridges neighboring thorium PBUs to construct a tetramer SBU inside the cavity of Th-Q[10] [133]. In a similar way, the fluoride-bearing thorium SBU has been revealed as dimers, hexamers, and chains (CN

= 7-9) based on bridging fluoride. It should be noted that the $Th_6(\mu_3\text{-}F)_8$ octahedral cluster precedes the commonly observed $Zr_6(\mu_3\text{-}O)_4(\mu_3\text{-}OH)_4$ hexamer in Zr-MOFs. Besides, by using linkers of different preferred coordination geometry under fluoride-bearing reaction condition, it leads to distinct vertex- or edge-sharing chain-like SBUs.

The oxygen-containing An(IV) monomer has a wide range of coordination numbers, in which every type of thorium PBU (CN = 8-10) has two geometries. In Th-BTC and Th-SINAP compounds, the coordination environment of PBUs differs by the number of coordinating solvent and the bridging mode of ligands. Moreover, a transition of the thorium PBU geometry can be achieved upon activation at high temperature. For example, the bicapped tetragonal prism of $[ThO_{10}]$ in SCU-11 transforms to tetragonal prism of $[ThO_8]$ by losing two water molecules, leaving open thorium sites for Xe/Kr gas separation[144]. Such solvent-tethering PBUs are also found in ten-coordinate bicapped square-antiprismatic U and Np polyhedra. Edge-sharing dimers, trimers and tetramers are observed in thorium and uranium SBUs. It is likely that the tritopic carboxylate ligands contributes to the formation of μ_3-O-centered trinuclear SBU consisting of Th(IV) and U(IV) PBUs mutually confocal in a strict trigonal plane. The Th-NU-1011[58] and U4-BDC-2[151] have eight-, and nine-coordinated PBUs and every two PBUs are bridged by two μ_3-O to form a rhombic shaped, tetranuclear cluster with planar D_{2h} symmetry, the connectivity number of which are eight and six, respectively. Such mixed PBUs can be found in An(IV) hexamer. The hexanuclear SBU consists of an inner core, in which six An(IV) occupy the vertices of the octahedron while the triangular faces of the octahedron are alternately capped by μ_3-O or μ_3-OH. The edges of the octahedron are bridged by carboxyl from either linkers or modulators. Together with hexamers built of nine-coordinated PBUs, these clusters are eight-, ten-, and twelve-connected (hereafter as 8-c, 10-c, 12-c) by organic linkers. Azole-Th-1 has thorium hexamers containing $[ThO_9]$, $[ThO_7N_2]$ or $[ThO_5N_4]$ PBUs, representing the first case of hybrid Th_6 cluster bearing nitrogen atoms[78].The glycine-decorated Pu(IV) based hexamer was reported in the literature[154], yet this $Pu_6(OH)_4O_4$ core has not been realized in Pu(IV)-MOFs despite that the recent Pu-UiO-66 was assumed to possess this hexanuclear SBU[50]. One particular hexamer is found in Th-IHEP-5, Th-IHEP-6[122] and NU-905[121]. The mixed PBUs are bridged by two μ_3-O to form a tetranuclear cluster, which is linked by another pair of $[ThO_9]$ via bridging carboxylate groups to form pseudo hexanuclear SBU simplified as 8-c node. The chain-like U(IV), Np(IV) SBUs are only found in the presence of 1,2-BDC.
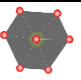
The organic linkers, modulators or solvents of versatile coordination geometry will stabilize An(IV) cores or clusters of different symmetry, connectivity, leading to a growing number of An (IV)-MOFs.

3.1.3 An(V) core/cluster

Np(V) is the predominant stable pentavalent actinide under reaction condition and there are merely eight cases of Np(V)-MOFs (Table 3), wherein the actinyl-actinyl

interaction (AAI) is prevalent presumably due to the strong coordination ability of axial oxygen. It leads to the formation of chain-, layer- and cluster-like SBUs. In NSS-1, NSS-2, and NSS-3, one double-wheel-shaped actinide node in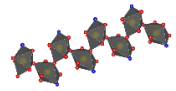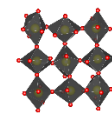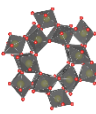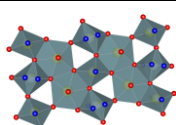 C_{6h} symmetry consists of twelve $[NpO_7]$ PBUs and six $[NpO_7]'$ PBUs. The $[NpO_7]$ PBUs share equatorial edge to form a dimer that aggregates into a double-wheel motif via AAI, wherein the $[NpO_7]'$ donate an AAI to a dimer and accept two AAI from another dimer. This configuration results in a strong distortion of $[NpO_7]'$ with one terminal oxygen[155]. The bridging role of fluoride should be emphasized in order to construct novel neptunyl clusters combining with AAI in the presence of multitopic linkers. Very recently, several stable U(V)-containing molecular structures have been isolated from aqueous medium using N,O-donor ligands[156–158]. One unique case includes a large rhombus-shaped cluster bearing eight P-type U(VI) and one central U(V), serving as one of the largest mixed-valent uranium cluster[158]. Besides, U(V)/U(VI) inorganic layers represent the first case of uranium-based coordination polymer with a unique Kagomé topology[159]. These findings indicate an expansion of U(V)-based clusters for redox-active An-MOFs.

Table 3 Summary of structural aspects of An(V)-MOFs

An-MOFs	Np(V) core/cluster	Ligand [a]	PBU Coordination [b]	Ref.
Np-C5	$[NpO_8]$	C5	3 η^2	[43]
NRCP-1		CB[6], C6BPCA	2 η^2, 1 H_2O, 1 C=O	[160]
Np-NIC	chain	NIC	$[NpO_6N]$: 2 η^1, 1 H_2O, 1 η^1-N, 1 Np=O	[42]
Np-INA		INA		
Np-MEL	layer	MEL	$[NpO_7]$: 1 η^1, 4 Np=O	[46]
NSS-1	$(NpO_2)_{18}(F/OH)_6(H_2O)_{18}(CO_2)_{12}$	TCPB	$[NpO_7]$: 1 η^1, 2 Np=O, 1 H_2O, 1 μ_2-F or OH	[155]
NSS-2		TCPB-Br$_2$	$[NpO_7]'$: 2 η^1, 2 Np=O, 1 H_2O	
NSS-3		TCPB-NO$_2$		
U-TAZ-2	layer	TAZ	$[U^VO_4N_2]$: 2 η^1-N, 4 μ_3-OH	[159]
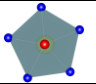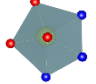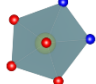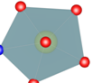
(a) Linkers are abbreviated as: **CB[6]** = Cucurbit[6]urils, **C6BPCA =** 1,1'-(hexane-1,6-diyl)bis(4-carboxypyridin-1-ium)**; NIC** = pyridine-3-carboxylic acid (nicotinic acid); **INA** = pyridine-4-carboxylic acid (isonicotinic acids); **TCPB** = 1,2,4,5-tetrakis(4-carboxyphenyl)benzene; **TCPB-NO$_2$** = 1-nitro-2,3,5,6-tetrakis(4-carboxyphenyl)benzene; **TAZ** = 1,2,4-triazole (b) η^1-N means one nitrogen atom provided by a N-donor ligand. Np=O refers to the axial oxygen atom from neighboring neptunyl.
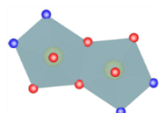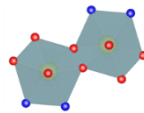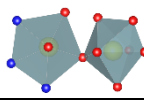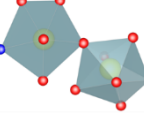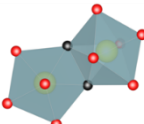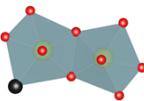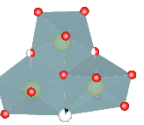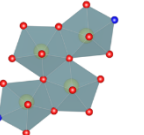
3.1.4 An (VI) core/cluster
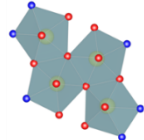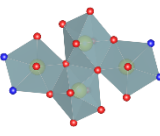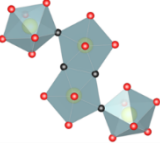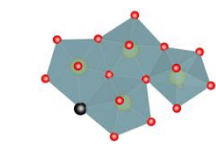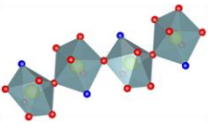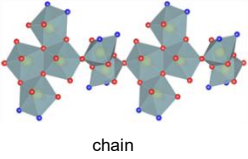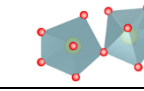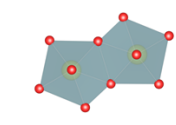
As the equatorial plane of uranyl center is four, five, or six-coordinated by four, five, or six oxygen atoms from O-donor ligands, it constructs tetragonal bipyramidal (T-

type), pentagonal bipyramidal (P-type), and hexagonal bipyramidal (H-type) as defined in a previous review[4]. Due to the relatively large number of mononuclear oxygen-bearing PBUs in uranyl-organic frameworks, the equatorial plane of T-, P-, or H-type PBU is briefed as an oxygen population, wherein oxygen atoms originate from O-donor ligands, or solvents (Table S2) and are abbreviated as (xyz), in which x, y, z represents the number of oxygen atoms from monodentate, bidentate carboxylate or phosphonate groups of ligand and solvent molecule, respectively. In the 6-, 7-, and 8-coordinated monomer, the (400), (221), and (060) are most likely to occur, respectively while othe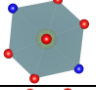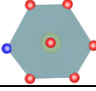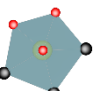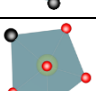r mononuclear polyhedra assemble in various coordination forms (Fig.S1). In the sole case of Pu(VI)-MOFs, the plutonyl monomer can be described as (221).
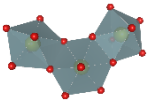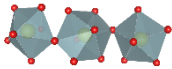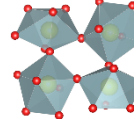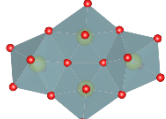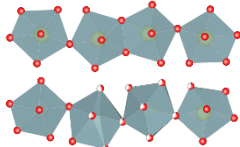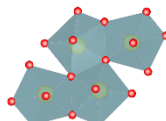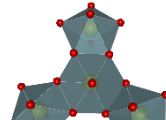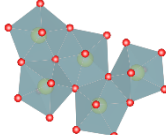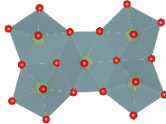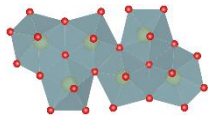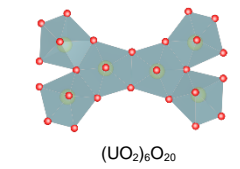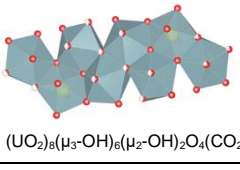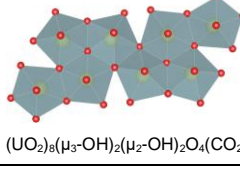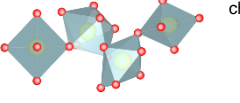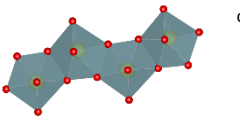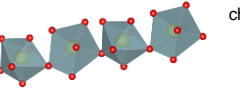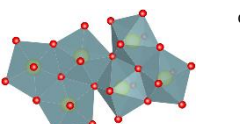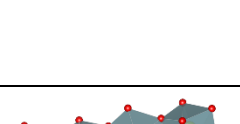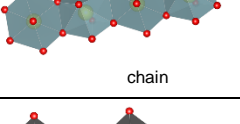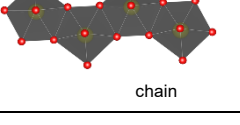
Table 4 Summary of structural aspects of An(VI)-MOFs

An-MOFs	An(VI) core/cluster	Ligand [a]	PBU Coordination [b]	Ref.
U-TAZ-1	[UO$_2$N$_5$]	TAZ	5 η^1-N	[161]
U-XBA-(6,7,10)	[UO$_4$N$_3$]	XBA, TPY		[162]
U-XBDC-(1-6)		XBDC, TPY	2 η^1, 1η^3-N	[163]
U-TDC-10		TDC, TPY		[163]
U-BCHBA-3	[UO$_5$N$_2$]	BCHBA, 1,10-phen	1 η^1, 1 η^2, 1 η^2-N	[164]
U-BPTCD-2		BPTCD, 1,10-phen		[96]
U-XBA-(1,3)		XBA, 1,10-phen		[162]
U-TDC-(5,6)		TDC, 1,10-phen		[165]
U-NIP-5		NIP, 2,2-bipy		[166]
UMON	[UO$_6$N]	IDA	2 η^1, 1 "NO$_2$"	[94]
CPP-U3		CPP, dib	2 η^1, 1 η^2, 1 η^1-N	[119]
CPP-U4		CPP, bbi	2 η^1, 1 η^2, 1 η^1-N	[119]
U-1,2-BDC-1		1,2-BDC, BPP	4 η^1, 1 η^1-N	[93]
U-1,2-BDC-2		1,2-BDC, BPE	4 η^1, 1 η^1-N	[93]
U-BDC-2		BDC-Br$_2$, 4,4-bipyidine	4 η^1, 1 η^1-N	[167]
U-BDC-1	[UO$_6$N$_2$]	BDC, dmpi	2 η^2, 2 η^1-N	[85]
U-DBSF-(1,2)		DBSF, 2,2-bipy		[168]
U-DBSF-(5,6)		DBSF, 2,2-bipy		[100]
U-H3		Histidine, 2,2-bipy		[169]
U-C6-2		C6, 2,2-bipy		[170]
U-C7		C7, 1,10-phen		[170]
U-C8		C8, 2,2-bipy		[170]
U-C9-(1,2)		C9, 1,10-phen		[170]
U-C13-1		C13, 2,2-bipy	2 η^2, 1 η^2-N	[170]
U-C13-2		C13, 1,10-phen		[170]
U-BQDC-1		BQDC, 1,10-phen		[171]
U-CHDC-(5,6)		CHDC, 2,2-bipy		[172]
U-2-CCN-3		2-CCN, 2,2-bipy		[114]
U-C-1,4-CHDC-4		C-1,4-CHDC, 2,2-bipy		[173]

U-TDC-4		TDC, 2,2-bipy		[165]
U-XBA-13		XBA, 2,2-bipy		[174]
U-XBA-15		XBA, 1,10-phen		[174]
UOM-1		DBTFA, 1,10-phen		[175]
UOM-2		DBSF, 1,10-phen		[175]
UOM-3		DBSF, 1,10-phen		[175]
U-1,2,6-BPTC-6		1,2,6-BPTC, 1,10-phen		[123]
U-PPBA	$[UO_6N_2]$	PPBA	2 η^2, 2 η^1-N	[176]
U-GDL	$[UO_7N]$	GDL	2 η^2, "NO"	[177]
U-Q[10]	$[UO_4Cl_3]$	Q[10]	2 H_2O, 3 Cl^-; $[UO_6Cl]$: 4 H_2O, 1 Cl^-	[133]
U-BCBP-5	$[UO_6Cl]$	BCBP	2 η^1, 1 η^2, 1 Cl^-	[83]
U-L2-OMe-2	$(UO_2)_2O_4N_4$	L2OMe, 1,10-phen	$[UO_5N_2]$: 1 η^1, 2 μ_2-O, 1 η^2-N	[178]
U-XBA-14		XBA, 1,10-phen		[174]
U-H2	$(UO_2)_2O_6N_4$	Histidine, 1,10-phen	$[UO_6N_2]$: 1 η^2, 2 μ_2-O, 1 η^2-N	[169]
U-C9-3		C9, 1,10-phen		[170]
U-XBA-(5,8,9,11,12)	$(UO_2)_2O_6N_3$	XBA, TPY	$[UO_7]$: 2 η^1, 1 η^2, 1 μ_2-O; $[UO_4N_3]$: 1 η^1, 1 μ_2-O, 1 η^3-N	[162]
U-IPBP-5	$(UO_2)_2O_8N$	IPBP	$[UO_7]$: 2 η^1, 1 η^2, 1 μ_2-O; $[UO_6N]$: 1 η^1, 1 η^2, 1 μ_2-O, 1 η^1-N	[107]
U-PBP-3	$(UO_2)_2O_6F_2$	PBP	$[UO_5F_2]$: 3 η^1, 2 μ_2-F	[112]
URCP7-C7	$(UO_2)_2O_7Br$	CB[6], C7BPCA	$[UO_7]$: 1 η^2, 2 μ_2-OH, 1H_2O; $[UO_6Br]$: 1 η^2, 2 μ_2-OH, 1Br$^-$	[35]
URCP8-C7	$(UO_2)_3O_9Br$	CB[6], C7BPCA	$[UO_7]$: 1 μ_3-O, 2 μ_2-OH, 2 H_2O; $[UO_6Br]$: 1 η^1, 1 μ_2-OH, 1 μ_3-O,1 Br$^-$, 1 H_2O	[35]
U-H1	$(UO_2)_4O_{12}N_2$	Histidine	$[UO_6N]$: 1 η^1, 1 "NO", 1 μ_2-O, 1 μ_3-O; $[UO_7]$: 2 η^1, 3 μ_3-O	[169]

U-L1-OMe-1	$(UO_2)_4O_8N_6$	L1-OMe, 1,10-phen	[UO_5N_2]: 1 η^2, 1 η^2-N, 1 μ_2-O, 1 μ_3-O [UO_6N]: 1 η^2, 1 η^1-N, 1 μ_2-O, 2 μ_3-O	[178]
UNSL-1	$(UO_2)_4O_{10}N_4$	SA, 1,10-phen	[UO_5N_2]: 1 η^1, 1 η^2-N, 1 μ_2-OH, 1 μ_3-O	[97]
U-XBA-4		XBA, 1,10-phen	[UO_7]: 1 η^1, 1 H_2O, 1 μ_2-OH, 2 μ_3-O	[162]
UPF-104	$(UO_2)_4O_{12}F_4$	TPPM	[UO_4F_3]: 2 η^1, 3 μ_2-F [UO_6F]: 3 η^1, 1 μ_2-F, 1 H_2O	[76]
URCP9-C7	$(UO_2)_4O_{12}Br$	CB[6], C7BPCA	[UO_7]: 1 η^2, 1 μ_3-O, 1 μ_2-OH, 2 H_2O; [UO_6Br]: 1 η^2, 2 μ_3-O,1 μ_2-Br, 1 H_2O; [UO_7]': 2 μ_3-O, 2 μ_2-OH, 1 H_2O; [UO_6Br]': 1 η^1, 1 μ_3-O, 1 μ_2-OH,1 μ_2-Br, 1 H_2O	[35]
U-3,5-DCPCA	chain	3,5-DCPCA	[UO_6N]: 1 η^2, 2 μ_2-O 1 η^1-N	[84]
U-3,5-DBPCA		3,5-DBPCA		[84]
U-L1-OMe-2	chain	L1-OMe, 1,10-phen	[UO_5N_2]: 1 η^1, 2 μ_2-O, 1 η^2-N	[178]
U-L2-OMe-1		L2-OMe, 1,10-phen	[UO_5N_2]': 1 η^1, 1 η^2-N, 1 μ_2-OH, 1 μ_3-O [UO_7]: 1 η^1, 1 H_2O, 1 μ_2-OH, 2 μ_3-O	[178]
U-BPDC-1	$(UO_2)_2O_9$	BPDC	[UO_7]: 2 η^1, 1 η^2, 1 μ_2-O	[179]
CPP-U1	$(UO_2)_2O_8$	CPP		[119]
CPP-U2		CPP		[119]
U-PMB-2		PMB	[UO_7]: 3 η^1, 1 η^2	[108]
DPTP-U2		DPTP		[180]
U-MPDP-1		MPDP		[34]
U-1,3-PDA-1		1,3-PDA		[181]
SCU-7		TTTPC	[UO_7]: 3 η^1, 2 μ_2-O	[182]
U-1,2-BDC-6		1,2-BDC	[UO_7]: 3 η^1, 2 μ_2-O	[183]
U-BQDC-2		BQDC	[UO_7]: 2 η^1, 2 μ_2-O, 1 H_2O	[171]
U-BCBP-4		BCBP	[UO_7]: 2 η^1, 2 μ_2-O, 1 H_2O	[83]
U-BDC-6		BDC		[184]
U-IPBP-3		IPBP		[107]
U-IPBP-4		IPBP	[UO_7]: 1 η^1, 1 η^2, 2 μ_2-OH	[107]
U-1,3-BDC-2		1,3-BDC		[185]
U-NIP-4		NIP		[185]
U-BDC-NH_2		BDC-NH_2		[185]

28

U-C1P2-1	(UO₂)₃O₁₂	C1P2	[UO₈]: 3 η²; [UO₇]: 5 η¹	[186]
U-1,2-BDC-5		1,2-BDC	[UO₈]: 2 η¹, 2 η² (μ₂-O); [UO₇]: 3 η¹, 2 μ₂-O	[183]
U-OA-1	(UO₂)₄(C₂O₄)₄(H₂O)₄	OA	[UO₇]: 2 μ₂-OH, 1 η², 1 H₂O	[187]
SCU-6	(UO₂)₄(OH)O(COOH)₆	TTTPC	[UO₇]: 2 η², 1 HCOOH [UO₇]': 2 η¹, 2 μ₂-O, 1 μ₃-O	[182]
UMOFUA		1,4-(DAO)Bz	[UO₇]: 1 η¹, 2 μ₂-O, 1 μ₃-O, 1 H₂O [UO₇]': 1 η¹, 2 μ₂-O, 2 μ₃-O	[36]
U-TDCS-1	(UO₂)₄(μ₂-OH)₄(H₂O)₂(CO₂)₆	TDCS	[UO₇]: 2 η¹, 1 η², 1 μ₂-O [UO₇]': 1 η¹, 1 H₂O, 3 μ₂-O [UO₇]'': 1 η¹, 2 H₂O, 2 μ₂-O	[188]
U-DBSF-3	(UO₂)₄O₁₄	DBSF	[UO₇]: 1 η¹, 1 η², 2 μ₃-O [UO₇]': 2 η¹, 1 η², 1 μ₃-O	[189]
U-DBSF-4		DBSF		[189]
U-DBSF-7		DBSF		[100]
U-BDC-9		BDC		[102]
U-MSTB		MSTB		[188]
URCP2-C8		CB[6], C8BPCA	[UO₇]: 1 η¹, 1 η², 2 μ₃-O; [UO₇]': 3 η¹, 1 H₂O, 1 μ₃-O	[88]
U-C1P2-2	(UO₂)₄O₁₅	C1P2	[UO₇]: 1 η¹, 2 η²; [UO₇]: 3 η¹, 1 η², [UO₇]': 2 η²,1 H₂O; [UO₈]: 3 η²	[186]
U-1,2,4-BTC-1	(UO₂)₅O₁₆	1,2,4-BTC	[UO₇]: 2 η¹, 1 μ₂-O, 2 μ₃-O; [UO₇]': 2 η¹, 3 μ₃-O; [UO₇]'': 3 η¹, 1 μ₂-O, 1 μ₃-O; [UO₇]''': 2 η¹, 2 μ₃-O, 1 HCOOH; [UO₇]'''': 2 η¹, 2 μ₂-O, 1 μ₃-O	[190]
URCP5-C7	(UO₂)₅O₁₆	CB[6], C7BPCA	[UO₇]: 1 η¹, 1 η¹-SO₄²⁻, 1 μ₂-OH, 1 μ₃-O, 1 H₂O; [UO₇]': 1 η¹-SO₄²⁻, 1 μ₂-OH, 1 μ₃-O, 2 H₂O; [UO₈]: 2 η¹-SO₄²⁻, 2 μ₃-O	[35]
U-IMDC-3	(UO₂)₆O₂₀	IMDC	[UO₈]: 2 μ₂-O, 1 μ₃-O, 1 η¹, 1 η²; [UO₇]: 1 μ₂-O, 2 μ₃-O, 1 η¹, 1 H₂O; [UO₇]': 1 μ₂-O, 3 μ₃-O, 1 η¹	[86]

U-C4A4-CB[6]-2	 $(UO_2)_6O_{20}$	CB[6], C4BPCA	[UO_7]: 1 μ_2-$C_2O_4^{2-}$, 1 η^2-$C_2O_4^{2-}$, 1 μ_2-OH, 1 μ_3-O; [UO_7]': 2 μ_2-OH, 1 μ_3-O, 2 H_2O	[191]
U-PSTB-9	 $(UO_2)_8(\mu_3$-$OH)_6(\mu_2$-$OH)_2O_4(CO_2)_{10}$	PSTB	[UO_7]: 2 η^1, 1 μ_3-OH, 1 μ_2-OH, 1 H_2O; [UO_7]': 2 η^1, 2 μ_3-OH, 1 μ_2-OH; [UO_7]'': 2 η^1, 3 μ_3-OH; [UO_7]''': 1 η^1, 3 μ_3-OH, 1 μ_2-O$^-$	[188]
U-XylBpy4CA-1	 $(UO_2)_8(\mu_3$-$OH)_2(\mu_2$-$OH)_2O_4(CO_2)_4$	XylBpy4CA	[UO_7]: 1 η^1, 1 μ_3-OH, 1 μ_2-OH, 1 η^2-$C_2O_4^{2-}$; [UO_7]': 1 η^1, 2 μ_3-OH, 1 η^2-$C_2O_4^{2-}$; [UO_7]'': 1 η^1, 3 μ_3-OH, 1 μ_2-OH; [UO_7]''': 1 η^1, 3 μ_3-OH, 1 μ_2-$C_2O_4^{2-}$	[192]
U-TDCS-2	chain	TDCS	[UO_6]: 2 η^1, 2 μ_2-OH; [UO_7]: 1 η^1, 1 η^2, 2 μ_2-OH	[188]
U-PAT	chain	PAT	[UO_7]: 2 η^1, 1 η^2, 1 μ_2-O	[105]
U-BPDA-1	chain	BPDA	[UO_7]: 2 η^1, 1 η^2, 1 μ_2-O	[193]
U-1,2,6-BPTC-1				[123]
U-IMDC-4	chain	IMDC	[UO_7]: 3 μ_3-OH, 1 μ_2-O , 1 η^1; [UO_7]': 3 μ_3-OH, 1 μ_2-OH, 1 η^1; [UO_7]'': 2 μ_3-OH, 1 μ_2-O, 2 η^1	[86]
U-TCI-1		TCI	[UO_7]: 2 η^1, 3 μ_3-OH	[194]
U-1,2-PDA-1	 chain	1,2-PDA	[UO_8]: 2 η^2, 2 η^1	[181]
Np-MeP-2	 chain	MeP	[NpO_7]: 3 η^1, 1 η^2	[44]
Pu-C5		C5	[PuO_7]: 2 η^1, 1 η^2, 1 H_2O	[43]
Pu-SA-1		SA	[PuO_7]: 4 η^1, 1 H_2O	[195]
Pu-SA-2		SA	[PuO_8]: 3 η^2	[195]

(a) Linkers are abbreviated as: **XBA** = X-benzoic acid (X = Br, I) ; **TPY** = 2,2':6',2''-terpyridine; **XBDC** = X-1,4-benzene dicarboxylic acid (X = Me, Cl, Br, I); **TDC** = 2,5-thiophenedicarboxylic acid ligand; BCHBA = 4,4'-(azanediylbis(methylene))dibenzoic acid; **BPTCD** = 3,3′,4,4′-benzophenonetetracarboxylic acid; **CPP** = 2-(carboxyethyl)phenylphosphinic acid; **dib** = 1,4-di(1H-imidazol-1-yl)benzene; **bbi** = 1,4-di(1H-imidazol-1-yl)butane; **BPP** = 1,3-di(4-pyridyl)propane); **BPE** =

4,4-vinylenedipyridine; **BDC-Br₂** = 2,5-dibromoterephthalic acid; **dmpi** = 1-(4-(1Himidazol-1-yl)-2,5-dimethylphenyl)-1H-imidazole; **DBSF** = 4,4'-dicarboxybiphenyl sulfone; **C7** = heptanedioic acid; **C8** = octanedioic acid; **C9** = nonanedioic acid; **C13** = tridecanedioic acid; **BQDC** = 2,2′-biquinoline-4,4′-dicarboxylic acid; **1,2-CHDC** = trans-1,2-cyclohexanedicarboxylic acid; **2-CCN** = 2-carboxycinnamic acid; **C-1,4-CHDC** = cis-1,4-cyclohexanedicarboxylic acid; **DBTFA** = 4,4'-(perfluoropropane-2,2-diyl)dibenzoic acid; **1,2,6-BPTC** = 1,1′-biphenyl-2,2′,6,6′-tetracarboxylic acid; **PPBA** = 2,6-bis(2-pyrazinyl)pyridine-4-benzoic acid; **GDL** = 4,6-bis(carboxymethyl-amino)-2-oxo-1,3,5-triazine; **BCBP** = 1,1′-bis(4-carboxyphenyl)-4,4′-bipyridinium; **L2-OMe** = (E)-methyl 3-(pyridin-4-yl)acrylate; **IPBP** = 1-(3, 5-dicarboxyphenyl)-4,4'-bipyridinium; **PBP** = 1,3-phenylenebis-(phosphonic acid); **C7BPCA =** 1,1'-(heptane-1,7-diyl)bis(4-carboxypyridin-1-ium); **L1-OMe** = (E)-methyl 3-(pyridin-4-yl)acrylate; **SA** = succinic acid (or C4); **TPPM** = tetrakis[4-(dihyroxyphosphoryl)phenyl]methane; **3,5-DCPCA** = 3,5-dichloroisonicotinic acid; **3,5-DBPCA** = 3,5-dibromoisonicotinic acid; **PMB** = 1,4-phenylenebis(methylene)bis(phosphonate); **DPTP** = 2,5-diphosphonoterephthalic acid; **MPDP** = (5-methyl-1,3-phenylene)diphosphonic acid; **1,3-PDA** = 1,3-phenylenediacetic acids; **TTTPC** = 1,1′,1″-(2,4,6-trimethylbenzene-1,3,5-triyl)-trimethylenetris(4-carboxypyridinium); **1,3-BDC** = 1,3-benzenedicarboxylic acid; **NIP** = 5-nitroisophthalic acid; **BDC-NH₂** = 2-aminoterephthalate; **1,4-(DAO)Bz** = 1,4-(diamidoximyl)benzene; **TDCS** = tetrakis-(3,5-dicarboxyphenyl) silicon; **MSTB** = 4,4′,4″-(methylsilanetriyl) tribenzoic acid; **C8BPCA** = 1,1'-(octatane-1,7-diyl)bis(4-carboxypyridin-1-ium); **1,2,4-BTC** = 1,2,4-benzenetricarboxylic acid; **IMDC** = 1,3-bis(carboxymethyl)imidazolium; **C4BPCA** = 1,1'-(butane-1,7-diyl)bis(4-carboxypyridin-1-ium); **PSTB** = 4,4,4-(phenylsilanetriyl)tribenzoic acid; **XylBpy4CA** = 1,1′-(1,3-phenylenebis(methylene))bis(4-(ethoxycarbonyl)pyridin-1-ium) bromide; **BPDA** = [1,1′-biphenyl]-2,4′-dicarboxylic acid; **1,2-PDA** = 1,2-phenylenediacetic acids; (b) η^2-N, η^3-N means a N-donor ligand offering two, three nitrogen atoms, respectively. U=O refers to the axial oxygen atom from neighboring uranyl. The η^1-SO$_4^{2-}$, η^2-SO$_4^{2-}$ refer to monodentate, bidentate sulfate ions, respectively.
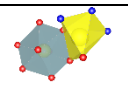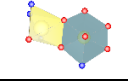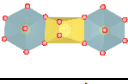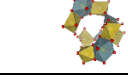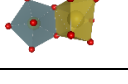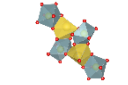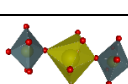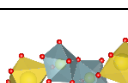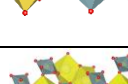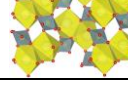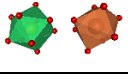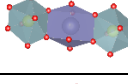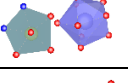
The majority of nitrogen-containing uranyl monomers are formed by the introduction of monodentate, bidentate or tridentate auxiliary N-donor ligands. UMON, U-GDL, U-IPBP-5, U-H1, U-3,5-DCPCA, and U-3,5-DBPCA have PBUs multiply bound with N,O-donor ligands. The fluoride-bridging uranyl clusters are observed in uranyl phosphonate frameworks whereas the chloride and bromide ions are apt to bind with uranyl in the presence of weakly coordinating ligand such as cucurbit[n]uril. It is noted despite that the predefinition of uranyl equatorial plane by auxiliary N-donor ligands can lead to rational crystal assembly, it inevitably exclude a variety of coordination modes in the resulting supramolecular frameworks (Table 4). Besides mononuclear PBUs, there are dimer, trimer, tetramer, pentamer, hexamer, octamer and chain-like SBU in U(VI)-MOFs. The edge-sharing dimer is more encountered than the vertex-sharing one. This structural motif of $(UO_2)_4O_{14}$ is the most common tetramer recorded in uranyl carboxylate frameworks. Actually, there are six types of tetramers in previously reported U(VI)-MOFs[26], two of which have been shared by recent U(VI)-MOFs. The pentanuclear SBUs remain quite scarce. In U-1,2,4-BTC-1, the pentamer is composed of five P-type PBUs terminated by the formate. The planar brick uranyl hexamer is supposed to be formed by two trimers sharing edges around an inversion center[190]. The octanuclear SBU in U-PSTB-9[188] and U-XylBpy4CA-1[192] represents the rare cases of an octanuclear uranium
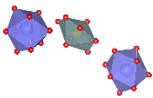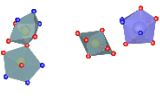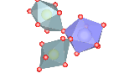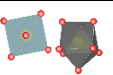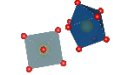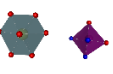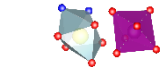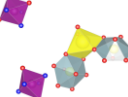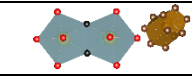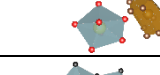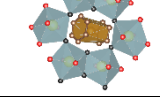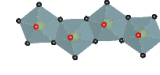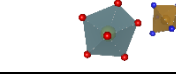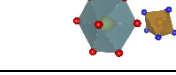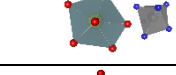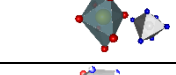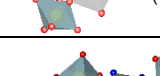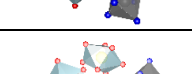
motif observed in uranyl carboxylates. The chain-like U(VI), Np(VI) SBUs consist of P-type PBUs except U-1,2-PDA-1[181], which is built of edge-sharing H-type PBU. There is still plenty of room in the coordination chemistry of An(VI) clusters, particularly for the unprecedented building units in An(VI)-MOFs that lead to unique photophysical properties.
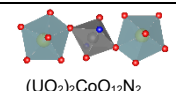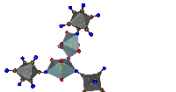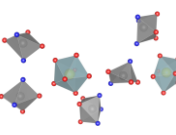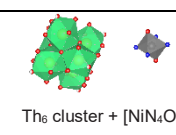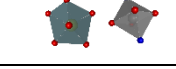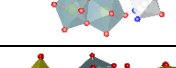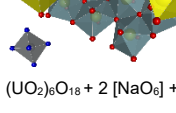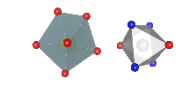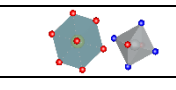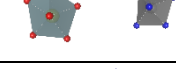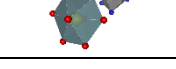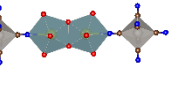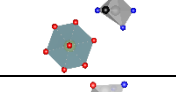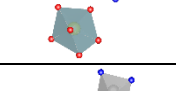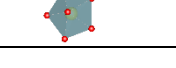
3.1.5 Heterometal core/cluster
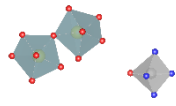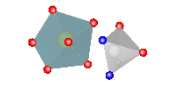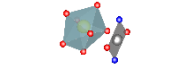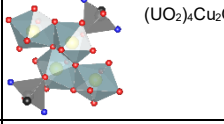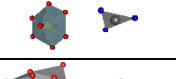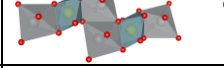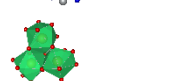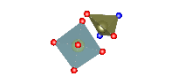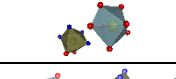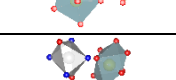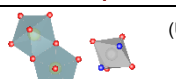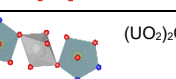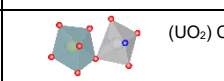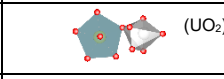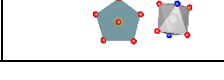
Heterometallic An-MOFs involve thorium, uranium and group 1, 2, 3, 7, 8, 9, 10, 11, 12 and 14 metals based building blocks, wherein actinide PBUs directly tether via oxolation or connect to heterometal PBUs through bridging organic linkers (Table 5).
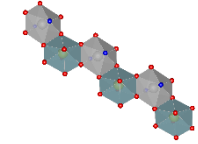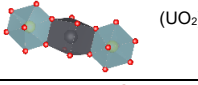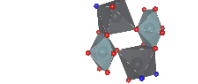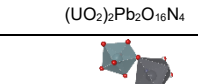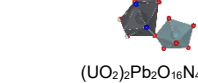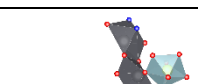
Table 5 Summary of structural aspects of heterometallic An-MOFs

An-MOFs	An(VI) core/cluster	Ligand [a]	PBUs coordination [b]	Ref.
UNa-1,4-NDC	$(UO_2)NaO_7N_3$	1,4-NDC, TPTZ	$[UO_8]$:3 η^2 (μ_2-O); $[NaO_3N_3]$:1 η^1, 2 μ_2-O, 1 η^3-N	[87]
UNa-9,10-ADC	$(UO_2)NaO_6N_4$	ADC, TPTZ, picolinic acid	$[UO_7N]$: 2 η^2, 1 "NO"; $[NaO_3N_3]$:1 H_2O, 2 η^1, 1 η^3-N	[87]
UNa-BQDC	$(UO_2)_2Na_2O_{16}$	BQDC	$[UO_8]$: 3 η^2; $[NaO_8]$: 4 μ_2-O, 2 η^1, 2 H_2O	[171]
UNa-C5	chain	C5	$[UO_8]$: 3 η^2 (μ_2-O); $[NaO_6]$: 2 η^1, 2 μ_2-O, 2 H_2O	[39]
UNa-C-1,2-CHDC	$(UO_2)NaO_{10}$	C-1,2-CHDC, 15C5	$[UO_7]$: 1 η^1, 2 η^2-$C_2O_4^{2-}$ (μ_2-O); $[NaO_7]$: 2 μ_2-O, 1 -O	[196]
UNa-TTHA	$(UO_2)_4Na_2O_{30}$	TTHA	$[UO_7]$: 3 η^1, 1 η^2; $[NaO_7]$: 1 η^2, 3 η^1, 1 U=O	[197]
UK-1,2-CHDC-1	chain	1,2-CHDC, 18C6	$[UO_7]$: 1 η^1, 2 η^2-$C_2O_4^{2-}$; $[UO_7]$: 2 η^1, 1 H_2O, 1 η^2-$C_2O_4^{2-}$; $[KO_8]$: 1 η^6-O, 2 U=O	[196]
UK-MDS	chain	MDS, CB[6]	$[UO_7]$: 2 η^1, 1 H_2O, 2 μ_2-OH; $[KO_6]$: 2 C=O, 3 H_2O, 1 U=O	[198]
UCs-1,2,4-BTC	layer	1,2,4-BTC	$[UO_8]$: 3 η^2; $[CsO_8]$: 5 η^1, 2 U=O, 1 H_2O	[199]
ThCa-OA-(1, 2)		OA	$[ThO_{10}]$: 5 $C_2O_4^{2-}$; $[CaO_8]$: 4 $C_2O_4^{2-}$	[142]
UBa-TCA	$(UO_2)_2BaO_{16}$	TCA	$[UO_8]$: 3 η^2; $[BaO_8]$: 4 μ_2-O, 4 H_2O	[200]
ULa-BPyTC		BPyTC	$[UO_5N_2]$: 1 "N_2O_2", 1 η^1; $[LaO_9]$: 1 η^1, 8 H_2O	[201]
ULa-DPA		DPA	$[UO_6N_3]$: 3 "NO_2"; $[LaO_8N]$: 1 "NO_2", 2 η^1, 4 H_2O	[202]

UCe-CB[6]		OA, CB[6]	[UO$_8$]: 2 C$_2$O$_4{}^{2-}$, 1 η^2-NO$_3{}^-$; [CeO$_9$]: 3 C=O, 1 η^2-C$_2$O$_4{}^{2-}$, 1 η^1-NO$_3{}^-$, 3 H$_2$O; [CeO$_9$]': 2 C=O, 1 η^2-C$_2$O$_4{}^{2-}$, 5 H$_2$O	[198]
UEu-TPC	(UO$_2$)$_2$O$_3$N$_6$	TPC, TPY	[UO$_4$N$_3$]: 1 η^1, 1 μ$_2$-O, 1 η^3-N; [UO$_8$]: 3 η^2; [EuO$_6$N$_3$]: 2 η^1, 2 η^2, 1 η^3-N	[203]
SCU-UEu-1	(UO$_2$)$_2$EuO$_{16}$	PAT	[UO$_7$]: 3 η^1, 1 η^2 (μ$_2$-O); [EuO$_8$]: 4 η^1, 2 μ$_2$-O, 2 H$_2$O	[204]
UNpC1P2-1		C1P2	[U^{VI}O$_6$]: 4 η^1; [Np^{IV}O$_8$]: 2 η^1, 2 η^2, 2 H$_2$O	[205]
UPu-1		C1P2	[U^{VI}O$_6$]: 4 η^1; [Pu^{IV}O$_8$]: 2 η^1, 2 η^2, 2 H$_2$O	[47]
UMn-1,4-PDA		1,4-PDA, 2,2-bipy	[UO$_8$]: 3 η^2; [MnO$_2$N$_4$]: 2 η^2-N, 2 η^1	[206]
UMn-BPyTC		BPyTC	[UO$_5$N$_2$]: 1 η^1, 1 "N$_2$O$_2$"; [MnO$_6$]: 3 η^1, 3 H$_2$O	[201]
IHEP-9	(UO$_2$)$_2$KO$_{14}$	TCPP	[UO$_8$]: 3 η^2; [MnO$_2$N$_4$]: 1 η^4-N, 2 H$_2$O; [KO$_6$]: 4 η^1, 2 H$_2$O	[207]
U-CpFeTP-1		CpFeTP	[UO$_5$F$_2$]: 1 η^1, 2 F$^-$, 2 H$_2$PO$_4{}^-$	[208]
U-CpFeTP-2		CpFeTP	[UO$_7$]: 3 η^1, 1 η^2	[208]
U-CpFeP-1	ring	CpFeP	[UO$_3$F$_4$]: 3 μ$_2$-F, 1 F$^-$, 1 H$_2$O; [UO$_5$F$_2$]: 3 η^1, 2 μ$_2$-F	[208]
U-CpFeP-2	chain	CpFeP	[UO$_2$F$_5$]: 2 μ$_2$-F, 3 F$^-$	[208]
UFe-CPTPY-1		CPTPY	[UO$_7$]: 1 η^1, 1 η^2, 2 HCOOH; [FeN$_6$]: 2 η^3-N	[209]
UFe-CPTPY-2		CPTPY	[UO$_8$]: 3 η^2; [FeN$_6$]: 2 η^3-N	[209]
UCo-CPTPY-1		CPTPY	[UO$_7$]: 1 η^1, 1 η^2, 2 HCOOH; [CoN$_6$]: 2 η^3-N	[209]
UCo-CPTPY-2		CPTPY	[UO$_8$]: 3 η^2; [CoN$_6$]: 2 η^3-N	[209]
UCo-MPDP	(UO$_2$)$_2$CoO$_6$N$_2$	MPDP, 2,2-bipy	[UO$_6$]: 4 η^1; [CoO$_3$N$_2$]: 2 η^1, 1 η^2-N, 1 U=O	[34]
UCo-2,4-BPYDC-1		2,4-BPYDC	[UO$_6$]: 4 η^1; [UO$_7$]: 3 η^1, 1 η^2; [CoN$_6$]: 3 η^2-N	[82]
UCo-2,4-BPYDC-2		2,4-BPYDC	[UO$_7$]: 3 η^1, 1 η^2; [UO$_7$]': 4 η^1, 1 H$_2$O; [CoN$_6$]: 3 η^2-N	[82]

UCo-CPP-1	 (UO$_2$)$_2$CoO$_{12}$N$_2$	CPP, dib	[UO$_6$]: 4 η^1; [UO$_7$]: 3 η^1, 1η^2; [CoO$_4$N$_2$]: 4η^1, 1 η^1-N	[210]
UCo-BPDO	layer 	BPDO	[UO$_5$N$_2$]: 2 CN$^-$, 1 η^1-NO$_3^-$, 1 μ$_2$-O; [Co(CN)$_6$]	[211]
Cage-U-Co-MOF		PIDC	[UO$_7$]: 4 η^1, 1 H$_2$O; [CoO$_3$N$_2$]: 2 "NO", 1 H$_2$O; [CoO$_3$N$_3$]: 3 "NO"	[212]
ThNi-INA	 Th$_6$ cluster + [NiN$_4$O$_2$]	INA	[ThO$_9$]: 4 η^1, 4 μ$_3$-O, 1 H$_2$O; [NiO$_2$N$_4$]: 4 η^1-N, 2 H$_2$O	[213]
UNi-NTA		NTA	[UO$_7$]: 2 η^1, 1 η^2, 1 NMP; [NiO$_4$N$_2$]: 2 "NO$_2$"	[95]
UNi-CIT		CIT	[UO$_7$]: 3 η^1, 2 μ$_2$-O; [NiO$_2$N$_4$]: 1 η^4-N, 2 η^1	[101]
UNaNi-BPYDC	 (UO$_2$)$_6$O$_{18}$ + 2 [NaO$_6$] + [NiN$_6$]	BPYDC	[UO$_7$]: 3 η^1, 2 μ$_3$-OH; [UO$_7$]: 2 η^1, 3 μ$_3$-OH; [UO$_7$]: 4 η^1, 1 μ$_3$-OH; [NiN$_6$]: 3 η^2-N; [NaO$_6$]: 4 η^1, 1 U=O, 1 H$_2$O	[104]
UNi-1,2-PDD		1,2-PDD, cyclam	[UO$_7$]: 3 η^1, 1 η^2; [NiO$_2$N$_4$]: 1 η^4-N, 2 η^1	[114]
UNi-C-1,2-CHDC-1		C-1,2-CHDC, cyclam	[UO$_7$]: 2 η^1, 1 η^2, 1 H$_2$O; [NiO$_2$N$_4$]: 1 η^4-N, 2 η^1	[214]
UNi-C-1,2-CHDC-2		C-1,2-CHDC, cyclam	[UO$_7$]: 3 η^1, 1 η^2; [NiO$_2$N$_4$]: 1 η^4-N, 2 η^1	[214]
UNi-ADC-2		ADC, cyclam	[UO$_7$]: 2 η^1, 1 η^2, 1 HCOOH; [NiO$_2$N$_4$]: 1 η^4-N, 1 η^1, 1 HCOOH	[215]
UNi-2-SB-2		2-SB, cyclam	[UO$_7$]: 5 η^1; [NiO$_2$N$_4$]: 1 η^4-N, 2 η^1	[216]
UNi-ADA		ADC, cyclam	[UO$_8$]: 2 η^1, 2 η^2; [NiO$_2$N$_4$]: 1 η^4-N, 2 η^1	[215]
UNi-CPTPY-1		CPTPY	[UO$_7$]: 1 η^1, 1 η^2, 2 HCOOH; [NiN$_6$]: 2 η^3-N	[209]
UNi-CPTPY-2		CPTPY	[UO$_8$]: 3 η^2; [NiN$_6$]: 2 η^3-N	[209]
UPt-BPDO	chain 	BPDO	[UO$_6$N]: 2 η^1, 1 CN$^-$, 2 μ$_2$-OH; [Pt(CN)$_6$]	[211]
UCu-2,4-BPYDC-2		2,4-BPYDC	[UO$_8$]: 2 η^2, 2 H$_2$O; [CuN$_4$Cl]: 2 η^2-N, Cl$^-$	[82]
UCu-2,4-BPYDC-3		2,4-BPYDC	[UO$_7$]: 2 η^1, 1 η^2, 1 H$_2$O; [CuON$_4$]: 1 η^1, 2 η^2-N	[82]
UCu-2-SB-1		2-SB, R,S-Me$_6$cyclam	[UO$_7$]: 1 η^1, 2 η^2; [CuON$_4$]: 1 η^1, 1 η^4-N	[216]

UCu-BPYDC-2	(UO₂)₂O₉ + [CuON₄]	BPYDC, TPY	[UO$_7$]: 1 η^1, 1 η^2, 1 μ$_2$-O, 1 HCOOH; [CuON$_4$]: 1 η^3-N, 1η^1-N, 1 η^1	[104]
UCu-1,2-CHDC-1		1,2-CHDC, 2,2-bipy	[UO$_7$]: 3 η^1, 1 η^2; [CuO$_3$N$_2$]: 1 η^2-N, 2 η^1, 1 H$_2$O	[172]
UCu-1,2-CHDC-2		1,2-CHDC, 2,2-bipy	[UO$_7$]: 3 η^1, 1 η^2; [CuO$_3$N$_2$]: 1 η^2-N, 3 η^1	[172]
UCu-MA		C3, 1,10-phen	[UO$_7$]: 5 η^1; [CuO$_3$N$_2$]: 1 η^2-N, 1 η^1, 1 η^2-C$_2$O$_4$$^{2-}$	[101]
UCu-2,4-BPYDC-1		2,4-BPYDC	[UO$_7$]: 2 η^1, 1 η^2, 1 η^1-SO$_4$$^{2-}$; [CuO$_3N_2$]: 2 η^2-N, 3 H$_2$O	[82]
UCu-T33PA-1		T33PA	[UO$_7$]: 3 η^1, 1 η^2; [CuO$_4$N$_2$]: 2 η^1-N, 2 η^1, 2 U=O	[217]
UCu-T33PA-2	(UO₂)₄Cu₂O₁₆Cl₂N₄	T33PA	[UO$_7$]: 3 η^1, 2 μ$_2$-O; [UO$_7$]': 1 η^1, 1 η^2, 1 H$_2$O, 1 μ$_3$-O; [CuO$_2$N$_2$Cl]: 2 η^1-N, 1 η^1, 1 U=O, 1 Cl$^-$	[217]
ECUT-92		PBA	[UO$_8$]: 3 η^2; [CuN$_3$]: 3 η^1-N	[218]
UAg-1,2,4-BTC	chain	1,2,4-BTC	[UO$_8$]: 2 η^1, 2 η^2; [AgO$_6$]: 3 η^1, 2 U=O, 1 H$_2$O	[199]
ThAg-BPYDC	Th₃O₂₁	BPYDC	[ThO$_{10}$]: 3 η^1, 1 η^2, 1 η^2-NO$_3$$^-$, 2 μ$_2$-OH, 1 μ$_3$-O; [AgN$_2$]: 1 η^2-N	[219]
UZn-MPDP		MPDP, 2,2-bipy	[UO$_6$]: 4 η^1; [ZnO$_2$N$_2$]: 2 η^1, 1 η^2-N	[34]
UZn-2,4-BPYDC		2,4-BPYDC	[UO$_7$]: 3 η^1, 1 η^2; [ZnO$_2$N$_4$]: 2 η^1, 2 η^2-N	[82]
UZn-CIT	(UO₂)₂O₈	CIT, 2,2-bipy	[UO$_7$]: 5 η^1 (μ$_2$-O); [ZnO$_2$N$_4$]: 1 η^1, 2 η^2-N, 1 H$_2$O	[101]
UZn-1,2-PDA-1		1,2-PDA, 1,10-phen	[UO$_8$]: 3 η^2; [ZnO$_2$N$_4$]: 1 η^1, 2 η^2-N	[206]
UZn-CPP		CPP, bpi	[UO$_7$]: 3 η^1, 1 η^2; [ZnO$_3$N]: 3 η^1, 1 η^1-N	[210]
UCd-2,4-BPYDC		2,4-BPYDC	[UO$_8$]: 2 η^1, 2 η^2; [CdO$_2$N$_4$]: 2 η^2-N, 2 H$_2$O	[82]
UCd-CIT-1	(UO₂)₂O₈	CIT, 2,2-bipy	[UO$_7$]: 5 η^1 (μ$_2$-O); [CdO$_4$N$_2$]: 2 η^1, 1 η^2-N, 2 H$_2$O	[101]
UCd-BPyTC	(UO₂)₂CdO₁₀N₄	BPyTC	[UO$_5$N$_2$]:1 "N$_2$O$_2$", 1 η^1; [CdO$_6$]: 4 η^1 (μ$_2$-O) , 2 H$_2$O	[201]
UCd-CPP-(1,2)	(UO₂) CdO₈N₂	CPP, dib	[UO$_7$]: 3 η^1, 1 η^2 (μ$_2$-O); [CdO$_4$N$_2$]: 4 η^1, 2 η^1-N	[210]
UCd-1,2-CHDC	(UO₂)CdO₁₀	1,2-CHDC	[UO$_7$]: 3 η^1, 2 H$_2$O; [CdO$_6$]: 2 η^2, 2 μ$_2$-O	[172]
UCd-C3-1		C3, 4,4-bipy	[UO$_7$]: 5 η^1; [CdO$_4$N$_2$]: 2 η^1, 2 η^1-N, 2 H$_2$O	[220]

UCd-C3-2	Chain	C3, 2,2-bipy	$[UO_8]$: 3 η^2 (μ_2-O) $[CdO_6N_2]$: 3 η^2, 1 η^2-N	[220]
UPb-TCA	$(UO_2)_2PbO_{16}$	TCA	$[UO_8]$: 3 η^2 (μ_2-O); $[PbO_8]$: 4 μ_2-O, 4 H_2O	[101]
UPb-1,3-PDA	$(UO_2)_2Pb_2O_{16}N_4$	1,3-PDA, 2,2-bipy	$[UO_8]$: 3 η^2 (μ_2-O); $[PbO_5N_2]$: 2 μ_2-O, 1 η^2, 1 U=O, 1 η^2-N	[221]
UPb-1,4-PDA	$(UO_2)_2Pb_2O_{16}N_4$	1,3-PDA, 1,10-phen	$[UO_7]$: 3 η^1, 1 η^2 (μ_2-O); $[PbO_5N_2]$: 1 η^1, 2 μ_2-O, 2 HCOOH, 1 η^2-N	[221]
UPb-C-1,4-CHDC	$(UO_2)Pb_2O_{12}N_4$	C-1,4-CHDC, 2,2-bipy	$[UO_7]$: 3 η^1, 1 η^2 (μ_2-O); $[PbO_5N_2]$: 3 η^1, 1 η^2 (μ_2-O), 1 η^2-N	[173]
U-POM-BPDO	$(UO_2)(HPW_{12}O_{40})$	BPDO	$[UO_7]$: 4 η^1, 1μ_2-O; POM: $[HPW_{12}O_{40}]^{2-}$	[222]

(a) Linkers are abbreviated as: **9,10-ADC** = 9,10-anthracenedicarboxylic acid; **TPTZ** = 2,4,6-tri(pyridine-2-yl)-1,3,5-triazine; **1,2-PDD** = 1,2-phenylenedioxydiacetic acid; **C-1,2-CHDC** = cis-1,2-cyclohexanedicarboxylic acid; **15C5** = 15-crown-5; **18C6** = 18-crown-6; **MDS** = methanedisulfonic acid; **BPDSDC** = biphenyl-3,3'-disulfonyl-4,4'-dicarboxylate; **TCA** = propane-1,2,3-tricarboxylic acid; **1,4-PDA** = 1,4-phenylenediacetic acids; **BPyTC** = 2,2'-bipyridine-3,3',6,6'-tetracarboxylic acid; **CpFeTP** = η^5-cyclopentadienyliron(II)-functionalized terephthalic acid; **CpFeP** = η^5-cyclopentadienyliron(II)-functionalized phthalic acid; **ADC** = 1,3-adamantanedicarboxylic acid; **CPTPY** = (4'-(4-carboxyphenyl)-2,2':6',2''-terpyridine); **2,4-BPYDC** = 2,2'-bipyridine-4, 4'-dicarboxylic acid; **BPDO** = 4,4-bipyridyl-N, N'-dioxide; **PIDC** = 2-propyl-2H-imidazole-4,5-dicarboxylic acid; **NTA** = Nitrilotriacetic acid; **CIT** = 2-hydroxy-1,2,3-propanetricarboxylic acid; **BPYDC** = 2,2'-bipyridine-3, 3'-dicarboxylic acid; **cyclam** = 1,4,8,11-tetraazacyclotetradecane; **R,S-Me6cyclam** = 7I,14(S)-5,5,7,12,12,14-hexamethylcyclam; **C3** = malonic acids; **T33PA** = trans-3,3(pyridyl)acrylic acid; **PBA** = 4-(4-pyridyl)benzoic acid; **TPC** = 2-thiophenecarboxylic acid; (b) The η^4-N, η^5-O, η^6-O means a N-donor ligand offering four nitrogen atoms and one crown ether provides five, six oxygen atoms, respectively. The μ_2-$C_2O_4^{2-}$ refers to the $C_2O_4^{2-}$ acts as bridging oxygen atom that connects two PBUs.

The free heterometal complexes inside the An-MOFs cannot be strictly classified as heterometallic An-MOFs but such "ship-in-bottle" effect on the ensuing properties will be discussed. For instance, $[Ni(2,2-bipy)_3]^{2+}$ acts as pore template as well as charge-balancing species for uranyl-organic assembly in UNi-BPDC-1[99].

The sodium or potassium PBUs connect uranyl PBUs via edge-sharing or cation-cation interactions to form dimer, trimer, hexamer or chain-like SBUs. In the nitrogen-bearing building blocks of UNa-1,4-NDC and UNa-ADC, the tridentate TPTZ exclusively coordinates with Na^+ while UO_2^{2+} bind with carboxylate groups, which is ascribed to the relatively stronger hard acid nature of uranyl[87]. As for alkali earth metals, the oxalate groups connect Th^{4+} and Ca^{2+} to form isolated

PBUs[142] while TCA ligands bridge uranyl and barium to yield an edge-sharing trimer[200].

The uranyl will outcompete lanthanum in coordinating N,O-donor ligands as implied by the isolated PBUs in ULa-BPyTC[201] and ULa-DPA[202]. SCU-UEu-1 has a vertex-sharing trimer consisting of two P-type uranyl and one [EuO_8] besides a corner-sharing uranyl dimer. This unique configuration results in an excitable, broad-band luminescence trait exploited to detect D_2O[204]. Furthermore, the incorporation of trivalent lanthanide into thorium or uranium based MOFs can provide structural insights into the immobilization of minor actinide. Likewise, Np(IV) and Pu(IV) can be anchored as PBUs within heterometallic UNpC1P2-1[205] and UPu-1[47], respectively. The Th_6U_4-Me$_2$BPDC-8 is formed by the grafting of uranyl ions on the thorium SBUs through binding with accessible oxo- or hydroxy groups in the preformed Th_6-Me$_2$BPDC-8[64]. In the presence of 2,2-bipy, Mn^{2+} constitutes [MnO_2N_4] PBU in UMn-1,4-PDA[206] while [MnO_6] PBU is formed due to the preferred coordination with carboxylate groups in relation to pyridine moieties in UMn-BPyTC[201].

Heterometallic An-MOFs bearing soft Lewis acid ions are common, in which these monovalent, bivalent cations coordinate with N,O-donor ligand or auxiliary N-donor ligand to form nitrogen-bearing PBU while the thorium or uranyl tend to form oxygen-containing monomer or oligomer. The UCd-BPyTC is the only exception where uranyl occupies both carboxylate and pyridine groups, leaving cadmium coordinate with carboxylate groups. Considering the similar coordination patterns in ULa-BPyTC and UMn-BPyTC, it can be attributed to that neighboring carboxylate and pyridine groups form a "N_2O_2" pocket that selectively bind with uranyl[201]. Soft metalloligands prove to be effective in constructing heterometallic An-MOFs. As the cyano group is a soft base, it tends to bind with soft metals to form 6-coordinated complexes. In UCo-BPDO and UPt-BPDO, uranyl dimers assemble with $Co(CN)_6$ and $Pt(CN)_6$ octahedra via CN^- to form layer- and chain-like SBUs, respectively, which illustrates the potential of metal cyanide as building blocks[211]. The nickel or cobalt complexation with INA in-situ generates tetratopic linker that further assemble with thorium, leading to the formation of ThNi-INA or ThCo-INA with cubic nanocage[213]. The CpFeP[208] and UNi-CPTPY[209] series are predefined metalloligands that behave like ditopic carboxylate acids. As for the group 14 metals, lead readily coordinates with N-donor ligand to form 7-coordinated PBUs, which share an edge or vertex with uranyl to yield trinuclear or tetranuclear SBU. Since polyoxometalates (POM) serve as anionic polynuclear metal-oxo clusters with oxygen-rich surfaces, they can be adopted as metalloid-ligands or as discrete templates to design MOFs incorporating POM[223]. Actinide-POMs complexes have been extensively studied as heterometallic assemblies[224] while the first case of POM-containing uranyl MOF was recently reported[222], unlocking the immobilization of POM within An-MOFs.

While the chemistry of An(IV) cluster lags behind the tetravalent transitional metal, the formation mechanism of An(III), An(V) and heterometal clusters remains as a mystery. The delicate control of actinide cluster has been recognized in building An-

MOFs with highly desired structure and ensuing properties. High-nuclearity actinide-oxo clusters such as Th_8[225], Th_{10}[226], U_{14}[149], U_{13}, U_{16}, U_{24}[227], Pu_{16}, Pu_{22}[228], U_{38}[229], Np_{38}[230], Pu_{38}[231] had been successfully isolated with varying labile neutral or negative coordinating ligands exposed on the surface. Surface engineering on the specific symmetric corners of high-nuclearity actinide clusters will probably enable stable coordination of heterometals or exchange of capping ligands. This modified assembly will combine multitopic linkers to yield giant cluster-based An-MOFs in accordance with the two-step modular construction of protein-MOFs[232].

3.2 Organic linkers

3.2.1 Aromatic N, O, S-carboxylate ligands
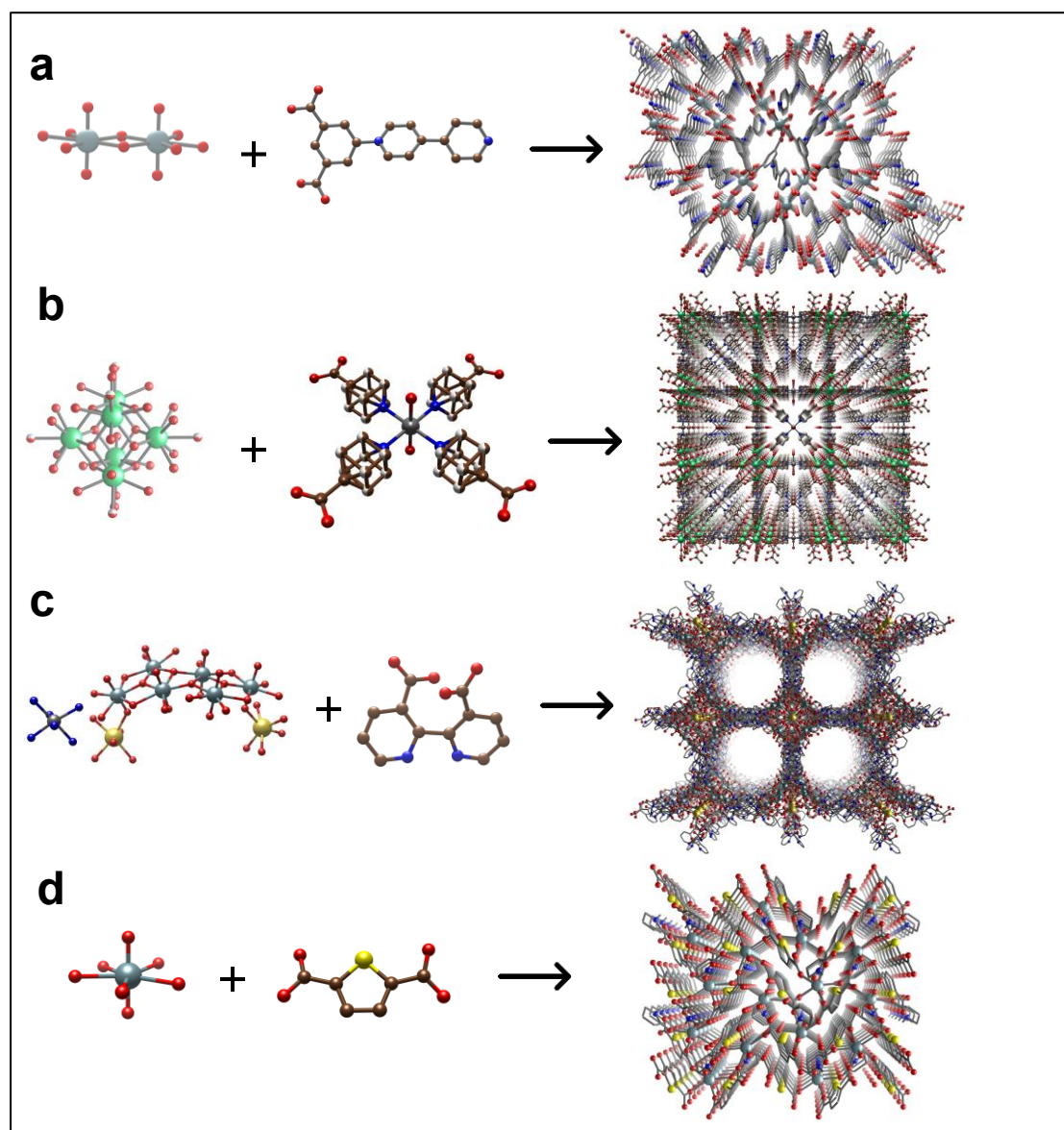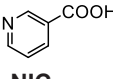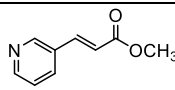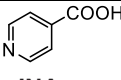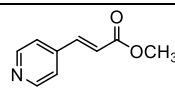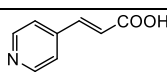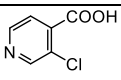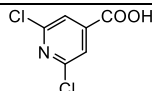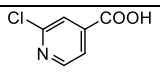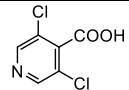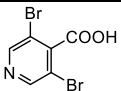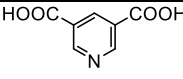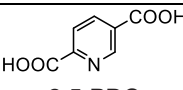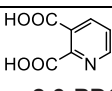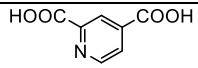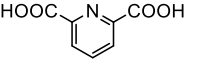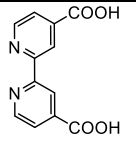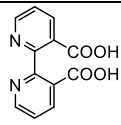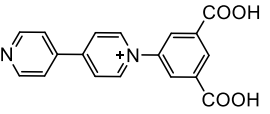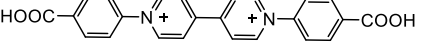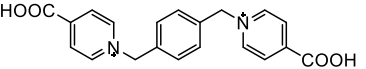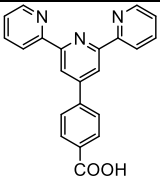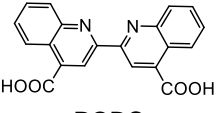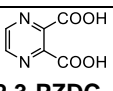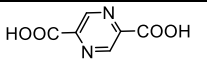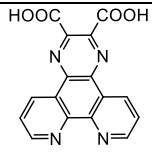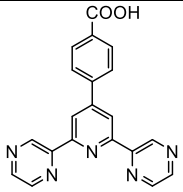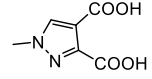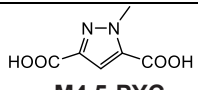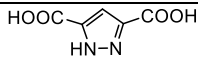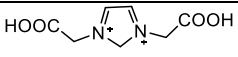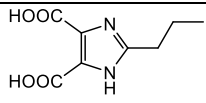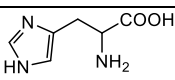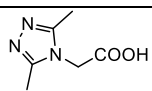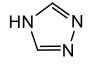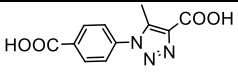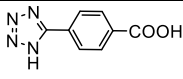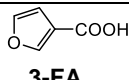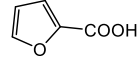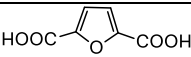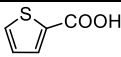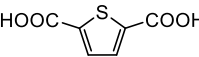
Figure 5. Representative An-MOFs based on aromatic N,O,S-carboxylate ligands: (a) U-IPBP-3; (b) ThNi-INA; (c) UNaNi-BPYDC; (d) U-TDC-2.

Table 6 Summary of An-MOFs based on aromatic N,O,S-carboxylate ligands

Linker	An-MOF	Network	Ref
NIC	U-NIC	1D	[187]
	Np-NIC	2D	[42]
L2-OMe	UZn-L2-OMe	3D supramolecular	[178]
INA	Np-INA	3D	[42]
	ThNi-INA	3D	[213]
	UAg-INA	1D	[233]
L1-OMe	U-L1-OMe-(1,2)	3D supramolecular	[178]
T33PA	UCu-T33PA-(1,2)	2D	[217]
MCPCA	UAg-MCPCA-2	3D	[233]
2,6-DCPCA	U-2,6-DCPCA	3D supramolecular	[84]
2-MCPCA	U-2-MCPCA	2D wave-shaped	[84]
3,5-DCPCA	UAg-DCPCA	3D supramolecular	[233]
	U-3,5-DCPCA	3D supramolecular	[84]
3,5-DBPCA	U-3,5-DBPCA	3D supramolecular	[84]
3,5-PDC	UEu-3,5-PDC	1D	[234]
2,5-PDC	TOF-1	3D	[72]
	Th-2,5-PDC	1D	[129]
2,3-PDC	Th-2,3-PDC	3D	[129]

Structure	Name	Dimensionality	Ref
2,4-PDC (HOOC–pyridine–COOH)	Th-2,4-PDC	3D	[129]
2,6-PDC (HOOC–N–COOH)	ULa-DPA	1D	[202]
	Pu^{III}-1	3D	[49]
	Pu$^{III, IV}$-3	3D	[49]
	Pu$^{III, IV}$-4	3D	[49]
2,4-BPYDC	UCu-2,4-BPYDC-1	(3,4)-c layer	[82]
	UCd-2,4-BPYDC	(4,4)-c layer	[82]
	UCo-2,4-BPYDC-1	(4,6)-c 3D	[82]
	UCu-2,4-BPYDC-3	(3,5)-c 3D	[82]
	UZn-2,4-BPYDC	(5,8)-c 3D	[82]
BPYDC	UCu-BPYDC-2	3D supramolecular	[104]
	UNaNi-BPYDC	(3,3,3,3,3,3,3,4,5)-c 3D	[104]
	ThAg-BPYDC	3D chiral	[219]
	UAg-BPYDC	3D chiral	[219]
PBA	ECUT-92	9-fold interpenetrated 3D	[218]
IPBP	U-IPBP-1	2D + 2D → 3D	[107]
	U-IPBP-2	2-fold interpenetrated 2D	[107]
	U-IPBP-3	3D	[107]
	U-IPBP-5	wave-shaped 2D	[107]
BCBP	U-BCBP-(1-4)	double-layer	[83]
	U-BCBP-5	rhombus-shaped layer	[83]
XylBpy4CA	U-XylBpy4CA-1	2D	[192]
CPTPY	UNi-CPTPY-1	3D supramolecular	[209]
	UNi-CPTPY-2	2D + 2D → 3D	[209]
BQDC	U-BQDC-(1,2)	double-layer	[171]
	UNa-BQDC	3D	[171]
2,3-PZDC	Th-2,3-PZDC	3D	[129]
2,5-PZDC	Th-2,5-PZDC	3D	[129]

PPDC	U-PPDC	2D supramolecular	[176]
PPBA	U-PPBA	2D	[176]
M3,4-PYC	Th-M3,4-PYC	3D supramolecular	[138]
M4,5-PYC	Th-M4,5-PYC	3D supramolecular	[138]
3,5-PYC	Th-3,5-PYC	3D	[131]
IMDC	U-IMDC-(1,4)	1D	[86]
	U-IMDC-(2,3)	Corrugated layer	[86]
PIDC	Cage-U-Co-MOF	3D	[212]
Histidine	U-H1	2D supramolecular	[169]
Me₂trGly-H	UAg-Me₂trGly-H	3D supramolecular	[235]
TAZ	U-TAZ-1	2D	[161]
	U-TAZ-2	3D	[159]
CMTC	U-CMTC	2D	[236]
TBA	Azole-Th-1	UiO-66(Zr)	[78]
3-FA	Th-3-FA	2D supramolecular	[63]
2-FA	U4-2-FA-1	3D supramolecular	[60]

HOOC—[furan]—COOH **2,5-FDC**	Th-2,5-FDC-2	3D	[63]
S—[thiophene]—COOH **TPC**	UEu-TPC	1D	[203]
HOOC—[thiophene-S]—COOH **TDC**	TDC-4	1D	[165]
	U-TDC-(13,14)	1D	[237]
	U-TDC-(12,15)	honeycomb layers	[237]
	U-TDC-11	3D supramolecular	[237]
	U-TDC-3	2-fold interpenetrated 2D	[165]
	U-TDC-(1,2)	3D	[95]

Linkers are abbreviated as: **Me2trGly-H** = 3,5-dimethyl-(1,2,4-triazole-4-yl)-acetic acid; **CMTC** = 1-(4-carboxyphenyl)-5-methyl-1H-1,2,3-triazole-4-carboxylic acid; **TBA** = 4-(1H-Tetrazol-5-yl) benzoic acid; **2-FA** = 2-furoic acid.

A large number of aromatic N,O,S-donor carboxylate ligands have witnessed success in preparing transition metal and lanthanide-based heterometallic MOFs while they have been less-frequently utilized to prepare monometallic or heterometallic An-MOFs (Table 6).

Zwitterionic pyridine monocarboxylic acids (e.g. NIC, INA), pyridinedicarboxylic isomers (i.e. 3,5-PDC, 2,3-, 2,4-, 2,5- and 2,6-PDC) and pyrazolecarboxylates (i.e. 3,5-PYC) emerge as an important category of N,O-donor bifunctional linkers in the early stage of monometallic An-MOFs. They can serve as multivariable ligand systems where tuning of relative location of functional groups, electronic substitution, backbone geometry and flexibility potentially lead to a vast array of structural motifs in An-MOFs. For instance, it is the 2-position carboxylate group that bridges adjacent PBUs to complete a 3D network in Th-2,4-PDC while the 5-position carboxylic group in 2,5-PDC remains protonated and does not coordinate with thorium. The instance of bidentate binding mode seen in 2,5-PDC increases to three as opposed to two in both 2,3-PDC and 2,4-PDC, giving rise to a lower number of accessible binding sites and a decreased dimensionality in Th-2,5-PDC[129]. Unfortunately, this effect of the position of the second carboxylate group on Th-MOF topology cannot be fully deduced, although powder X-ray diffraction data suggest that the pyridine nitrogen atoms are not coordinated to Th(IV) due to the steric effect of two neighboring carboxylate groups in polycrystalline Th-2,6-PDC[67]. The Cahill group investigated the effect of functional group location on the resulting topology of a heterometallic U(VI)-MOF[238] and then extended their work to prepare Th-3,5-PYC, in which the 2-position nitrogen remains uncoordinated due to the steric effect and charge balance requirements of the pyrazole ring[131]. The substitution by electron-withdrawing halogen groups at ortho- or meta-position of the nitrogen in pyridinecarboxylate induces significant halogen-halogen interactions[84] that stabilize the whole framework, bearing a resemblance to hydrogen bonding in substituted pyrazolecarboxylate facilitated by uncoordinated nitrogen atoms[138]. PBA, IPBP, BCBP, and XylBpy4CA have all been utilized to lengthen the backbone so as to enhance the framework's potential porosity while the substitution of a carboxylate

group with an acrylic acid group contribute to an increase in backbone flexibility in T33PA, L1-OMe, and L2-OMe relative to INC and NIC.

Since the "nitrogen pocket" readily anchors transitional metals, BPYDC, 2,4-BPYDC, CPTPY, BQDC, PPDC, and PPBA have been used to construct heterometallic An-MOFs, allowing a rational design of a preassembled metalloligand for actinide complexation. Due to vital functionalities in natural systems, the pyrazine-, imidazole-, triazole-, tetrazole -, furan- and thiophene-carboxylate ligands have been adopted to diversify the structural aspects of An-MOFs (Fig.5) besides pyridinecarboxylate-based ones. It is noted that TAZ is an exceptional pure N-donor ligand finding its utility in preparing U(VI)-MOFs[159,161].

The aromatic N,O,S-donor carboxylate ligands can be further explored in building heterometallic An-MOFs as molecular platform to analyze (i) coordination covalency trends of An-N or An-S bonds; (ii) coordination discrepancies between actinide and heterometal; (iii) complexity in framework topologies and electronic structures.

3.2.2 Ditopic carboxylate ligand
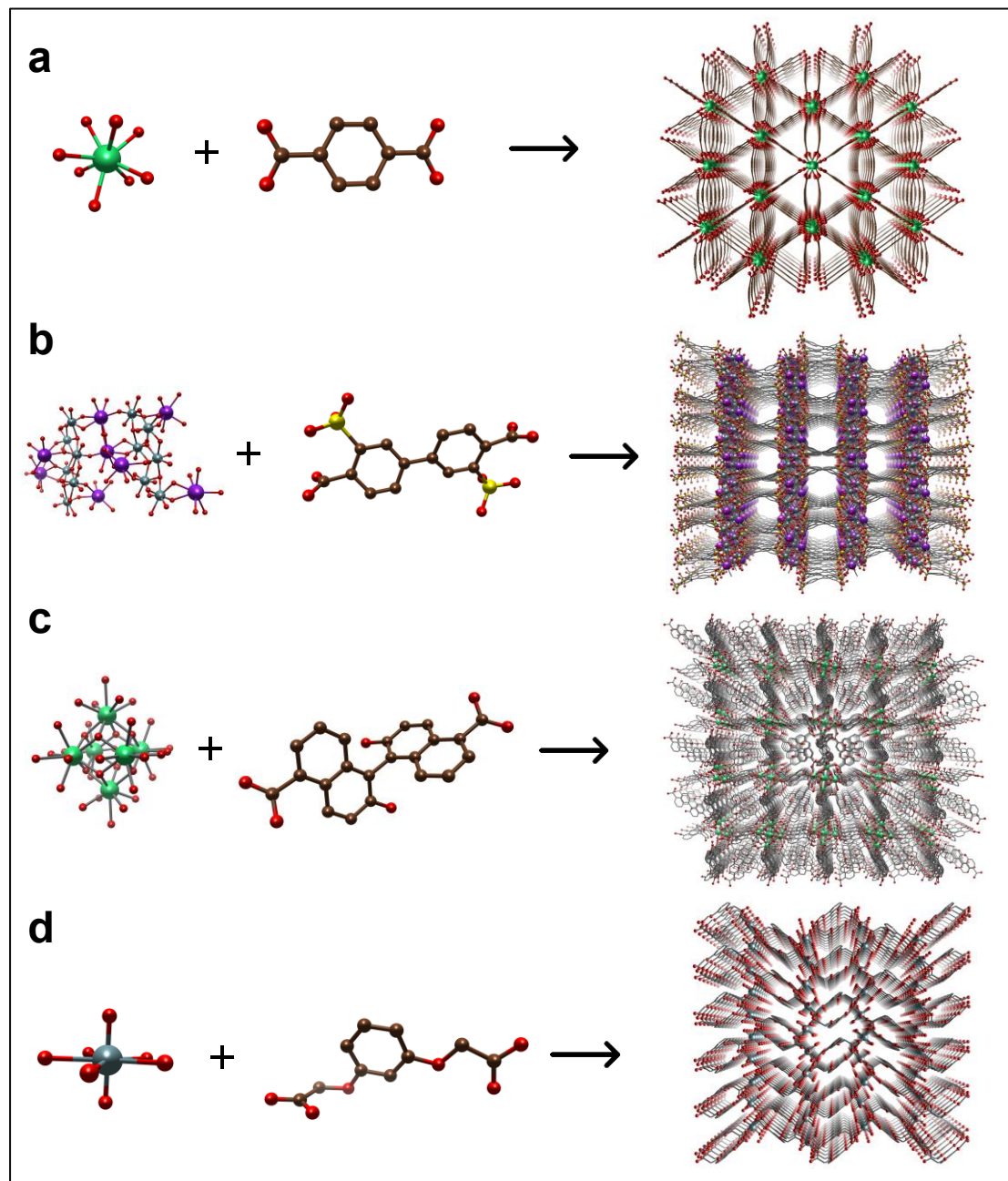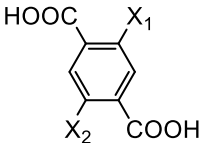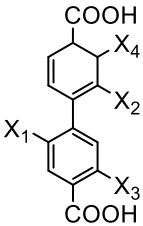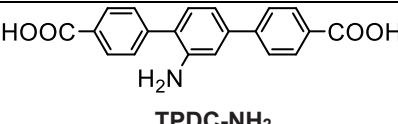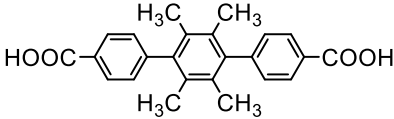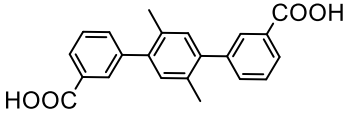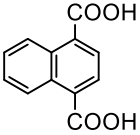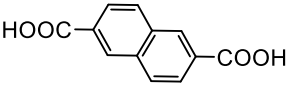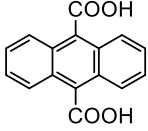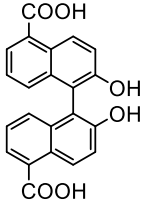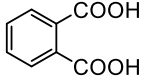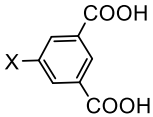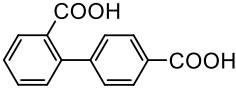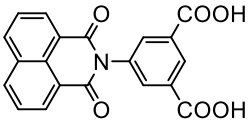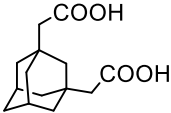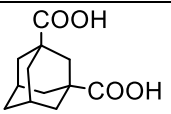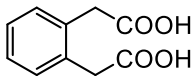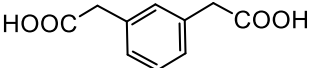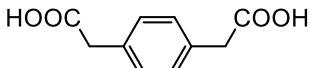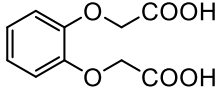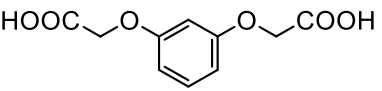
Figure 6. Representative An-MOFs based on linear and angular ditopic carboxylate ligands: (a) Th-BDC-2; (b) UK-BPDSDC-1; (c) TOF-16; (d) U-1,3-PDD-1.
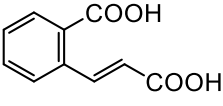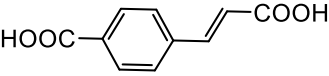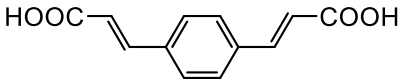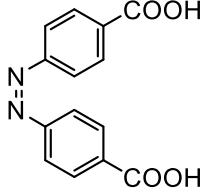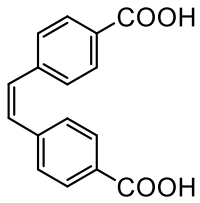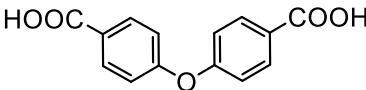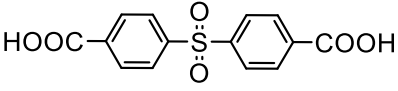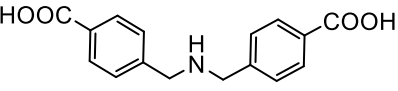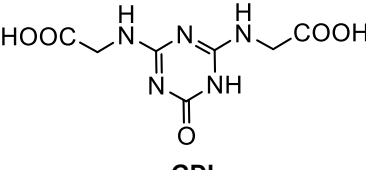
Table 7 Summary of An-MOFs based on ditopic carboxylate ligands

Linker	An-MOF	Network	Ref
	Th-BDC-1	2D	[61]
	U4-BDC-3	2D	[59]
	U4-BDC-5	2D	[59]
	Np-BDC-1	2D	[153]

HOOC—X₁ / X₂—COOH (benzene ring) $X_1=X_2=H$, BDC $X_1= NH_2$, BDC-NH₂ $X_1= NO_2$, NTP $X_1= OH$, BDC-OH $X_1= CH_3$, MeBDC $X_1=Cl$, BDC-Cl $X_1=Br$, BDC-Br $X_1=I$, BDC-I $X_1=X_2=Cl$, BDC-Cl₂ $X_1=X_2=Br$, BDC-Br₂ $X_1=X_2=CH_3$, BDC-Me₂ $X_1= X_2=NH_2$, BDC-(NH₂)₂ $X_1=X_2=CF_3$, BDC-(CF₃)₂ $X_1=X_2=OCH_3$, BDC-(OMe)₂	Th-BDC-2	3D	[61]
	U4-BDC-4	3D	[59]
	U4-BDC-6	3D	[150]
	U4-BDC-2	3D	[151]
	Th-BDC-3	UiO-66(Zr)	[61]
	Th-UiO-66	UiO-66(Zr)	[239]
	Np-BDC-2	UiO-66(Zr)	[153]
	Th-UiO-66-R	UiO-66(Zr)	[148]
	Pu-UiO-66	UiO-66(Zr)	[50]
	U-BDC-5	close-packed layer	[184]
	U-BDC-11	close-packed layer	[39]
	U-BDC-(6-8)	polycatenated 2D	[184]
	U-BDC-9	non-interpenetrated 3D	[102]
	U-BDC-1	3-fold interpenetrated 3D	[85]
	U-BDC-2	(2,4)-c 3D	[167]
	U-BDC-3	(4,4)-c 3D	[95]
	U-BDC-CB[6]	2D	[120]
	UNa-BDC-CB[5]	2D	[120]
	UK-BDC-CB[5]-CB[6]	2D	[120]
	U-BDC-NH₂	3D supramolecular	[39]
	U-NTP-(1,2)	3D supramolecular	[167]
COOH / X₄ / X₂ / X₁ / X₃ / COOH (biphenyl ring) $X_1= X_2=X_3=X_4=H$, BPDC $X_1= NH_2$, BPDC-NH₂ $X_1= X_2=CH_3$, BPDC-Me₂ $X_3 =X_4=SO_3$, BPDSDC	Th-SINAP-13	UiO-67(Zr)	[77]
	U4-BPDC	UiO-67(Zr)	[152]
	Th-BPDC	UiO-67(Zr)	[153]
	Np-BPDC	UiO-67(Zr)	[153]
	U-BPDC-(1,2)	2D	[179]
	U-BPDC-(3-5)	2D	[99]
	NU-1302-DMF	2D	[240]
	NU-1302-EtOH	2D	[240]
	NU-1302-SA	2D	[240]
	UNi-BPDC-(2,3)	2D + 2D → 3D	[99]
	Th-BPDC-NH₂	UiO-67(Zr)	[153]
	Np-BPDC-NH₂	UiO-67(Zr)	[153]
	Th₆-Me₂BPDC-8	UiO-67(Zr)	[64]
	U₆-Me₂BPDC-8	UiO-67(Zr)	[64]
	Th₆-Me₂BPDC-NO₃-10	UiO-67(Zr)	[64]
	U₆-Me₂BPDC-TFA-10	UiO-67(Zr)	[64]
	UK-BPDSDC-(1-3)	3D	[241]
HOOC——————COOH / H₂N TPDC-NH₂	Np-TPDC-NH₂	UiO-68(Zr)	[153]
	Th₆-TPDC-NH₂-12	UiO-68(Zr)	[65]

Structure	Name	Topology	Ref
TMTDC	U-TMTDC	entangled 3D	[242]
DMTDC	U-DMTDC-(1,2)	2D	[242]
1,4-NDC	Th-SINAP-7	UiO-66(Zr)	[92]
	U-1,4-NDC-(1-4)	catenated 3D	[103]
	UNa-1,4-NDC	2D	[103]
	U-1,4-NDC-(5,6)	zigzag chains	[103]
2,6-NDC	Th-SINAP-8	UiO-66(Zr)	[92]
	Th-2,6-NDC	3D	[135]
9,10-ADC	UNa-9,10-ADC	zigzag chains	[87]
2,5-BNDC	TOF-16	3D	[79]
1,2-BDC	U-1,2-BDC-1	4-c binodal 3D	[93]
	U-1,2-BDC-2	6-c binodal 3D	[93]
	U-1,2-BDC-3	3D supramolecular	[93]
	U-1,2-BDC-4	3D supramolecular	[187]
	U4-1,2-BDC	3D supramolecular	[46]
	Np-1,2-BDC	3D supramolecular	[46]
	U-1,2-BDC-5	2D	[183]
	U-1,2-BDC-5	2D	[183]
X= H,1,3-BDC X= NO$_2$, NIP X= OH, 1,3-BDC-OH	U-1,3-BDC-2	(3,4)-c binodal 3D	[243]
	U-1,3-BDC-3	3D supramolecular	[244]
	U-NIP-1	2D	[81]
	U-NIP-2	2D	[245]
	U-NIP-5	2D supramolecular	[166]
	U-NIP-6	3D	[166]
	U-NIP-7	2D supramolecular	[166]
	U-NIP-8	3D supramolecular	[166]
	U-NIP-9	3D supramolecular	[166]
	U-1,3-BDC-OH	(4,4)-c 3D	[185]

Structure	Name	Dimensionality	Ref
BPDA (COOH, COOH biphenyl)	U-BPDA-1	Honeycomb layer	[193]
	U-BPDA-2	3D supramolecular	[193]
L135 (naphthalimide dicarboxylic)	Th-L$_{135}$	2D supramolecular	[141]
ADA	TOF-3	3D	[74]
	U-ADA-3	2D	[113]
	U-ADA-4	2D supramolecular	[198]
ADC	UK-ADC	2D supramolecular	[198]
	UNi-ADC-1	double-stranded chains	[215]
	UNi-ADC-2	corrugated layers	[215]
1,2-PDA	U-1,2-PDA-(1,2,6)	2D	[181]
	U-1,2-PDA-(3,4)	ladder-like chain	[181]
	U-1,2-PDA-(5,7)	zigzag chain	[181]
	UZn-1,2-PDA-(1,2)	ladder-like chain	[206]
	UNi-1,2-PDA	2D	[206]
	UCu-1,2-PDA	2D	[206]
	UAg-1,2-PDA	2D	[206]
1,3-PDA	U-1,3-PDA-1	2D	[181]
	U-1,3-PDA-(2-4)	zig-zag chain	[181]
	UZn-1,3-PDA-1	2D	[221]
	UZn-1,3-PDA-2	ladder-like chain	[221]
	UPb-1,3-PDA	2D	[221]
1,4-PDA	U-1,4-PDA-(1,2)	2D	[181]
	U-1,4-PDA-(3-5)	zig-zag chain	[181]
	UCu-1,4-PDA	2D + 2D → 2D	[206]
	UPb-1,4-PDA	ladder-like chain	[221]
	URu-1,4-PDA	ladder-like chain	[221]
	UZn-1,4-PDA	2D	[221]
	UNi-1,4-PDA-1	2D	[221]
	UMn-1,4-PDA	1D	[221]
1,2-PDD	UNa-1,2-PDD-1	2D	[114]
	UNa-1,2-PDD-2	1D	[114]
	UNi-1,2-PDD	2D	[114]
1,3-PDD	U-1,3-PDD-1	3D	[114]
	U-2-CCN-(1-3)	racemic layer	[114]

Structure	Name	Type	Ref
2-CCN (structure with COOH groups)	UNi-2-CCN	racemic layer	[114]
4-CCN (structure)	Th-SINAP-11	UiO-67(Zr)	[77]
PEDA (structure)	Th-SINAP-12	UiO-67(Zr)	[77]
ABDC (structure)	Th-SINAP-14	UiO-67(Zr)	[77]
SDC (structure)	Th-SINAP-15	UiO-67(Zr)	[77]
OBA (structure)	GWMOF-13	Hub-and-spoke chains	[98]
DBSF (structure)	U-DBSF-1	triple-stranded helix	[168]
	U-DBSF-2	3D supramolecular	[168]
	U-DBSF-3	3D supramolecular	[100]
	UDBSF-5	3D supramolecular	[189]
	U-DBSF-6	3D supramolecular	[100]
	U-DBSF-7	3D supramolecular	[100]
BCHBA (structure)	U-BCHBA-1	interpenetrating 3D	[164]
	U-BCHBA-2	3D supramolecular	[164]
GDL (structure)	U-GDL	1D	[177]

Linkers are abbreviated as: **TMTDC** = 2′,3′,5′,6′-tetramethyl-(1,1′:4′,1″-terphenyl)-4,4″-dicarboxylic acid; **DMTDC** = 2′,5′-dimethyl-(1,1′:4′,1″-terphenyl)-3,3″-dicarboxylic acid; **BDC-OH** = 5-hydroxyisophthalic acid; **1,3-PDD** = 1,3-phenylenedioxydiacetic acid; **BCNOBA** = 4,4'-((nitrosoazanediyl)bis(methylene))dibenzoic acid.

Linear and angular ditopic carboxylates are the most extensively used linkers for An-

MOFs largely due to their structural controllability. In other words, the well-established MOF chemistry based on ditopic carboxylate linkers can be used as reliable references for An-MOFs (Table 7), which can be illustrated by UiO-66(Zr), UiO-67(Zr), and UiO-68(Zr)-like frameworks using BDC, BPDC, and TPDC ligands. The use of auxiliary ligands, backbone substitution, and heterometals enhances the diversity of An-MOFs (Fig.6). As illustrated in mixed-linker syntheses, the common close-packed layer for uranyl-BDC compounds can be modified by introducing a series of pillaring ligands. Besides, protonated and neutral organic molecules or heterometal complexes exert a template effect in forming distinct uranyl-BDC layers, in which arrays of templates located within layers induce hydrogen bonds or π-π stacking. Some substituted groups (e.g. 1,8-naphthalimido tecton[141]) have been intentionally installed on BDC to construct frameworks via significant intermolecular interactions.

The substitution of functional groups on a biphenyl or terphenyl backbone or the insertion of functional groups between benzene and terminal carboxylate groups will lead to a significant variation in scaffold conformation relative to prototype ligands. For instance, adding methylene between benzene and carboxylate in 1,2-BDC enables a chiral pseudo-C_2 conformation in 1,2-PDA to assemble uranyl chains into layers involving π-π stacking[181]. Likewise, for adamantane-based bulky ditopic ligands, the insertion of a C-C bond between adamantyl and carboxylate in ADA allows a higher degree of conformational freedom compared with ADC and contributes to the high dimensionality of ADA-based An-MOFs[74,113].

Naphtalenedicarboxylate and anthracenedicarboxylate ligands have been recognized as large conjugating π-systems that contribute to a handful of An-MOFs. However, the fact that TOF-16[79] has a tightly-packed microporous framework with remarkable radiolytic stability, indicates a great potential in making intrinsically luminescent, radiolytically stable An-MOFs based on conjugated ditopic carboxylate ligands.

It will be of practical importance to modify prototype An-MOFs (e.g. UiO-67(Zr)) for target properties meanwhile multitopic ligands (or metalloligand) can be introduced into dicarboxylate ligand system in order to prepare An-MOFs with unusual topologies.

3.2.3 Tritopic carboxylate ligand
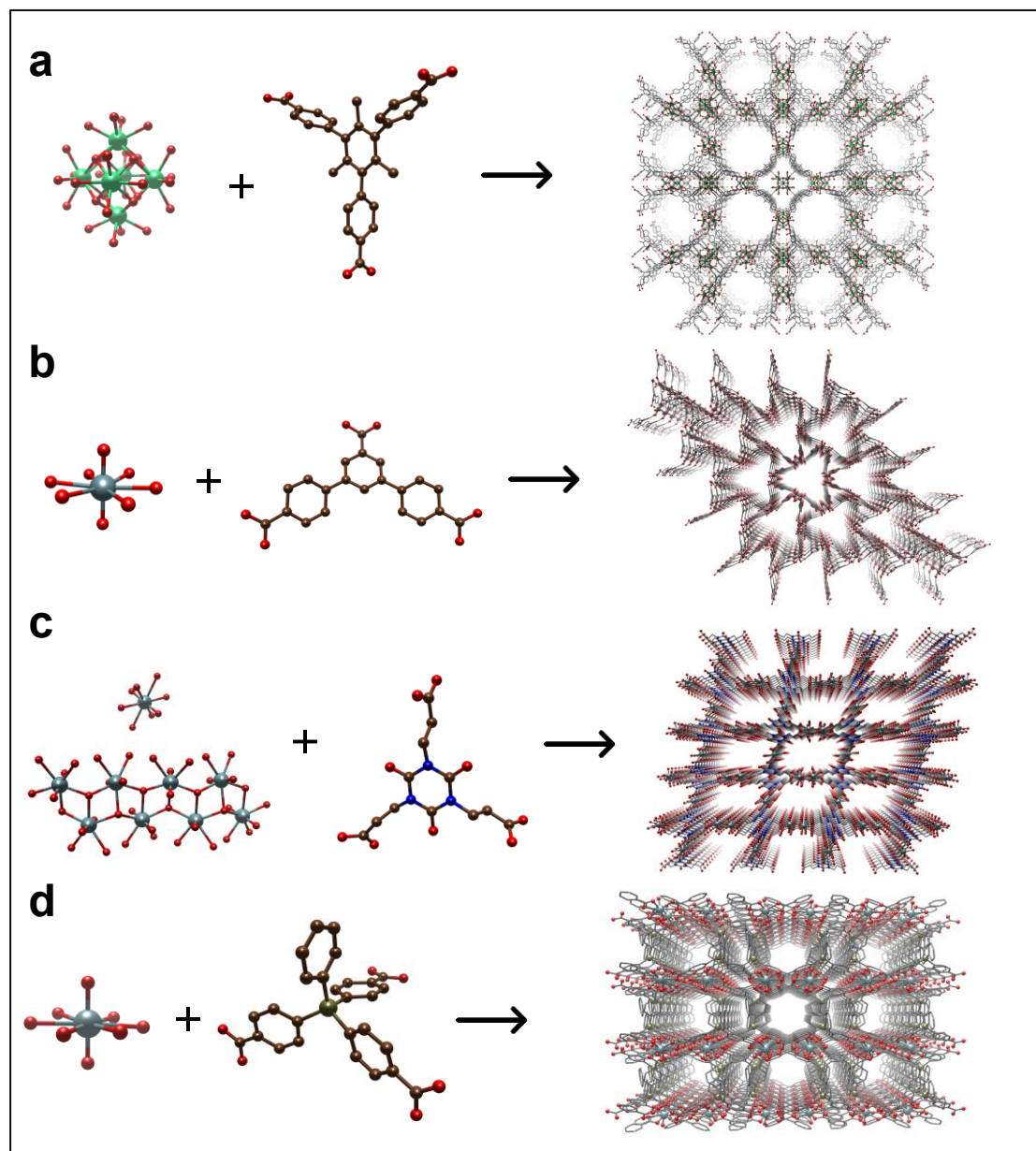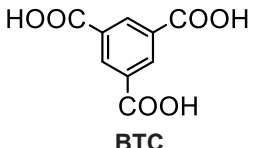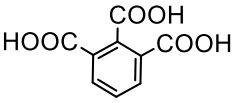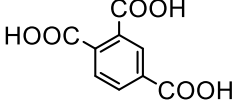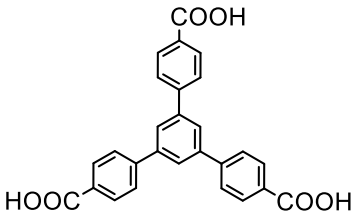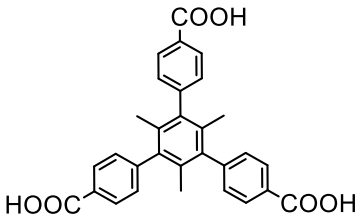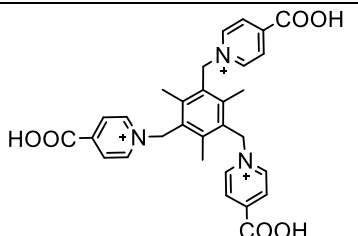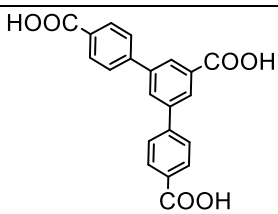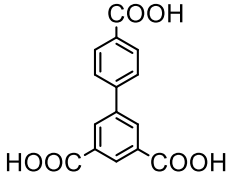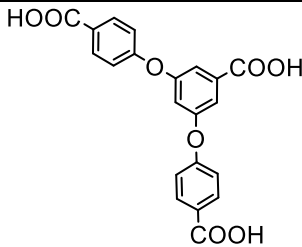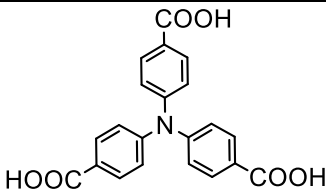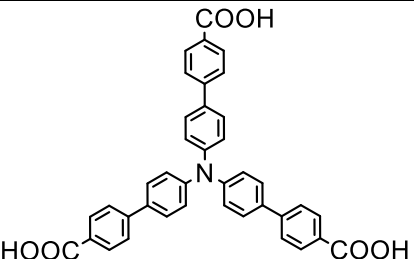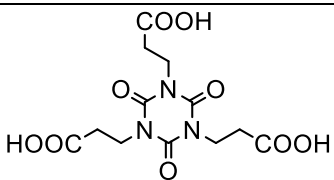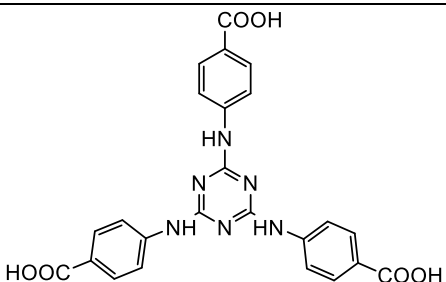
Figure 7. Representative An-MOFs based on tritopic carboxylate ligands: (a) Th-NU-1200; (b) U-BDB; (c) U-TCl-1; (d) U-PSTB-3.

Table 8 Summary of An-MOFs based on tritopic carboxylate ligands

Linker	An-MOF	Network	Ref
HOOC—⬡—COOH / COOH **BTC**	U-BTC-2	1D	[95]
	Th-BTC-(2-4)	2D	[62]
	U-BTC-1	2D	[95]
	U-BTC-3	2D	[102]
	SCU-9	interpenetrated 2D	[246]
	TOF-2	dense 3D	[73]

	Th-BTC-(5,6)	dense 3D	[62]
	Th-BTC-1	honey-comb 3D	[62]
	U4-BTC-1	honey-comb 3D	[37]
1,2,3-BTC	U4-1,2,3-BTC	3D	[149]
1,2,4-BTC	U-1,2,4-BTC-(1,2)	3D	[190]
	U-1,2,4-BTC-3	ribbon-like chain	[199]
	U-1,2,4-BTC-4	ladder-like chain	[199]
	U-1,2,4-BTC-5	2D	[199]
	U-1,2,4-BTC-6	chiral 2D	[199]
	U-1,2,4-BTC-7	3D	[199]
	U-1,2,4-BTC-(8,9)	ribbon-like chain	[199]
	UAg-1,2,4-BTC-1	3D	[199]
	UAg-1,2,4-BTC-2	3D	[199]
	URb-1,2,4-BTC	interpenetrated 3D	[199]
	UCs-1,2,4-BTC	interpenetrated 3D	[199]
BTB	Th-BTB	honeycomb layers	[116]
	U-BTB	honeycomb layers	[247]
TMTB	NU-1301	quaternary structure	[248]
	Th-NU-1200	mesoporous 3D	[249]
TTTPC	SCU-6	(3,6)-c 2D	[182]
	SCU-7	3D supramolecular	
BDB	U-BDB	2D + 2D → 3D	[247]

BPTC	SCU-8	(3,9)-c 3D	[117]
BCPBA	Th-BCPBA	(4,6)-c 3D	[136]
	U-BCPBA-(1,2)	zigzag layer	[250]
NTB	Th-NTB	graphene-like layer	[116]
	ECUT-36	(3,9)-c 3D	[140]
	U-NTB-1	honeycomb layer	[251]
	U-NTB-2	(3,10)-c 3D	[251]
NTBPC	U-NTBPC-1	2D	[251]
	U-NTBPC-2	2D + 2D → 3D	[251]
TCI	Th-TCI	(3,8)-c 3D	[147]
	U-TCI-1	(4,8)-c 3D	[194]
	U-TCI-2	4-fold interpenetrated	[194]
	U-TCI-3	wave-like layer	[194]
	UMn-TCI	2D	[194]
	UNi-TCI	4-fold interpenetrated	[194]
TATAB	Th-TATAB	3D	[145]
	U-TATAB	graphene-like layer	[252]

Linker	MOF	Topology	Ref.
TTSTB	SCU-14	woven 3D	[253]
BTPCA	U-BTPCA-(1-4)	2-fold interpenetrated	[115]
	U-BTPCA-5	3D	[115]
MTSB	U-MSTB	(6,3)-c layer	[188]
PSTB	U-PSTB-1	2-fold interpenetrating	[254]
	U-PSTB-2	3-fold interlocked 3D	[254]
	U-PSTB-3	2-fold interpenetrating	[255]
	U-PSTB-6	spider-type web	[255]
	U-PSTB-9	4-nodal 3D	[188]

Linkers are abbreviated as: **1,2,3-BTC** = 1,2,3-benzenetricarboxylic acid; **BDB** = 3,5-di(4′-carboxylphenyl) benzoic acid; **TMTB** = 4,4',4''-(2,4,6-trimethylbenzene-1,3,5-triyl)tribenzoic acid; **NTBPC** = 4',4''',4'''''-nitrilotris([1,1'-biphenyl]-4-carboxylic acid; **BTPCA** = 1,1′,1″-(benzene-1,3,5-triyl)tripiperidine-4-carboxylic acid; **TTSTB** = 4,4',4''-((1,3,5-triazine-2,4,6-triyl)tris(sulfanediyl))tribenzoic acid.

The design of tritopic carboxylate ligands generally involves symmetric expansion, partial substitution, and backbone desymmetrization, manifesting a higher level of complexity to assemble An-MOFs (Table 8) relative to those based on ditopic carboxylate with default topologies.

Starting from the most commonly used tritopic carboxylate ligand, namely BTC, the symmetric expansion leads to BTB, which converts to TMTB (or TTTPC) by linker substitution. The substitution of methyl into the benzene ring of BTB exerts additional intramolecular interaction, leading to the formation of NU-1301with highly complex quaternary structures, whose unit cell size is the largest for a porous crystal reported to date[248]. Changing the number of benzene rings or the relative position of tethering carboxylate groups, implements linker desymmetrization, replacing BTB with BDB, BPTC, and BCPBA or BTC with 1,2,3-BTC and 1,2,4-BTC, respectively. The equatorial plane of uranyl affords an umbrella-shaped geometry instead of an idealized geometry thus generating a series of wavy layers that assemble into a polycatenated framework in U-BDB due to the "linker mismatch" [247].

Replacing the central benzene ring in BTB with a ternary amine leads to the redox-

active tri(biphenyl)amine skeleton. Th-NTB demonstrates that low-valent actinides can adopt anisotropic coordination environments that resemble a high-valent actinyl, potentially rendering new 5f-5f heterobimetallic MOFs with a low- and high-valent actinide located on the same lattice sites[116]. Since NTB can undergo remarkable changes from a nearly flat to a non-coplanar conformation, a two-fold interpenetrating net can be observed in U-NTB-2 in contrast to the honeycomb-like layer in U-NTB-1[251]. The ligand expansion and central substitution result in NTBPC, TCI, TATAB, TTSTB and BTPCA, respectively. As the parallel networks are spatially arranged to pass through large hexagonal loops of inclined subnets, a 3D polycatenated framework is observed in U-NTBPC-2[251]. The nitrogen-rich center and flexible deprotonated carboxyl arms of these tripodal ligands are able to display a bowl- or chair-shaped configuration due to different torsion angles between the arms and the nitrogen heterocycle. These interchangeable configurations and various deprotonated states of the tricarboxylate groups lead to distinct stacking modes of layers or assemblies of 3D frameworks. One structural tendency is that free heterometal complexes are confined in the channels of TCI based U(VI)-MOFs probably due to the reduced reactivity of TCI towards relatively soft heterometals[194].

MSTB and PSTB are tetrahedral-like carboxylate ligands, in which three of the aromatic rings in tripodal configuration feature a large degree of spatial rotation and stretch in different directions around the silicon center. Considering the steric effect of methyl or benzene on the configuration of tripodal carboxylate groups, it yields layer-like or interpenetrating 3D frameworks[188,254,255].

The diverse configurations of tritopic carboxylate ligands has contributed to a few highly porous An-MOFs (Fig.7) and should be further exploited to build An-MOFs with nondefault topologies and porosities.

3.2.4 Tetratopic carboxylate ligand
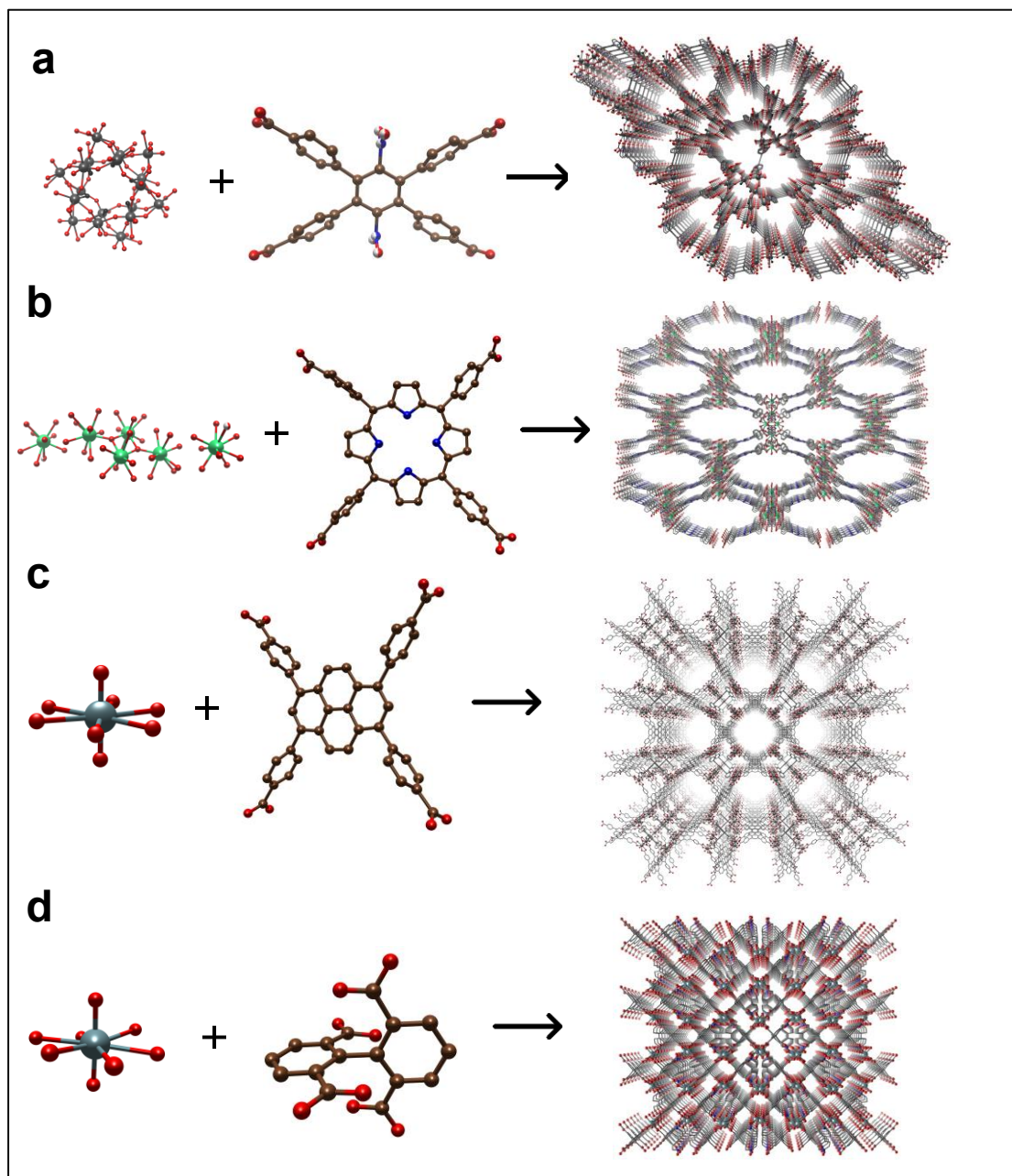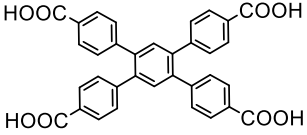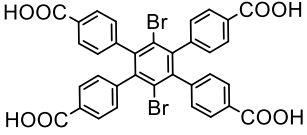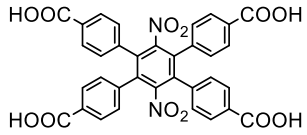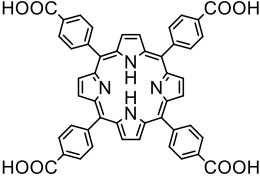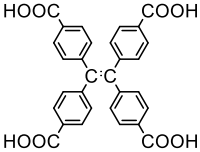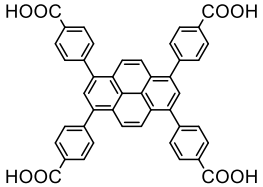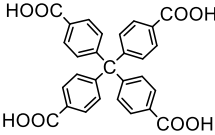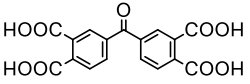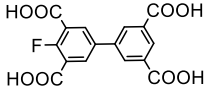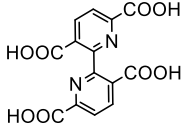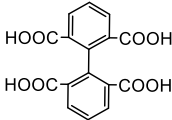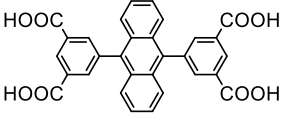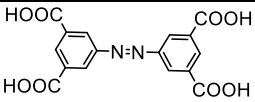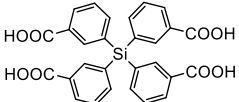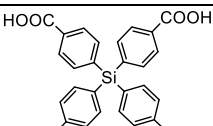
Figure 8. Representative An-MOFs based on tetratopic carboxylate ligands: (a) NNS-3; (b) Th-IHEP-5; (c) NU-1300; (d) U-1,2,6-BPTC-4.

Table 9 Summary of An-MOFs based on tetratopic carboxylate ligands

inker	An-MOF	Network	Ref
HOOC COOH HOOC COOH **PM**	U-PM	non-interpenetrating 2D	[102]
	RPL-1	3D	[80]

Structure	Name	Dimensionality	Ref
TCPB	NSS-1	3D	[155]
TCPB-Br₂	Th-NU-1008	3D	[58]
	Th-NU-1011	3D	[58]
	NSS-2	3D	[155]
TCPB-NO₂	NSS-3	3D	[155]
TCPP	NU-905	non-interpenetrating 3D	[121]
	Th-IHEP-5	3D	[122]
	Th-IHEP-6	3D	[122]
	U-IHEP-4	3D	[91]
	TCPP-U1	2-fold interpenetrating	[256]
	TCPP-U2	non-interpenetrating 3D	[256]
	IHEP-9	2-fold interpenetrating	[207]
TCPE	FJI-H-U1	3D	[257]
TBAPy	NU-1300	3D	[258]
	U-TBAPy-1	2-fold interpenetrating	[259]
	U-TBAPy-2	non-interpenetrating 3D	[259]
MTB	U-MTB-1	2-fold interpenetrating	[260]
	U-MTB-2	non-interpenetrating 3D	[260]
BPTCD	U-BPTCD-1	double chains	[96]
	U-BPTCD-2	zigzag layers	[96]
mF-BPTC	U-mF-BPTC	2D	[261]
	ULa-BPyTC	double-stranded chains	[201]
	UCd-BPyTC	(4,6)-c 3D	[201]

Structure	Name	Dimensionality	Ref
BPyTC	UMn-BPyTC	(3,5)-c 3D	[201]
1,2,6-BPTC	U-1,2,6-BPTC-5	1D	[123]
	U-1,2,6-BPTC-(1-3,6)	2D	[123]
	U-1,2,6-BPTC-4	2-fold interpenetrating	[123]
DPATC	HNU-39	3D supramolecular	[262]
ABTC	U-ABTC	3D	[263]
T3CPS	U-T3CPS	3D	[110]
T4CPS	U-T4CPS	3-fold interpenetrating	[110]

Linkers are abbreviated as: **TCPE** = tetrakis(4-carboxyphenyl)ethylene; **TBAPy** = 4,4',4'',4'''-(pyrene-1,3,6,8-tetrayl)tetrabenzoic acid; **PM** = pyromellitic acid (or 1,2,4,5-benzenetetracarboxylic acid); **4-mF-BPTC** = 4-monofluorobiphenyl-3,3,5,5-tetracarboxylate; **DPATC** = 5,5'-(anthracene-9,10-diyl)diisophthalic acid; **DTATC** = 5,5'-(9,10-dihydroxy-4a,9,9a,10-tetrahydroanthracene-9,10-diyl)diisophthalic acid; **ABTC** = 3,3',5,5'-azobenzenetetracarboxylic; **T3CPS** = tetrakis(3-carboxyphenyl)silicon; **T4CPS** = tetrakis(4-carboxyphenyl)-silicon.

Tetratopic carboxylate ligands predominate in constructing highly porous An-MOFs (Table 9) due to their extended dynamic configurations including square, rectangular and tetrahedral geometries, giving rise to opportunities of ligand design as well as challenges in framework control. The design principles also cover linker expansion, substitution and desymmetrization imposing on the simplest tetracarboxylic acid, namely PM. Specifically, these "descendent" ligands can be classified into three categories with respect to the phenyl backbone. The first consists of an inner functional core tethering outer tetraphenyl rings (i.e. TCPB, TCPP, TCPE, TBAPy, T3CPS, MTB, T4CPS). They feature distinct central functionality or moderate flexibility of pendant benzoate groups that are amenable for high-dimensional complex An-MOFs. Although that the benzoic carboxylates of TBAPy are perfectly perpendicular to the plane of the pyrene core, the alignment of metal nodes is dictated by the conformation of adjacent benzoate groups on TBAPy, resulting in NU-1000 and NU-901 as polymorphs[70]. This polymorphism can partly account for distinct structural motifs in TBAPy based U(VI)-MOFs. The second (DTATC, ABTC, and

BPTCD) and third category (4-mF-BPTC, BPyTC, 1,2,6-BPTC) can be simplified as terphenyl and biphenyl backbone tethering tetracarboyxlate groups, respectively. These multidentate linkers usually display high structural flexibility that contributes to a large diversity of dimensionalities in An-MOFs.

While tetratopic carboxylate based An-MOFs hold promise for the synthesis of porous functional materials (Fig.8), the explicit effect of synthetic conditions on linker conformation should be investigated in order to rationalize the formation of ultraporous An-MOFs for practical applications.

3.2.5 Hexa- and octa- carboxylate ligand
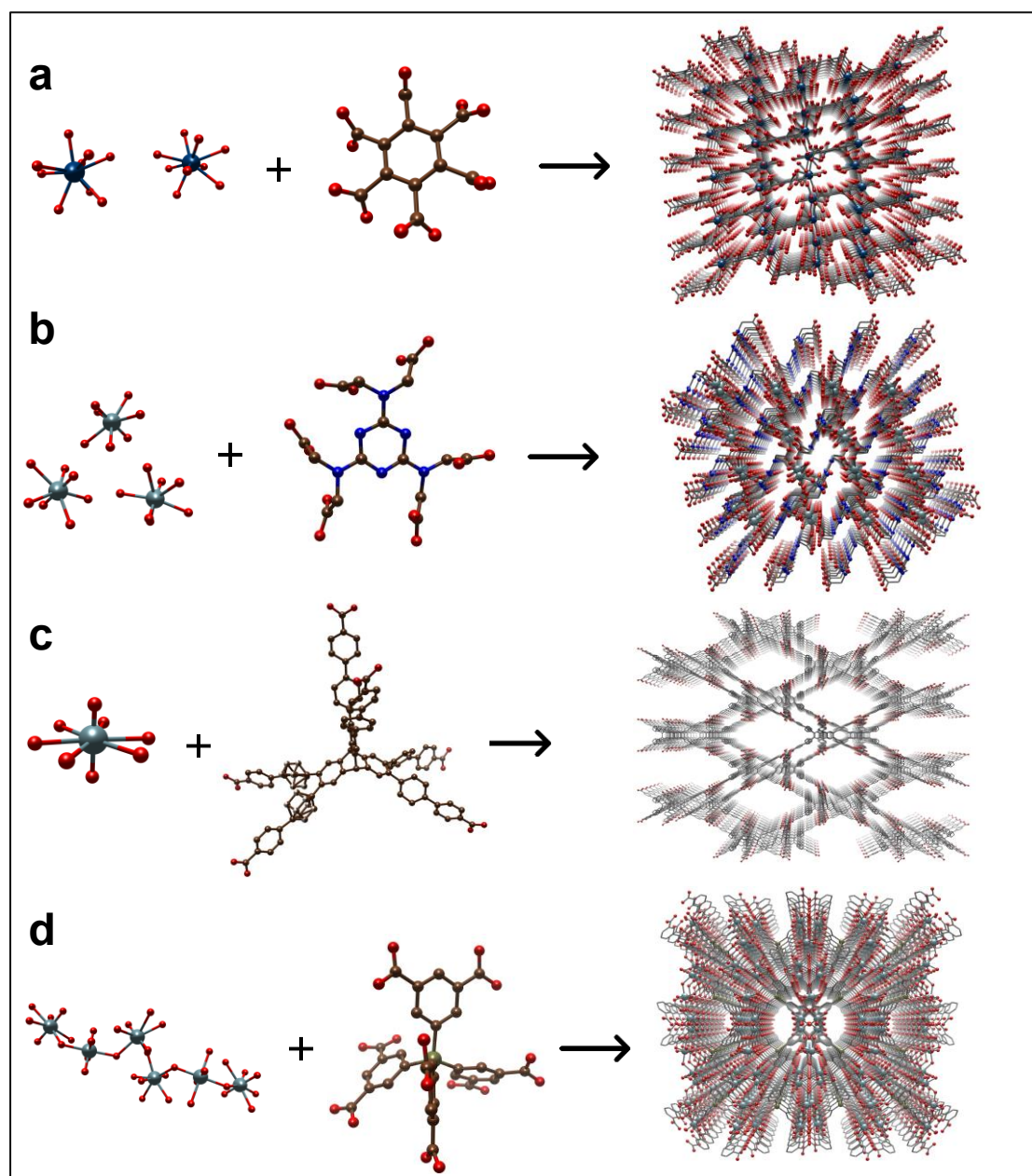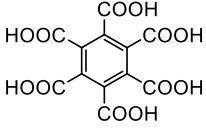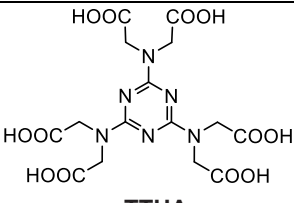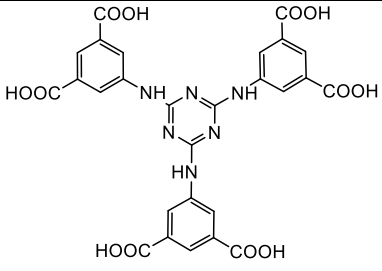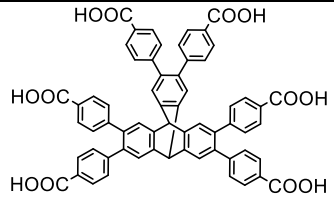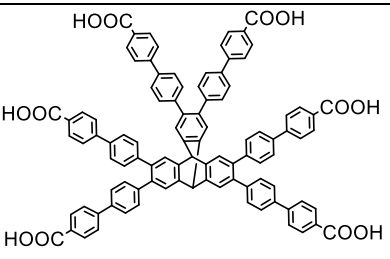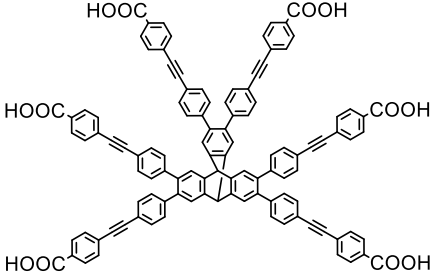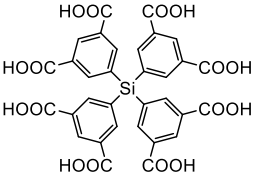
Figure 9. Representative An-MOFs based on hexa- and octa-carboxylate ligands: (a) Pu-1α; (b) U-TTHA-2; (c) NU-1351; (d) U-TDCS-2.

Table 10 Summary of An-MOFs based on hexa- and octa-carboxylate ligands

Linker	An-MOF	Network	Ref
COOH HOOC COOH HOOC COOH COOH **MEL**	Cf-1	chains	[128]
	U4-MEL	dense 3D	[46]
	Np-MEL	dense 3D	[46]
	Pu-1α	3D	[48]
	Pu-1β	3D	[48]
	1-Am	3D	[127]
	Cm-2	3D	[54]
HOOC COOH N N N HOOC COOH HOOC COOH **TTHA**	Th-TTHA	3D	[146]
	U-TTHA-4	3D	[197]
	UNa-TTHA	3D	[197]
	U-TTHA-1	(3,3,6)-c 3-nodal 3D	[197]
	U-TTHA-2	3D	[197]
	U-TTHA-3	(3,4,5,6)-c 4-nodal 3D	[264]
	U-TTHA-5	2D	[236]
COOH COOH HOOC NH N N NH COOH N HN HOOC COOH **TDPAT**	U-TDPAT	3D	[265]
HOOC COOH HOOC COOH HOOC COOH **PET-1**	NU-1350	3D	[266]
HOOC COOH HOOC COOH HOOC COOH **PET-2**	NU-1351	3-fold catenated	[266]

59

PET-3	NU-1352	3D	[266]
TDCS	U-TDCS-(1,2)	3D	[188]

Linkers are abbreviated as: **TDPAT** = 2,4,6-tris(3,5-dicarboxylphenylamino)-1,3,5-triazine; **PET** = peripherally extended triptycene.

Zhou and coworkers recently summarized MOFs based on multicarboxylate linkers[267] and only a small number of hexa- or octa-topic carboxylate linkers have been utilized for An-MOFs (Table 10). MEL is a primary hexatopic organic linker that displays various coordination modes with uranyl and transuranium metals, mostly yielding dense 3D frameworks[46,48]. Both TTHA and TDPAT have six carboxyl functional groups and three flexible arms, enabling them to act as μ_n-bridge (n = 6, 7, 8, 10, 12) to assemble actinide PBUs or SBUs into 3D frameworks[197,265]. PET is a trigonal-prismatic rigid linker for hydrogen-bonded organic frameworks and MOFs. Isomers of PET have been used to prepare NU-1350, NU-1351, and NU-1352. The distortions of shorter PET-1 result in an octahedral linker geometry while longer and flexible PET-3 leads to close to ideal trigonal prismatic geometry and experiences less strain in the coordination with trigonal planar uranyl nodes, forming different topologies[266]. TDCS is the only octacarboxylate ligand that has been utilized for An-MOFs, generating porous 3D frameworks[188].

The use of multicarboxylate linkers, particularly penta-, hexa-, octa-, and dodeca-carboxylate linkers (Fig.9), will expand the topologies and porosities of An-MOFs in light of the paucity of mesoporosity or nondefault topologies in An-MOFs.

3.2.6 Aliphatic carboxylate ligand
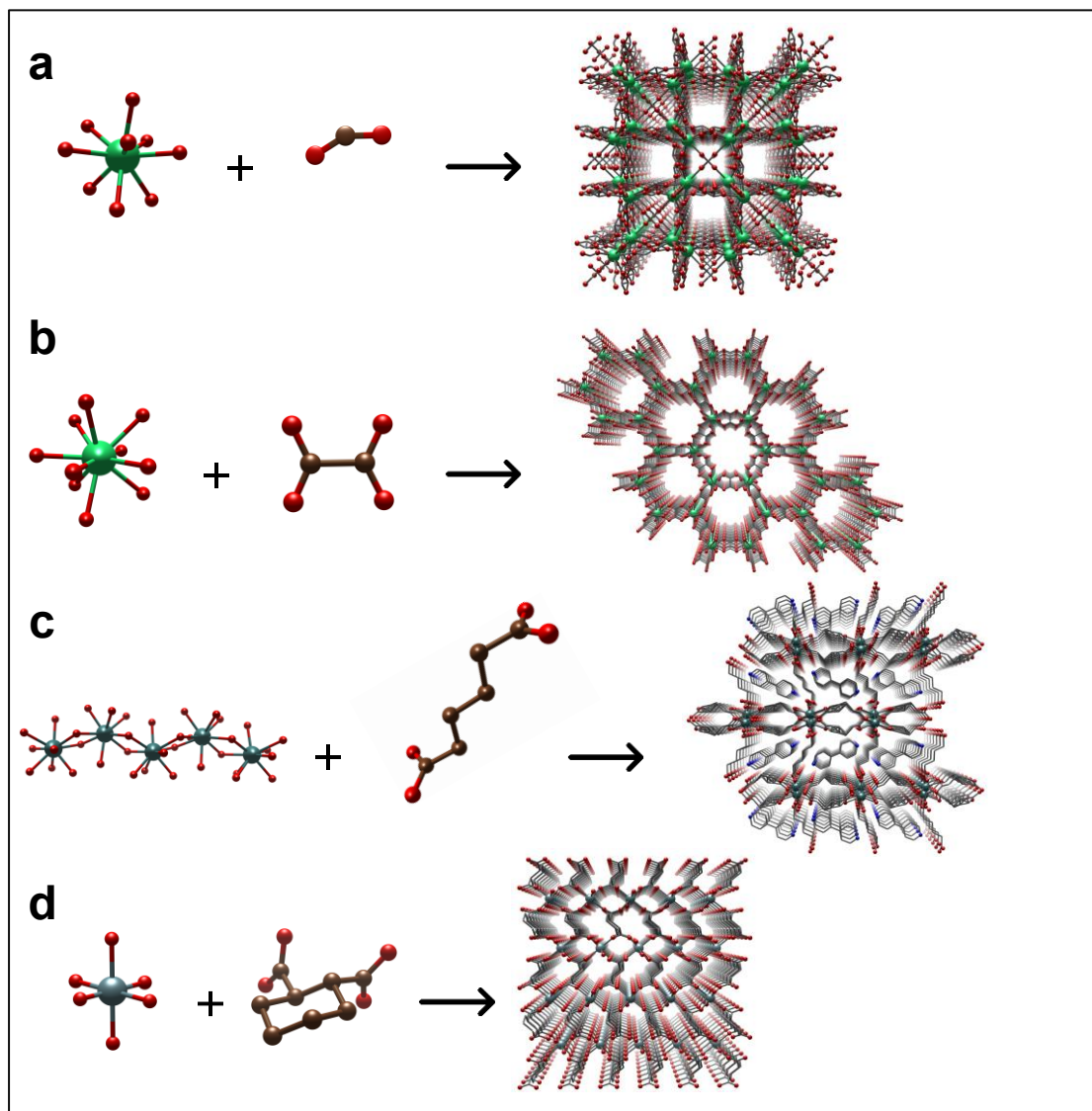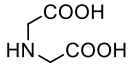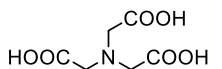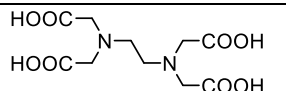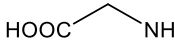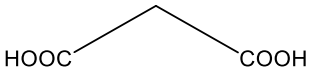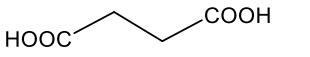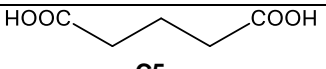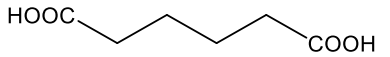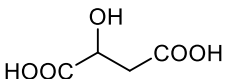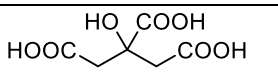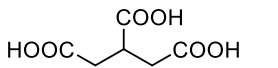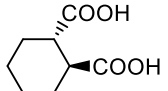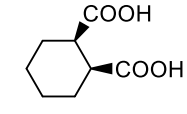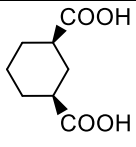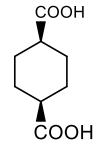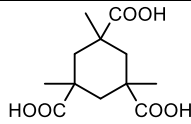
Figure 10. Representative An-MOFs based aliphatic carboxylate ligands: (a) Th-SINAP-4; (b) Th-OA-2; (c) Am-GWMOF-6; (d) U-CHDC-1.

Table 11 Summary of An-MOFs based on aliphatic carboxylate ligands

Linker	An-MOF	Network	Ref
HCOOH	Th-SINAP-1	2-fold interpenetrating	[89]
	Th-SINAP-2	2D grid	[89]
	Th-SINAP-4	3D	[89]
	Th-SINAP-5	3D	[89]
	Th-SINAP-6	3D chiral	[89]
H$_2$C$_2$O$_4$	Th-OA-3	1D	[142]
	U-OA-1	2D	[187]
	U-OA-2	2D	[268]

	U-OA-4	3D supramolecular	[269]
	Th-OA-2	3D	[142]
	ThCa-OA-(1,2)	3D	[142]
IDA	UMON	1D nanotubes	[94]
	Th-IDA	2D	[130]
NTA	Th-NTA	2D	[130]
	UNi-NTA	2D	[95]
EDTA	Th-EDTA	2D	[130]
glycine	U-G1	wavy layers	[169]
C3	UCd-C3-1	2D supramolecular	[220]
	UCd-C3-2	graphite-like layer	[220]
SA (or C4)	U-SA-1	helical chain	[33]
	UNSL-1	3D supramolecular	[97]
	U-SA-(2,3)	3D	[109]
	Pu-SA	3D	[195]
C5	U-C5	graphite-like layer	[43]
	Np-C5	graphite-like layer	[43]
	Pu-C5	3D	[43]
	UNa-C5	3D	[39]
C6	Am-GWMOF-6	3D	[52]
MA	U-MA	2D	[101]
	UCu-MA	2D	[101]
CIT	UZn-CIT	1D	[101]
	UNi-CIT	compact layer	[101]
	UCd-CIT-1	uninodal 3D	[101]
	UCd-CIT-2	compact layer	[101]
TCA	UCo-TCA	1D hexagonal tubule	[200]
	UBa-TCA	2-nodal 3D	[101]
	UNi-TCA	2-nodal 3D	[101]
	UCu-TCA	2-nodal 3D	[200]
	UPb-TCA	2-nodal 3D	[101]
CHDC	U-CHDC-(1-4)	2D	[270]
	U-CHDC-(5,6)	homochiral helical	[270]
	UCu-CHDC-(1,2)	2D supramolecular	[172]
	UCd-CHDC	2D	[172]

	UNi-CHDC-(2,3)	2D	[214]
	UNa-CHDC-2	compact 3D	[172]
	UK-CHDC-(1-3)	compact 3D	[196]
C-CHDC	U-C-CHDC-2	2D	[270]
	UNa-C-CHDC	2D	[196]
	UK-C-CHDC	compact 3D	[196]
	UNi-C-CHDC-2	compact 3D	[196]
C-1,3-CHDC	U-C-1,3-CHDC	ladder-like ribbon	[196]
C-1,4-CHDC	U-C-1,4-CHDC-1	1D	[173]
	U-C-1,4-CHDC-(2,3)	2D	[173]
	U-C-1,4-CHDC-4	zigzag chains	[173]
	U-C-1,4-CHDC-6	ladder-like chain	[173]
	U-C-1,4-CHDC-7	3-fold interpenetrating	[173]
	U-C-1,4-CHDC-(5,8)	3D compact	[173]
	UZn-C-1,4-CHDC	2D	[173]
	UCd-C-1,4-CHDC	compact 3D	[173]
	UCo-C-1,4-CHDC	compact 3D	[173]
	UPb-C-1,4-CHDC	compact 3D	[173]
	UCu-C-1,4-CHDC	3-fold interpenetrating	[173]
KTA	UCs-KTA	2D network	[271]

Linkers are abbreviated as: **MA** = malic acid; **KTA** = *cis*,*cis*-1,3,5-trimethylcyclohexane-1,3,5-tricarboxylic acid (Kemp's triacid).

Aliphatic carboxylate ligands with alkyl backbone are less rigid compared to aromatic carboxylate ligands and have been employed in constructing An-MOFs with potential dynamic flexibility (Table 11). Formic acid, as the simplest aliphatic monocarboxylic acid, has been normally used as a coordination modulator for An-MOFs. The Lin group prepared a series of Th-MOFs by varying the HCOOH/Th ratio and addition of water. These atypical thorium formates have been utilized as open-frameworks for I_2 adsorption[89]. Oxalic acid is the simplest aliphatic dicarboxylic acid that has been extensively used in the nuclear fuel cycle. The structures of actinide oxalates were summarized by Abraham and coworkers[272] and we herein only present recent actinide oxalate frameworks, into which actinide nodes assemble by tetrapodally bridging OA.

Flexible alkyl chain-based dicarboxylate ligands including FA, HOOC-$(CH_2)_{n-2}$-COOH (C_n, n = 3-11) readily coordinate with actinide to generate chains, layers or 3D motifs in the presence or absence of N-donor ligands[170]. Aminopolycarboxylate ligands (IDA, NTA, EDTA and glycine)[130,169], hydroxyl-substituted C_n (MA, CIT)

[101], and tricarboxylate TCA[200] have been adopted as multidentate ligands for actinide ions, yielding different dimensionalities in An-MOFs. CHDC, 1,3-CHDC, 1,4-CHDC and KTA are representative cyclohexane-based carboxylate ligands featuring different stereo forms (e.g. linear *trans* or kinked *cis*). They display multiple coordination modes with uranyl and heterometals, in which some heterometal species will exert structure-directing effects on the uranyl-carboxylate assembly[173,196,271].

The structural complexity of An-MOFs (Fig.10) based on aliphatic carboxylate ligands had been underestimated meanwhile engineering their structural dynamics for gas separation should be emphasized in parallel with Zr-MOFs[273].

3.2.7 Phosphonate ligand
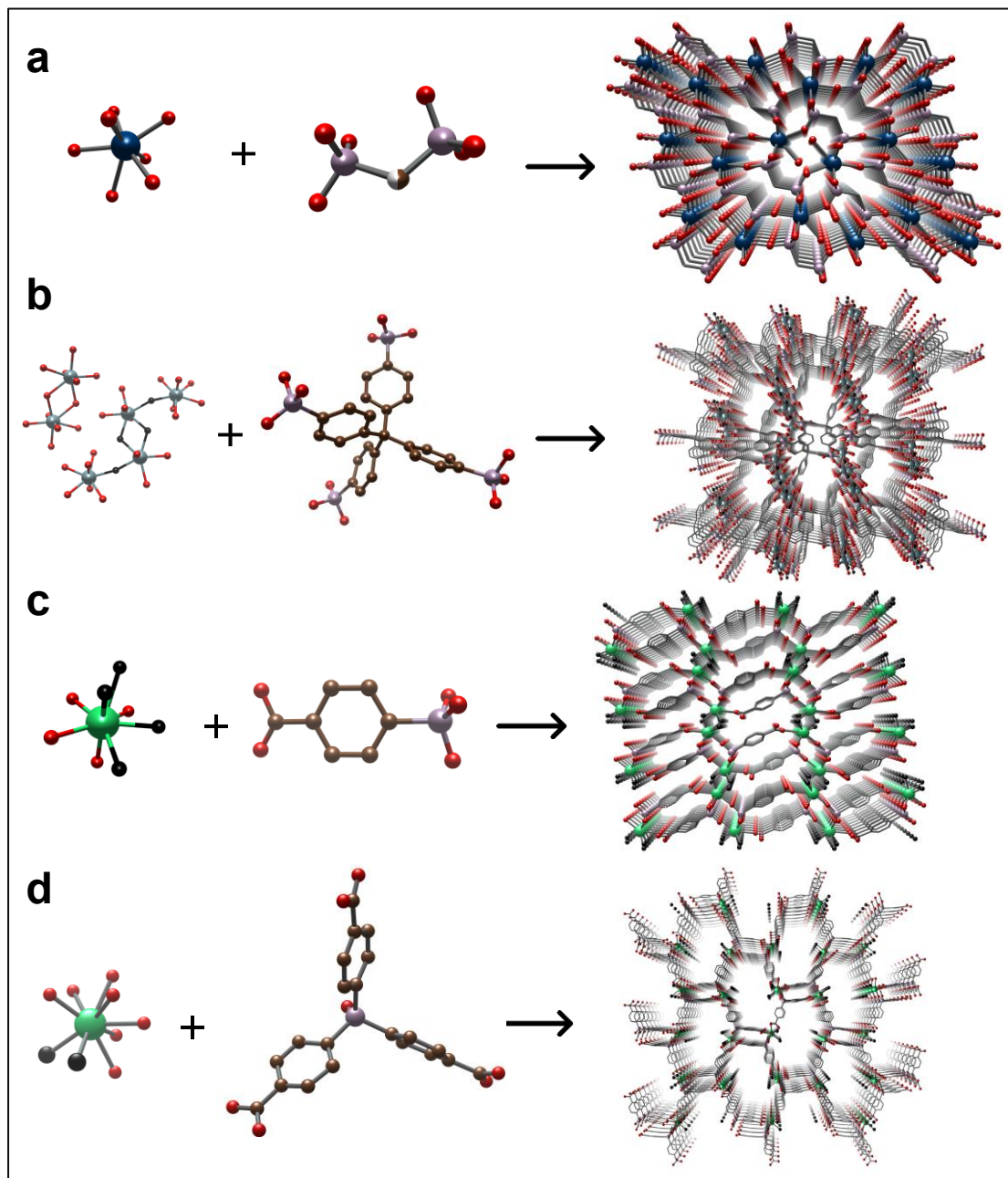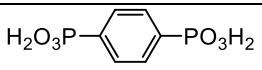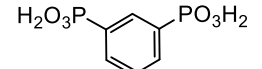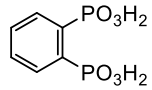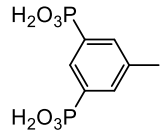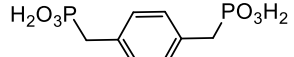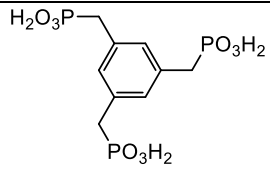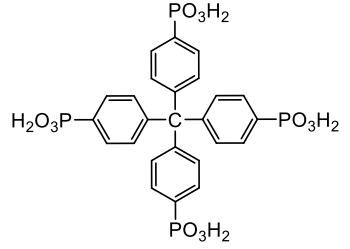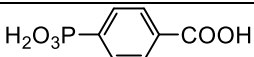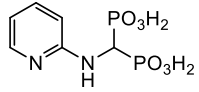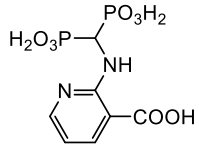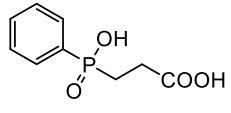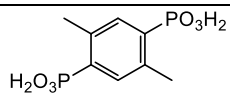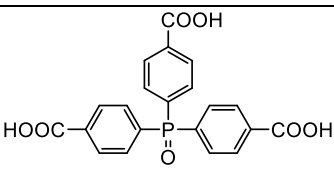
Figure 11. Representative An-MOFs based on phosphonate ligands: (a) Pu-2; (b) UPF-104; (c) Th-4-CPP; (d) Th-TPO-2.

Table 12 Summary of An-MOFs based on phosphonate ligands

Linker	An-MOF	Network	Ref
$CH_2(PO_3H_2)_2$ **C1P2**	U4-2-H_2O	1D	[111]
	U6-1	1D	[111]
	U4-2-K	1D	[111]
	U6-2	2D	[111]

	U4-3	3D	[111]
	U4-4	3D	[111]
	U4-5	3D	[111]
	U4-6	3D	[111]
	U-C1P2-(1,2)	3D	[186]
	NpC1P2-1	3D	[45]
	PuC1P2	3D	[126]
	Pu-2	3D	[47]
	UPu-1	3D	[47]
CH$_3$PO$_3$H$_2$ **MeP**	Np-MeP-2	2D	[44]
	Pu-1	(3,6)-c 3D	[47]
H$_2$O$_3$P—⬡—PO$_3$H$_2$ **BBP**	Th-BBP-1	3D	[31]
	Th-BBP-2	3D	[31]
H$_2$O$_3$P—⬡—PO$_3$H$_2$ **PBP**	U-PBP-(1,2)	3D	[106]
	U-PBP-3	3D	[112]
⬡ PO$_3$H$_2$ / PO$_3$H$_2$ **PDP**	UAg-PDP	2D	[274]
H$_2$O$_3$P ⬡ PO$_3$H$_2$ CH$_3$ **MPDP**	U-MPDP-(1,2)	3D	[34]
	U-MPDP-3	2D	[34]
	UCo-MPDP	3D supramolecular	[34]
	UZn-MPDP	3D supramolecular	[34]
H$_2$O$_3$P—CH$_2$—⬡—CH$_2$—PO$_3$H$_2$ **PMB**	U-PMB-1	3D supramolecular	[108]
	U-PMB-(2,4)	wave-like layer	[108]
	U-PMB-3	3D	[108]
H$_2$O$_3$P ⬡ PO$_3$H$_2$ PO$_3$H$_2$ **BTTP**	U-BTTP-1	3D	[275]
	U-BTTP-2	3D	[75]
	U-BTTP-(3-5)	3D	[75]
PO$_3$H$_2$ H$_2$O$_3$P—C—PO$_3$H$_2$ PO$_3$H$_2$ **TPPM**	UPF-101	(4,4)-c 2-nodal 3D	[76]
	UPF-102	(6,4,5)-c 3-nodal 3D	[76]
	UPF-104	(6,8,10)-c 3-nodal 3D	[76]
HOOCCH$_2$PO$_3$H$_2$ **PAT**	U-PAT	2D	[276]
	Th-PAT	3D	[105]
	SCU-UEu-1	3D	[204]

Linker	MOF	Dimensionality/Topology	Ref
H_2O_3P—⬡—COOH **4-CPP**	Th-4-CPP	3D	[134]
PO_3H_2 / PO_3H_2 (pyridine–NH) **PMBP**	U-PMBP	3D supramolecular	[277]
H_2O_3P–CH(PO_3H_2)–NH–pyridine–COOH **DPAN**	U-DPAN	1D	[277]
Ph–P(=O)(OH)–CH₂CH₂–COOH **CPP**	CPP-U1	(2,4)-c 2D	[119]
	CPP-U2	(3,6)-c 2D	[119]
	UCo-CPP-1	(3,4)-c 2D	[210]
	CPP-U3	Pillared-layer 3D	[119]
	CPP-U4	Pillared-layer 3D	[119]
	UCo-CPP-2	Pillared-layer 3D	[210]
	UZn-CPP	Pillared-layer 3D	[210]
	UCd-CPP-2	Pillared-layer 3D	[210]
PO_3H_2 / H_2O_3P (2,5-dimethyl benzene) **DMPDP**	DPTP-U1	2D	[180]
	DPTP-U2	3D	[180]
COOH / HOOC–⬡–P(=O)(–⬡–COOH)–⬡–COOH **TPO**	Th-TPO-1	(4,3)-c 3D	[132]
	Th-TPO-2	(4,4)-c 3D	[132]
	SCU-3	2-fold (3,3)-c 3D	[278]

Linkers are abbreviated as: **PDP** = 1,2-bis(dimethoxyphosphoryl)benzene; **DPB** = 3,5-diphosphonobenzoic acid; **PMBP** = (pyridine-2-ylamino)methylene)bis(phosphonic acid; **BTTP** = benzene-1,3,5-triyltris(methylene)-triphosphonic acid; **DMPDP** = (2,5-dimethyl-1,4-phenylene)diphosphonic acid; **DPAN** = 2-((diphosphonomethyl)amino)nicotinic acid.

Due to the strong coordination ability with actinides in acidic solution, phosphonate ligands have been extensively used in solvent-extraction based actinide separation processes while phosphonate-based An-MOFs (Table 12), especially for An(IV), lag behind carboxylate-based ones largely due to challenges in isolating single-crystals. Simple alkylphosphonate ligands including MeP, C1P2 have been employed to prepare An-MOFs, revealing structural periodic trends across the accessible light actinides. It is noted that the 2D layer in Pu-1 is closely related to R-Zr(HPO$_4$)$_2$, representing a case where a non-radioactive surrogate like Zr(IV) provides a good mimic of Pu(IV) and vice versa[47]. While BBP, PBP and PDP complete the isomers of benzenebisphosphonic acid for An-MOFs, BTTP and TPPM are the only tri-, and tetratopic phosphonate linker for An-MOFs to date.

The deprotonation states (monoprotonated, deprotonated and triply deprotonated), coordination modes (tetradentate, pentadentate, and hexadentate, chelating and/or

bridging), ligand conformation (*trans*, *cis*), hydrogen bonding (dangling, uncoordinated P-OH) of phosphonate groups in di-, tri-, tetra-phosphonate, or carboxyphosphonate ligands collectively enable their versatile binding modes with actinides and allows them to assemble into diverse frameworks. Since both carboxylate and phosphonate groups in carboxyphosphonates act as strong donors in a competitive manner, the high effective charge and anisotropic coordination environment allow thorium and uranyl to interact with carboxylic acid groups in 4-CPP[134] and CPP[119]. TPO also displays multiple coordination modes with Th and U due to the presence of tricarboxylate groups and P=O group[132]. In SCU-3, TPO bridges three neighboring uranyl PBUs by chelating carboxylate groups since the terminal P=O loses the coordination competition with carboxylate groups, generating a "DNA-like" homochiral double-helical structure[278].

The unique phosphonate crystal chemistry relative to its carboxylate counterparts forecasts a huge opportunity of preparing porous An-MOFs (Fig.11) with elevated stabilities for target applications.

3.2.8 Rotaxane ligand
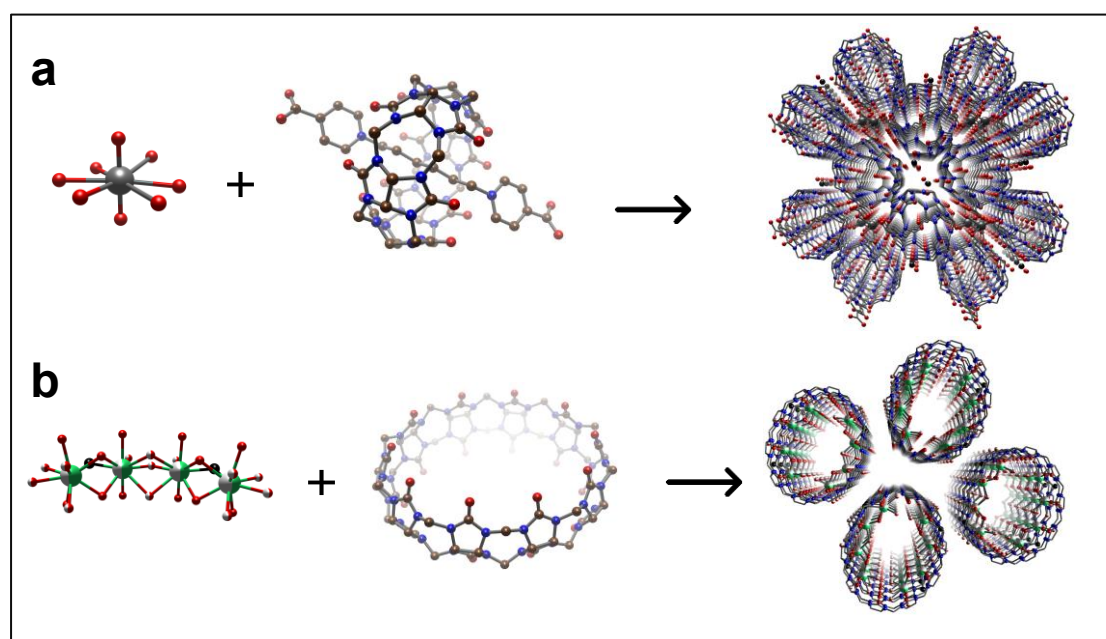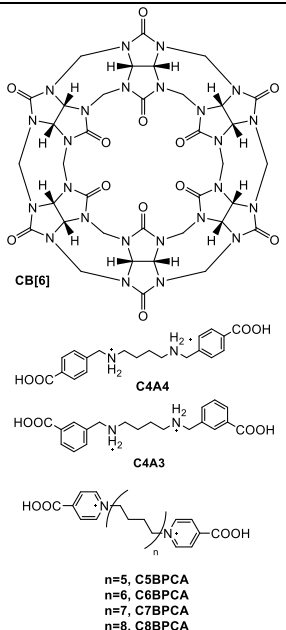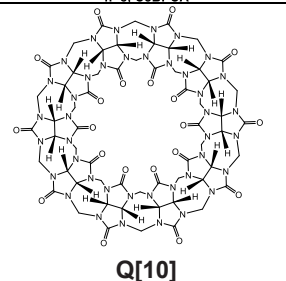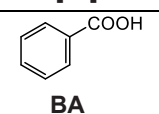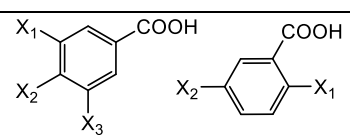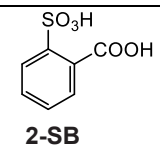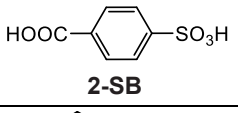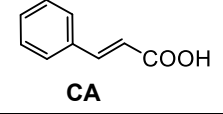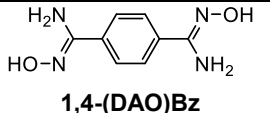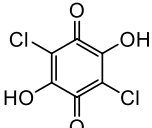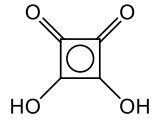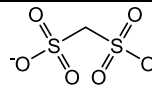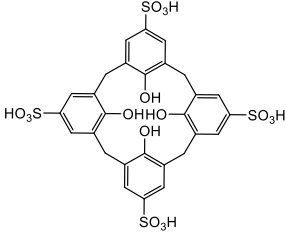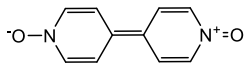
Figure 12. Representative An-MOFs based on rotaxane ligands: (a) NRCP-1; (b) Th-Q[10].

Table 13 Summary of An-MOFs based on rotaxane, monocarboxylate and non-carboxylate ligands

Linker	An-MOF	Network	Ref
	UCe-CB[6]	zigzag chain	[198]
	U-C4A3-CB[6]-5	zigzag chain	[191]
	U-C4A4-CB[6]-2	2-fold layer	[191]

	NRCP-1	interlocked layer	[160]
	URCP1-C5	2D	[279]
	URCP3-C7-1	2D	[279]
	URCP6-C7	2D	[35]
	URCP5-C7	2D	[35]
	URCP4-C7-1	1D	[279]
	URCP4-C7-2	1D	[35]
	URCP5-C7	1D	[35]
	URCP8-C7	1D	[35]
	URCP9-C7	1D	[35]
	URCP3-C8	1D biaxial kinked helix	[88]
	URCP4-C8	1D	[88]
	Th-Q[10]	1D nanotubular	[133]
	Th-BA	2D supramolecular	[137]
	U-BA	2D supramolecular	[280]
	U-XBA-(1,3,6,7)	2D supramolecular	[162]
	U-XBA-(15-17)	2D supramolecular	[174]
	U-XBA-(5,8)	2D supramolecular	[162]
	U-XBA-14	2D supramolecular	[174]
	U-XBA-4	2D supramolecular	[162]
	U-XBA-(18,19)	2D supramolecular	[280]
	Th-2-SB	1D	[139]
	UNi-2-SB-1	3D supramolecular	[139]
	UNi-2-SB-2	2D	[216]
	UCu-2-SB-2	2D	[216]
	UNi-4-SB	3D supramolecular	[139]
	U-CA	3D supramolecular	[187]
	UMOFUA	non-interpenetrating	[36]

Structure	Name	Dimensionality	Ref
Cl₂DHBQ (structure)	U4-Cl2DHBQ	3D	[38]
Squarate (structure)	Am1	2D	[51]
	Am2	3D	[51]
	Cf1	2D	[51]
	Cf2	3D	[51]
MDS (structure)	UK-MDS	1D	[198]
SC4A (structure)	U-SC4A-2	2D	[216]
BPDO (structure)	UCo-BPDO	dense 3D	[211]
	UPt-BPDO	dense 3D	[211]
	U-POM-BPDO	3D	[222]

Linkers are abbreviated as: **4-SB** = 4-sulfocarboxylbenzoic acid; **CA** = Cinnamic acid; **SC4A** = p-sulfonatocalix[4]arene.

Cucurbit[n]urils (CB[n]) are pumpkin-shaped cyclic, bismethylene-linked glycoluril oligomers with carbonyl functionality at the ring edges. Deemed as unconventional O-donor linkers, they promote either direct coordination or hydrogen bonding with uranyl species, leading to monomers, tetramers, or infinite chain-like uranyl species in a family of uranyl cucurbit[n]uril (n = 5-8) complexes[281]. By introducing axles-like linear ditopic linker into closed rings of CB[n], these mechanically interlocked systems, namely supramolecular pseudorotaxane, have been utilized to prepare actinide coordination polymers, as elaborated in the review by Shi from 2018[282]. For clarity, only recent actinide polyrotaxane polymers are illustrated (Table 13). Different string ditopic carboxylate (C4A3, C4A4, CnBPCA, n = 5-8) have been employed along with CB[6] to build chain- or layer-like An-MOFs. For instance, in NRCP-1, CB[6] coordinated to neptunyl PBU and encapsulates C6BPCA, resulting in a daisy chain wherein two C6BPCA are bridged by two neptunyl nodes. An array of chains is cross-linked via neptunyl centers, forming two sets of independent but mechanically interlocked neptunyl-rotaxane layers with quadrilateral holes[160]. CB[10] (or Q[10]) has the largest portal size and cavity featuring a rich host-guest chemistry. However, its coordination chemistry with actinide is far less developed compared to its smaller CB[n] counterparts. In Th-Q[10], two tetranuclear SBUs connect with Q[10] from opposite directions to form 1D nanotubular frameworks[133].

While progress in rotaxane-based An-MOFs (Fig.12) has revealed their structural

tunability, much of their chemistry remains to be discovered. Eventually, the integration of rotaxane supramolecular chemistry with actinide coordination chemistry should lead to a complex and versatile molecular platform.

3.2.9 Monocarboxylate and non-carboxylate ligand
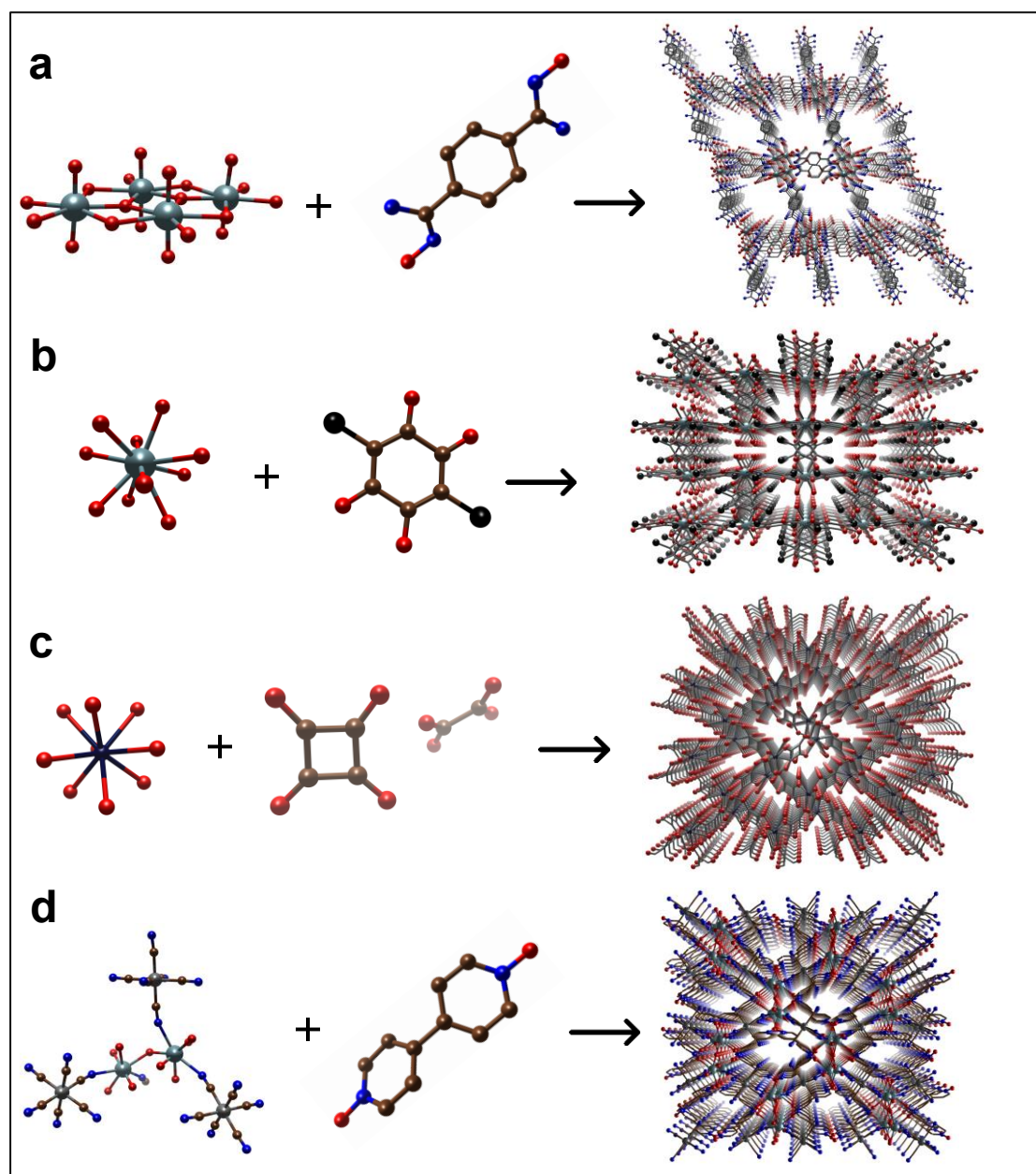
Figure 13. Representative An-MOFs based on monocarboxylate and non-carboxylate ligands: (a) UMOFUA ; (b) U4-Cl$_2$DHBQ; (c) Cf2; (d) UCo-BPDQ.

Aromatic monocarboxylate ligands (BA, XBA, 2-SB, 4-SB, CA) have been employed to build actinide supramolecular framework stabilized by π-π stacking, hydrogen bonding, halogen-halogen interaction, localized halogen-π interactions, or van der Waals interactions. The weak coordinating ability of sulfonates explains why they have been seldom used as ligands for actinides. However, sulfonate coordination may

be promoted when strongly coordinating carboxylate groups are located in a suitable position. The dimensionality and geometry of An-MOFs formed with sulfonate-based ligands arises from intramolecular hydrogen bonding as well as structure-directing effects exerted by various heterometal counterions(Table 13).

To investigate the cooperativity and electronic effects on the coordination behavior of the amidoxime group, 1,4-(DAO)Bz in either zwitterionic or doubly deprotonated, dianionic form, has been adopted as a representative ligand to prepare non-interpenetrating UMOFUA[36]. Cl₂DHBQ is a frequently used redox-active ligand while squaric acid offers relatively soft oxo donors, both featuring various coordination modes with actinides. Linear BPDO has a bipyridine backbone with two deprotonated oxygen atoms, which readily coordinate with uranyl to form flat layers via {U-BPDO-U} linkages and are stabilized by hydrogen bonds between cyanides, hydroxide bridges, and water[211]. In this sense, noncarboxylate ligands open up an avenue to exploring An-MOFs based on unconventional coordinating ligands (Fig.13).

3.3 Framework modularity, topology, and porosity
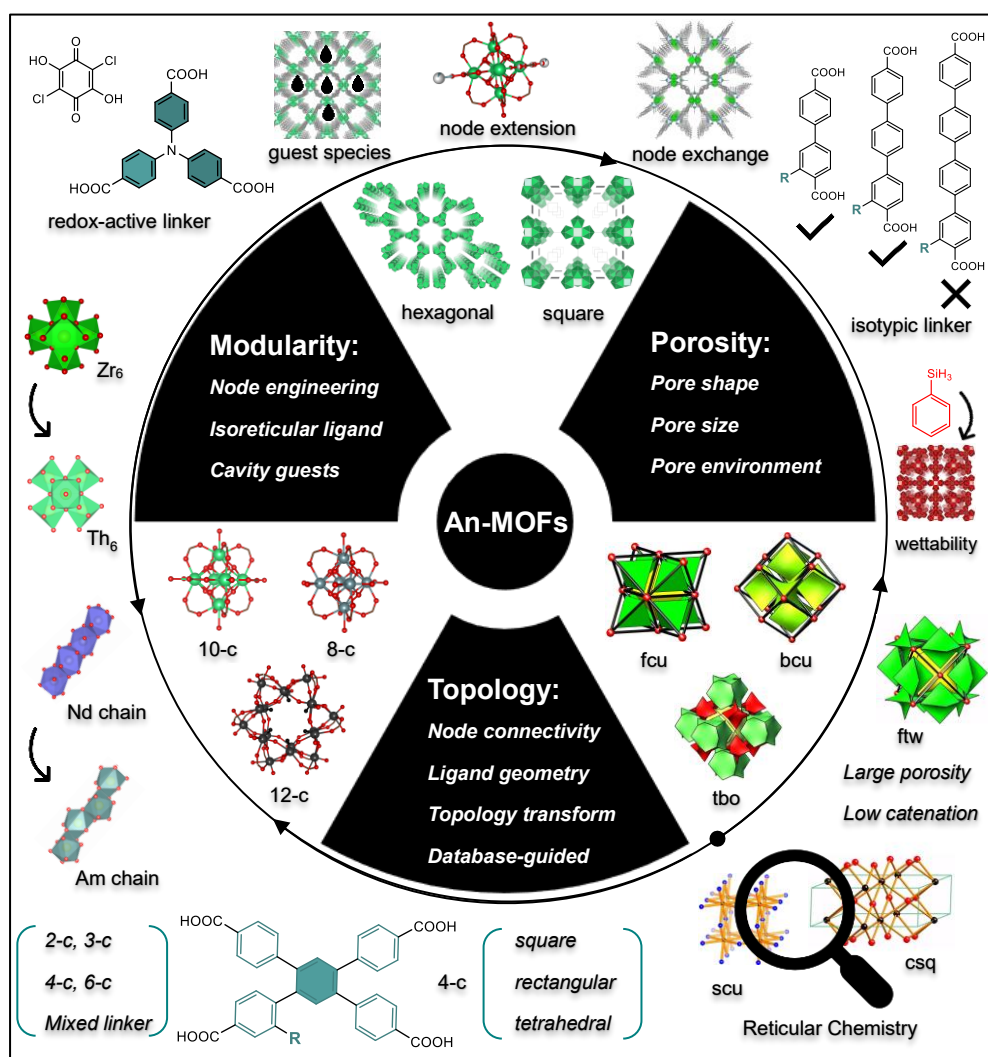
Figure 14. The relationship between framework modularity, topology, and porosity of An-MOFs. The topologies have been acquired from the Reticular Chemistry Structure Resource (RCSR; http://rcsr.anu.edu.au/).

The framework modularity, topology, and porosity comprise the most significant descriptor of An-MOFs and they interplay with each other to allow the rational design of An-MOFs (Fig.14). The actinide node extension including the incorporation of secondary metals or ligands will lead to the shrinkage of porosity while the metal exchange at nodes can maintain the porous architecture. By utilizing the isotypic linker, the pores of the isoreticular frameworks will vary according to the ligand geometry. Upon incorporating guest species into the framework void, the accessible porosity is expected to decrease. Moreover, it is essential to tune the pore parameters by modular control of labile coordination or covalent bonds, or varying the types of modules and organizing the linkage through sequence-controlled methodologies[283]. Certain generic strategies have been designed for building porous An-MOFs: (1) using multitopic ligand with out-of-the-plane connectivity or ligand decoration with an additional functional group. (2) incorporating alkali, transition metal ions, or exploiting cation-cation interaction to increase framework connectivity. (3) introduction of ancillary ligand or organic structure-directing agents. Generally, tuning the framework modularity will systematically lead to the variation of porosity. On the contrary, the pore geometry will determine the feasibility of the installation of capping linkers on unsaturated nodes or the incorporation of guest species due to the size exclusion effect.

By judicious choice of modular actinide nodes and multitopic carboxylate ligands, different combinations of nodes connectivity and ligands geometries will lead to a manifold of framework topologies. By replacing modular trivalent lanthanide, tetravalent transition metal nodes with actinide nodes bearing identical connectivities, the topologies of existing lanthanide or tetravalent transition metal based MOFs will readily transfer to An(III)- and An(IV)-MOFs. However, it is noted that dynamic topological transformation might occur on An-MOFs due to the exchange of metal nodes of different connectivities[284]. To realize missing topologies in An-MOFs, it requires a deep understanding of how the synthetic parameters control actinide clusters and linker conformation. As for the topology versus porosity, a recent minireview presented the relations between topological descriptors and free space of networks[285], which will apply to the topology-guided construction of desired porosity in An-MOFs. One significant structural aspect of An-MOFs is their defects engineering (e.g. the distribution of missing-linker, missing-node defects and ensuing functionalities) that remain unexplored, thus we will not discuss it hereafter.

3.3.1 Framework modularity

The design of framework modularity will tune of the electronic structures of An-MOFs as well as develop platform materials for probing into the interactions between actinide (including decay particles) and external metals, organic ligands, biological species under mild or extreme conditions, which is relevant to practical applications

such as nuclear waste management. One of the most intriguing aspect of An-MOFs electronic structures is their elusive redox-active properties due to typical framework construction (i.e. hard actinide bound by redox-inactive organic ligands). However, as illustrated in redox-active MOFs, three pathways for redox-active An-MOFs are proposed as (1) redox-active metal nodes; (2) redox-active organic linker; (3) redox-active guest species[286].

The interchangeable valences of actinide in solution chemistry provide an opportunity for building redox-active actinide nodes, which prove to be exceedingly rare in An-MOFs. The mixed-valent plutonium-organic frameworks $Pu^{III, IV}$-3, $Pu^{IV, III}$-4 falls into incipient class II and I of Robin–Day system[49]. Guided by this seminal work, redox-active uranium, neptunium, or americium-based MOFs might exhibit unique intervalence charge transfer. The simultaneous incorporation of redox-active main group or transitional metal and actinide into MOFs matrices by using bifunctional linkers[287] is considered as a burgeoning alternative to construct redox-active heterometallic An-MOFs. Zhao and coworkers adopt this strategy to prepare a multifunctional, robust ThNi-INA framework. The partial density of states (DOS) of this MOF indicates that the superior stability attributes to both electrostatic and covalent interactions between Th^{4+}, $Ni^{2+,}$ and INA anions[213]. By analogy, bivalent redox-active metals such as V^{2+}, Cr^{2+}, Mn^{2+}, Fe^{2+}, Sn^{2+} are expected to complex with N-donor moieties of the bifunctional linker to predefine in-situ generated, modular metalloligand for heterometallic An(IV)-MOFs. The challenge lies in the fact that one-pot synthesis parameters need to be optimized and will cost tremendous trials-and-errors. To tackle it, porphyrins, ferrocene, or terpyridine ligands can be used to predefine redox-active metals in heterometallic An-MOFs[91,208,209]. Moreover, redox-active metals are inclined to be incorporated into actinide SBUs by post-synthetic node exchange or extension. Shustova group demonstrated that cobalt node extension in $U_{1.23}Th_{4.77}$-Me$_2$BPDC-8 resulted in changes in the electronic structure near the Fermi edge and led to conductivity enhancement of three orders of magnitude[65]. In the realm of actinide node engineering, it is requisite to use structural descriptors of heterometallic nodes (saturation degree, heterometal pairing, node nuclearity, and geometry) and elucidate the variation of electronic structure assisted by theoretical calculations[288].

In contrast, redox-active An-MOFs with electroactive ligands have been much less studied. The interplay between delocalized electrons of redox-active organic linkers and frontier orbitals of actinide core/cluster can lead to a fruitful of An-MOFs with exquisite electronic structure. Electroactive ligands have been categorized as: (1) naphthalenediimide (NDI); (2) tetrathiafulvalene (TTF); (3) triphenylamine (TPA); (4) quinone[286]. The last two categories had already been utilized for the construction of An-MOFs. Since TPA is readily one-electron oxidized by electrochemical or chemical process to form a stable radical cation, TPA derived ligands have been employed to generate redox-active Th-NTB[116], ECUT-36[140], U-NTB-(1,2), and U-NTBPC-(1,2)[251], wherein the "propeller-like" TPA geometry was interrogated rather than the redox state of the triarylamine core. Practically, polycarboxylate groups can be anchored to triphenylamine core to assemble a variety

of TPA-based ligands[289], which will be transferred to build redox-active An-MOFs. The electron-deficient quinone can evolve into aromatic-like pro-quinoid by reduction and vice versa. Since the reducing nature of U(IV) is comparable to Fe(II), U(IV) quinone coordination polymer may parallel valence tautomerism in iron quinone to exhibit magnetic interaction and electronic conductivity through ligand-based mixed-valency. However, the absence of strong 2p-5f covalency in U4-Cl_2DHBQ might impede metal-ligand electron-transfer as found in 3d metal analogs[38].

The last approach to redox-active An-MOF is to introduce redox-active species (free metal nanoparticles, ligands) into the frameworks cavity, which may destroy the porous architecture of An-MOFs but provide a confined reactor for highly mobile, variable fission products by contingent "guest-guest" reactions. The capping linker installation can further immobilize these radionuclide species through blocking pore windows. A portion of transitional metal complexes reside in the cavity of An-MOFs as redox-active counterion species. For instance, $Cu(2,2-bipy)_2^+$ counterion in UCu-1,4-PDA had been structurally resolved[206], yet leaving the redox-active property unexplored.

The modularity of actinide node, linker strut and guest species allows us to prepare a vast array of photoresponsive or redox-active An-MOFs for detailed understanding of tunable electronic structure and desired chemical properties that show transformative effects on heterogeneous catalysis, chemical sensing, nuclear waste management. One notable example is both monometallic and heterometallic An-MOFs that reveal distinctions in conductivity upon integrating photoresponsive units or guest species, paving a rational avenue for tailoring electronic structures of actinide-containing scaffolds[125]. The modularity design also allows enhancing the radiation stability of An-MOFs by combining a high-energy-delocalized modular π-system linker with a high-nuclearity actinide clusters. The naphthalene-based Th-SINAP-(7,8) displayed good radiation resistance up to 200 kGy[92]presumably due to strong interactions between π-system linker and Lewis acidic thorium SBU. As the naphthalene is replaced by a more π-conjugated binaphthol, TOF-16 tolerates 4 MGy γ-irradiation and 7 MGy He^{2+} irradiation[79]. Overall, the framework modularity involves actinide or heterometal node engineering, isotypic linker design and host-guest chemistry and remains largely underexplored. Besides the combination of d-, p-, and 4f-block with actinide, NDI-, TTF- and other redox-active linkers will be extensively utilized for modular non-innocent An-MOFs.

3.3.2 Framework topology

In principle, reticular chemistry in the MOF area[290–292] enables preconceived An-MOFs to be realized with high synthetic accessibility by judicious selection of actinide nodes, organic linkers of appropriate geometry, connectivity, symmetry, and spatial orientation. A reticular table of representative An-MOFs is briefed (Table 14) but about half of the node-linker connectivities along with 6-c hexagon, 12-c icosahedron node, and 6-c hexagon linker have not been realized in An-MOFs.

Table 14 Topologies of representative An-MOFs built on polytopic linkers

Node \ Linker	(2-c) linear	(3-c) tri	(4-c) squ	(4-c) tet	(6-c) oct
(3-c) tri	**hcb** NU-1302, U-TDC-3	**nun** NU-1301	**tbo** NU-1300, TCPP-U2, U-IHEP, FJI-H-U **pto** TCPP-U1	**ctn** U-MTB-1 **bor** U-MTB-2, U-T3CPS	**cml-c3** NU-1351,1352
(4-c) squ	**sql** Th-SINAP-2	NA	NA	**pts** U-ABTC, U-T4CPS	NA
(6-c) oct	**pcu** U-1,2-BDC-2, Th-SINAP-4	NA	NA	NA	NA
(6-c) trp	NA	**spn** Th-MOF-808, Th-TTHA, Th-TATAB	NA	**tpt** Th-BCPBA	NA
(8-c) cub	**bcu** Th$_6$-Me$_2$BPDC-8, Np-BDC-2, TOF-16	**the** Th-NU-1200	**csq** Th-NU-1008, Th-NU-1011, Th-BDC-4 **scu** NU-905	**flu** SCU-11	NA
(12-c) cuo	**fcu** Th$_6$-BPDC-12, Th-UiO-66, Th-SINAP-(7,8), Azole-Th-1	NA	**ftw** ThNi-INA	NA	NA
(12-c) hpr	NA	NA	**shp** NNS-(1-3)	NA	NA

Abbreviations: **tri** = Triangle or trigonal pyramid; **squ** = Square (or rectangular); **tet** = Tetrahedron; **oct** = Octahedron; **trp** = Trigonal antiprism; **cub** = Cube; **cuo** = cuboctahedron; **hpr** = hexagonal prism.

The burgeoning topologies of Zr-MOFs built on Zr cluster with polytopic linkers offer a guide for the design of An(IV) cluster-based MOFs. Yet, less connected clusters, which are common in Zr-MOFs, are rarely observed in An(IV)-MOFs since An^{4+} allows for multiple directionality of coordinated ligands. By using 2-c linear ditopic linker, Th-MOFs are predicted to possess **fcu**, **bcu**, **sql** topology when Th$_6$ cluster is 12-, 8-, and 4-c, which are represented by Th-SINAP-(7,8)[92] (or Th-UiO-66[239]), TOF-16[79] and Th-SINAP-2[89], respectively. Np-BDC-2 has **bcu** topology as Np$_6$ cluster equals to 8-c cube[153]. The pending connectivities for unsaturated Th$_6$ comprise 11, 10, 6, which will lead to **ela**, **bct**, **llb** topology, respectively. As thorium PBU in Th-2,6-NDC[135], Th-SINAP-4[89] are simplified as 6-c octahedra, the **pcu** topology is embedded. For a 2-c angular ditopic linker, Th$_6$ cluster connectivity of 8,10 can produce **reo**, **bct** topology, however only (2,8)-c **srs-a** is observed in GWMOF-13[98]. Combing 3-c linkers of triangle geometry with Th$_6$ cluster connectivity of 8, 6, Th-NU-1200[249], Th-MOF-808[239] representative of **the**, **spn** topology is achieved while **tbo** (or **pto)**, **qnf** topology with cluster connectivity of 4, 10 are yet to be realized. As this geometry transforms to a trigonal pyramid, only (3,12)-c **llj** topology is doable. The planar square, rectangular and tetrahedral shapes contribute to the conformation complexity of 4-c tetratopic linkers. The square geometry with ideal D$_{4h}$ symmetry has been defined in porphyrin-based or certain in-

situ metalloligands. As Th$_6$ connectivity reaches 12, 8, and 6, **ftw** (or **shp**), **scu** (or **csq**, **sqc**), **she** (or **soc**, **stp**) topology can be produced and first two types are represented by ThNi-INA[213] and NU-905[121], respectively. When each Th$_6$ connects to four, eight, and twelve rectangular linkers (e.g. TCPB-Br$_2$), the framework topology corresponds to **lvt** (or **sql**, **nbo**, **cds**), **csq** (or **scu**, **sqc**), **shp** (or **ftw**), respectively. The **csq** topology is observed in Th-NU-1008, Th-NU-1011[58], and applies to Th-BDC-4[136] since its thorium PBU equals to 8-c Th$_6$ cube. As Np$_{18}$ SBU in NSS-(1-3) can be treated as a 12-c hexagonal prism, the **shp** topology fits[155]. By using tetratopic linkers with T$_d$ symmetry, Th$_6$ connectivity of 12, 8, 6, 4 forecasts **ith** (or **edc**, **cen**), **flu**, **ifl** (or **ibd**, **toc**, **tpt**, **gar**, **iac**), and **pts** (or **pth**) topology, respectively. When applies to the thorium PBUs, the **flu** and **tpt** topology can be found in SCU-11[144] and Th-BCPBA[136], respectively. These topologies database will apply to the design of An-MOFs made from hexanuclear SBU (or geometrically equivalent nodes) and polytopic linkers of different connectivities. Besides topological analysis on tetravalent An$_6$, the topologies of uranyl-organic frameworks are briefly presented. The (2,3)-c **hcb** is frequently encountered in U(VI)-MOFs bearing H-type PBUs and ditopic linkers, represented by NU-1302 series[240], U-IPBP-1[107], U-BTPCA-2[115], U-MSTB[188], U-1,2-PDA-6[181], and heterometallic UZn-1,3-PDA-1[206], UMn-TCI[194], UCo-TCA[200], UCs-KTA[271]. By combing 3-c H-type uranyl PBU with 3-c trigonal pyramid linker and 6-c octahedra-like linker, the **nun** and **clm-c3** topology can be witnessed in NU-1301[248] and NU-1351[266], respectively. The slight distortions of 6-c linkers when coordinated to uranyl nodes might contribute to the **nun** topology in NU-1350[266]. When it comes to a 4-c square linker, it is likely to generate **tbo** or **pto** topology. The difference between **pto** and **tbo** can be attributed to the distinct dihedral angles between the central planar ring of linker and the triangular nodal plane of PBU. In the case of a 4-c tetrahedral linker, the **ctn**, **bor**, **pts** topology is observed for U-MTB-1, U-MTB-2[260], U-ABTC[263] and U-T4CPS[110], respectively. In addition to common **hcb**, **cds**, **sql**, **pcu,** and **srs** topology, heterometallic U(VI)-MOFs have rare **geg1**, **hms**, **xww**, **mbc**, **fes**, **ths**, **umc**.

Generally, only a handful of topologies for An-MOFs has been accomplished due to the lack of delicate control of predefined building blocks. The combination of mixed-linker (e.g. trigonal with hexagonal) with mixed-cluster (e.g. 8-c cube with 12-c hexagonal prism) will further complicate the topology-guided design of An-MOFs. A growing practice of reticular chemistry[293,294] will transfer its applicability to turn unprecedented topologies of An-MOFs into facile reality.

3.3.3 Framework porosity

The key function of An-MOFs is to efficiently immobilize actinide-bearing species into the pores via size exclusion and/or selective binding besides the immanent incorporation of actinide as nodes. Owing to high surface area and low structural density, An-MOFs hold great promise in loading a high amount of actinide by utilization of framework porosity[26]. By fine-tuning of ultramicropore regime,

unsaturated states of actinide nodes, or framework electronegativity, flexible Th-, U-MOFs are likely to solve certain gas separation conundrums as shown U4-BDC-6[150]. Mesoporous Th-, U-MOFs can readily expose terminal hydroxyl groups (e.g. Th-NU-1200[249]), or actinide nodes (e.g. Th-NU-1008[58]), which potentially lead to the grafting of secondary active metal species or enhanced sorption or catalytic performance for target molecules. By incorporating functional guest species into An-MOFs porosity, this ship-in-bottle mode will offer tunable luminescent properties. This host-guest interaction will enable us to investigate the variation of the electronic structure of An-MOFs as a function of substrate dynamics. Another appealing yet challenging aspect is to build intricate actinide cages from simple building blocks as demonstrated in NU-1301[248]. Their great potential in adsorption-related applications remains unleashed. The pore engineering such as inserting hydrophobic group to metal nodes[295] is expected to be implemented on Th-, and U-MOFs in order to capture radionuclide ions of low hydration energy.

The activation of An-MOFs in organic solvents or elevated temperature may lead to distinct porosity[240] or structure transformation[65]. Admittedly, only a few An-MOFs has potentially accessible porosity (Table 15) and the pore size and free pore volume are mostly estimated by single-crystal structural analysis. Most An-MOFs lack experimental porosity probably due to the insufficient amount for characterizations, but it is highly recommended that such pore properties of Th and U-MOFs are provided for structural comparison. It is noted that the porosities of TOF-2[73] and U4-BTC-1[37] are inaccessible to N_2, which are ascribed to either considerable quadrupole interaction of N_2 with the electrostatic field gradients near the pore window or an incomplete removal of encapsulated solvent. A majority of An-MOFs based on aliphatic carboxylate linkers or certain simple linkers have dense framework packing (or no accessible porosity), but also find applications such as efficient X-ray sensing in SCU-9[246].

Table 15 The potentially accessible porosity of representative An-MOFs

An-MOFs	Pore size (Å)	Volume	S_{BET} (m²/g)	Ref
TOF-1	3.3 × 3.8 ellipsoidal	-	-	[72]
TOF-2	13.7 × 14.7 hexagonal	41%	293 (CO_2)	[73]
TOF-3	-	10%	-	[74]
TOF-16	10 × 10 square	51%	1220	[79]
GWMOF-13	7.2 × 10.8 ellipsoidal	17%	5.0	[98]
Th-BTB	15 ×15 hexagonal	2.4%	-	[116]
Th-NTB	12 × 12 hexagonal	56%	-	[116]
Th-BCPBA	10.7 × 2.9 rectangular	13%	-	[136]
ECUT-36	7.8 × 10.1 rhombic	23%	41	[140]
ThNi-INA	11 × 11 square	41%	-	[213]
Th-TATAB	17 × 17 square	42%	-	[145]
Th-TTHA	4.5 × 2.2 rectangular	18%	-	[146]
Azole-Th-1	9.2 × 9.2 square	50%	983	[78]
Th-BDC-3	6.9 × 6.9 equilateral triangle	0.27 cm³/g	730	[61]
Th-BDC-4	6.8 ×10.0 rhombic	21%	-	[136]

Th-TPO-1	6 × 9.7, 6.7 × 16 rhombic	55%	-	[132]
Th-TPO-2	17.5 × 8 hexagonal, 6 × 6 quadrilateral	66%	623	[132]
Th-IHEP-5	6 -18 (experimental)	48%	260	[122]
Th-PAT	10.8 × 5.3 rhombic	9.1%	-	[105]
Th-SINAP-2	8.5 × 5.8 ellipsoidal	22%	-	[89]
Th-SINAP-4	3.7 × 3.7 square	14 %	-	[89]
Th-SINAP-5	5.0 × 4.2 rhombic	22%	-	[89]
Th-SINAP-7	6.3 × 7.3 rhombic	35%	426.0	[92]
Th-SINAP-8	7.3 × 9.5 rhombic	57%	650.4	[92]
Th-SINAP-9	6.2 tetrahedral, 7.2 octahedral	45%	265.2	[77]
Th-SINAP-10	7.5 tetrahedral, 9.5 octahedral	55%	647.3	[77]
Th-SINAP-11	10 tetrahedral, 13 octahedral	58%	977.5	[77]
Th-SINAP-12	11 tetrahedral, 13.2 octahedral	67%	-	[77]
Th-SINAP-13	10.9 tetrahedral, 13.2 octahedral	71%	3396	[77]
Th-SINAP-14	12.2 tetrahedral, 16 octahedral	74%	1419	[77]
Th-SINAP-15	12.2 tetrahedral, 16 octahedral	73%	-	[77]
NU-905	14 × 25, 4× 25, 6 × 8 rhombic	60%	800 (Ar)	[121]
Th-NU-1008	15 × 15 triangular, 32 × 32 hexagonal; 11, 29 nm	73%	800 (Ar)	[58]
Th-NU-1011	3 × 3 triangular, 10 × 10 hexagonal	53%	700 (Ar)	[58]
Th-NU-1200	14 × 14, 22 × 22 quadrilateral	0.77 cm^3/g	1300	[249]
Th-UiO-66	6.9 × 6.9 equilateral triangle	54%	741	[148]
Th-UiO-66-(CF$_3$)$_2$	6.9 × 6.9 equilateral triangle	34%	212	[148]
Th-BPDC	11.2 × 11.2 equilateral triangle	64%	791	[153]
Th-BPDC-NH$_2$	11.2 × 11.2 equilateral triangle	63%	342	[153]
Th-2,6-PDC	-	-	2240	[67]
Th$_6$-TPDC-NH$_2$-12	19.4 × 7.1 triangular	-	880	[64]
NU-1300	27 × 27, 39 × 39 quadrilateral	91%	2100	[258]
NU-1301	50 × 50 icosidodecahedra, 62 × 62 hexakaidecahedra	3.9 cm^3/g	4750	[248]
NU-1302-DMF	12 × 12 hexagonal	63%	-	[240]
NU-1302-EtOH	2.5 × 2.5 hexagonal	53%	-	[240]
NU-1302-SA	3.5 × 3.5 hexagonal	32%	-	[240]
U-1,2,4-BTC-1	10 × 3 rhombic	11%	-	[190]
U-1,2,4-BTC-2	4 × 6 rhombic	10%	-	[190]
U4-BDC-6	5 × 5 rhombic	26%	497.6	[150]
U4-BPDC	11.2 × 11.2 equilateral triangle	64%	254	[152]
U-BDC-6	8.6 × 8.6 rhombic	28%	-	[184]
U-BDC-8	7.9 × 7.9 , 7.9 × 9.1 , 9.1 × 9.1 rhombic	62%	-	[184]
SCU-3	8 × 8, 20 × 20 rhombic	68%	-	[278]
SCU-6	5.6 × 7.0 rhombic	7.7%	18.5	[182]
SCU-7	4.9 × 7.2 rhombic	6.8%	34.5	[182]
SCU-8	22 × 22 hexagonal	63%	1360	[117]
SCU-11	8.3 × 8.3 rhombic	60%	1272	[144]
SCU-14	15.5 × 15.5 adamantane-shaped octahedron	38%	-	[253]
U-BTB	15 × 15 triangular	44%	-	[247]

U-BDB	10 × 10 triangular	48%	924	[247]
UNaNi-BPYDC	5.6 × 5.6, 19.6 × 19.6 cylindrical	37%	-	[104]
UNa-BQDC	10.07 ×13.86 ellipsoidal	34%	-	[171]
U-TATAB	18.54 × 21.37 ellipsoidal	45%	-	[252]
U-TCI-1	12.9 × 7.3 rhombic	35%	-	[194]
U-PSTB-1	9 × 9 quadrilateral	21%	-	[254]
RPL-1	22.8 (experimental)	76%	9.6	[80]
U-IHEP-4	16 × 16, 27 × 27, 37 × 37 quadrilateral	90%	-	[91]
TCPP-U1	11 × 11 square, 10 × 20 quadrilateral	74%	-	[256]
TCPP-U2	19.8 octahedron, cuboctahedron 41.4	90%	-	[256]
IHEP-9	15 × 15, 7 × 15 quadrilateral	71%	121	[207]
FJI-H-U1	14.89 octahedron, 15.55 cuboctahedron	85%	-	[257]
U-TBAPy-1	17 × 19, 23 × 19 rhombic	62%	-	[259]
U-TBAPy-2	17 × 12, quadrilateral	56%	-	[259]
U-MTB-1	9.8 × 16 ellipsoidal	82%	-	[260]
U-MTB-2	5.61 octahedral	65%	-	[260]
U-T3CPS	11.3 × 11.3 hexagonal	46%	198.83	[110]
U-T4CPS	8.8 × 8.8 quadrilateral	3.8%	-	[110]
U4-6	9.8 × 10.3 quadrilateral	26%	-	[111]
U-MPDP-2	6.7 × 13.2 rhombic	20%	-	[34]
U-BTTP-3	8.6 × 8.7, 6.3 × 12 ellipsoidal	39%	-	[75]
U-BTTP-5	4.68 × 7.43, 5.52 × 6.52 ellipsoidal	19%	-	[75]
U-BPDA-2	12.4 × 4.4 rectangular	1.5		[193]
SCU-UEu-1	10 × 7 quadrilateral	0.5%	-	[204]
UMOFUA	6.7 × 6.7 square	40%	-	[36]
U-TMTDC	17.8 × 6.9, 12.2 × 7.4 rhombic	29%		[242]
U-POM-BPDO	13 × 13 square	24%	-	[222]
Cage-U-Co-MOF	4×7.2 ellipsoidal	45%	208	[212]
Pu-UiO-66	-	0.3 cm^3/g	709	[50]

4. Properties and applications

Previous research emphasizes the structural aspects of An-MOFs, while their ion exchange, Lewis acidity, photoluminescence, conducting, or semiconducting properties hold potential for various applications. To put promising An-MOFs into practical applications, their mechanical, thermal, radiolytic and chemical stability under real conditions need to be systematically investigated. Take An-MOFs as hierarchical wasteform for example, the effect of autogenous pressure, decay heat, alpha self-irradiation, groundwater environment on the structural integrity should be evaluated in the scenario of nuclear waste management. It is worth to note that some seemingly stable An-MOFs become amorphous in water due to the atypical, anisotropic nature of the actinide PBU[116] or SBU[58], while the superior stability of certain An-MOFs is attributed to both electrostatic and covalent interactions

between metal cation and ligand anion[213]. This accentuates an overall assessment of stability of An-MOFs that is directly relevant to their coordination modes. The opposite of stabilities is the labilities of An-MOFs, which remain barely explored but enable their transformation into varying actinide-containing materials similar to the utilization of MOF destruction[296].The reactivity of An-MOFs and their derivatives, particularly with guest-responsive properties should be of application-related concern. Recent uranyl-organic materials displayed spring-like stress-induced elastic flexure and a thermosalient effect, setting up an example of multi-responsive U-MOFs as a result of mechanical lability[175]. Since TRU-MOFs accumulate an insufficient amount for any target application, only Th- and U-MOFs have been utilized as an exceptional family of functional materials. In this section, the conventional applications of Th- and U-MOFs including adsorption, catalysis, and luminescence will be discussed to illustrate their practical utility besides the emerging applications such as conducting and semiconducting properties, and fabrication of nuclear target.

4.1 Selective adsorbents

It is of fundamental significance to exploit An-MOFs as adsorbents for water vapor, organic pollutants, biomolecules, gas separation besides radioactive metal ions, iodine, or gas. Herein, we summarize the uptake of iodine, metal ions and organic pollutants on Th(IV)- and U(VI)-MOFs for environmental remediation (Table 16). For any real-world applications, secondary radioactive contamination by thorium or uranium leaching in aqueous solution must be avoided. Thus, it is recommended that practices for evaluating the hydrolytic stability of An-MOFs be implemented.

Table 16 Summary of adsorption performance of Th(IV)-, U(VI)-MOFs

Target	An-MOFs	C_0 (mg/L)[a]	S/L (g/L)[b]	T_{equ} (hrs)[c]	Q_{ads} (mg/g)[d]	Ref.
	UNi-CPTPY-1	2530	4	48	240	[209]
	Th-TATAB	2530	20	24	126	[145]
	U-TATAB	200	8	24	31.3	[252]
	Th-TTHA	800	10	24	562	[146]
	Th-SINAP-7				69.4	[92]
	Th-SINAP-8				79.2	[92]
	Th-SINAP-9				62.7	[77]
I_2 solution	Th-SINAP-10				79.8	[77]
	Th-SINAP-11	200	2.5	24	72.2	[77]
	Th-SINAP-12				77.8	[77]
	Th-SINAP-13				72.0	[77]
	Th-SINAP-14				44.9	[77]
	Th-SINAP-15				69.5	[77]
	ThNi-INA	25300	20	3	181	[213]
	Th-UiO-66-NH₂	300	2.5	24	101	[148]
	Th-UiO-66-(NH₂)₂			24	110	[148]
	Th-SINAP-7			2	352	[92]

I$_2$ vapor [e]	Th-SINAP-8			3	473	[92]
	Th-SINAP-9			4.5	810	[77]
	Th-SINAP-10			4.5	334	[77]
	Th-SINAP-11			4.5	430	[77]
	Th-SINAP-12			4.5	592	[77]
	Th-SINAP-13	50 [f]	1 [g]	4.5	596	[77]
	Th-SINAP-14			4.5	358	[77]
	Th-SINAP-15			4.5	700	[77]
	Th-SINAP-1			3	1240	[89]
	Th-SINAP-4			3	340	[89]
	Th-UiO-66-NH$_2$			4.5	846	[148]
	Th-UiO-66-(NH$_2$)$_2$			4.5	969	[148]
ReO$_4^-$ [h]	U-BCBP-4	40	0.5	3.3	63.2 (pH = 4)	[83]
	SCU-6	1	3	2.5	0.3	[182]
	SCU-7	1	3	2.5	0.046	[182]
	ThNi-INA	12.5	NA	10	807 [i]	[213]
	SCU-8	12	4	0.16	2.46 (pH = 6.15)	[117]
Cr$_2$O$_7^{2-}$	SCU-8	64.8	4	0.5	14.9 (pH = 5.11)	[117]
Cs$^+$	U-BDB	0.98	5	0.33	0.18	[247]
	U-BDC-CB[6]	136	0.2	48	45.7	[120]
	U-TBAPy-1	1	1	0.5	0.86	[259]
	U-TBAPy-2	1	1	0.33	0.89	[259]
Eu^{3+} [j]	U-ABTC	1	0.4	12	2.47 (pH= 5.97)	[263]
UO$_2^{2+}$	U-TDPAT	100	1	24	18.9 (pH = 2)	[265]
Th^{4+}	SCU-3	2000	1	24	209 (pH = 2.87)	[278]
PFOS	SCU-8	1	5	0.033	0.192	[117]
MB	SCU-8	6.4	4	1.5	1.56 (pH = 6.77)	[117]
	ThNi-INA	31.9	NA	NA	266	[213]
	U-TTHA-5	5	0.2	12	41.1	[236]
	U-CMTC	5	0.2	12	7.05	[236]
	U-POM-BPDO	10	0.2	0.083	~ 50	[222]
	U-TDPAT	10	1	48	8.19	[265]
	U-BDC-4	5	0.2	12	21.3	[243]
	U-BTC-3	10	0.2	1.67	50	[102]
MO	Th-TATAB	10	1	23	9.79	[145]
RhB	U-TTHA-5			12	5.25	[236]
	U-CMTC			12	6.53	[236]
	U-1,2-BDC-4			24	2.61	[187]
	U-NIC	50	0.2	24	2.86	[187]
	U-CA			24	4.22	[187]
	U-OA-1			24	0.05	[187]
ST	U-TDPAT	10	1	48	5.92	[265]

(a) initial concentration; (b) the ratio of solid to liquid; (c) equilibrium time; (d) adsorption capacity; (e)

heating temperature is 353K; (f) adsorbent weight is fixed at 50 mg; (g) solid I_2 weight for vapor adsorption is fixed at 1g; (h) surrogate for TcO_4^-; (i) this value was calculated by in relative to the content of Ni^{2+}; (j) surrogate for Am^{3+}.

4.1.1 Water vapor adsorbent

The uptake of water vapor and controlled release at operation pressure and temperature together with high working capacity make cost-effective MOFs as promising adsorbents for humidity control and heat reallocation[297]. The corrugated nanotubular arrays in uranyl metal-organic nanotube (UMON) have an internal diameter of 1.2 nm and water molecules are confined within the nanotubes at two crystallographically unique positions, forming a hydrogen-bonding hexagonal ring in chair configuration that partially identical to a hexagonal polymorph of ice, thus show selectivity to water in the presence of other polar and nonpolar solvents. The water adsorption-desorption cycle could be repeated multiple times with no apparent loss of crystallinity or overall stability[94](Fig.15). Hydrogen bonding of macrocyclic arrays in UMON leads to a robust material that is comparable to other MOFs. Due to their tunable components, actinide metal-organic nanotube-like materials hold great promise in solvent storage and exchange properties for advanced separation applications[94]. SCU-11 has a water vapor sorption capacity of 34 cm^3/g, wherein predominant sorption occurred at rhombic dodecahedral cages while minor contributions came from thorium open metal sites[144].
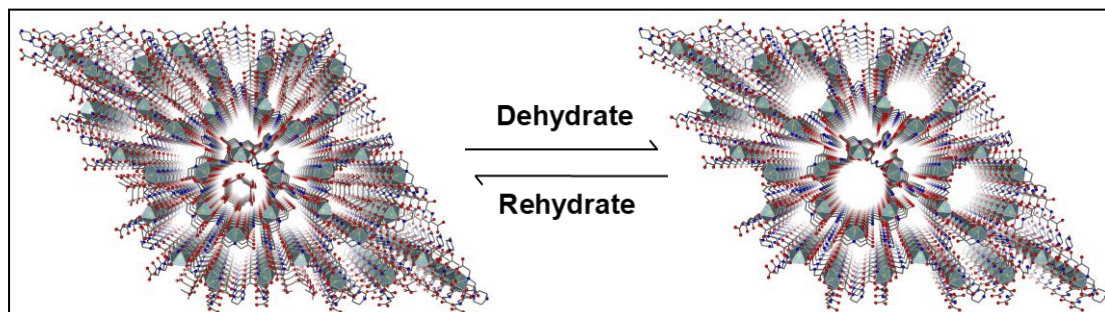
Figure 15. Structural showing of dehydration-rehydration cycles in UMON. It can be rehydrated multiple times by equilibrating the sample on the benchtop for 30 minutes[94].

4.1.2 Iodine adsorbent

Radioactive iodine isotopes such as ^{129}I, ^{131}I in the form of molecular I_2, organic iodides, HI, or HOI generated from spent fuel processing need to be safely disposed of due to their high radioactivity, volatility, and reactivity in the metabolic process. The sorbent-loaded fixed-bed technique becomes advantageous by its simplicity and cost-effectiveness when compared with wet-scrubbing using caustic or acidic scrubbing solution[298]. The conventional microporous silver-loaded zeolites suffer from a lack of active adsorption sites within limited porosity besides the usage of a noble metal. MOFs found their application as an alternative sorbent for iodine in

recent decades. Stable, low-cost MOFs such as MIL-51(Al)[299], MIL-101(Cr)[300], SBMOF[301], MFM-300[302], UiO-66-PYDC[303] or functionalized MOFs such as amine-modified MIL-101[298], imidazolium-incorporated PCN-333(Al)[304], AgNPs@UiO-66[305] represent state-of-the-art sorbents or sensors for iodine. With the emergence of stable An-MOFs in recent years, it is of research rather than industrial interest to verify their feasibility as scavengers for I_2. Due to the presence of a double-walled truncated tetrahedral cage with a size of 1.7nm, Th-TATAB was exploited to remove 90% I_2 in cyclohexane in 3 hours, far exceeding the performance of MIL-101-NH$_2$ (90% in 30 h)[145]. The affinity of Th-TATAB (or U-TATAB) for I_2 can be expectedly attributed to strong charge-transfer interactions between I_2 and π-electron moieties including triazine ring, aromatic rings, and accessible secondary-amine groups. The mechanism can be depicted as: first, iodine is adsorbed inside pores of An-MOFs through I_2-N bonds and I_2-π halogen bonds. Second, these intermolecular interactions between I_2 and π-electron double walls restrict I_2 in the nanochannels, resulting in n-σ charge transfer. Likewise, the triazine ring, uncoordinated carboxyl oxygen atoms, and tertiary amine in Th-TTHA offer effective sorption sites for polyiodide anions[252].
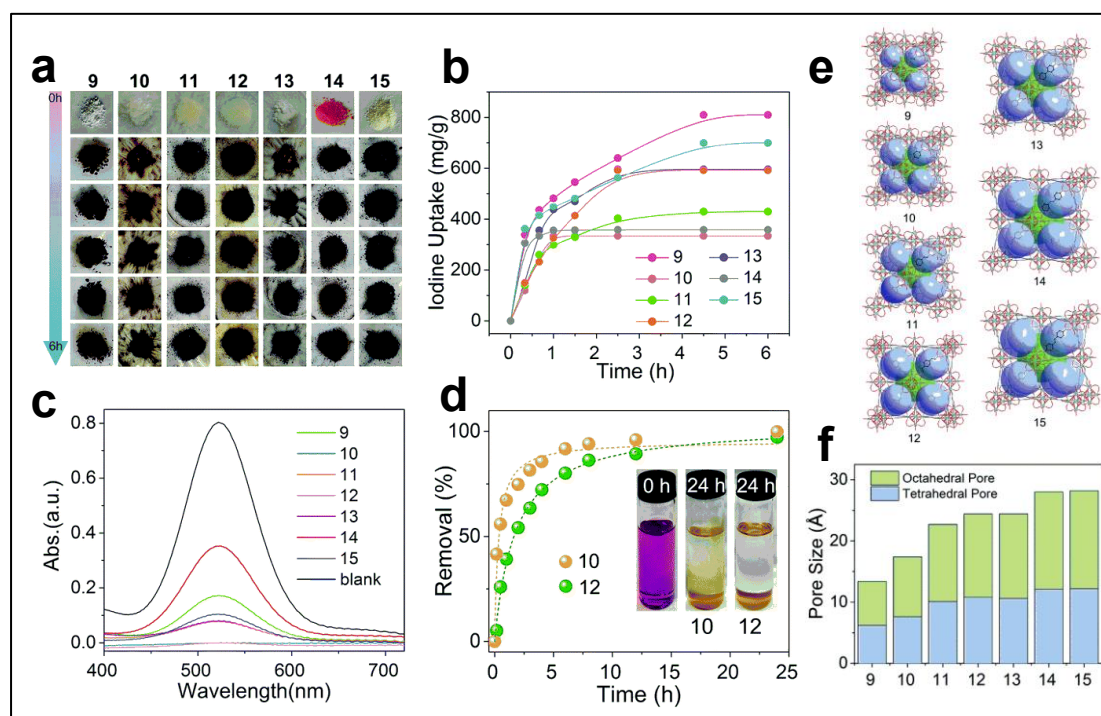
Figure 16. (a) Color changes of Th-SINAP-(9-15) upon iodine vapor uptake; (b) Gravimetric iodine vapor uptake of Th-SINAP-(9-15) as a function of time; (c) UV-vis absorption spectra of iodine/cyclohexane solutions in the presence of Th-SINAP-(9-15) after 24 hours; (d) Iodine adsorption kinetics of Th-SINAP-10 and Th-SINAP-12 with pseudo-second-order kinetics fittings; (e) Single-crystal structures of Th-SINAP-(9-15) showing the pore sizes; (f) Two types of estimated pore sizes of Th-SINAP-(9-15) (Reproduced from ref. [77] with permission from The Royal Society of Chemistry, Copyright 2020).

Following this I_2 capture mechanism involving conjugated π-electrons, Th-SINAP-7,

and Th-SINAP-8 were used to capture I_2 from solution and gas phase. Both have thermal stabilities up to ~500 °C and stabilities from pH 1 to 12. The frameworks remained intact after a total of 2×10^5 Gy β or 2×10^5 Gy γ irradiation with a dose rate of 2×10^4 or 1.2×10^3 Gy/hour, respectively, which corroborated their practical utilities in the capture of β-emitting iodine isotopes[92]. Due to their stability in water as well as in diverse polar organic solvents, the variable pore size, void volume, and rich π-conjugated skeletons of the reticular MOFs Th-SINAP-(9-15) hold potential in capturing iodine species. Th-SINAP-9 features the highest adsorption capacity even though it has the smallest pore size and BET surface area, which could be ascribed to its pore matching the kinetic diameter of iodine, confining iodine vapor in small voids. It appears that a large pore diameter and surface area of materials will promote the diffusion of iodine from the solvent media to the voids of Th-MOFs. However, smaller voids that are comparable in size to I_2 will enable the thermodynamic-driven confinement effect that favors I_2 adsorption in Th-SINAP-10, and Th-SINAP-12 compared to Th-MOFs with larger voids. The mass uptake of iodine was converted to 1.5 I_2 molecules per Th atom for Th-SINAP-15, which is comparable to the value of ZIF-8. It can be inferred that charge transfer occurred between aromatic π-electrons of Th-MOFs and guest iodine to form adsorbed I_2 and a dominant I_3^- species[77] (Fig.16). The anionic MOF Th-SINAP-1, Th-SINAP-4 and cationic ThNi-INA can also remove I_2. The latter remains intact up to a total dose of 4×10^5 Gy β irradiation and 1×10^5 Gy γ irradiation with a dose rate of 2×10^4 Gy/h, as well as at pH 1-13, and in various solvents[213]. To explore the role of substituents of Th-UiO-66 on iodine adsorption, the Lin group investigated the uptake of iodine on Th-UiO-66-R. Functional groups R including $-NH_2$, -Cl, -OH, and -Br boost the iodine adsorption kinetics compared to Th-UiO-66. An extra amino substituent further promotes the iodine removal rate, while disubstituted MOFs Th-UiO-66-R (R = Cl, Br, CH_3) inhibited on the iodine adsorption. Both amine-functionalized Th-MOFs show decline in iodine removal and surface area upon exposure to 5.1×10^5 Gy γ-ray radiation. The synergistic effects of the variations of conjugated π-electron density and pore sizes/environments upon substitution determine the uptake performance among these isoreticular MOFs implies the conjugation of electron-donating groups plays a key role in improving vapor iodine uptake via enhanced charge transfer interactions. The high radiation resistance of Th-UiO-66-NH_2 and Th-UiO-66-$(NH_2)_2$ is attributed to the rich electron density of the conjugated π-electrons system that stabilizes the frameworks, which makes them promising candidate adsorbents for gaseous iodine relevant to fuel reprocessing[148].

In general, the large-void Th- and U-MOF with relatively small pore opening will be preferable for the imprisonment of radioactive iodine while both actinide nodes engineering and incorporation of auxiliary ligands that contribute to a tunable charge-transfer process will maximize the reversibility of the capture of iodine.

4.1.3 Metal ion adsorbent

Radioactive $^{99}TcO_4^-$, $^{137}Cs^+$, $^{232}Th^{4+}$, $^{235}UO_2^{2+}$, $^{241}Am^{3+}$ and other nuclear waste-related metal ions pose a great radiological or toxicological threat to the biosphere. Cationic, neutral, or anionic MOFs have been exploited as efficient adsorbents to decontaminate these environmentally concerned radionuclide ions from aquatic media or simulated legacy liquid waste. Stable MOFs for the aqueous removal of radionuclide have been comprehensively reviewed[306–310]. However, An-MOFs for the capture of liquid-borne radionuclides were scarcely included in these reviews. Cationic An-MOFs can combine accessible channels, and varied counteranions with uncoordinated functional groups, and represent promising scavengers for radionuclide oxoanions such as $^{99}TcO_4^-$. The relatively high uptake of perrhenate at pH 2.0 suggests that U-BCBP-4 has the potential to remove ReO_4^- under harsh conditions such as a high acidity for the reprocessing of spent nuclear fuel[83]. ThNi-INA displays good selectivity towards ReO_4^- in the presence of an excess of Cl^-, SO_4^{2-}, and OAc^-. ReO_4^- is captured within the nanocages cavities by anion exchange and adsorption as precipitation outside the MOF was excluded upon repeated washing. Each $[Th_{48}Ni_6]$ cage in ThNi-INA contains 5.01 residual K^+ and captures 10.91 ReO_4^-, which is potentially stabilized in the cage by both OH^- anion and a hydrogen-bonding network induced by Ni-coordinated H_2O. The uptake of Re exhibits only a negligible influence by the aforemtioned dose[213]. Due to exchangeable Cl^- in the 1D hexagonal tubular channel in cationic SCU-8, it can be used to remove $Cr_2O_7^{2-}$ and ReO_4^-[117].

Anionic frameworks enable the removal of cationic radionuclides from aqueous solution. U-BDB has a pH stability range from 3 to 12 and withstands 200 kGy ^{60}Co γ irradiation with a dose rate of 1.2 kGy/hour and 200 kGy β irradiation with the dose rate of 20 kGy/hour. U-BDB shows appreciable selectivity towards Cs^+ even in the presence of 5 or 20 mass equivalences of competing Li^+, Na^+, K^+, Rb^+, Mg^{2+}, or Ca^{2+}, removal rates from 71.8% to 93.5% can still be achieved[247]. By immersing U-PSTB-8 in a solution containing 100 mg/L Li^+, Na^+, K^+, and Cs^+, nearly 100% of NH_4^+ in the pseudo channel can be quickly replaced with K^+ and Cs^+, whereas only 50% of NH_4^+ is substituted by Na^+, and Li^+ was not substituted into the framework sites at all. This selective ion-exchange may be attributed to the delicate match between guest ionic radius and the aperture of interpenetrated layers[255]. Two sets of competitive ion exchange reactions with an excess of Rb^+, K^+, Na^+ Mg^{2+}, Sr^{2+}, and La^{3+} were carried out for U-TBAPy-1 and U-TBAPy-2. As the ion radius increases, a competitive trend with Na^+, K^+, Rb^+ is observed. When divalent and trivalent ions are used, the selectivity for Cs^+ decrease, indicating that this selectivity is subjective to effective charge density. The selectivity for Cs^+ for U-TBAPy-1 was weaker than that for U-TBAPy-2, which is attributed to steric hindrance around the adsorption sites, where the adsorbed Cs^+ bridged two neighboring uranyl PBUs, defining an enthalpy-driven adsorption process[259](Fig.17b).

Anionic U-ABTC can eliminate over 95% Eu^{3+} via cation exchange in the presence of

equal equivalents of competing Ni^{2+}, Mn^{2+}, Zn^{2+}[263] (Fig.17a). U-TDPAT shows selectivity for UO_2^{2+} in the presence of Zn^{2+}, Ni^{2+}, Pb^{2+}, Sr^{2+}, Co^{2+}, Al^{3+} and Cr^{3+}. The adsorbed U(VI) can be effectively eluted by 0.1 mol/L HCl or 0.1 mol/L HNO_3 while deionized water shows no elution effect, suggesting a pH dependent mechanism[265]. About 72% of the P=O groups in SCU-3 are coordinated to Th^{4+} in aqueous solution, assuming 0.25 equivalence of Th^{4+} is adsorbed through an ion-exchange process with $[(CH_3)_2NH_2]^+$ counterion. Th^{4+} was incorporated into the crystal of SCU-3 instead of being absorbed on the surface via a combined coordination and ion exchange process. It gives rise to an example of 5f/5f heterobimetallic An-MOFs through adsorptive post-metalation[278]. Besides the aforementioned few cases of Th- and U-MOFs as radionuclide sorbent, cationic U-CB[6]-2 has potential anion exchange capacity[311] while due to the presence of phosphonate groups, stable UPF-(101-104) are potential adsorbents for cationic species in relatively strong acidic solution [76].
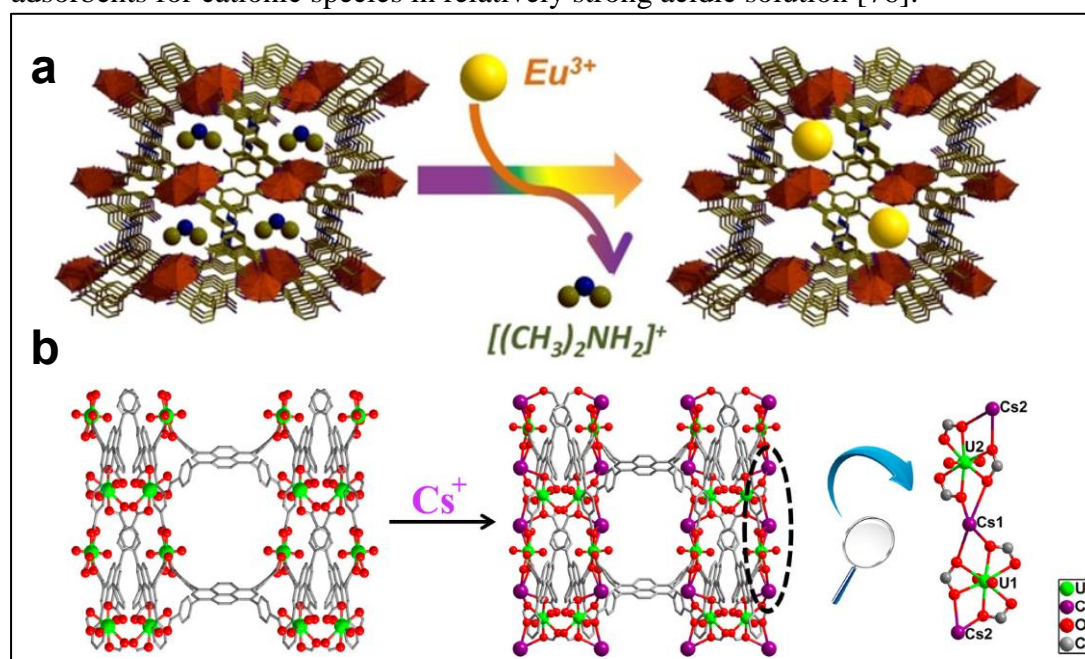
Figure 17. (a) Cation exchange between guest Eu^{3+} and host counter ion in U-ABTC (Reproduced from ref. [263] with permission from Wiley Online Library, Copyright 2019); (b) Ball and stick representation of pristine U-TBAPy-2, Cs^+-exchanged one and 1D chain of exchanged U-TBAPy-2 (Reproduced from ref. [259] with permission from American Chemical Society, Copyright 2018).

Actinide-ligand coordination assemblies are likely to selectively form well-defined nanoclusters[312] or An-MOFs in multicomponent solution, which leads to a paradigm for actinide species sequestration during synthesis or post-modification in contrast to the conventional MOFs for actinide sorption. By direct synthesis, up to 40-50 wt% of actinide can be achieved inside porous Th- and U-MOFs. Heating of unsaturated Th_6-Me_2BPDC-10 in the presence of $ThCl_4$ precursor and TPDC-NH_2 ligand led to simultaneous capping linker installation and thorium species incorporation inside the framework, resulting in the formation of a material with 52 wt% of Th. This linker-capped Th-MOF increased the Th content by 62 μg/g of material compared with the pristine scaffold. Besides, heating of transmetallated

Th$_{5.65}$U$_{0.35}$-Me$_2$BPDC in the presence of ThCl$_4$ and SDC ligand resulted in a material with an overall actinide content of 67 wt%, which is the highest actinide content among all Th-based frameworks known to date. Overall, further loading of actinide could be achieved through transmetallation, or metal node extension combined with linker installation, enabling capped heterometallic An-MOFs to resist radiation damage and leaching[64]. However, the actinide node and incorporated radionuclide will cause radiation damage to framework porosity. Therefore, the microscopic structural damage and macroscopic leaching behavior should be of concern for this promising waste form in nuclear waste management [313].

4.1.4 Organic pollutants adsorbent

The ever-increasing amount of organic pollutants in ecosystems needs to be reduced by remediation technologies. In this area, porous stable MOFs are a versatile platform for the decontamination of organic emerging contaminants, which had been recently reviewed[314,315]. However, the ability of An-MOFs to remove common organic contaminants such as dyes, or polyaromatic hydrocarbons (abbreviations in supplementary materials) were often neglected.

Anionic PFOS species are one example of highly chemically stable species, which are mobile in the aqueous environment. Hence, it becomes pressing to develop means to eliminate PFOS via adsorption, and cationic SCU-8 was tested as a candidate scavenger. The ultrafast adsorption kinetic of SCU-8 is better than the state-of-the-art anion sorbents such as Mg-Al-LDH, IRA-67 resin, powdered activated carbon, and Na-Y zeolite under identical experimental condition. In the presence of 50 mg/L inorganic anion, it can reduce the initial concentration of 1 µg /L to 0.021µg /L. The sorption rate remains 44% after four sorption-desorption cycles using salt solution meanwhile the leaching percentage of thorium is as low as 0.01% after 30 minutes of contact with PFOS solution, lower than average thorium concentration in soil or the maximum alpha activity contamination level. The binding mechanism of PFOS into SCU-8 was revealed by molecular dynamic simulations. The strong hydrophobic interaction between the fluorinated alkyl chain of PFOS and SCU-8 first drives the anion-exchange adsorption of PFOS towards the channel of SCU-8 whilst a hydrogen bond forms between a RSO$_3^-$ group and a channel water molecule. The hydrophobic interaction between the tail of PFOS and benzene rings of the framework ligand breaks the initial hydrogen bond and the nanoscale dewetting along with van-der-Waals interactions pushes the tail of PFOS fully into the cavity. Finally, a new hydrogen bond between RSO$_3^-$ group and another coordinating water formed and anchored the PFOS anion into the final binding site in SCU-8. Both electrostatic and non-covalent interactions were involved in this three-stage adsorption[117].

Porous An-MOFs with intrinsic framework charge can remove carcinogenic organic dyes with varied charges. Among the adsorption of MO, EY, alizarin, RhB, and MB on Th-TATAB, its efficiency for anionic MO ranks highest while linear dyes are captured more efficiently than triangular dyes[145]. Anionic U-MTB-1 and U-MTB-2 have been evaluated for the adsorption of four dye molecules, cationic MB and RhB,

neutral TB, anionic MO. Positively charged dyes can be efficiently adsorbed over 24 hours as the yellow crystals gradually became mazarine and pink for MB and RhB, respectively while no obvious adsorption was observed for MO and TB[260]. About 78%, 87%, and 63% of EV, JB, and RhB, respectively are captured by FJI-H-U1 after 20 hours[257]. U-IHEP-4 adsorb positively charged MG and RhB over 12 hours while it shows virtually no adsorption of neutral TB and negatively charged CR[91]. U-TATAB can eliminate MB from aqueous solution in the presence of two anionic dyes and no desorption behavior is observed probably due to the presence of uncoordinated, exchangeable cations between graphene-like layers and voids and the secondary amine groups of TATAB on the pore surfaces. However, its framework partly collapses after adsorbing the dye[252]. TCPP-U1, TCPP-U2 can selectively absorb positively charged CV from the methanol solution while negatively charged MR cannot be exchanged[256]. The coordinating DMF played the most important role in the removal of MB by U-BDC-4 since the lone pair of nitrogen has strong interactions with MB. Although -COOH groups in U-1,3-BDC-1 could have interactions with MB, the hydrogen bonds formed between building blocks hindered interactions with MB[243]. U-1,2-BDC-4, U-NIC, U-CA, and U-OA-1 exhibit selective adsorption towards cationic RhB in wastewater, but show no adsorption of MB or MO. This selectivity is probably due to hydrogen bond interactions with the carboxylate groups of RhB, which is not possible for MO and MB. In case of U-CA, its CA ligand forms a large conjugated system with UO_2^{2+}, which may contribute to the resulting uptake capacity[187]. Anionic U-BTC-3 just barely adsorbs AO, while U-PM and U-BDC-9 do not adsorb MB or AO at all, which implies the hydrogen bonding and covalent bonds in these U-MOFs induce stronger interlayer interactions that remarkably hinder cation exchange[102]. Neutral RPL-1 can remove 30, 60, and 80% MO after intervals of 1, 24, and 72 hours and pale yellow-green crystal changed to magenta, brightened over a 72-hour period, and remained deep magenta for six weeks thereafter. No selectivity for MO or MB over the other was observed and ethanol-activated RPL-1 demonstrated a strong colorimetric response upon their uptake of RhB, EB, GV, TA, MO, MB, and a mixture of RhB and MB, with no obvious signs of selectivity[80] (Fig.18).

The host-guest interaction between dye molecules and porous framework results in the selective or concurrent surface adsorption of dyes on An-MOFs, which not only rely on the size, shape, charge of guest dye, but also depend on porosity exclusion, framework charge, and π-π interactions between ligand aromatic rings and dyes. Unraveling the molecular mechanism will contribute to unleash the potential of An-MOFs for the treatment of troublesome organic pollutants including organic radwaste.
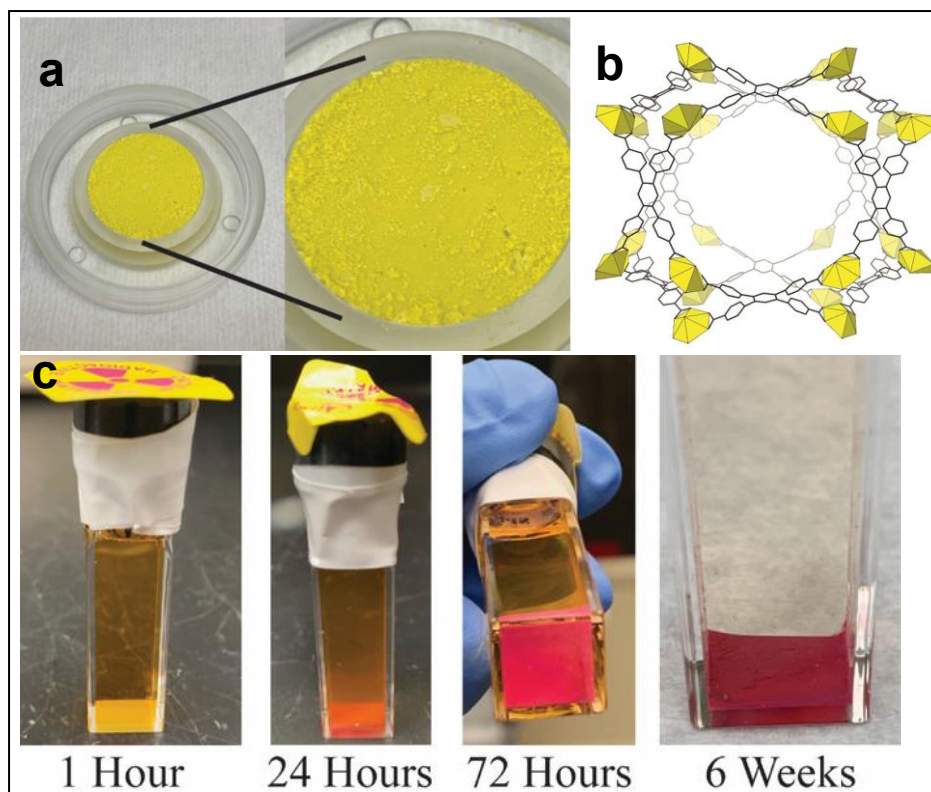
Figure 18. (a) RPL-1 in yellow powder form. (b) Single-channel along a-axis for adsorption. (c) The color of the RPL-1 changed from pale yellow-green to magenta upon adsorption of MO dye (Reproduced from ref. [80] with permission from Wiley Online Library, Copyright 2020).

4.1.5 Macromolecule adsorbent

Hierarchically porous An-MOFs, particularly with micro-mesoporosity are able to incorporate large biomolecules. NU-1300 is stable from acidic (pH down to 1) to weakly basic conditions (pH up to 8). As NU-1300 is negatively charged above pH 2.7, it can adsorb proteins with overall positive surface charges via electrostatic interactions. Consequently, it can separate positively charged Cytochrome c (Cyt-c) and Alpha-lactalbumin (α-La), as a representative pair of biological macromolecules. The isolated solid can be recycled and reused for protein separation at least three times[258] (Fig.19). NU-1301 is also equipped with giant porosity and can adsorb cationic dyes as well as Cyt-c. Besides, the hydrophilicity or lipophilicity of NU-1301 can be tuned through cation exchange with a suitably charged surfactant-containing ethylene glycol or aliphatic groups[248]. Beyond the application of An-MOFs as macromolecules adsorbents, An-MOFs can be considered a suitable platform for investigating the intricate interactions between biomolecules and actinide PBUs, SBUs of An-MOFs, which might be considered analogues for metalloenzyme active sites.
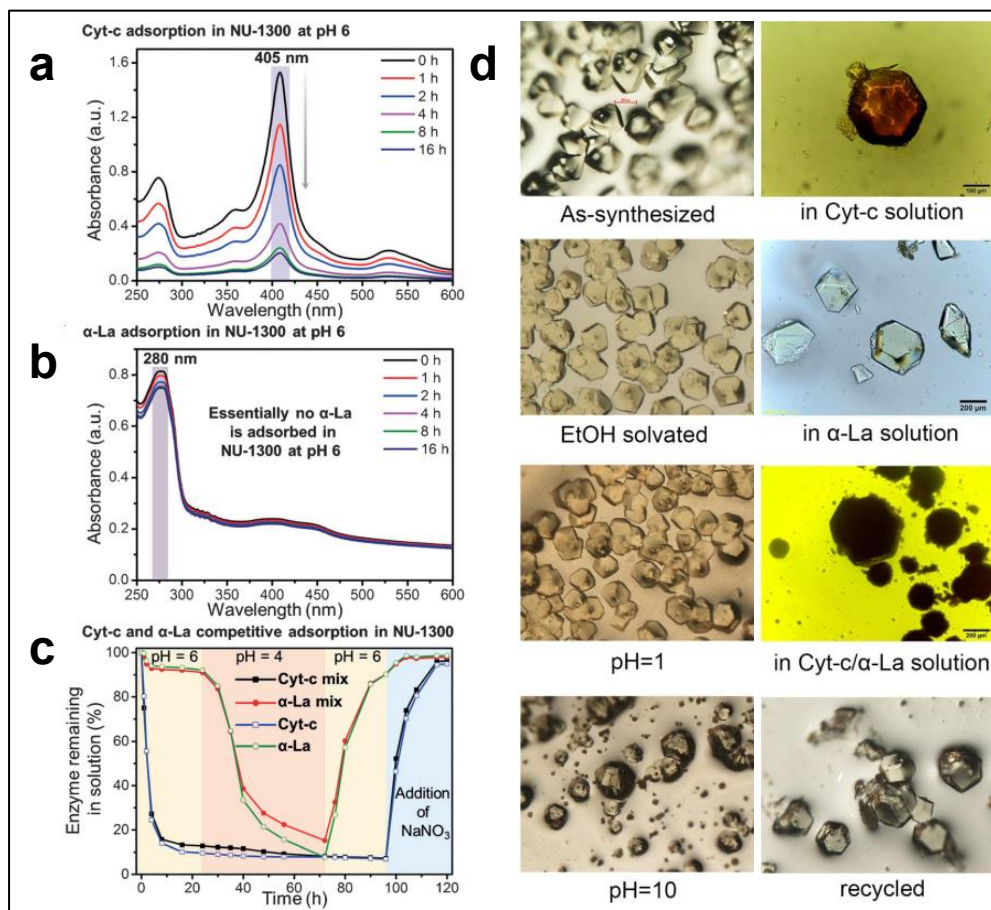
Figure 19. UV/Vis spectra of single biomolecule (a) Cyt-c and (b) α-La in the presence of NU-1300 monitored with time; (c) Percentage of Cyt-c and a-La in both single-component and equimolar Cyt-c/α-La mixture monitored with time; (d) Optical images of NU-1300 after different treatment (Reproduced from ref. [258] with permission from Wiley Online Library, Copyright 2016).

4.1.6 Gas adsorbent

MOFs have long been used for gas storage and separation due to their tunable pore environment while it was only recently that challenging gas separations (e.g. Xe/Kr), storage (e.g. H_2), and elimination (e.g. SO_2) were made possible using Th- and U-MOFs. The Xe/Kr separation, in particular, has been useful in the nuclear industry and nuclear forensics. SCU-11 transforms to SCU-11-A as two coordinated water molecules are removed by vacuum heating. It not only kept the original molecular cage of ca. 0.9×0.9 nm but also exposed 8-coordinate unsaturated thorium nodes. The Kr, and Xe uptakes amount to 0.77, and 3.17 mmol/g, respectively, with Xe/Kr selectivity calculated to be 5.7, which is ascribed to a size-matching effect as well as polarized pores due to open metal sites leading to a preference for more polarized Xe over Kr[144].

The removal of ethane and acetylene byproducts that inevitably arise during thermal cracking of hydrocarbons is one of the most challenging chemical separations due to the similarity of the molecules' physicochemical properties. Its adsorption amounts

for C_2H_6 at 273 and 298 K (121.7 and 100.2 cm^3/g) were higher than those of C_2H_4 (111.3 and 80.7 cm^3/g) as well as the adsorption heat enthalpy of C_2H_6, and C_2H_4 with 28.6 kJ/mol, and 26.1 kJ/mol at zero coverage, respectively. Both properties suggest Azole-Th-1 has a higher affinity for C_2H_6 than C_2H_4. At 298 K and 100 kPa, Azole-Th-1 affords an adsorption capacity of C_2H_6 up to 100.2 cm^3/g, exceeding most advanced adsorbents such as MAF-49, ZIF-8, ZIF-7, PCN-245, MIL-142A. In breakthrough experiments, C_2H_4 broke through the adsorption bed and yielded a high purity gas (> 99.9%), whereas C_2H_6 subsequently slowly eluted and reached equilibrium. Thus, polymer-grade C_2H_4 can be generated at the outlet. A maximum working capacity of 1.13 mmol/g with > 99.9% purity for C_2H_4 was harvested from a 90/10 (v/v) gas mixture, which is nearly 1.3 times that of $Fe_2(O_2)$ (dobdc) and 3.6 times that of MAF-49 as two of the best materials for C_2H_6/C_2H_4 separation. The breakthrough time interval for C_2H_6/C_2H_4 mixtures in five cycles is comparable, exhibiting a good regenerability of Azole-Th-1. Highly efficient separation of C_2H_4 from a 90:1:9 (v/v/v) gas mixture of $C_2H_6/C_2H_2/C_2H_4$ was achieved by adopting a packed column of activated Azole-Th-1. It can produce a high purity C_2H_4 (> 99.9%) after only a single-breakthrough operation and its working capacity is up to 1.34 mmol/g (Fig.20). According to GCMC simulations, the C-H-π interactions between gas and the ligand benzene ring contribute to the preferable adsorption capacity of C_2H_6[78].

The ultramicropore nature of ECUT-36 is utilized for D_2/H_2 separation that normally requires microporosity via kinetic quantum sieving effect. This Th-MOF affords H_2 uptake of 65.6 cm^3/g at 1 bar and 77 K, while D_2 uptake is 72.4 cm^3/g. The D_2/H_2 ratio in the range 1.16-1.10 did not change significantly over 0-1.1 bar. According to the ideal adsorbed solution theory, the adsorption selectivity is calculated to be 1.5, comparable with certain benchmark MOFs. ECUT-36 was selected as a candidate for the removal of highly hazardous NH_3, as release of $[NH_2(CH_3)_2]^+$ from its structure via proton transfer is expected to function as a "molecular imprint". This calcined ECUT-36 shows NH_3 uptake of 6.6, 3.6 mmol/g at 273 K, and 298K, respectively. Though this adsorption capacity is lower than certain benchmark materials such as 13X zeolite, COF-10, and MCM-41, it shows a recorded ammonia packing density up to 0.76 g/cm^3, which is remarkably close to solid ammonia (0.82 g/cm^3). NH_4^+ formation is caused by a reversible proton transfer from protonated carboxyl groups to adsorbed NH_3 in conjunction with the molecular imprint effect[140].

U4-BDC-6 shows strong adsorption sites for energy gas. The low-pressure H_2 adsorption isotherm at 77 K exhibits an initial steep rise to 3.5 mmol/g at 115 mbar. With increasing pressure, the adsorption capacity increases gradually to a saturation value of 4.9 mmol/g at 1.2 bar. For loadings up to 2.5 mmol/g, H_2 is adsorbed exclusively at primary binding sites in the framework pockets to give an isosteric heat of 8.6 kJ/mol, larger in magnitude than that in activated carbon and the majority of MOFs with coordinatively-saturated metal sites. Likewise, a strong interaction between CH_4 and binding pockets in U4-BDC-6 occur, which implies this flexible framework may distort to optimize interactions with guest molecules of different sizes[150]. The desulfurization by Cage-U-Co-MOF due to its hydrophobic nature

and drum-like nanocages has very recently been demonstrated. It enables SO_2/CO_2 selectivity up to 80-60 in a 1:99 v/v SO_2/CO_2 mixture while the SO_2/N_2 selectivity reaches 2078-35620. The corresponding residence time for SO_2 was 100 min/g while these of CO_2 and N_2 were 3 min/g in the breakthrough experiments for a ternary $SO_2/CO_2/N_2$ mixture bearing 1000 ppm SO_2. This performance was not affected in the presence of water vapor (3% H_2O in He). The preferable uptake for SO_2 is attributed to the open cobalt and uranyl sites formed by withdrawing the terminal coordinated H_2O[212].

Porous Th- and U-MOFs, particularly with cage-like structures stand as emerging adsorbents for challenging gas-related processes. Systematic tuning of unsaturated states of actinide or heterometal nodes, porous cavities, supramolecular interactions, and framework flexibility will contribute to contribute to enhancing their separation, storage, and removal performances.
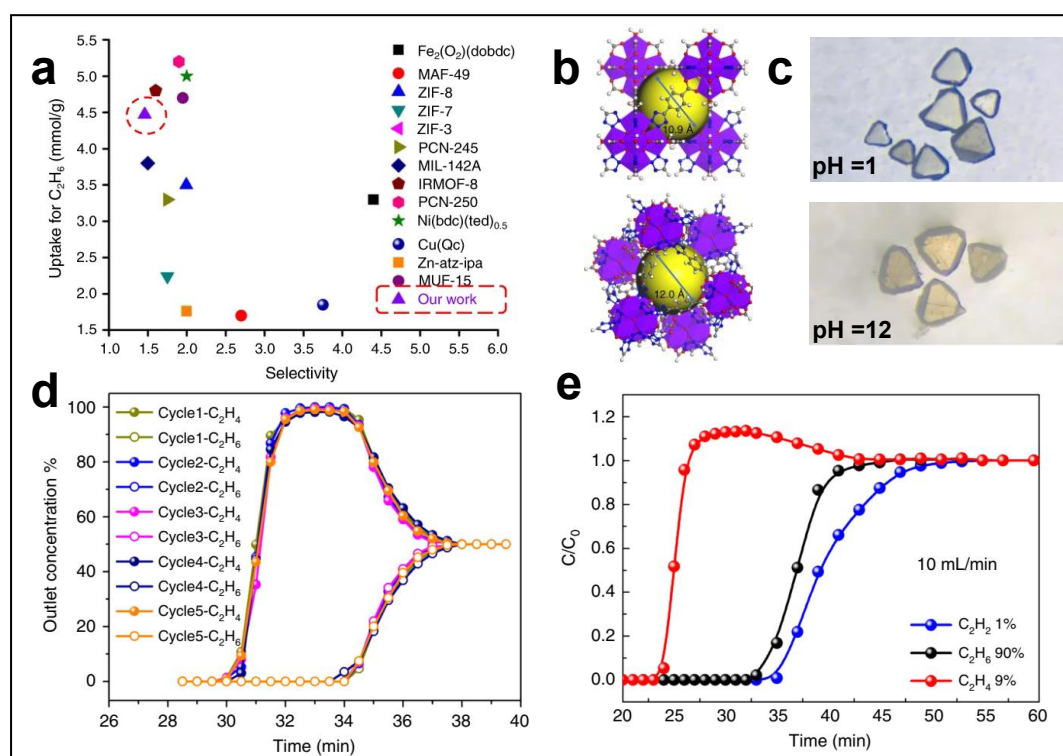
Figure 20. (a) Comparison in selectivity and C_2H_6 adsorption capacity at 298 K and 1 bar between the reported top-performing porous adsorbents for C_2H_6/C_2H_4 separation and Azole-Th-1; (b) super tetrahedron cage (up) and super octahedron cage (down); (c) crystal images after soaking in different pH solvents for 30 days; (d) C_2H_6/C_2H_4 (50/50, v/v) binary mixture for five cycles. (e) $C_2H_6/C_2H_4/C_2H_2$ (90/9/1, v/v/v) ternary mixture separation (Reproduced from ref. [78]).

4.2 Heterogeneous catalyst

The actinide centers have been recognized in heterogenous catalytic transformations of small molecules, where early actinide nanomaterials are preferably utilized[316]. The thorium or uranium based MOFs emerge as potential heterogenous catalysts in

recent years. Since the 2p bonding orbitals of uranyl axial oxygen contribute to HOMO (highest occupied molecular orbital) and empty uranium orbitals contribute to LUMO (lowest unoccupied molecular orbital), the photoexcitation of UO_2^{2+} under visible light will excite oxygen electrons from HOMO to LUMO and this ligand to metal charge transfer (LMCT) produces a singly reduced UO_2^+ and an oxygen radical, allowing excited-state species with a standard reduction potential of +2.6 V to oxidize a great range of molecules. This visible-light photocatalytic activity can be tuned by the addition of hydrogen bonding, ligand exchange. However, the resulting UO_2^+ will disproportionate to UO_2^{2+} and insoluble U^{4+} species, which leads to the deactivation of UO_2^+ as photocatalyst. The uranyl complexes such as $UO_2(NO_3)_2 \cdot 6H_2O$, $UO_2(CH_3COO)_2 \cdot 2H_2O$, $UO_2(CF_3SO_3)_2$ recently demonstrate their underexplored yet efficient utilities in C-H functionalization[317], late-stage oxygenation[318], and hydrosilylation of aldehydes[319]. It will inspire the exploitation of U(VI)-MOFs as multifunctional photocatalysts. The incorporation of uranyl as nodes within An-MOFs provides precise structural control of spatially isolated uranyl species, which circumvent the stabilization of UO_2^+ complexes by creating steric hindrance around uranyl ions or doping and grafting of uranyl on porous supports as heterogeneous catalysis[320]. Besides U-MOFs as a stable heterogeneous catalyst, the strong Lewis acidity of thorium nodes in Th-MOFs exhibits promising catalytic properties different from tetravalent transition metal MOFs. Current design strategies for MOF catalysis include electronic tuning of a metal node, modulation of node spatial environments, and site uniformity[321]. Following this strategy will lead to the efficient fabrication of abundant active sites within An-MOFs.

4.2.1 Degradation of pollutants

Due to the richness of uranyl nodes and organic bridging linkers, uranyl-organic frameworks can absorb UV and visible light that enhances the photocatalytic degradation of pollutants in water as compared with conventional photocatalysts such as metal oxides and sulfides. We summarize the degradation performances of U(VI)-MOFs (Table 17), which are closely related to the photocatalyst activity, the substrate property, batch experiment parameters.

Table 17 Summary of pollutant degradation performance of U(VI)-MOFs

Target	U(VI)-MOFs	Lamp	C_0 (mg/L)[a]	S/L (g/L)[b]	R (%)[c]	T (hrs)[d]	Ref.
	CPP-U4	300 W Xe	10	0.625	~ 100	3	[119]
	U-H1	18 W Hg	-	-	17.4	3	[169]
	U-H1	125 W Xe	-	-	1.6	0.5	[169]
	U-TTHA-4	Hg	40	-	92	2	[197]
	UNa-TTHA	Hg	40	-	82	2	[197]
RhB	U-NIP-4	500W Xe	30	0.5	94	2.67	[185]
	U-BDC-OH	500W Xe	30	0.5	78	2.67	[185]
	U-NIP-4	700W Xe	30	0.5	95	2.67	[185]

			(a)	(b)	(c)	(d)	
	U-BPDA-1	300W Xe	10	0.5	85	0.67	[193]
	U-BPDA-2	300W Xe	10	0.5	81	0.67	[193]
	UCd-C3-2	300W Hg	20	1.0	94	4.5	[220]
MB	U-H1	18 W Hg	-	-	54	3	[169]
	U-H1	125 W Xe	-	-	40	3	[169]
	UNSL-1	150 W Xe	40	1.0	64	1.67	[97]
IC	U-TDC-15	125 W Hg	10	0.5	~ 100	4	[237]
	U-1,2-BDC-1				88.8	3	[93]
	U-1,2-BDC-2				78	3	[93]
	U-NTP-1	120 W LED	40	1.0	91	2.5	[167]
	U-BDC-2				82	2.5	[167]
	U-NTP-2				95	1.08	[167]
TC	U-1,4-NDC-1				86.5	1.5	[103]
	U-1,4-NDC-2				46.6	1.5	[103]
	U-1,4-NDC-3				60.7	1.5	[103]
	U-1,4-NDC-4	300 W Hg	40	1.0	50.2	1.5	[103]
	U-1,4-NDC-5				79.2	1.5	[103]
	U-1,4-NDC-6				95.4	1.5	[103]

(a) initial concentration; (b) the ratio of solid to liquid; (c) degradation rate; (d) elapsed time for the degradation rate.

To study the photocatalytic properties of U-MOFs, RhB, which is difficult to be degraded in nature, is selected as a diagnostic dye. The degradation rate under UV is usually better than that upon visible light[169]. U-BPDA-1 and U-BPDA-2 represent effective RhB photocatalysis in terms of degradation kinetics among those U(VI)-MOFs[193] (Fig.21a). The release of TC as one of the most widely used antibiotics into the biosphere will pose a major health risk to ecological systems. Photocatalytic technology based on U-MOFs offers an alternative in eliminating TC. The mechanism for uranyl-catalyzed photo-oxidation of organic pollutant or bio-hazard involves the photoexcitation of uranyl centers, and generation of molecular oxygen. Take RhB for example, as RhB arrives at the photoexcited uranyl centers in U-MOFs, it begins to decompose with hydrogen abstraction and transforms into active intermediates that finally crack into small organic acids and CO_2[193]. As for TC, once a hydrogen atom of TC occupies the HOMO, the excited electrons in active uranyl intermediates will be permanently retained in the LUMO unless they are captured by electronegative substances. The captured electrons are transferred to highly active peroxide anions, which further oxidizes TC[103].

4.2.2. Conversion of CO_2

Due to abundant Lewis acidic sites at Th_6 clusters, Th-MOFs has been tested for CO_2 cycloaddition of styrene. The micro- and meso-porosity of M-NU-1008 (M = Zr, Hf, Ce, Th) offered sufficient pore space for the catalytic reaction and the conversion on Th-NU-1008 was determined to be 65% after 72 hours of catalysis. The trend of

catalytic activity (Ce > Zr > Hf > Th) deviated from the strength of Lewis acidity (Hf ~ Zr > Ce > Th), which was associated with the dissociation of terminal water. The extra terminal water of Th_6 cluster made this dissociation process even harder, leading to a lower tendency of exposing Lewis acidic sites[322] (Fig.21b). The maximum adsorption capacity of CO_2 reached 42.44 cm^3/g on ThNi-INA. The decisive Th_6 cluster performed well as a catalyst for CO_2 cycloaddition, in which 89-99 % styrene oxide transformed into cyclic carbonates and no obvious loss in catalytic activity upon 10 cycle runs. The mechanism for this cycloaddition reaction was proposed as: (1) ThNi-INA captures CO_2 and enriches styrene oxide in the $[Th_{48}Ni_6]$ nanocage. (2) a coupling reaction occurs between the Th_6 cluster and the oxygen atom of the epoxide, and the epoxy ring was activated. (3) nucleophilic Br^- attacks the carbon atom in the epoxy ring, resulting in ring-opening. (4) CO_2 reacts with the oxygen anion in the opened epoxy ring, and the Th_6 cluster stabilized the resulting alkyl carbonate salt, which is finally converted into cyclic carbonate through intramolecular ring closure[213]. The chemical yield of styrene carbonate from CO_2 and epoxy styrene with Th-IHEP-5 was 71% while the conversion on Th-IHEP-6 and NU-905 were less than 1%. After three cycles of cyclical circulation, no significant loss of catalytic activity was observed for Th-IHEP-5[122]. The bipyridine unit as part of the mixed ligand contributes to improving the photocatalytic activity of Th-IHEP-5. The uranyl nodes have been recently examined for conversion of CO_2. The single Mn^{2+} sites at metalloporphyrin in IHEP-9 exhibit photocatalytic CO_2 cycloaddition on a variety of epoxides with yield of 78-99%. The appreciable efficiency of CO_2 conversion on metalloporphyrin-based frameworks is ascribed to that the photogenerated free radical CO_2^- react with ring-opened epoxy compounds induced by epoxide radical cation, Mn^{2+} and nucleophilic Br^-[207]. In a typical reaction condition, UNi-CPTPY-1 and UNi-CPTPY-2 showed 69%, and 80% conversion to the target product, respectively. Since transition metals (Co^{2+}, Fe^{2+}) and ligands have no appreciable catalytic effect on this reaction, the catalytic capabilities of isomorphous frameworks are originated from uranyl nodes as well as framework porosity. Due to the 3D interpenetrating framework in UNi-CPTPY-2 offering more binding sites, it exhibited higher catalytic efficiency than in UNi-CPTPY-1[209].

4.2.3 Catalysis for organic reactions

1,2,3,4-tetrahydroquinaldine was selected as a model substrate to test the catalytic activity of anionic U-IHEP-4 for dehydrogenation in various solvents. When polar aprotic DMF was used as the solvent, 85% of the substrate was converted to quinoline with U-IHEP-4 (0.5 mol%) at the selectivity of 82%. If the solvent was replaced by DMSO, the selectivity was only 64% although the conversion rate increased to 99%. The reaction selectivity reached a plateau at 80 °C while the maximum conversion rate was not obtained until 120 °C. By using 2 mol% U-IHEP-4, both conversion and selectivity reached 99% at approximately 9 hours. A series of N-heterocyclic compounds were effectively dehydrogenated to yield corresponding aromatic products based on this optimal reaction condition. Compared to homogeneous Co-

TCPP, heterogeneous U-IHEP-4 showed better catalytic performance[91]. As a case of utilizing the intrinsic catalytic properties of porphyrin-based Th-MOFs, NU-905 demonstrated 2-chloroethyl ethyl sulfide (CEES) oxidation under light irradiation. It converted 65% of the starting materials in 5 minutes and 100% in 10 minutes (1 mol%). The estimated half-life of CEES is 4 minutes[121]. Th-IHEP-5 and Th-IHEP-6 demonstrated 100% catalytic oxidation efficiency to CEES in 20 minutes, which was better than TCPP, $Th(NO_3)_4$, and NU-905. This catalytic performance was mainly ascribed to the large conjugated porphyrin of high singlet oxygen quantum yield. Despite that bipyridine did not affect the oxidation of CEES, it served as a photosensitizer to enhance the photocatalytic activity of porphyrin in the visible region[122] (Fig.21c).

When NU-1301 was employed as a photocatalyst (0.5 mol%) for $C(sp^3)$-H fluorination reactions using N-fluorobenzenesulfonimide as fluorination reagent with a blue-light-emitting-diode light source at 298 K, a significant increase in the yield of 1-fluorooctane (99%) was observed compared to the homogeneous $UO_2(NO_3)_2$ (52%), supporting a stabilizing effect of carboxylate ligands on uranyl nodes. In the cases of other alkanes such as cyclopentane and n-octane as substrates, NU-1301 exhibited better catalytic activity compared to $UO_2(NO_3)_2$. For instance, it had a yield of 25% for 1-fluorocyclooctane (versus 13% by $UO_2(NO_3)_2$) in the presence of toluene[320]. To compare the support effect of isostructural MOFs, 4-methoxybenzyl alcohol oxidation was chosen as a model aerobic oxidation reaction to test the reactivity of grafted vanadium atoms. V-Th-NU-1200 showed a conversion of 58% after 5 hours. A constancy in substrate conversion during three runs was solely observed for V-Th-NU-1200, indicating considerable chemical stability upon repeating the catalytic process. The electronegativity and oxidation states of the supporting Th-NU-1200 nodes played an important role in the catalytic performance of the single vanadium ion[249]. NU-1000-U (5 mol%) exhibited a conversion of 12% after 24 hours under blue light in an O_2 atmosphere in an alcohol oxidation experiment. When UO_2^{2+} is present, the rate of reaction decreases in relative to pristine NU-1000, which suggests the uranyl excited state is quenched by the exciplexes produced by the excited pyrene linker, and vice versa[323].
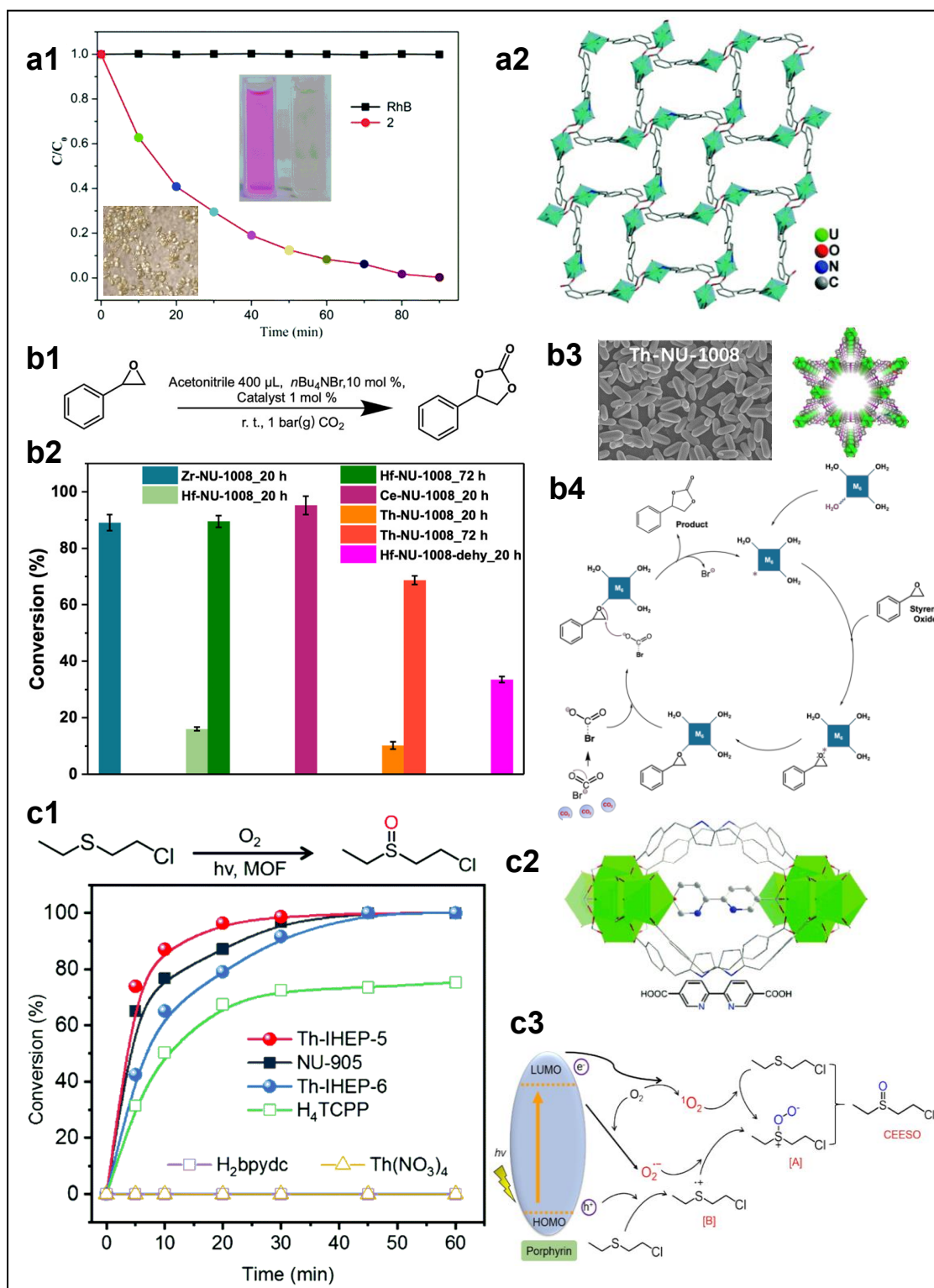
Figure 21. (a1) the concentration change of RhB versus irradiation time with or without U-BPDA-2 under xenon lamp, the inset picture reveal the pristine crystals and the degradation of RhB, (a2) 2D rectangle net of U-BPDA-2 along a-axis (Reproduced from ref. [193] with permission from The Royal Society of Chemistry, Copyright 2020); (b1) Reaction scheme of CO_2 fixation into styrene oxide; (b2) CO_2 fixation behavior on four NU-1008 and partially dehydrated Hf-NU-1008. (b3) scanning electron microscopy images and structures of Th-NU-1008. (b4) Proposed reaction mechanism by M-NU-

1008 with nBu₄NBr as co-catalyst (Reproduced from ref. [322] with permission from American Chemical Society, Copyright 2019); (c1) Reaction profiles of different Th-MOFs, ligands, and thorium precursor were irradiated with the fluorescent lamp of the same power density. (c2) Thorium clusters are linked by porphyrin derivative. (c3) Mechanism diagram of Th-IHEP-5 photocatalytic oxidation of CEES (Reproduced from ref. [122] with permission from The Royal Society of Chemistry, Copyright 2020).

4.3 Luminescent sensing materials

The use of U(VI)-MOFs as luminescence sensing materials are rather limited when compared with their lanthanide counterparts. Natrajan presented an overview of photophysics and photochemistry of actinide ions and their coordination polymers, in which the luminescence properties of uranyl-bearing compounds were underscored[324]. Actinides-bearing luminescent coordination polymers had been hardly delineated but, in principle, follow the same rules as their lanthanide homologs, together with a tendency towards higher participation of other orbitals[325]. Nevertheless, it is well-known that U(VI) has characteristic green emissions due to the HOMO-LUMO transition. By incorporating uranyl nodes into MOFs, U(VI)-MOFs can exhibit luminescence properties that are sensitive to guest species including metal ions, organic molecules (Table 18), ionizing or electromagnetic radiation. U(IV)-based compounds have luminescence properties but have not exhibited sensing applications. Moreover, by combining luminescence-innocent Th(IV) with scintillating organic linkers, Th(IV)-MOFs exhibit radioluminescence[135] that portends promise as self-calibrated luminescent sensors.

Table 18 Summary of detection performance of U(VI)-MOFs

Target	An-MOFs	C_0 range (mg/L)	S/L (g/L)	K_{sv}	LOD (mg/L)	Ref
Fe³⁺	U-NIP-1	0-60	1.0	2.6×10^4	6.3×10^{-3}	[81]
	U-TCI-2	0-200	1.5	8.9×10^4	0.21	[194]
	U-TCI-3	0-200	1.5	6.3×10^4	0.55	[194]
	U-1,3-BDC-3	0-200	0.50	9.7×10^3	1.0	[244]
Fe²⁺	UNSL-1	0-1424	0.40	7.7×10^{-2}	1.2×10^2	[97]
Ru³⁺	U-GDL	0-101	0.60	8.0×10^4	2.1	[177]
MnO₄⁻	U-NIP-8	0-56	0.1	1.8×10^4	0.21	[166]
Nitrobenzene	U-TTHA-1	0-1000	0.67	-	-	[264]
2,4,6-trinitrophenol	U-PPDC	0-1000	0.67	1.6×10^6	15	[176]
	U-PPBA	0-1000	0.67	8.5×10^5	20	[176]
Benzaldehyde	U-PPBA	0-1.06	0.67	-	-	[176]
TC	U-1,3-BDC-3	0-200	0.50	4.1×10^4	0.82	[244]
Arginine	U-NIP-5	0-38	0.037	-	0.18	[166]
	U-NIP-8	0-38	0.037	-	1.1	[166]

K_{sv}: quenching constant; LOD: limit of detection.

4.3.1 Detection of ionic species

The luminescence quenching effect of Fe^{3+} were significantly higher than alkali, alkali earth and some transitional metal ions, which has been observed in a few U(VI)-MOFs represented by U-NIP-1[81] (Fig.22a). Since the UV/Vis spectrum of Fe^{3+} exhibited a broad adsorption band overlapping with the excitation spectrum of U-TCI-2, U-TCI-3, it was speculated that absorbed Fe^{3+} gathered on the framework surface and the competitive energy absorption weakens or even eliminates the U(VI) luminescence intensity, thus offering selective detection of Fe^{3+}[194]. Another plausible account for quenching was a charge transfer from Fe^{2+} to the ligand, but the energy transfer paths exhibited partial overlap with the UNSL-1 spectra, which hindered the emission to some degree[97]. Both, energy transfer from the conduction band of U-1,3-BDC-3 to semi-filled molecular orbitals of Fe^{3+} and a competitive relationship between the emission of the MOF and the absorption of Fe^{3+} are illustrated as driving forces for luminescent extinction[244]. These dual factors also lead to the quenching of U-NIP-8 contact with MnO_4^-[166].
Since GDL containing -NH or -OH donor functionalities is apt to form hydrogen bond interactions, the quenching mechanism of U-GDL for Ru^{3+} might be due to the energy transfer between the excited molecule and target quencher by way of collision[177]. HNU-39 exhibited increasing fluorescence with pH in the range of 9.4-11.5 with a response time in alkaline solution of 20 seconds. Mono-, and divalent anions showed little effect on pH sensing, rendering a reliable detection of pH in real wastewater possible. This "turn-on" sensing mechanism was ascribed to the destruction of the conjugated system and electron transfer upon the deprotonation of the carboxylic acid groups by hydroxyl ions[262].

4.3.2 Detection of organic molecules

Highly sensitive, selective, and cost-effective detection of organic hazards such as explosive and toxic nitroaromatics have been long pursued by using luminescent MOFs. An-MOFs scarcely found applications in sensing such category of organic chemicals. The luminescence of U-TTHA-1 displayed the most obvious quenching upon contact with nitrobenzene among an array of organic solvents, leading to its sensing of nitrobenzene in dimethyl sulfoxide. U-PPDC and U-PPBA exhibited similar luminescence quenching among a series of nitroaromatics including 2,4,6-trinitrophenol, 2,4-dinitrotoluene, p-nitroaniline, m-dinitrobenzene, sodium nitrobenzene sulfonate, nitrobenzene[176]. This "turn-off" detection mechanism arose from electron-withdrawing nitro groups and significant donor-acceptor electron transfer from ligands to solid frameworks. For instance, the LUMO of nitrobenzene is a low-lying π^* type orbital stabilized by the nitro group through conjugation that should be energetically lower than the LUMOs of TTHA and uranyl. Thus, the electron-deficient nitrobenzene withdrew an electron from the excited ligand and uranyl, to transfer the excited state electrons from U-TTHA-1 to nitrobenzene[264].

U-PPBA demonstrated a "turn-on" fluorescence response to aldehyde, which was interpreted as π*-π conjugation between ligand and aldehyde to strengthen the rigid skeleton[176].

U-1,3-BDC-3 had been tested to detect seven different antibiotics, among which the highest quenching efficiency was observed for TC. Both host-to-guest electron transfer and abundant hydrogen bonds account for this fluorescence quenching[244]. The sensing of amino acids in living organisms is essential to monitor the human metabolism. U-NIP-5 and U-NIP-8 exhibited quantitative determination of arginine concentration in deionized water by means of "turn-on" luminescence response. It was speculated that the protonated guanidine group of arginine interacted with the U(VI)-MOFs, enhancing their luminescence in solution[166].

4.3.3 Detection of radiation

In the realm of radiation detection, scintillating materials have gradually evolved from classical inorganic/organic scintillators to luminescent An-MOFs. Radioluminescent Th-MOFs not only show better radiolytic stability but also act as a ratiometric sensor as intrinsic decay energy provides a constant internal reference. Rigid aromatic ligands such as NDC, ADC proved to be efficient scintillators since they could avoid excessive ligand flexibility and conformation that may lead to unpredictable scintillating properties. By comparing solid-state fluorescence spectra of Th-2,6-NDC and the free ligand, the solid framework exhibited a blue-shift with a small shape modification with better-resolved bands. The absolute quantum yield was 39.8%, larger than that of 2,6-NDC (34.5%) although the ligand showed a much longer lifetime under identical conditions. Th-2,6-NDC had a count per minute per milligram (0.35 mg Th) ratio of 173.0, resulting in a 20-fold enhancement of the ligand autoluminescence. By comparing with a physical mixture of precursors, it had been proved that a molecular level mixing within a crystalline structure strongly improved the autoluminescent properties. The crystallinity of Th-2,6-NDC was unaffected by α self-irradiation from ^{232}Th and its autoluminescence count did not vary even after one year[135].

The intrinsic uranyl emission had been long forgotten as a potential self-activated scintillator. Recently, the X-ray excited luminescence (XEL) intensity of SCU-9 showed a linear response as a function of increased X-ray power. Compared with the commercially available CsI:Tl scintillator, SCU-9 had a comparable fitting slope value and a shorter X-ray attenuation length in the energy region above 20 keV, implying a higher X-ray attenuation efficiency. The luminescence intensity of CsI:Tl was sharply quenched after receiving 30 Gy X-ray radiation while SCU-9 maintained 65% of its luminescence intensity after exposure to 53 Gy X-ray radiation. SCU-9 maintained 80% luminescence intensity after being subjected to 95% relative humidity for 30 minutes due to its decent hygroscopy hardness while the XEL of CsI:Tl was nearly quenched under identical conditions[246]. The photoluminescence of U-SA-2 was significantly quenched after being exposed to 40 Gy X-rays or 60 Gy γ-rays, and complete recovery of quenched photoluminescence could be achieved by

heating the irradiated sample at 473 K for 12 hours. Its detection limit of γ- and X-ray dosage were calculated to be $1.6×10^{-4}$ and, $5.2×10^{-4}$ Gy, respectively[109], while the values were calculated to be $1.4×10^{-5}$, $1.1×10^{-5}$ Gy for U-OA-4[269], performing approximately one order of magnitude better than U-SA-2. This significant advance was attributed to (i) low self-quenching due to a long uranium-uranium atomic distance; (ii) intense oxo-based radicals. This type of radiation dosimeter could be fully recycled, as illustrated by the multiple cycles of irradiation/heating procedure. Besides ionizing radiation, U-MOFs are susceptible to UV irradiation. The emission intensity of U-SA-2 significantly decreased as UV exposure extended, which dropped to 50% of its original intensity after 20 minutes of exposure and completely quenched after 5 hours[109]. The emission intensity of U-L1-OMe-1 and U-L2-OMe-1 decreased gradually over the exposure time of UV irradiation. This light-induced fluorescence attenuation ascertained them to be photo-responsive and attributable to the fact that the vinylpyridine motif adsorbed energy from UV irradiation, activated the C=C bond, and enabled the pyridinyl group to slightly rotate around it[178]. The photoluminescence of U-OA-2 was quenched up to ~93% within 57 seconds upon continuous UV irradiation. The quenched photoluminescence intensity could not be recovered by exposure to air at elevated temperature, assuming that generated radicals were trapped and stabilized within intact layers. The detection limit of UV dosage was calculated to be $6.9×10^{-9}$ J, two orders of magnitude compared to the current top-performing chemical UV detectors (Fig.22b). Three reactions might occur during the detection of UV: (1) enhanced bonding between radical-based oxo donors and uranyl led to a more effective energy release via a nonradiative process. (2) an increase of the O-N distance resulted in a decrease in energy transfer efficiency between uranyl and phen species. (3) an increase of adjacent phen-phen distance weakened face-to-face π-π stacking interactions[268]. U-IPBP-3 underwent a slow color change from brownness to puce when exposed to UV light for 2 hours. When kept in the dark at 298 K for two weeks or at 423 K for 4 hours, the puce could restore to the original color. Repeating this reversible experiment several times, there was no noticeable color loss. Such photochromic property holds potential in detecting UV light[107].

4.3.4. Detection of D$_2$O

The chemical analysis of D$_2$O in the presence of H$_2$O by current methods including nuclear magnetic resonance (NMR), or infrared laser spectroscopy suffers from high cost-effectiveness and D$_2$O detection materials have been rarely reported. SCU-UEu-1 represented the unique case of detection of D$_2$O and might find application in the production of high-purity heavy water. Under 365 nm UV irradiation, two groups of emission peaks of SCU-UEu-1 could be observed, including the weak peaks of UO_2^{2+} located in the green region and the relatively strong sharp band of Eu^{3+} in the red region. Due to the energy transfer from UO_2^{2+} to Eu^{3+}, the emission intensity of Eu^{3+} was much higher than that of UO_2^{2+}. However, since some uranyl PBUs were not linked to Eu centers, this energy transfer was not sufficient to quench the uranyl emission. Thus, the 4f/5f bimodal emission was observed and could be tuned by the

substitution of certain coordinated guest molecules. When SCU-UEu-1 was soaked in D_2O, it displayed the highest Eu^{3+} emission intensity, significantly higher than those when soaked in other solvents including CH_3OH, H_2O, CH_3CN, THF, and DMF. As the D_2O content increased to 60% wt, a sharp increase in luminescence intensity ratio occurred. The emission intensity reached 90% of the maximum intensity within 30 seconds and 100% in the following 10 minutes, indicating that this U-MOF could be adopted for full-range, real-time monitoring of D_2O with a detection limit lower than 1%. Besides the energy transfer between heterometals, the presence of labile $Eu-O_w$ (water oxygen) bond and abundant coordinated H_2O per Eu site led to facile H_2O-D_2O exchange of $Eu-O_w$ when compared with $U-O_w$, resulting in a specialized luminescence intensity response of SCU-UEu-1 towards heavy water. The solid-state ^3H-NMR results supported that D_2O had strong chemical interactions with SCU-UEu-1, and coordinated H_2O was substituted by D_2O or DHO on Eu centers[204] (Fig.22c).

In UEu-3,5-PDC, the characteristic photoluminescence emission bands of uranyl(VI) and europium(III) ions coexisted in the spectra which were measured from 450 to 750 nm and the photographs showed a gradual change in color from bright red to yellow to bright green. The luminescence was highly dependent on the Eu content or coordination environments, leading to the application of a ship-in-bottle heterometallic An-MOF as LED or sensing materials[234]. One understudied area can be achieved with heterometallic Th- and U-MOFs is tandem luminescence sensing for target species in complex samples and relevant development of portable devices.
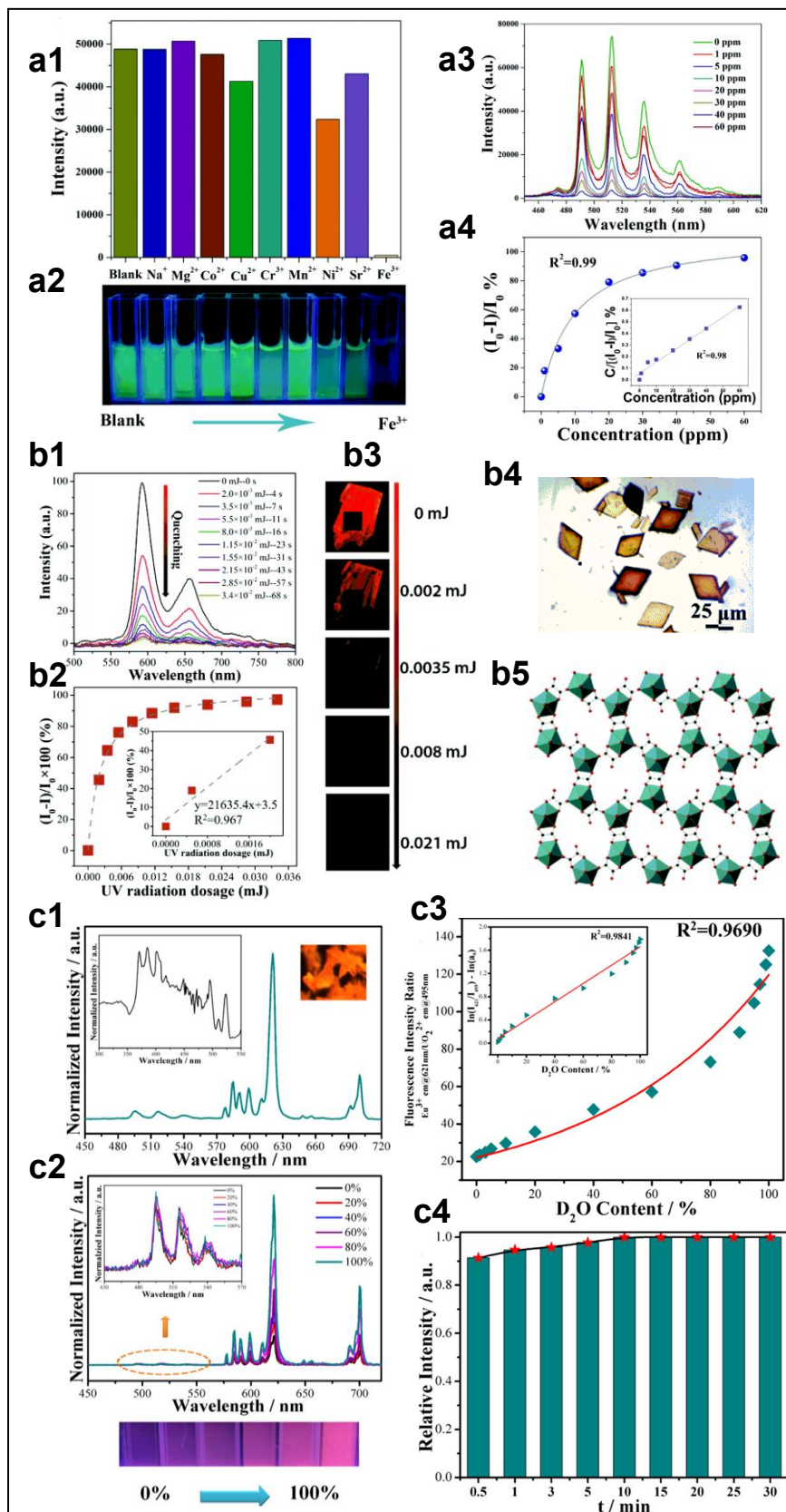
Figure 22. (a1) The luminescence intensity of U-NIP-1 dispersed into different metal salt solutions (excited at 364 nm, monitored at 512 nm). (a2) Corresponding luminescence photograph immersed in these metal salt solutions (excited at 365 nm). (a3) Emission

spectra at various concentrations of Fe^{3+} solution. (a4) Simulated correlation between the quenching ratio and Fe^{3+} concentration using the Langmuir model (Reproduced from ref. [81] with permission from The Royal Society of Chemistry, Copyright 2018); (b1) Photoluminescence spectra of U-OA-2 with increasing dosages of UV radiation. (b2) Relative photoluminescence quenching (measured at 592 nm) and linear fitting in the low dosage range as inset. (b3) Corresponding photoluminescence photographs of a single crystal after receiving continuous UV radiation. (b4) Crystal images after continuous UV (365 nm) irradiation. (b5) Extended uranyl-oxalate sheets (Reproduced from ref. [268] with permission from The Royal Society of Chemistry, Copyright 2019); (c1) Emission spectrum of SCU-UEu-1 excited at 365 nm. The inset shows the excitation spectrum upon monitoring Eu^{3+} emission at 621 nm. (c2) Luminescence spectra soaked in solutions with different contents of D_2O. (c3) Correlation between relative intensity and D_2O content. (c4) Luminescence intensity changes after soaking in pure D_2O for different periods (Reproduced from ref. [204] with permission from American Chemical Society, Copyright 2020).

4.4 Conducting and semiconducting materials

Porous MOFs have been extensively investigated as an advanced solid-state proton conductor due to their intrinsic high porosity and framework tunability, which had been recently reviewed by the Kitagawa group[326]. The conducting or semiconducting property of An-MOFs had been greatly underappreciated since few Th- and U-MOFs displayed good proton-conducting properties when compared with inorganic conductors or semiconductors. Considering the anion-exchangeable nature of SCU-7, proton-conducting experiments were executed through the exchange of $H_2PO_4^-$ into SCU-7. The exchanged SCU-7 improved its proton conductivity by nearly 80 times compared to pristine SCU-7[182]. At 95 and 98% relative humidity (RH), UK-BPDSDC-2 exhibited typical Nyquist plots for proton-conducting materials featuring an arc in the high-frequency region and a spike in the low-frequency region. At 85 °C, the proton conductivity (σ) was elevated from 1.58×10^{-5} to 1.07×10^{-3} S/cm upon RH increasing from 55% to 98%, suggesting the proton conductivity was highly humidity dependent. The high σ value under 85 °C and 98% RH was comparable with those of the lanthanide-BPDSDC coordination polymers and much higher than those of classic MOFs such as MIL-53. The pore wall of UK-BPDSDC-2 was made of hydrophilic sulfonate groups and the coordinated water molecules point to the pore surface, which promoted water enrichment inside the pores. The abundant adsorbed water acts as a proton carrier, resulting in a vehicle-type proton transfer[241].

In virtue of heavy atomic constituents, wide-bandgap actinide-based semiconducting material holds great promise in the application of high energy photon detection that has been widely used in space science, medical imaging, and nuclear technology. Due to the independence of each uranyl-organic cage contributes to the enhancement of the carrier transport pathway, SCU-14 displayed an experimental bandgap of 2.61 eV and an intrinsic resistivity of 5.23×10^{10} $\Omega \cdot$cm, ensuring a low leakage current. The

photocurrent was significantly increased with increasing X-ray dose rate and the charge-carrier mobility and lifetime product of SCU-14 is 6.30×10^{-4} cm^2/V, comparable to those of the newly developed perovskite materials. The current density at different dose rates gave a record value of the sensitivity of 54.93 µC Gy$_{air}^{-1}$cm^{-2} among reported MOF based X-ray detection materials. After continuous exposure with a cumulative dose of around 120 Gy$_{air}$, the photoelectric response of SCU-14 was almost unchanged[253] (Fig.23).

The incorporation of a photoresponsive TNDA unit into Th$_6$-Me$_2$BPDC-8 and U$_{1.23}$Th$_{4.77}$-Me$_2$BPDC-8 enables the investigation of conductivity as a function of external excitation wavelength. An approximate one order of magnitude enhancement in "static" conductivity were observed by either integrating a second actinide metal or doping with iodine or an electron acceptor, revealing the rationale to tune the conductivity of An-MOFs for practical applications[125].
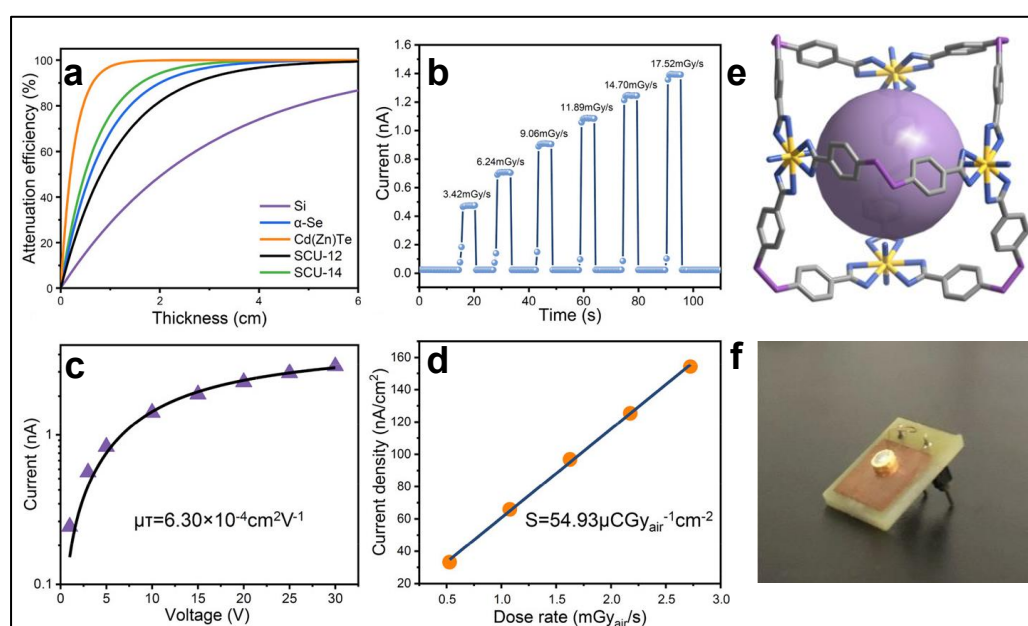
Figure 23. (a) X-ray attenuation efficiencies as a function of material thickness for SCU-14, SCU-12, and commercial materials (X-ray photon energy = 150 keV). (b) Photocurrent versus time plots under increasing X-ray dose rates. (c) The charge-carrier mobility and lifetime product (µτ) for SCU-14. (d) X-ray generated photocurrent density at different dose rates (Bias voltage=100 V). (e) Each cage is constructed from four uranyl hexagonal bipyramids and six bidentate flexible ligands. (f) The device with the symmetric structure of Ag/SCU-14/Ag was further embedded into a cathode irradiation configuration to test electrical properties (Reproduced from ref. [253] with permission from American Chemical Society, Copyright 2020).

4.5 Nuclear target materials

The use of An-MOFs as nuclear target materials for the selective isolation of fission products (FP) from a post-irradiated nuclear target is a reverse process to remove heavy metal ions from the digestion solution. In this process, the selective release of

FPs does not require the dissolution of an actinide target and it is beneficial for various applications such as nuclear medicine, creation of nuclear forensic standards, environmental standards, and melt-glass surrogates. Since pore sizes of An-MOFs can be easily tuned for a specific set of molecules or ions, they act as an ideal means of selective release of FPs of interest. Presumably, three uranyl-dicarboxylate frameworks (U-2,4-PDC, U-2,5-PDC, U-2,6-PDC) and one uranyl-tetracarboyxlate framework (U-PM) were not significantly altered during irradiation. They were contacted with 0.01 mol/L HNO_3 solution and remained undissolved. The solution is removed from these solid U-MOFs and both vials are counted on a BEGe detector. Compared to the traditional UO_2 nuclear target, these U-MOF targets were not as successful at allowing for the isolation of FPs, though the extraction percentage was above 50% in many cases, the range of FPs extracted was much smaller[327]. Nevertheless, MOF stabilities under neutron irradiation or in digestion solution need to be elaborated to find parameters determining the extraction efficiency of fission products.

5. Concluding remarks and future directions

While a variety of commercially available or lab-made actinide precursors contribute to the burgeoning preparation of An-MOFs, novel precursors finely controlling the release of actinide cations into solution should be sought. Dissociable actinide oxalates (e.g. $(NH_4)_4Th(C_2O_4)_4 \cdot 4H_2O$[142]), or organic complexes (e.g. UI_4(1,4-dioxane)$_2$[150]) are emerging precursors for An-MOFs. Besides, the electrochemical preparation of actinide precursors of pure valency should be systematically investigated together with methods featuring minimal chemical intervention (e.g. using ozone as oxidant[328]). As transuranium precursors become accessible to a few radiochemistry labs, adventurous isolation of TRU-MOFs can be anticipated in the next decades, wherein the mobile robotic chemist[329] might play a role either inside a glovebox or in a controlled radioactive area, thus reducing the difficulties associated with TRU-MOFs syntheses and handling.

As for the synthetic methodology of An-MOFs, the currently predominant modulator synthesis led to many successful cases of single-crystals that allow structure-property elucidation. PSM gradually proves to be a reliable strategy in preparing mixed-metal, mixed-linker multivariate An-MOFs that seem inaccessible by one-pot modulated synthesis. Moreover, two synthetic aspects of An-MOFs are waiting to be addressed (1) large-scale production of Th- and U-MOFs by microwave, ultrasonic, or mechanic methods, and subsequent packaging and (2) An-MOFs as precursors to fabricate actinide hydrides, carbides, nitrides, or phosphides for versatile applications. Despite its great relevance to real applications, the formation mechanism of An-MOFs, particularly by coordination modulation is underexplored. Innovative in-situ, time-resolved transmission electron microscopy[330] and X-ray diffraction[331], time-of-flight secondary ion mass spectrometry[332], and other advanced characterization

techniques[333] will not only open avenue to the mechanistic investigation of thermodynamic and/or kinetic nucleation and growth, but also unravel the multi-scale actinide speciation and bonding[334], and structure dynamics in porous An-MOFs[335].

Structural information of An-MOFs has revealed a considerable diversity of building blocks and their connectivities and ensuing porosities, but it is merely the first step towards understanding the versatility of An-MOFs. A milestone will be reached once that an unambiguous framework modularity-topology-porosity relationship is established and transferred to fine-tuning of intricate electronic, thermochemical, and photophysical properties of An-MOFs. The modular design and construction in An-MOFs discovery will lead to a vast library of well-ordered, dynamic structures and topologies meanwhile the topology-guided prediction of porosity and pore engineering is expected to lead to porosity-related applications from separation to sensing and catalysis. To optimize material performance for the emerging applications, one should contemplate both structural stability and lability when designing functional An-MOFs.

Th- and U-MOFs as selective adsorbents have become competitive in recent years and some even rank as top-performing adsorbents for radionuclide sorption and gas separation. The bigger picture is to develop a "waste to MOFs" technology to efficiently convert raw liquid radwaste to stable An-MOFs as hierarchical wasteform, which will alleviate the pressing demand from nuclear waste management. Despite a growing number of Th- and U-MOFs in heterogeneous catalysis, their rational design should be reinforced as they did not exhibit superior performances compared with their transitional metal counterparts. Meanwhile, the unrevealed potential of heterometallic Th- and U-MOFs should be brought to the forefront to solve challenging issues such as small molecules activation. U(VI)-MOFs have been gradually recognized as potent luminescent sensing materials, particularly for ionizing irradiation. To maximize utility of Th- and U-MOFs in detection-related applications, it is essential to uncover the explicit influences of the MOFs structure on single or multimodal quenching (or "turn-on") behavior as well as the fabrication of An-MOF-based devices. The next decade will witness a steady increase in the number of thorium or depleted uranium MOFs as the next generation of ionizing-responsive materials in complex scenarios. The paradigm of An-MOFs as nuclear target materials can be generalized to prepare a diversity of nuclear targets in a facile manner. Besides, An-MOFs can be considered as a category of promising nanomaterials for α-RPT. Some general conclusions with a personal view on trends of An-MOFs are briefly summarized as (i) implement automatic, controllable syntheses of An-MOFs, particularly of TRU-MOFs, and their derivatives, (ii) utilize advanced characterization techniques to reveal the formation mechanism of An-MOFs, particularly the evolution of the actinide clusters with implications for actinide hydrolysis chemistry in natural and engineered aqueous systems, (iii) construct An-MOFs to delineate the triadic modularity-topology-porosity relationship meanwhile building heterometallic An-MOFs with emphasis on interrogating their electronic structures and redox properties, and (iv) integrate stable An-MOFs with open

108

frameworks (e.g. covalent organic framework), macroporous polymers, and POM as simple composites or tailored architectures for ever-broadening applications. Through the advancement of synthetic methodology and specific mechanism, the overall efforts in An-MOFs will lead to unparalleled structures and properties but also real-world multifunctionality that addresses critical energy and health-related issues as well as environmental concerns in the near future.

Declaration of Competing Interest

The authors declare that they have no known competing interests.

Acknowledgments

References

[1]   T.E. Albrecht-Schmitt, Actinide Chemistry at the Extreme, Inorg. Chem. 58 (2019) 1721–1723. https://doi.org/10.1021/acs.inorgchem.8b03603.

[2]   B.W. Stein, A. Morgenstern, E.R. Batista, E.R. Birnbaum, S.E. Bone, S.K. Cary, M.G. Ferrier, K.D. John, J.L. Pacheco, S.A. Kozimor, V. Mocko, B.L. Scott, P. Yang, Advancing Chelation Chemistry for Actinium and Other +3 f-Elements, Am, Cm, and La, J. Am. Chem. Soc. 141 (2019) 19404–19414. https://doi.org/10.1021/jacs.9b10354.

[3]   G. Sgouros, L. Bodei, M.R. McDevitt, J.R. Nedrow, Radiopharmaceutical therapy in cancer: clinical advances and challenges, Nat. Rev. Drug Discov. 19 (2020) 589–608. https://doi.org/10.1038/s41573-020-0073-9.

[4]   T. Loiseau, I. Mihalcea, N. Henry, C. Volkringer, The crystal chemistry of uranium carboxylates, Coord. Chem. Rev. 266–267 (2014) 69–109. https://doi.org/10.1016/j.ccr.2013.08.038.

[5]   C.D. Tutson, A.E.V. Gorden, Thorium coordination: A comprehensive review based on coordination number, Coord. Chem. Rev. 333 (2017) 27–43. https://doi.org/10.1016/j.ccr.2016.11.006.

[6]   L. Öhrström, Let's Talk about MOFs—Topology and Terminology of Metal-Organic Frameworks and Why We Need Them, Crystals. 5 (2015) 154–162. https://doi.org/10.3390/cryst5010154.

[7]   D.M.P. Mingos, Lanthanide Metal-Organic Frameworks, Springer Berlin Heidelberg, Berlin, Heidelberg, 2015. https://doi.org/10.1007/978-3-662-45773-3.

[8]   S.K. Elsaidi, M.H. Mohamed, D. Banerjee, P.K. Thallapally, Flexibility in Metal–Organic Frameworks: A fundamental understanding, Coord. Chem.

Rev. 358 (2018) 125–152. https://doi.org/10.1016/j.ccr.2017.11.022.

[9] J. Winarta, B. Shan, S.M. Mcintyre, L. Ye, C. Wang, J. Liu, B. Mu, A Decade of UiO-66 Research: A Historic Review of Dynamic Structure, Synthesis Mechanisms, and Characterization Techniques of an Archetypal Metal–Organic Framework, Cryst. Growth Des. 20 (2020) 1347–1362. https://doi.org/10.1021/acs.cgd.9b00955.

[10] S. Yuan, J.-S. Qin, C.T. Lollar, H.-C. Zhou, Stable Metal–Organic Frameworks with Group 4 Metals: Current Status and Trends, ACS Cent. Sci. 4 (2018) 440–450. https://doi.org/10.1021/acscentsci.8b00073.

[11] J. Bitzer, W. Kleist, Synthetic Strategies and Structural Arrangements of Isoreticular Mixed-Component Metal–Organic Frameworks, Chem. - A Eur. J. 25 (2019) 1866–1882. https://doi.org/10.1002/chem.201803887.

[12] S.L. Griffin, N.R. Champness, A periodic table of metal-organic frameworks, Coord. Chem. Rev. 414 (2020) 213295. https://doi.org/10.1016/j.ccr.2020.213295.

[13] X. Zhang, B. Wang, A. Alsalme, S. Xiang, Z. Zhang, B. Chen, Design and applications of water-stable metal-organic frameworks: status and challenges, Coord. Chem. Rev. 423 (2020) 213507. https://doi.org/10.1016/j.ccr.2020.213507.

[14] H.C. Zur Loye, T. Besmann, J. Amoroso, K. Brinkman, A. Grandjean, C.H. Henager, S. Hu, S.T. Misture, S.R. Phillpot, N.B. Shustova, H. Wang, R.J. Koch, G. Morrison, E. Dolgopolova, Hierarchical Materials as Tailored Nuclear Waste Forms: A Perspective, Chem. Mater. 30 (2018) 4475–4488. https://doi.org/10.1021/acs.chemmater.8b00766.

[15] S.A. McMaster, R. Ram, N. Faris, M.I. Pownceby, Radionuclide disposal using the pyrochlore supergroup of minerals as a host matrix—A review, J. Hazard. Mater. 360 (2018) 257–269. https://doi.org/10.1016/j.jhazmat.2018.08.037.

[16] V. Proust, R. Jeannin, F.D. White, T.E. Albrecht-Schmitt, Tailored Perovskite Waste Forms for Plutonium Trapping, Inorg. Chem. 58 (2019) 3026–3032. https://doi.org/10.1021/acs.inorgchem.8b02832.

[17] K.A. Pace, V. V. Klepov, T.K. Deason, M.D. Smith, G.B. Ayer, D.P. Diprete, J.W. Amoroso, H. Loye, Expansion of the Na3MIII(Ln/An)6F30 Series: Incorporation of Plutonium into a Highly Robust and Stable Framework, Chem. – A Eur. J. 26 (2020) 12941–12944. https://doi.org/10.1002/chem.202002774.

[18] K. Wang, B. Wang, H. Li, X. Tuo, K. Xiong, M. Yan, J. Courtois, Janus multi-responsive superparamagnetic nanoparticles functionalized with two on-demand and independently cleavable ligands for Actinide separation, J. Colloid Interface Sci. 538 (2019) 546–558. https://doi.org/10.1016/j.jcis.2018.12.026.

[19] W. Yantasee, G.E. Fryxell, K. Pattamakomsan, T. Sangvanich, R.J. Wiacek, B. Busche, R.S. Addleman, C. Timchalk, W. Ngamcherdtrakul, N. Siriwon, Selective capture of radionuclides (U, Pu, Th, Am and Co) using functional

nanoporous sorbents, J. Hazard. Mater. 366 (2019) 677–683.
https://doi.org/10.1016/j.jhazmat.2018.12.043.

[20]   C.L. Cahill, L.A. Borkowski, U(VI)-containing metal-organic frameworks and coordination polymers, in: Struct. Chem. Inorg. Actin. Compd., Elsevier, 2007: pp. 409–442. https://doi.org/10.1016/B978-044452111-8/50012-0.

[21]   C.L. Cahill, D.T. De Lill, M. Frisch, Homo- and heterometallic coordination polymers from the f elements, CrystEngComm. 9 (2007) 15–26. https://doi.org/10.1039/b615696g.

[22]   K. Wang, J. Chen, Extended Structures and Physicochemical, Acc. Chem. Res. 44 (2011) 531–540.

[23]   W. Yang, T.G. Parker, Z.-M. Sun, Structural chemistry of uranium phosphonates, Coord. Chem. Rev. 303 (2015) 86–109. https://doi.org/10.1016/j.ccr.2015.05.010.

[24]   P. Thuéry, J. Harrowfield, Recent advances in structural studies of heterometallic uranyl-containing coordination polymers and polynuclear closed species, Dalt. Trans. 46 (2017) 13660–13667. https://doi.org/10.1039/c7dt03105j.

[25]   K.P. Carter, R.G. Surbella, M. Kalaj, C.L. Cahill, Restricted Speciation and Supramolecular Assembly in the 5f Block., Chemistry. 24 (2018) 12747–12756. https://doi.org/10.1002/chem.201801044.

[26]   E.A. Dolgopolova, A.M. Rice, N.B. Shustova, Actinide-based MOFs: a middle ground in solution and solid-state structural motifs, Chem. Commun. 54 (2018) 6472–6483. https://doi.org/10.1039/C7CC09780H.

[27]   O.K. Farha, X. Zhang, J.G. Knapp, S.L. Hanna, Z. Chen, P. Li, Coordination Chemistry in the Structural and Functional Exploration of Actinide-Based Metal-Organic Frameworks, Bull. Japan Soc. Coord. Chem. 75 (2020) 3–12. https://doi.org/10.4019/bjscc.75.3.

[28]   L. Feng, J. Pang, P. She, J.-L. Li, J.-S. Qin, D.-Y. Du, H.-C. Zhou, Metal-Organic Frameworks Based on Group 3 and 4 Metals, Adv. Mater. 66 (2020) 2004414. https://doi.org/10.1002/adma.202004414.

[29]   K. Jin, B. Lee, J. Park, Metal-organic frameworks as a versatile platform for radionuclide management, Coord. Chem. Rev. 427 (2021) 213473. https://doi.org/10.1016/j.ccr.2020.213473.

[30]   S. Pandey, B. Demaske, O.A. Ejegbavwo, A.A. Berseneva, W. Setyawan, N. Shustova, S.R. Phillpot, Electronic structures and magnetism of Zr-, Th-, and U-based metal-organic frameworks (MOFs) by density functional theory, Comput. Mater. Sci. 184 (2020) 109903. https://doi.org/10.1016/j.commatsci.2020.109903.

[31]   P.O. Adelani, T.E. Albrecht-Schmitt, Thorium and uranium diphosphonates: Syntheses, structures, and spectroscopic properties, J. Solid State Chem. 192 (2012) 377–384. https://doi.org/10.1016/j.jssc.2012.04.017.

[32]   T. Cantat, B.L. Scott, J.L. Kiplinger, Convenient access to the anhydrous thorium tetrachloride complexes ThCl4(DME)2, ThCl4(1,4-dioxane)2 and

ThCl4(THF)3.5 using commercially available and inexpensive starting materials, Chem. Commun. 46 (2010) 919. https://doi.org/10.1039/b923558b.

[33] J. Wang, Z. Wei, F. Guo, C. Li, P. Zhu, W. Zhu, Homochiral 3D coordination polymer with unprecedented three-directional helical topology from achiral precursor: synthesis, crystal structure, and luminescence properties of uranyl succinate metal–organic framework, Dalt. Trans. 44 (2015) 13809–13813. https://doi.org/10.1039/C5DT02111A.

[34] C. Liu, W. Yang, N. Qu, L.J. Li, Q.J. Pan, Z.M. Sun, Construction of Uranyl Organic Hybrids by Phosphonate and in Situ Generated Carboxyphosphonate Ligands, Inorg. Chem. 56 (2017) 1669–1678. https://doi.org/10.1021/acs.inorgchem.6b02765.

[35] F.Z. Li, L. Mei, K.Q. Hu, S.W. An, S. Wu, N. Liu, Z.F. Chai, W.Q. Shi, Uranyl Compounds Involving a Weakly Bonded Pseudorotaxane Linker: Combined Effect of pH and Competing Ligands on Uranyl Coordination and Speciation, Inorg. Chem. 58 (2019) 3271–3282. https://doi.org/10.1021/acs.inorgchem.8b03353.

[36] M.K. Mishra, Y.P. Patil, S.P. Kelley, R.D. Rogers, A Uranyl Metal Organic Framework Arising from the Coordination of a Partially Hydrolyzed Tetrauranyl Node with the Tautomerically Diverse 1,4-(Diamidoximyl)benzene Ligand, Cryst. Growth Des. 19 (2019) 5466–5470. https://doi.org/10.1021/acs.cgd.9b00544.

[37] C. Volkringer, I. Mihalcea, J.F. Vigier, A. Beaurain, M. Visseaux, T. Loiseau, Metal-organic-framework-type 1D-channel open network of a tetravalent uranium trimesate, Inorg. Chem. 50 (2011) 11865–11867. https://doi.org/10.1021/ic2021963.

[38] V.E. Refn, M. Kubus, S. Mossin, R.W. Larsen, K.S. Pedersen, A Redox-Innocent Uranium(IV)-Quinoid Metal-Organic Framework, ACS Omega. 5 (2020) 3462–3466. https://doi.org/10.1021/acsomega.9b03727.

[39] R.A. Zehnder, J.M. Boncella, J.N. Cross, S.A. Kozimor, M.J. Monreal, H.S. La Pierre, B.L. Scott, A.M. Tondreau, M. Zeller, Network dimensionality of selected uranyl(VI) coordination polymers and octopus-like uranium(IV) clusters, Cryst. Growth Des. 17 (2017) 5568–5582. https://doi.org/10.1021/acs.cgd.7b01165.

[40] M.J. Monreal, R.K. Thomson, T. Cantat, N.E. Travia, B.L. Scott, J.L. Kiplinger, UI4(1,4-dioxane)2, [UCl4(1,4-dioxane)]2, and UI3(1,4-dioxane)1.5: Stable and Versatile Starting Materials for Low- and High-Valent Uranium Chemistry, Organometallics. 30 (2011) 2031–2038. https://doi.org/10.1021/om200093q.

[41] S.S. Rudel, F. Kraus, Facile syntheses of pure uranium halides: UCl4 , UBr4 and UI4, Dalt. Trans. 46 (2017) 5835–5842. https://doi.org/10.1039/C7DT00726D.

[42] N.A. Budantseva, G.B. Andreev, A.M. Fedoseev, M.Y. Antipin, J.C. Krupa, Interaction of neptunium(V) with picolinic, nicotinic and isonicotinic acids,

Radiochim. Acta. 94 (2006) 69–74.
https://doi.org/10.1524/ract.2006.94.2.69.

[43] L.B. Serezhkina, M.S. Grigoriev, A.M. Fedoseev, S.A. Novikov, V.N. Serezhkin, Synthesis and Structure of New Glutarate-Containing U(VI), Np(V), and Pu(VI) Compounds, Crystallogr. Reports. 65 (2020) 63–71. https://doi.org/10.1134/S1063774520010228.

[44] T.H. Bray, A.G.D. Nelson, B.J. Geng, R.G. Haire, T.E. Albrecht-Schmitt, In situ hydrothermal reduction of neptunium(VI) as a route to neptunium(IV) phosphonates, Inorg. Chem. 46 (2007) 10959–10961. https://doi.org/10.1021/ic702136h.

[45] A.G.D. Nelson, T.H. Bray, W. Zhan, R.G. Haire, T.S. Sayler, T.E. Albrecht-Schmitt, Further examples of the failure of surrogates to properly model the structural and hydrothermal chemistry of transuranium elements: Insights provided by uranium and neptunium diphosphonates, Inorg. Chem. 47 (2008) 4945–4951. https://doi.org/10.1021/ic800255h.

[46] N.P. Martin, J. März, C. Volkringer, N. Henry, C. Hennig, A. Ikeda-Ohno, T. Loiseau, Synthesis of Coordination Polymers of Tetravalent Actinides (Uranium and Neptunium) with a Phthalate or Mellitate Ligand in an Aqueous Medium, Inorg. Chem. 56 (2017) 2902–2913. https://doi.org/10.1021/acs.inorgchem.6b02962.

[47] A.G.D. Nelson, T.H. Bray, F.A. Stanley, T.E. Albrecht-Schmitt, Periodic trends in actinide phosphonates: Divergence and convergence between thorium, uranium, neptunium, and plutonium systems, Inorg. Chem. 48 (2009) 4530–4535. https://doi.org/10.1021/ic900484w.

[48] J.M. Sperling, A.N. Gaiser, C.J. Windorff, B.E. Klamm, M.A. Whitefoot, A.T. Chemey, B.N. Long, J.G. Campbell, T.E. Albrecht-Schmitt, Structural and Spectroscopic Investigation of Two Plutonium Mellitates, Inorg. Chem. 59 (2020) 3085–3090. https://doi.org/10.1021/acs.inorgchem.9b03432.

[49] S.K. Cary, S.S. Galley, M.L. Marsh, D.L. Hobart, R.E. Baumbach, J.N. Cross, J.T. Stritzinger, M.J. Polinski, L. Maron, T.E. Albrecht-Schmitt, Incipient class II mixed valency in a plutonium solid-state compound, Nat. Chem. 9 (2017) 856–861. https://doi.org/10.1038/nchem.2777.

[50] A.M. Hastings, D. Ray, W. Jeong, L. Gagliardi, O.K. Farha, A.E. Hixon, Advancement of Actinide Metal-Organic Framework Chemistry via Synthesis of Pu-UiO-66, J. Am. Chem. Soc. 142 (2020) 9363–9371. https://doi.org/10.1021/jacs.0c01895.

[51] N. Brenner, J.M. Sperling, T.N. Poe, C. Celis-Barros, K. Brittain, E.M. Villa, T.E. Albrecht-Schmitt, M.J. Polinski, Trivalent f-Element Squarates, Squarate-Oxalates, and Cationic Materials, and the Determination of the Nine-Coordinate Ionic Radius of Cf(III), Inorg. Chem. 59 (2020) 9384–9395. https://doi.org/10.1021/acs.inorgchem.0c01254.

[52] J.A. Ridenour, R.G. Surbella, A. V. Gelis, D. Koury, F. Poineau, K.R. Czerwinski, C.L. Cahill, An Americium-Containing Metal–Organic Framework: A Platform for Studying Transplutonium Elements, Angew.

Chemie Int. Ed. 58 (2019) 16508–16511.
https://doi.org/10.1002/anie.201909988.

[53]   S.S. Galley, J.M. Sperling, C.J. Windorff, M. Zeller, T.E. Albrecht-Schmitt, S.C. Bart, Conversion of Americia to Anhydrous Trivalent Americium Halides, Organometallics. 38 (2019) 606–609. https://doi.org/10.1021/acs.organomet.8b00840.

[54]   J.M. Sperling, E.J. Warzecha, C. Celis-Barros, D.C. Sergentu, X. Wang, B.E. Klamm, C.J. Windorff, A.N. Gaiser, F.D. White, D.A. Beery, A.T. Chemey, M.A. Whitefoot, B.N. Long, K. Hanson, P. Kögerler, M. Speldrich, E. Zurek, J. Autschbach, T.E. Albrecht-Schönzart, Compression of curium pyrrolidine-dithiocarbamate enhances covalency, Nature. 583 (2020) 396–399. https://doi.org/10.1038/s41586-020-2479-2.

[55]   C.J. Dares, A.M. Lapides, B.J. Mincher, T.J. Meyer, Electrochemical oxidation of 243Am(III) in nitric acid by a terpyridyl-derivatized electrode, Science. 350 (2015) 652–655. https://doi.org/10.1126/science.aac9217.

[56]   M.J. Lopez, M. V. Sheridan, J.R. McLachlan, T.S. Grimes, C.J. Dares, Electrochemical oxidation of trivalent americium using a dipyrazinylpyridine modified ITO electrode, Chem. Commun. 55 (2019) 4035–4038. https://doi.org/10.1039/c9cc00837c.

[57]   J.L. Doyle, K. Kuhn, B. Byerly, L. Colletti, J. Fulwyler, K. Garduno, R. Keller, E. Lujan, A. Martinez, S. Myers, D. Porterfield, K. Spencer, F. Stanley, L. Townsend, M. Thomas, L. Walker, N. Xu, L. Tandon, Nuclear forensic analysis of a non-traditional actinide sample, Talanta. 159 (2016) 200–207. https://doi.org/10.1016/j.talanta.2016.06.028.

[58]   P. Li, X. Wang, K.I. Otake, J. Lyu, S.L. Hanna, T. Islamoglu, O.K. Farha, Synthetic Control of Thorium Polyoxo-Clusters in Metal-Organic Frameworks toward New Thorium-Based Materials, ACS Appl. Nano Mater. 2 (2019) 2260–2265. https://doi.org/10.1021/acsanm.9b00188.

[59]   C. Falaise, A. Assen, I. Mihalcea, C. Volkringer, A. Mesbah, N. Dacheux, T. Loiseau, Coordination polymers of uranium (IV) terephthalates, Dalt. Trans. 44 (2015) 2639–2649. https://doi.org/10.1039/C4DT02343A.

[60]   N.A. Vanagas, R.F. Higgins, J.N. Wacker, D.R.C. Asuigui, E. Warzecha, S.A. Kozimor, S.L. Stoll, E.J. Schelter, J.A. Bertke, K.E. Knope, Mononuclear to Polynuclear UIV Structural Units: Effects of Reaction Conditions on U-Furoate Phase Formation, Chem. - A Eur. J. 26 (2020) 5872–5886. https://doi.org/10.1002/chem.201905759.

[61]   C. Falaise, J.-S. Charles, C. Volkringer, T. Loiseau, Thorium Terephthalates Coordination Polymers Synthesized in Solvothermal DMF/H2O System, Inorg. Chem. 54 (2015) 2235–2242. https://doi.org/10.1021/ic502725y.

[62]   N.P. Martin, C. Volkringer, C. Falaise, N. Henry, T. Loiseau, Synthesis and Crystal Structure Characterization of Thorium Trimesate Coordination Polymers, Cryst. Growth Des. 16 (2016) 1667–1678. https://doi.org/10.1021/acs.cgd.5b01746.

[63]   A. V. Murray, N.A. Vanagas, J.N. Wacker, J.A. Bertke, K.E. Knope, From

Isolated Molecular Complexes to Extended Networks: Synthesis and Characterization of Thorium Furanmono- and Dicarboxylates, Eur. J. Inorg. Chem. (2020). https://doi.org/10.1002/ejic.202000467.

[64] E.A. Dolgopolova, O.A. Ejegbavwo, C.R. Martin, M.D. Smith, W. Setyawan, S.G. Karakalos, C.H. Henager, H.C. Zur Loye, N.B. Shustova, Multifaceted Modularity: A Key for Stepwise Building of Hierarchical Complexity in Actinide Metal-Organic Frameworks, J. Am. Chem. Soc. 139 (2017) 16852–16861. https://doi.org/10.1021/jacs.7b09496.

[65] O.A. Ejegbavwo, C.R. Martin, O.A. Olorunfemi, G.A. Leith, R.T. Ly, A.M. Rice, E.A. Dolgopolova, M.D. Smith, S.G. Karakalos, N. Birkner, B.A. Powell, S. Pandey, R.J. Koch, S.T. Misture, H.C. Zur Loye, S.R. Phillpot, K.S. Brinkman, N.B. Shustova, Thermodynamics and Electronic Properties of Heterometallic Multinuclear Actinide-Containing Metal-Organic Frameworks with "structural Memory," J. Am. Chem. Soc. 141 (2019) 11628–11640. https://doi.org/10.1021/jacs.9b04737.

[66] G. Sargazi, D. Afzali, A. Mostafavi, A novel synthesis of a new thorium (IV) metal organic framework nanostructure with well controllable procedure through ultrasound assisted reverse micelle method, Ultrason. Sonochem. 41 (2018) 234–251. https://doi.org/10.1016/j.ultsonch.2017.09.046.

[67] G. Sargazi, D. Afzali, A. Mostafavi, A novel microwave assisted reverse micelle fabrication route for Th (IV)-MOFs as highly efficient adsorbent nanostructures with controllable structural properties to CO and CH4 adsorption: Design, and a systematic study, Appl. Organomet. Chem. 33 (2019) 1–12. https://doi.org/10.1002/aoc.4816.

[68] Y. Bai, Y. Dou, L.-H. Xie, W. Rutledge, J.-R. Li, H.-C. Zhou, Zr-based metal–organic frameworks: design, synthesis, structure, and applications, Chem. Soc. Rev. 45 (2016) 2327–2367. https://doi.org/10.1039/C5CS00837A.

[69] R.S. Forgan, Modulated self-assembly of metal–organic frameworks, Chem. Sci. 11 (2020) 4546–4562. https://doi.org/10.1039/D0SC01356K.

[70] T. Islamoglu, K. Otake, P. Li, C.T. Buru, A.W. Peters, I. Akpinar, S.J. Garibay, O.K. Farha, Revisiting the structural homogeneity of NU-1000, a Zr-based metal–organic framework, CrystEngComm. 20 (2018) 5913–5918. https://doi.org/10.1039/C8CE00455B.

[71] Y. Chen, X. Zhang, M.R. Mian, F.A. Son, K. Zhang, R. Cao, Z. Chen, S.-J. Lee, K.B. Idrees, T.A. Goetjen, J. Lyu, P. Li, Q. Xia, Z. Li, J.T. Hupp, T. Islamoglu, A. Napolitano, G.W. Peterson, O.K. Farha, Structural Diversity of Zirconium Metal–Organic Frameworks and Effect on Adsorption of Toxic Chemicals, J. Am. Chem. Soc. 142 (2020) 21428–21438. https://doi.org/10.1021/jacs.0c10400.

[72] J.Y. Kim, A.J. Norquist, D. O'Hare, [(Th2F5)(NC7H5O4)2(H2O)][NO3]: An Actinide-Organic Open Framework, J. Am. Chem. Soc. 125 (2003) 12688–12689. https://doi.org/10.1021/ja036832p.

[73] K.M. Ok, J. Sung, G. Hu, R.M.J. Jacobs, D. O'Hare, TOF-2: A large 1D channel thorium organic framework, J. Am. Chem. Soc. 130 (2008) 3762–3763.

https://doi.org/10.1021/ja800395q.

[74] K.M. Ok, D. O'Hare, Synthesis, structure, and characterization of a new thorium–organic framework material, Th3F5[(C10H14)(CH2CO2)2]3(NO3), Dalt. Trans. 3 (2008) 5560. https://doi.org/10.1039/b812629a.

[75] S.F. Tang, X. Hou, D. Liu, X. Zhao, Fabrication of New Uranyl Phosphonates by Varying Quaternary Ammonium Cation: Synthesis, Structure, Luminescent Properties, and Single-Crystal to Single-Crystal Transformation, Inorg. Chem. 56 (2017) 14524–14532. https://doi.org/10.1021/acs.inorgchem.7b02231.

[76] Y. Wang, X. Wang, Y. Huang, F. Zhou, C. Qi, T. Zheng, J. Li, Z. Chai, S. Wang, Reticular Chemistry of Uranyl Phosphonates: Sterically Hindered Phosphonate Ligand Method is Significant for Constructing Zero-Dimensional Secondary Building Units, Chem. – A Eur. J. 25 (2019) 12567–12575. https://doi.org/10.1002/chem.201902310.

[77] Z.-J. Li, Y. Ju, B. Yu, X. Wu, H. Lu, Y. Li, J. Zhou, X. Guo, Z.-H. Zhang, J. Lin, J.-Q. Wang, S. Wang, Modulated synthesis and isoreticular expansion of Th-MOFs with record high pore volume and surface area for iodine adsorption, Chem. Commun. 56 (2020) 6715–6718. https://doi.org/10.1039/D0CC02841J.

[78] Z. Xu, X. Xiong, J. Xiong, R. Krishna, L. Li, Y. Fan, F. Luo, B. Chen, A robust Th-azole framework for highly efficient purification of C2H4 from a C2H4/C2H2/C2H6 mixture, Nat. Commun. 11 (2020) 3163. https://doi.org/10.1038/s41467-020-16960-9.

[79] S.E. Gilson, M. Fairley, P. Julien, A.G. Oliver, S.L. Hanna, G. Arntz, O.K. Farha, J.A. LaVerne, P.C. Burns, Unprecedented Radiation Resistant Thorium–Binaphthol Metal–Organic Framework, J. Am. Chem. Soc. 142 (2020) 13299–13304. https://doi.org/10.1021/jacs.0c05272.

[80] R.G. Surbella, K. Carter, T. Lohrey, D. Reilly, M. Kalaj, B. McNamara, J. Schwantes, R. Abergel, Rational design of a uranyl metal-organic framework for the capture and colorimetric detection of organic dyes, Chem. – A Eur. J. (2020) chem.201905766. https://doi.org/10.1002/chem.201905766.

[81] W. Liu, J. Xie, L. Zhang, M.A. Silver, S. Wang, A hydrolytically stable uranyl organic framework for highly sensitive and selective detection of Fe 3+ in aqueous media, Dalt. Trans. 47 (2018) 649–653. https://doi.org/10.1039/C7DT04365A.

[82] R. Zhao, L. Mei, K. Hu, M. Tian, Z. Chai, W. Shi, Bimetallic Uranyl Organic Frameworks Supported by Transition-Metal-Ion-Based Metalloligand Motifs: Synthesis, Structure Diversity, and Luminescence Properties, Inorg. Chem. 57 (2018) 6084–6094. https://doi.org/10.1021/acs.inorgchem.8b00634.

[83] L.W. Zeng, K.Q. Hu, L. Mei, F.Z. Li, Z.W. Huang, S.W. An, Z.F. Chai, W.Q. Shi, Structural Diversity of Bipyridinium-Based Uranyl Coordination Polymers:

Synthesis, Characterization, and Ion-Exchange Application, Inorg. Chem. 58 (2019) 14075–14084. https://doi.org/10.1021/acs.inorgchem.9b02106.

[84] L. Mei, C.Z. Wang, L. Wang, Y.L. Zhao, Z.F. Chai, W.Q. Shi, Halogen bonded three-dimensional uranyl-organic compounds with unprecedented halogen-halogen interactions and structure diversity upon variation of halogen substitution, Cryst. Growth Des. 15 (2015) 1395–1406. https://doi.org/10.1021/cg501783d.

[85] F. Chen, C. Wang, Z. Li, J. Lan, Y. Ji, Z. Chai, New Three-Fold Interpenetrated Uranyl Organic Framework Constructed by Terephthalic Acid and Imidazole Derivative, Inorg. Chem. 54 (2015) 3829–3834. https://doi.org/10.1021/acs.inorgchem.5b00013.

[86] N.P. Martin, C. Falaise, C. Volkringer, N. Henry, P. Farger, C. Falk, E. Delahaye, P. Rabu, T. Loiseau, Hydrothermal Crystallization of Uranyl Coordination Polymers Involving an Imidazolium Dicarboxylate Ligand: Effect of pH on the Nuclearity of Uranyl-Centered Subunits, Inorg. Chem. 55 (2016) 8697–8705. https://doi.org/10.1021/acs.inorgchem.6b01232.

[87] S.G. Thangavelu, C.L. Cahill, A Family of Uranyl Coordination Polymers Containing O-Donor Dicarboxylates and Trispyridyltriazine Guests, Cryst. Growth Des. 16 (2016) 42–50. https://doi.org/10.1021/acs.cgd.5b00778.

[88] F.Z. Li, L. Mei, S.W. An, K.Q. Hu, Z.F. Chai, N. Liu, W.Q. Shi, Kinked-Helix Actinide Polyrotaxanes from Weakly Bound Pseudorotaxane Linkers with Variable Conformations, Inorg. Chem. 59 (2020) 4058–4067. https://doi.org/10.1021/acs.inorgchem.0c00037.

[89] Z.-J. Li, S. Guo, H. Lu, Y. Xu, Z. Yue, L. Weng, X. Guo, J. Lin, J.-Q. Wang, Unexpected structural complexity of thorium coordination polymers and polyoxo cluster built from simple formate ligands, Inorg. Chem. Front. 7 (2020) 260–269. https://doi.org/10.1039/C9QI01263J.

[90] Y.-F. Zhang, Q. Wang, D.-X. Xue, J. Bai, Single-Crystal Synthesis and Diverse Topologies of Hexanuclear CeIV -Based Metal–Organic Frameworks, Inorg. Chem. 59 (2020) 11233–11237. https://doi.org/10.1021/acs.inorgchem.0c01646.

[91] K.Q. Hu, Z.W. Huang, Z.H. Zhang, L. Mei, B.B. Qian, J.P. Yu, Z.F. Chai, W.Q. Shi, Actinide-Based Porphyrinic MOF as a Dehydrogenation Catalyst, Chem. - A Eur. J. 24 (2018) 16766–16769. https://doi.org/10.1002/chem.201804284.

[92] Z.J. Li, Z. Yue, Y. Ju, X. Wu, Y. Ren, S. Wang, Y. Li, Z.H. Zhang, X. Guo, J. Lin, J.Q. Wang, Ultrastable Thorium Metal-Organic Frameworks for Efficient Iodine Adsorption, Inorg. Chem. 59 (2020) 4435–4442. https://doi.org/10.1021/acs.inorgchem.9b03602.

[93] W. Xu, Z.-X. Si, M. Xie, L.-X. Zhou, Y.-Q. Zheng, Experimental and Theoretical Approaches to Three Uranyl Coordination Polymers Constructed by Phthalic Acid and N, N'-Donor Bridging Ligands: Crystal Structures, Luminescence, and Photocatalytic Degradation of Tetracycline

Hydrochloride, Cryst. Growth Des. 17 (2017) 2147–2157. https://doi.org/10.1021/acs.cgd.7b00097.

[94] D.K. Unruh, K. Gojdas, A. Libo, T.Z. Forbes, Development of metal-organic nanotubes exhibiting low-temperature, reversible exchange of confined "ice channels," J. Am. Chem. Soc. 135 (2013) 7398–7401. https://doi.org/10.1021/ja400303f.

[95] P. Thuéry, J. Harrowfield, Uranyl-organic frameworks with polycarboxylates: Unusual effects of a coordinating solvent, Cryst. Growth Des. 14 (2014) 1314–1323. https://doi.org/10.1021/cg4018163.

[96] L.-Z. Zhu, C.-Z. Wang, L. Mei, L. Wang, Y.-H. Liu, Z.-T. Zhu, Y.-L. Zhao, Z.-F. Chai, W.-Q. Shi, Two novel uranyl complexes of a semi-rigid aromatic tetracarboxylic acid supported by an organic base as an auxiliary ligand or a templating agent: an experimental and theoretical exploration, CrystEngComm. 17 (2015) 3031–3040. https://doi.org/10.1039/C5CE00223K.

[97] G.E. Gomez, D. Onna, R.F. D'vries, B.C. Barja, J. Ellena, G.E. Narda, G.J.A.A. Soler-Illia, Chain-like uranyl-coordination polymer as a bright green light emitter for sensing and sunlight driven photocatalysis, J. Mater. Chem. C. 8 (2020) 11102–11109. https://doi.org/10.1039/D0TC02623A.

[98] K.P. Carter, J.A. Ridenour, M. Kalaj, C.L. Cahill, A Thorium Metal-Organic Framework with Outstanding Thermal and Chemical Stability, Chem. - A Eur. J. 25 (2019) 7114–7118. https://doi.org/10.1002/chem.201901610.

[99] P. Thuéry, J. Harrowfield, Structural Variations in the Uranyl/4,4′-Biphenyldicarboxylate System. Rare Examples of 2D → 3D Polycatenated Uranyl–Organic Networks, Inorg. Chem. 54 (2015) 8093–8102. https://doi.org/10.1021/acs.inorgchem.5b01323.

[100] S.W. An, L. Mei, K.Q. Hu, F.Z. Li, C.Q. Xia, Z.F. Chai, W.Q. Shi, Bipyridine-Directed Syntheses of Uranyl Compounds Containing Semirigid Dicarboxylate Linkers: Diversity and Consistency in Uranyl Speciation, Inorg. Chem. 58 (2019) 6934–6945. https://doi.org/10.1021/acs.inorgchem.9b00452.

[101] P. Thuéry, J. Harrowfield, Uranyl Ion Complexes with Chiral Malic and Citramalic, and Prochiral Citric and Tricarballylic Acids: Influence of Coligands and Additional Metal Cations, Eur. J. Inorg. Chem. 2018 (2018) 1016–1027. https://doi.org/10.1002/ejic.201701406.

[102] Y. Dai, H.M. Chai, R.X. Zhang, J.A. Min, Z. Wang, M. Zhang, Y. Zhang, J. Feng, C. Zhang, J. Wang, A series of uranium-organic frameworks: Crucial role of the protonation ability of auxiliary ligands, Inorg. Chem. Commun. 111 (2020) 107628. https://doi.org/10.1016/j.inoche.2019.107628.

[103] W. Xu, Y.N. Ren, M. Xie, L.X. Zhou, Y.Q. Zheng, Six uranyl-organic frameworks with naphthalene-dicarboxylic acid and bipyridyl-based spacers: Syntheses, structures, and properties, Dalt. Trans. 47 (2018) 4236–4250. https://doi.org/10.1039/c7dt04909a.

[104] G.E. Gomez, J.A. Ridenour, N.M. Byrne, A.P. Shevchenko, C.L. Cahill, Novel

Heterometallic Uranyl-Transition Metal Materials: Structure, Topology, and Solid State Photoluminescence Properties, Inorg. Chem. 58 (2019) 7243–7254. https://doi.org/10.1021/acs.inorgchem.9b00255.

[105] P. Ramaswamy, R. Prabhu, S. Natarajan, Synthesis, Structure, and Solid-State Transformation Studies of Phosphonoacetate Based Hybrid Compounds of Uranium and Thorium, Inorg. Chem. 49 (2010) 7927–7934. https://doi.org/10.1021/ic101043z.

[106] T. Zheng, Y. Gao, D. Gui, L. Chen, D. Sheng, J. Diwu, Z. Chai, T.E. Albrecht-Schmitt, S. Wang, Atypical temperature-dependence of symmetry transformation observed in a uranyl phosphonate, Dalt. Trans. 45 (2016) 9031–9035. https://doi.org/10.1039/C6DT01011C.

[107] K.Q. Hu, Q.Y. Wu, L. Mei, X.L. Zhang, L. Ma, G. Song, D.Y. Chen, Y.T. Wang, Z.F. Chai, W.Q. Shi, Novel Viologen Derivative Based Uranyl Coordination Polymers Featuring Photochromic Behaviors, Chem. - A Eur. J. 23 (2017) 18074–18083. https://doi.org/10.1002/chem.201704478.

[108] T. Zheng, Q.Y. Wu, Y. Gao, D. Gui, S. Qiu, L. Chen, D. Sheng, J. Diwu, W.Q. Shi, Z. Chai, T.E. Albrecht-Schmitt, S. Wang, Probing the influence of phosphonate bonding modes to uranium(VI) on structural topology and stability: A complementary experimental and computational investigation, Inorg. Chem. 54 (2015) 3864–3874. https://doi.org/10.1021/acs.inorgchem.5b00024.

[109] J. Xie, Y. Wang, W. Liu, X. Yin, L. Chen, Y. Zou, J. Diwu, Z. Chai, T.E. Albrecht-Schmitt, G. Liu, S. Wang, Highly Sensitive Detection of Ionizing Radiations by a Photoluminescent Uranyl Organic Framework, Angew. Chemie - Int. Ed. 56 (2017) 7500–7504. https://doi.org/10.1002/anie.201700919.

[110] C. Liu, F.Y. Chen, H.R. Tian, J. Ai, W. Yang, Q.J. Pan, Z.M. Sun, Interpenetrated Uranyl-Organic Frameworks with bor and pts Topology: Structure, Spectroscopy, and Computation, Inorg. Chem. 56 (2017) 14147–14156. https://doi.org/10.1021/acs.inorgchem.7b02274.

[111] L. Chen, J. DiWu, D. Gui, Y. Wang, Z. Weng, Z. Chai, T.E. Albrecht-Schmitt, S. Wang, Systematic Investigation of the in Situ Reduction Process from U(VI) to U(IV) in a Phosphonate System under Mild Solvothermal Conditions, Inorg. Chem. 56 (2017) 6952–6964. https://doi.org/10.1021/acs.inorgchem.7b00480.

[112] Y. Wang, D. Zeng, F. Zhou, D. Zhang, J. Li, T. Zheng, A supramolecular uranyl phosphonate [BTEA]2[(UO2)2(1,3-pbpH2)2F2]: Synthesis, structure, and spectroscopic characterization, J. Mol. Struct. 1173 (2018) 183–187. https://doi.org/10.1016/j.molstruc.2018.06.107.

[113] P. Thuéry, Y. Atoini, J. Harrowfield, Closed Uranyl-Dicarboxylate Oligomers: A Tetranuclear Metallatricycle with Uranyl Bridgeheads and 1,3-Adamantanediacetate Linkers, Inorg. Chem. 57 (2018) 7932–7939. https://doi.org/10.1021/acs.inorgchem.8b01047.

[114] P. Thuéry, Y. Atoini, J. Harrowfield, Functionalized Aromatic Dicarboxylate Ligands in Uranyl-Organic Assemblies: The Cases of Carboxycinnamate

and 1,2-/1,3-Phenylenedioxydiacetate, Inorg. Chem. 59 (2020) 2923–2936. https://doi.org/10.1021/acs.inorgchem.9b03273.

[115] X.L. Zhang, K.Q. Hu, L. Mei, Y.B. Zhao, Y.T. Wang, Z.F. Chai, W.Q. Shi, Semirigid Tripodal Ligand Based Uranyl Coordination Polymer Isomers Featuring 2D Honeycomb Nets, Inorg. Chem. 57 (2018) 4492–4501. https://doi.org/10.1021/acs.inorgchem.8b00168.

[116] Y. Li, Z. Weng, Y. Wang, L. Chen, D. Sheng, J. Diwu, Z. Chai, T.E. Albrecht-Schmitt, S. Wang, Surprising coordination for low-valent actinides resembling uranyl(VI) in thorium(IV) organic hybrid layered and framework structures based on a graphene-like (6,3) sheet topology, Dalt. Trans. 45 (2016) 918–921. https://doi.org/10.1039/C5DT04183J.

[117] Y. Li, Z. Yang, Y. Wang, Z. Bai, T. Zheng, X. Dai, S. Liu, D. Gui, W. Liu, M. Chen, L. Chen, J. Diwu, L. Zhu, R. Zhou, Z. Chai, T.E. Albrecht-Schmitt, S. Wang, A mesoporous cationic thorium-organic framework that rapidly traps anionic persistent organic pollutants, Nat. Commun. 8 (2017) 1–10. https://doi.org/10.1038/s41467-017-01208-w.

[118] J.-S. Qin, S. Yuan, Q. Wang, A. Alsalme, H.-C. Zhou, Mixed-linker strategy for the construction of multifunctional metal–organic frameworks, J. Mater. Chem. A. 5 (2017) 4280–4291. https://doi.org/10.1039/C6TA10281F.

[119] W. Yang, H. Wang, W.G. Tian, J. Li, Z.M. Sun, The first family of actinide carboxyphosphinates: Two- and three-dimensional uranyl coordination polymers, Eur. J. Inorg. Chem. 2014 (2014) 5378–5384. https://doi.org/10.1002/ejic.201402592.

[120] S.W. An, L. Mei, K.Q. Hu, Z.H. Zhang, C.Q. Xia, Z.F. Chai, W.Q. Shi, Noncomplexed Cucurbituril-Mediated Structural Evolution of Layered Uranyl Terephthalate Compounds, Inorg. Chem. 59 (2020) 943–955. https://doi.org/10.1021/acs.inorgchem.9b03215.

[121] P. Li, S. Goswami, K.I. Otake, X. Wang, Z. Chen, S.L. Hanna, O.K. Farha, Stabilization of an Unprecedented Hexanuclear Secondary Building Unit in a Thorium-Based Metal-Organic Framework, Inorg. Chem. 58 (2019) 3586–3590. https://doi.org/10.1021/acs.inorgchem.8b03511.

[122] Z.W. Huang, K.Q. Hu, L. Mei, X.H. Kong, J.P. Yu, K. Liu, L.W. Zeng, Z.F. Chai, W.Q. Shi, A mixed-ligand strategy regulates thorium-based MOFs, Dalt. Trans. 49 (2020) 983–987. https://doi.org/10.1039/c9dt04158c.

[123] J.-F. Qian, W.-J. Tian, S. Yang, Z.-H. Sun, L. Chen, M.-J. Wei, Z. Wu, M.-Y. He, Z.-H. Zhang, L. Mei, Auxiliary Ligand-Dependent Adaptive Regulation of Uranyl Coordination in Mixed-Ligand Uranyl Compounds of Flexible Biphenyltetracarboxylic Acid, Inorg. Chem. 59 (2020) 17659–17670. https://doi.org/10.1021/acs.inorgchem.0c02904.

[124] T. Islamoglu, S. Goswami, Z. Li, A.J. Howarth, O.K. Farha, J.T. Hupp, Postsynthetic Tuning of Metal-Organic Frameworks for Targeted Applications, Acc. Chem. Res. 50 (2017) 805–813. https://doi.org/10.1021/acs.accounts.6b00577.

[125] C.R. Martin, G.A. Leith, P. Kittikhunnatham, K.C. Park, O.A. Ejegbavwo, A.

Mathur, C.R. Callahan, S.L. Desmond, M.R. Keener, F. Ahmed, S. Pandey, M.D. Smith, S.R. Phillpot, A.B. Greytak, N.B. Shustova, Heterometallic Actinide-Containing Photoresponsive Metal-Organic Frameworks: Dynamic and Static Tuning of Electronic Properties, Angew. Chemie Int. Ed. (2021) anie.202016826. https://doi.org/10.1002/anie.202016826.

[126] J. Diwu, D.J. Grant, S. Wang, L. Gagliardi, T.E. Albrecht-Schmitt, Periodic Trends in Lanthanide and Actinide Phosphonates: Discontinuity between Plutonium and Americium, Inorg. Chem. 51 (2012) 6906–6915. https://doi.org/10.1021/ic300742p.

[127] J.M. Sperling, E. Warzecha, B.E. Klamm, A.N. Gaiser, C.J. Windorff, M.A. Whitefoot, T.E. Albrecht-Schönzart, Pronounced Pressure Dependence of Electronic Transitions for Americium Compared to Isomorphous Neodymium and Samarium Mellitates, Inorg. Chem. (2020). https://doi.org/10.1021/acs.inorgchem.0c03293.

[128] J.M. Sperling, E. Warzecha, C.J. Windorff, B.E. Klamm, A.N. Gaiser, M.A. Whitefoot, F.D. White, T.N. Poe, T.E. Albrecht-Schönzart, Pressure-Induced Spectroscopic Changes in a Californium 1D Material Are Twice as Large as Found in the Holmium Analog, Inorg. Chem. 59 (2020) 10794–10801. https://doi.org/10.1021/acs.inorgchem.0c01290.

[129] M. Frisch, C.L. Cahill, Thorium(IV) coordination polymers in the pyridine and pyrazinedicarboxylic acid systems, Cryst. Growth Des. 8 (2008) 2921–2928. https://doi.org/10.1021/cg800029z.

[130] P. Thuéry, Solid State Structure of Thorium(IV) Complexes with Common Aminopolycarboxylate Ligands, Inorg. Chem. 50 (2011) 1898–1904. https://doi.org/10.1021/ic102359q.

[131] K.L. Ziegelgruber, K.E. Knope, M. Frisch, C.L. Cahill, Hydrothermal chemistry of Th(IV) with aromatic dicarboxylates: New framework compounds and in situ ligand syntheses, J. Solid State Chem. 181 (2008) 373–381. https://doi.org/10.1016/j.jssc.2007.12.008.

[132] Y. Li, Z. Weng, Y. Wang, L. Chen, D. Sheng, Y. Liu, J. Diwu, Z. Chai, T.E. Albrecht-Schmitt, S. Wang, Centrosymmetric and chiral porous thorium organic frameworks exhibiting uncommon thorium coordination environments, Dalt. Trans. 44 (2015) 20867–20873. https://doi.org/10.1039/c5dt03363b.

[133] Y. Zhang, K. Lu, M. Liu, I. Karatchevtseva, Z. Tao, G. Wei, Thorium(IV) and uranium(VI) compounds of cucurbit[10]uril: from a one-dimensional nanotube to a supramolecular framework, Dalt. Trans. 49 (2020) 404–410. https://doi.org/10.1039/C9DT04299G.

[134] P.O. Adelani, T.E. Albrecht-Schmitt, Comparison of thorium(IV) and uranium(VI) carboxyphosphonates, Inorg. Chem. 49 (2010) 5701–5705. https://doi.org/10.1021/ic1006132.

[135] J. Andreo, E. Priola, G. Alberto, P. Benzi, D. Marabello, D.M. Proserpio, C. Lamberti, E. Diana, Autoluminescent Metal-Organic Frameworks (MOFs): Self-Photoemission of a Highly Stable Thorium MOF, J. Am. Chem. Soc. 140

(2018) 14144–14149. https://doi.org/10.1021/jacs.8b07113.

[136] F. Chen, C. Wang, J. Lan, Y. Ji, Z. Chai, Two novel thorium organic frameworks constructed by bi- and tritopic ligands, Radiochim. Acta. 105 (2017) 531–539. https://doi.org/10.1515/ract-2015-2484.

[137] C. Falaise, C. Volkringer, T. Loiseau, Isolation of thorium benzoate polytypes with discrete ThO8 square antiprismatic units involved in chain-like assemblies, Inorg. Chem. Commun. 39 (2014) 26–30. https://doi.org/10.1016/j.inoche.2013.10.030.

[138] K.P. Carter, A.T. Kerr, I. V. Taydakov, C.L. Cahill, Molecular and polymeric uranyl and thorium hybrid materials featuring methyl substituted pyrazole dicarboxylates and heterocyclic 1,3-diketones, Solid State Sci. 76 (2018) 20–32. https://doi.org/10.1016/j.solidstatesciences.2017.12.002.

[139] P. Thuéry, Molecular and polymeric uranyl and thorium complexes with sulfonate-containing ligands, Eur. J. Inorg. Chem. (2014) 58–68. https://doi.org/10.1002/ejic.201301258.

[140] L.J. Sun, Y.L. Fan, M.J. Yin, H.P. Zhang, H. Feng, L.J. Guo, F. Luo, Thhorium Metal-Organic Framework Showing Proton Transformation from [NH2(CH3)2]+to the Carboxyl Group to Enhance Porosity for Selective Adsorption of D2 over H2 and Ammonia Capture, Cryst. Growth Des. 20 (2020) 3605–3610. https://doi.org/10.1021/acs.cgd.0c00388.

[141] D.L. Reger, A.P. Leitner, M.D. Smith, Supramolecular Metal–Organic Frameworks of s- and f-Block Metals: Impact of 1,8-Naphthalimide Functional Group, Cryst. Growth Des. 16 (2016) 527–536. https://doi.org/10.1021/acs.cgd.5b01575.

[142] F. Blanchard, M. Rivenet, N. Vigier, I. Hablot, S. Grandjean, F. Abraham, Solid State Chemistry of Ten-Fold Coordinate Thorium(IV) Complexes with Oxalates in the Presence of Ammonium and Hydrazinium Ions, Cryst. Growth Des. 18 (2018) 4593–4601. https://doi.org/10.1021/acs.cgd.8b00565.

[143] P. Farger, B. Haidon, P. Roussel, B. Arab-Chapelet, M. Rivenet, Crystal Growth in the Thorium-TEDGA-Oxalate-Nitrate System: Description and Comparison of the Main Structural Features, Inorg. Chem. 58 (2019) 1267–1277. https://doi.org/10.1021/acs.inorgchem.8b02744.

[144] Y. Wang, W. Liu, Z. Bai, T. Zheng, M.A. Silver, Y. Li, Y. Wang, X. Wang, J. Diwu, Z. Chai, S. Wang, Employing an Unsaturated Th4+ Site in a Porous Thorium-Organic Framework for Kr/Xe Uptake and Separation, Angew. Chemie. 130 (2018) 5885–5889. https://doi.org/10.1002/ange.201802173.

[145] N. Zhang, L.X. Sun, Y.H. Xing, F.Y. Bai, A Double-Walled Thorium-Based Metal-Organic Framework as a Promising Dual-Function Absorbent for Efficiently Capturing Iodine and Dyes, Cryst. Growth Des. 19 (2019) 5686–5695. https://doi.org/10.1021/acs.cgd.9b00671.

[146] N. Zhang, L.X. Sun, F.Y. Bai, Y.H. Xing, Thorium-Organic Framework Constructed with a Semirigid Triazine Hexacarboxylic Acid Ligand: Unique

Structure with Thorium Oxide Wheel Clusters and Iodine Adsorption Behavior, Inorg. Chem. 59 (2020) 3964–3973. https://doi.org/10.1021/acs.inorgchem.9b03639.

[147] L. Liang, R. Zhang, J. Zhao, C. Liu, N.S. Weng, Two actinide-organic frameworks constructed by a tripodal flexible ligand: Occurrence of infinite {(UO2)O2(OH)3}4n and hexanuclear {Th6O4(OH)4} motifs, J. Solid State Chem. 243 (2016) 50–56. https://doi.org/10.1016/j.jssc.2016.07.026.

[148] J. Lin, Z.-J. Li, Y. Ju, H. Lu, X. Wu, X. Yu, Y. Li, X. Wu, Z.-H. Zhang, Y. Qian, M.-Y. He, J.-Q. Wang, Boosting the Iodine Adsorption and Radioresistance of Th-UiO-66 MOFs via Aromatic Substitution, Chem. – A Eur. J. (2020). https://doi.org/10.1002/chem.202003621.

[149] M. Dufaye, N.P. Martin, S. Duval, C. Volkringer, A. Ikeda-Ohno, T. Loiseau, Time-controlled synthesis of the 3D coordination polymer U(1,2,3-Hbtc)2 followed by the formation of molecular poly-oxo cluster {U14} containing hemimellitate uranium(IV), RSC Adv. 9 (2019) 22795–22804. https://doi.org/10.1039/c9ra03707a.

[150] D.P. Halter, R.A. Klein, M.A. Boreen, B.A. Trump, C.M. Brown, J.R. Long, Self-adjusting binding pockets enhance H2 and CH4 adsorption in a uranium-based metal-organic framework, Chem. Sci. 11 (2020) 6709–6716. https://doi.org/10.1039/d0sc02394a.

[151] C. Falaise, C. Volkringer, T. Loiseau, Mixed formate-dicarboxylate coordination polymers with tetravalent uranium: Occurrence of tetranuclear {U4O4} and hexanuclear {U6O4(OH)4} motifs, Cryst. Growth Des. 13 (2013) 3225–3231. https://doi.org/10.1021/cg400643g.

[152] C. Falaise, C. Volkringer, J.F. Vigier, N. Henry, A. Beaurain, T. Loiseau, Three-dimensional MOF-type architectures with tetravalent uranium hexanuclear motifs (U6O8), Chem. - A Eur. J. 19 (2013) 5324–5331. https://doi.org/10.1002/chem.201203914.

[153] N.P. Martin, J. März, H. Feuchter, S. Duval, P. Roussel, N. Henry, A. Ikeda-Ohno, T. Loiseau, C. Volkringer, Synthesis and structural characterization of the first neptunium based metal-organic frameworks incorporating {Np6O8} hexanuclear clusters, Chem. Commun. 54 (2018) 6979–6982. https://doi.org/10.1039/c8cc03121e.

[154] K.E. Knope, L. Soderholm, Plutonium(IV) cluster with a hexanuclear [Pu6(OH)4O4]12+ core, Inorg. Chem. 52 (2013) 6770–6772. https://doi.org/10.1021/ic4007185.

[155] S.E. Gilson, P. Li, J.E.S. Szymanowski, J. White, D. Ray, L. Gagliardi, O.K. Farha, P.C. Burns, In Situ Formation of Unprecedented Neptunium-Oxide Wheel Clusters Stabilized in a Metal-Organic Framework, J. Am. Chem. Soc. 141 (2019) 11842–11846. https://doi.org/10.1021/jacs.9b06187.

[156] R. Agarwal, R.M.R. Dumpala, M.K. Sharma, A.K. Yadav, T.K. Ghosh, Stabilization of uranyl(V) by dipicolinic acid in aqueous medium, Dalt. Trans. 50 (2021) 1486–1495. https://doi.org/10.1039/D0DT03961F.

[157] R. Faizova, F. Fadaei-Tirani, A. Chauvin, M. Mazzanti, Synthesis and Characterization of Water Stable Uranyl(V) Complexes, Angew. Chemie. 133 (2021) 8308–8316. https://doi.org/10.1002/ange.202016123.

[158] M. Zhang, C. Liang, G. Cheng, J. Chen, Y. Wang, L. He, L. Cheng, S. Gong, D. Zhang, J. Li, S. Hu, J. Diwu, G. Wu, Y. Wang, Z. Chai, S. Wang, Intrinsic Semiconducting Behavior in a Large Mixed-Valent Uranium(V/VI) Cluster, Angew. Chemie Int. Ed. (2021) anie.202017298. https://doi.org/10.1002/anie.202017298.

[159] V. Smetana, S.P. Kelley, H. Pei, A.-V. Mudring, R.D. Rogers, Sandwiched Kagomé Lattices in a Coordination Polymer Based on Mixed-Valent Uranium, Cryst. Growth Des. 21 (2021) 1727–1733. https://doi.org/10.1021/acs.cgd.0c01626.

[160] L. Mei, C. Xu, Q.Y. Wu, K.Q. Hu, L.Y. Yuan, J. Chen, C.L. Xiao, S. Wang, Z.F. Chai, W.Q. Shi, A neptunium(v)-mediated interwoven transuranium-rotaxane network incorporating a mechanically interlocked [c2]daisy chain unit, Chem. Commun. 54 (2018) 8645–8648. https://doi.org/10.1039/c8cc05122d.

[161] V. Smetana, S.P. Kelley, A.-V. Mudring, R.D. Rogers, A fivefold UO22+ node is a path to dodecagonal quasicrystal approximants in coordination polymers, Sci. Adv. 6 (2020) eaay7685. https://doi.org/10.1126/sciadv.aay7685.

[162] K.P. Carter, C.L. Cahill, Combining coordination and supramolecular chemistry to explore uranyl assembly in the solid state, Inorg. Chem. Front. 2 (2015) 141–156. https://doi.org/10.1039/c4qi00183d.

[163] S.G. Thangavelu, S.J.A. Pope, C.L. Cahill, Synthetic, structural, and luminescence study of uranyl coordination polymers containing chelating terpyridine and trispyridyltriazine ligands, CrystEngComm. 17 (2015) 6236–6247. https://doi.org/10.1039/c5ce00984g.

[164] X.-H. Kong, K.-Q. Hu, Q.-Y. Wu, L. Mei, J.-P. Yu, Z.-F. Chai, C.-M. Nie, W.-Q. Shi, In situ nitroso formation induced structural diversity of uranyl coordination polymers, Inorg. Chem. Front. 6 (2019) 775–785. https://doi.org/10.1039/C8QI01394B.

[165] S.G. Thangavelu, R.J. Butcher, C.L. Cahill, Role of N-Donor Sterics on the Coordination Environment and Dimensionality of Uranyl Thiophenedicarboxylate Coordination Polymers, Cryst. Growth Des. 15 (2015) 3481–3492. https://doi.org/10.1021/acs.cgd.5b00549.

[166] L. Wang, B. Tu, W. Xu, Y. Fu, Y. Zheng, Uranyl Organic Framework as a Highly Selective and Sensitive Turn-on and Turn-off Luminescent Sensor for Dual Functional Detection Arginine and MnO4–, Inorg. Chem. 59 (2020) 5004–5017. https://doi.org/10.1021/acs.inorgchem.0c00236.

[167] C. Wang, W. Xu, Y.N. Ren, H.L. Zhu, Y.Q. Zheng, Removal of tetracycline hydrochloride from aqueous solution by three 3D uranyl-organic frameworks, Inorganica Chim. Acta. 493 (2019) 29–37. https://doi.org/10.1016/j.ica.2019.04.046.

[168] S. An, L. Mei, C. Wang, C. Xia, Z. Chai, W. Shi, The first case of actinide triple helices: pH-dependent structural evolution and kinetically-controlled transformation of two supramolecular conformational isomers, Chem. Commun. 51 (2015) 8978–8981. https://doi.org/10.1039/C5CC02646F.

[169] X.T. Xu, Y.N. Hou, S.Y. Wei, X.X. Zhang, F.Y. Bai, L.X. Sun, Z. Shi, Y.H. Xing, UO22+-amino hybrid materials: Structural variation and photocatalysis properties, CrystEngComm. 17 (2015) 642–652. https://doi.org/10.1039/c4ce01473a.

[170] P. Thuéry, J. Harrowfield, Anchoring flexible uranyl dicarboxylate chains through stacking interactions of ancillary ligands on chiral U(VI) centres, CrystEngComm. 18 (2016) 3905–3918. https://doi.org/10.1039/C6CE00603E.

[171] K.Q. Hu, L.Z. Zhu, C.Z. Wang, L. Mei, Y.H. Liu, Z.Q. Gao, Z.F. Chai, W.Q. Shi, Novel Uranyl Coordination Polymers Based on Quinoline-Containing Dicarboxylate by Altering Auxiliary Ligands: From 1D Chain to 3D Framework, Cryst. Growth Des. 16 (2016) 4886–4896. https://doi.org/10.1021/acs.cgd.6b00429.

[172] P. Thuéry, J. Harrowfield, Coordination Polymers and Cage-Containing Frameworks in Uranyl Ion Complexes with rac- and (1R,2R)-trans-1,2-Cyclohexanedicarboxylates: Consequences of Chirality, Inorg. Chem. 56 (2017) 1455–1469. https://doi.org/10.1021/acs.inorgchem.6b02537.

[173] P. Thuéry, J. Harrowfield, Structural Consequences of 1,4-Cyclohexanedicarboxylate Cis/Trans Isomerism in Uranyl Ion Complexes: From Molecular Species to 2D and 3D Entangled Nets, Inorg. Chem. 56 (2017) 13464–13481. https://doi.org/10.1021/acs.inorgchem.7b02176.

[174] K.P. Carter, M. Kalaj, C.L. Cahill, Harnessing uranyl oxo atoms: Via halogen bonding interactions in molecular uranyl materials featuring 2,5-diiodobenzoic acid and N-donor capping ligands, Inorg. Chem. Front. 4 (2017) 65–78. https://doi.org/10.1039/c6qi00352d.

[175] L. Mei, S.W. An, K.Q. Hu, L. Wang, J.P. Yu, Z.W. Huang, X.H. Kong, C.Q. Xia, Z.F. Chai, W.Q. Shi, Molecular Spring-like Triple-Helix Coordination Polymers as Dual-Stress and Thermally Responsive Crystalline Metal–Organic Materials, Angew. Chemie - Int. Ed. 59 (2020) 16061–16068. https://doi.org/10.1002/anie.202003808.

[176] S. Li, L.X. Sun, J.C. Ni, Z. Shi, Y.H. Xing, D. Shang, F.Y. Bai, Two uranyl heterocyclic carboxyl compounds with fluorescent properties as high sensitivity and selectivity optical detectors for nitroaromatics, New J. Chem. 41 (2017) 3073–3081. https://doi.org/10.1039/C6NJ03933B.

[177] H.H. Tian, L.T. Chen, R.L. Zhang, J.S. Zhao, C.Y. Liu, N.S. Weng, A novel stable 3D luminescent uranyl complex for highly efficient and sensitive recognition of Ru3+ and biomolecules, J. Solid State Chem. 258 (2018) 674–681. https://doi.org/10.1016/j.jssc.2017.11.032.

[178] S. Wu, L. Mei, F.Z. Li, S.W. An, K.Q. Hu, C.M. Nie, Z.F. Chai, W.Q. Shi, Uranyl-Organic Coordination Compounds Incorporating Photoactive

Vinylpyridine Moieties: Synthesis, Structural Characterization, and Light-Induced Fluorescence Attenuation, Inorg. Chem. 57 (2018) 14772–14785. https://doi.org/10.1021/acs.inorgchem.8b02523.

[179] P.M. Cantos, L.J. Jouffret, R.E. Wilson, P.C. Burns, C.L. Cahill, Series of uranyl-4,4′-biphenyldicarboxylates and an occurrence of a cation-cation interaction: Hydrothermal synthesis and in situ Raman studies, Inorg. Chem. 52 (2013) 9487–9495. https://doi.org/10.1021/ic401143g.

[180] D. Wu, X. Bai, H.R. Tian, W. Yang, Z. Li, Q. Huang, S. Du, Z.M. Sun, Uranyl Carboxyphosphonates Derived from Hydrothermal in Situ Ligand Reaction: Syntheses, Structures, and Computational Investigations, Inorg. Chem. 54 (2015) 8617–8624. https://doi.org/10.1021/acs.inorgchem.5b01266.

[181] P. Thuéry, Y. Atoini, J. Harrowfield, Structure-Directing Effects of Coordinating Solvents, Ammonium and Phosphonium Counterions in Uranyl Ion Complexes with 1,2-, 1,3-, and 1,4-Phenylenediacetates, Inorg. Chem. 59 (2020) 2503–2518. https://doi.org/10.1021/acs.inorgchem.9b03404.

[182] Z. Bai, Y. Wang, Y. Li, W. Liu, L. Chen, D. Sheng, J. Diwu, Z. Chai, T.E. Albrecht-Schmitt, S. Wang, First Cationic Uranyl-Organic Framework with Anion-Exchange Capabilities, Inorg. Chem. 55 (2016) 6358–6360. https://doi.org/10.1021/acs.inorgchem.6b00930.

[183] G. Andreev, N. Budantseva, A. Levtsova, M. Sokolova, A. Fedoseev, Formation of uranyl phthalate coordination polymers with unusual 2D net topologies in the presence of organic cations, CrystEngComm. (2020). https://doi.org/10.1039/D0CE01323D.

[184] L. Mei, C.Z. Wang, L.Z. Zhu, Z.Q. Gao, Z.F. Chai, J.K. Gibson, W.Q. Shi, Exploring New Assembly Modes of Uranyl Terephthalate: Templated Syntheses and Structural Regulation of a Series of Rare 2D → 3D Polycatenated Frameworks, Inorg. Chem. 56 (2017) 7694–7706. https://doi.org/10.1021/acs.inorgchem.7b00312.

[185] X.S. Zhai, W.G. Zhu, W. Xu, Y.J. Huang, Y.Q. Zheng, A family of 3D UO22+-5-X-1,3-dicarboxylate (X = -H, -NO2, -NH2, -OH) hybrid materials: Structural relevance with variation of substituent groups and photochemical properties, CrystEngComm. 17 (2015) 2376–2388. https://doi.org/10.1039/c4ce02307b.

[186] L. Chen, Y. Zhang, Z. Weng, Z. Liu, J. Zhang, Y. Wang, S. Wang, Uranyl Phosphonates with Multiple Uranyl Coordination Geometries and Low Temperature Phase Transition, Chinese J. Chem. 39 (2021) 597–604. https://doi.org/10.1002/cjoc.202000510.

[187] X. Gao, J. Song, L.X. Sun, Y.H. Xing, F.Y. Bai, Z. Shi, A family of uranium-carboxylic acid hybrid materials: Synthesis, structure and mixed-dye selective adsorption, New J. Chem. 40 (2016) 6077–6085. https://doi.org/10.1039/c6nj00109b.

[188] C. Liu, X.X. Yang, S. Niu, X.Y. Yi, Q.J. Pan, Occurrence of polyoxouranium

motifs in uranyl organic networks constructed by using silicon-centered carboxylate linkers: Structures, spectroscopy and computation, Dalt. Trans. 49 (2020) 4155–4163. https://doi.org/10.1039/d0dt00379d.

[189] S.W. An, L. Mei, K.Q. Hu, C.Q. Xia, Z.F. Chai, W.Q. Shi, The templated synthesis of a unique type of tetra-nuclear uranyl-mediated two-fold interpenetrating uranyl-organic framework, Chem. Commun. 52 (2016) 1641–1644. https://doi.org/10.1039/c5cc09314g.

[190] Y. Zhang, L. Chen, J. Guan, X. Wang, S. Wang, J. Diwu, A unique uranyl framework containing uranyl pentamers as secondary building units: Synthesis, structure, and spectroscopic properties, Dalt. Trans. 49 (2020) 3676–3679. https://doi.org/10.1039/c9dt03871j.

[191] Y.C. Ge, L. Mei, F.Z. Li, K.Q. Hu, C.Q. Xia, Z.F. Chai, W.Q. Shi, Template-Driven Assembly of Rare Hexameric Uranyl-Organic Rotaxane Networks Threaded on Dimeric Uranyl Chains, Cryst. Growth Des. 18 (2018) 3073–3081. https://doi.org/10.1021/acs.cgd.8b00219.

[192] W. Si, M. Lei, H. Kong-Qiu, C. Zhi-Fang, N. Chang-Ming, S. Wei-Qun, pH-dependent Synthesis of Octa-nuclear Uranyl-Oxalate Network Mediated by U-shaped Linkers, J. Inorg. Mater. (2019) 118. https://doi.org/10.15541/jim20190118.

[193] X. Tong, S. Wang, H. Gao, Y. Ge, J. Zuo, F. Liu, J. Ding, J. Xiong, Hydrothermal synthesis of two 2D uranyl coordination polymers: structure, luminescence, and photocatalytic degradation of rhodamine B, CrystEngComm. 22 (2020) 5716–5722. https://doi.org/10.1039/D0CE01091J.

[194] L.L. Liang, L.L. Liang, R.L. Zhang, J.S. Zhao, Counterion-Controlled Formation of Layered Honeycomb and Polythreading Uranyl Networks and the Highly Sensitive and Selective Detection of Fe3+ in Aqueous Media, Inorg. Chem. 59 (2020) 7980–7990. https://doi.org/10.1021/acs.inorgchem.9b03576.

[195] I.A. Charushnikova, A.M. Fedoseev, A.A. Bessonov, Crystal Structure of An(VI) Complexes with Succinate Anions, [PuO2(C4H4O4)(H2O)] and Cs2[(AnO2)2(C4H4O4)3]·H2O (An = U, Np, Pu), Radiochemistry. 61 (2019) 137–145. https://doi.org/10.1134/S1066362219020024.

[196] P. Thuéry, Y. Atoini, J. Harrowfield, Crown Ethers and Their Alkali Metal Ion Complexes as Assembler Groups in Uranyl-Organic Coordination Polymers with cis -1,3-, cis -1,2-, and trans -1,2-Cyclohexanedicarboxylates, Cryst. Growth Des. 18 (2018) 3167–3177. https://doi.org/10.1021/acs.cgd.8b00266.

[197] L.L. Liang, Y.Q. Hu, J.S. Zhao, Two uranium coordination polymers constructed by a polycarboxylic acid: Structural variation, photoluminescent and photocatalysis properties, J. Solid State Chem. 282 (2019) 121085. https://doi.org/10.1016/j.jssc.2019.121085.

[198] P. Thuéry, Uranyl Complexes as Scaffolding or Spacers for Cucurbit[6]uril Molecules in Homo- and Heterometallic Species, Including a Uranyl–

Lanthanide Complex, Eur. J. Inorg. Chem. 2017 (2017) 2876–2882. https://doi.org/10.1002/ejic.201700283.

[199] P. Thuéry, Y. Atoini, J. Harrowfield, Isomerism in Benzenetricarboxylates: Variations in the Formation of Coordination Polymers with Uranyl Ion, Cryst. Growth Des. 20 (2020) 7368–7383. https://doi.org/10.1021/acs.cgd.0c01050.

[200] P. Thuéry, Y. Atoini, J. Harrowfield, Uranyl Tricarballylate Triperiodic and Nanotubular Species. Counterion Control of Nanotube Diameter, Inorg. Chem. 59 (2020) 6953–6962. https://doi.org/10.1021/acs.inorgchem.0c00450.

[201] R. Zhao, F. Li, J. Yu, L. Mei, K. Hu, Z. Chai, W. Shi, A New Preorganized Metalloligand Linker for the Construction of Luminescent Coordination Polymers, Cryst. Growth Des. (2020) acs.cgd.0c01007. https://doi.org/10.1021/acs.cgd.0c01007.

[202] N.P. Martin, C. Volkringer, N. Henry, S. Duval, D. Mara, R. Van Deun, T. Loiseau, Molecular Assemblies of a Series of Mixed Tetravalent Uranium and Trivalent Lanthanide Complexes Associated with the Dipicolinate Ligand, in Aqueous Medium, Cryst. Growth Des. 18 (2018) 2165–2179. https://doi.org/10.1021/acs.cgd.7b01617.

[203] J.A. Ridenour, C.L. Cahill, Nine isomorphous lanthanide-uranyl f-f bimetallic materials with 2-thiophenecarboxylic acid and terpyridine: Structure and concomitant luminescent properties, CrystEngComm. 20 (2018) 4997–5011. https://doi.org/10.1039/c8ce00811f.

[204] Y. Zhang, L. Chen, Z. Liu, W. Liu, M. Yuan, J. Shu, N. Wang, L. He, J. Zhang, J. Xie, X. Chen, J. Diwu, Full-Range Ratiometric Detection of D2O in H2O by a Heterobimetallic Uranyl/Lanthanide Framework with 4f/5f Bimodal Emission, ACS Appl. Mater. Interfaces. 12 (2020) 16648–16654. https://doi.org/10.1021/acsami.0c02783.

[205] A.G.D. Nelson, T.H. Bray, T.E. Albrecht-Schmitt, Capitalizing on differing coordination environments and redox potentials to prepare an ordered heterobimetallic UVI/NpIV diphosphonate, Angew. Chemie - Int. Ed. 47 (2008) 6252–6254. https://doi.org/10.1002/anie.200801981.

[206] P. Thuéry, Y. Atoini, J. Harrowfield, Tubelike Uranyl-Phenylenediacetate Assemblies from Screening of Ligand Isomers and Structure-Directing Counterions, Inorg. Chem. 58 (2019) 6550–6564. https://doi.org/10.1021/acs.inorgchem.9b00804.

[207] Z.-W. Huang, K.-Q. Hu, L. Mei, C.-Z. Wang, Y.-M. Chen, W.-S. Wu, Z.-F. Chai, W.-Q. Shi, Potassium Ions Induced Framework Interpenetration for Enhancing the Stability of Uranium-Based Porphyrin MOF with Visible-Light-Driven Photocatalytic Activity, Inorg. Chem. 60 (2021) 651–659. https://doi.org/10.1021/acs.inorgchem.0c02473.

[208] A.T. Kerr, S.A. Kumalah, K.T. Holman, R.J. Butcher, C.L. Cahill, Uranyl Coordination Polymers Incorporating η^5-Cyclopentadienyliron-Functionalized η^6-Phthalate Metalloligands: Syntheses, Structures and

Photophysical Properties, J. Inorg. Organomet. Polym. Mater. 24 (2014) 128–136. https://doi.org/10.1007/s10904-013-9980-0.

[209] X. Kong, K. Hu, L. Mei, Q. Wu, Z. Huang, K. Liu, Z. Chai, C. Nie, W.-Q. Shi, Construction of Hybrid Bimetallic Uranyl Compounds Based on a Preassembled Terpyridine Metalloligand, Chem. – A Eur. J. 27 (2021) 2124–2130. https://doi.org/10.1002/chem.202004344.

[210] W. Yang, D. Wu, C. Liu, Q.J. Pan, Z.M. Sun, Structural Variations of the First Family of Heterometallic Uranyl Carboxyphosphinate Assemblies by Synergy between Carboxyphosphinate and Imidazole Ligands, Cryst. Growth Des. 16 (2016) 2011–2018. https://doi.org/10.1021/acs.cgd.5b01595.

[211] S. Chorazy, J.J. Zakrzewski, M. Reczyński, B. Sieklucka, Multi-colour uranyl emission efficiently tuned by hexacyanidometallates within hybrid coordination frameworks, Chem. Commun. 55 (2019) 3057–3060. https://doi.org/10.1039/c8cc09757g.

[212] Y. Fan, M. Yin, R. Krishna, X. Feng, F. Luo, Constructing a robust gigantic drum-like hydrophobic [Co24U6] nanocage in a metal–organic framework for high-performance SO2 removal in humid conditions, J. Mater. Chem. A. 9 (2021) 4075–4081. https://doi.org/10.1039/D0TA10004H.

[213] H. Xu, C. Cao, H. Hu, S. Wang, J. Liu, P. Cheng, N. Kaltsoyannis, J. Li, B. Zhao, High Uptake of ReO4– and CO2 Conversion by a Radiation-Resistant Thorium-Nickle [Th48Ni6] Nanocage-Based Metal-Organic Framework, Angew. Chemie Int. Ed. 58 (2019) 6022–6027. https://doi.org/10.1002/anie.201901786.

[214] P. Thuéry, J. Harrowfield, [Ni(cyclam)]2+ and [Ni(R,S-Me6cyclam)]2+ as Linkers or Counterions In Uranyl-Organic Species with cis- and trans-1,2-Cyclohexanedicarboxylate Ligands, Cryst. Growth Des. 18 (2018) 5512–5520. https://doi.org/10.1021/acs.cgd.8b00834.

[215] P. Thuéry, Y. Atoini, J. Harrowfield, 1,3-Adamantanedicarboxylate and 1,3-Adamantanediacetate as Uranyl Ion Linkers: Effect of Counterions, Solvents and Differences in Flexibility, Eur. J. Inorg. Chem. 2019 (2019) 4440–4449. https://doi.org/10.1002/ejic.201900957.

[216] P. Thuéry, Y. Atoini, J. Harrowfield, The sulfonate group as a ligand: A fine balance between hydrogen bonding and metal ion coordination in uranyl ion complexes, Dalt. Trans. 48 (2019) 8756–8772. https://doi.org/10.1039/c9dt01024f.

[217] A.T. Kerr, J.A. Ridenour, A.A. Noring, C.L. Cahill, Two uranyl-copper(II) bimetallic coordination polymers containing trans-3,3(pyridyl)acrylic acid: Structural variance through synthetic subtleties, Inorganica Chim. Acta. 494 (2019) 204–210. https://doi.org/10.1016/j.ica.2019.05.024.

[218] Z. hui Pang, F. Luo, A highly rare 3D U-Cu metal-organic framework showing three-connected srs topology and nine-fold interpenetration, Inorg. Chem. Commun. 119 (2020) 108041. https://doi.org/10.1016/j.inoche.2020.108041.

[219] R. Zhao, L. Mei, K.Q. Hu, L. Wang, Z.F. Chai, W.Q. Shi, Two Three-Dimensional Actinide–Silver Heterometallic Coordination Polymers Based on 2,2′-Bipyridine-3,3′-dicarboxylic Acid with Helical Chains Containing Dimeric or Trimeric Motifs, Eur. J. Inorg. Chem. 2017 (2017) 1472–1477. https://doi.org/10.1002/ejic.201601369.

[220] Y.N. Ren, W. Xu, L.X. Zhou, Y.Q. Zheng, Efficient tetracycline adsorption and photocatalytic degradation of rhodamine B by uranyl coordination polymer, J. Solid State Chem. 251 (2017) 105–112. https://doi.org/10.1016/j.jssc.2017.04.005.

[221] P. Thuéry, Y. Atoini, J. Harrowfield, 1,2-, 1,3-, and 1,4-Phenylenediacetate Complexes of the Uranyl Ion with Additional Metal Cations and/or Ancillary N-Donor Ligands: Confronting Ligand Geometrical Proclivities, Cryst. Growth Des. 19 (2019) 6611–6626. https://doi.org/10.1021/acs.cgd.9b01032.

[222] C. Zhang, F. Guo, Y. Dai, Y. Zhang, J. Feng, N. Wang, J. Wang, [(UO2)(C10H8N2O2)2][HPW12O40]: The First Case of a Uranyl Coordination Network Containing a Keggin-Type Polyoxometalate, Eur. J. Inorg. Chem. 2020 (2020) 4577–4580. https://doi.org/10.1002/ejic.202000877.

[223] C.T. Buru, O.K. Farha, Strategies for Incorporating Catalytically Active Polyoxometalates in Metal–Organic Frameworks for Organic Transformations, ACS Appl. Mater. Interfaces. 12 (2020) 5345–5360. https://doi.org/10.1021/acsami.9b19785.

[224] T. Auvray, E.M. Matson, Polyoxometalate-based complexes as ligands for the study of actinide chemistry, Dalt. Trans. 49 (2020) 13917–13927. https://doi.org/10.1039/D0DT02755C.

[225] K.E. Knope, M. Vasiliu, D.A. Dixon, L. Soderholm, Thorium(IV)–Selenate Clusters Containing an Octanuclear Th(IV) Hydroxide/Oxide Core, Inorg. Chem. 51 (2012) 4239–4249. https://doi.org/10.1021/ic202706s.

[226] P. Woidy, F. Kraus, [Th10(μ-F16)(μ3-O4)(μ4-O4)(NH3)32](NO3)8·19.6 NH3 - the Largest Thorium Complex from Solution known to Date, Zeitschrift Für Anorg. Und Allg. Chemie. 640 (2014) 1547–1550. https://doi.org/10.1002/zaac.201400138.

[227] L. Chatelain, R. Faizova, F. Fadaei-Tirani, J. Pécaut, M. Mazzanti, Structural Snapshots of Cluster Growth from {U6} to {U38} During the Hydrolysis of UCl4, Angew. Chemie Int. Ed. 58 (2019) 3021–3026. https://doi.org/10.1002/anie.201812509.

[228] G.E. Sigmon, A.E. Hixon, Extension of the Plutonium Oxide Nanocluster Family to Include {Pu16} and {Pu22}, Chem. - A Eur. J. 25 (2019) 2463–2466. https://doi.org/10.1002/chem.201805605.

[229] C. Falaise, C. Volkringer, J.F. Vigier, A. Beaurain, P. Roussel, P. Rabu, T. Loiseau, Isolation of the large {actinide}38 poly-oxo cluster with uranium, J. Am. Chem. Soc. 135 (2013) 15678–15681. https://doi.org/10.1021/ja4067207.

[230] N.P. Martin, C. Volkringer, P. Roussel, J. März, C. Hennig, T. Loiseau, A. Ikeda-Ohno, {Np38} clusters: the missing link in the largest poly-oxo cluster series of tetravalent actinides, Chem. Commun. 54 (2018) 10060–10063. https://doi.org/10.1039/C8CC03744B.

[231] L. Soderholm, P.M. Almond, S. Skanthakumar, R.E. Wilson, P.C. Burns, The Structure of the Plutonium Oxide Nanocluster [Pu38O56Cl54(H2O)8]14–, Angew. Chemie Int. Ed. 47 (2008) 298–302. https://doi.org/10.1002/anie.200704420.

[232] J.B. Bailey, F.A. Tezcan, Tunable and Cooperative Thermomechanical Properties of Protein–Metal–Organic Frameworks, J. Am. Chem. Soc. 142 (2020) 17265–17270. https://doi.org/10.1021/jacs.0c07835.

[233] L. Mei, K.Q. Hu, Z.H. Zhang, S.W. An, Z.F. Chai, W.Q. Shi, Stepwise ortho Chlorination of Carboxyl Groups for Promoting Structure Variance of Heterometallic Uranyl-Silver Coordination Polymers of Isonicotinate, Inorg. Chem. 57 (2018) 4673–4685. https://doi.org/10.1021/acs.inorgchem.8b00402.

[234] J. Xie, Y. Wang, M.A. Silver, W. Liu, T. Duan, X. Yin, L. Chen, J. Diwu, Z. Chai, S. Wang, Tunable 4f/5f Bimodal Emission in Europium-Incorporated Uranyl Coordination Polymers, Inorg. Chem. 57 (2018) 575–582. https://doi.org/10.1021/acs.inorgchem.7b02304.

[235] G.A. Senchyk, A.B. Lysenko, H. Krautscheid, K. V. Domasevitch, Control over the coordination preferences in Ag+ and Ag+/UO22+ 1,2,4-triazolecarboxylate frameworks, Inorg. Chem. Commun. 113 (2020) 107813. https://doi.org/10.1016/j.inoche.2020.107813.

[236] X.M. Wang, C. Wang, N. Zhang, D.Q. Liu, Y. Wang, F.Y. Bai, Multifunctional Inorganic-Organic U-MOF Materials with Nitrogen Heterocyclic Carboxylate: Synthesis, Structure and Properties, ChemistrySelect. 5 (2020) 8625–8634. https://doi.org/10.1002/slct.201904850.

[237] S.J. Jennifer, A.K. Jana, Influence of pyrazine/piperazine based guest molecules in the crystal structures of uranyl thiophene dicarboxylate coordination polymers: Structural diversities and photocatalytic activities for the degradation of organic dye, Cryst. Growth Des. 17 (2017) 5318–5329. https://doi.org/10.1021/acs.cgd.7b00826.

[238] M. Frisch, C.L. Cahill, Syntheses, structures and fluorescent properties of two novel coordination polymers in the U-Cu-H3pdc system, Dalt. Trans. (2005) 1518–1523. https://doi.org/10.1039/B500127G.

[239] T. Islamoglu, D. Ray, P. Li, M.B. Majewski, I. Akpinar, X. Zhang, C.J. Cramer, L. Gagliardi, O.K. Farha, From Transition Metals to Lanthanides to Actinides: Metal-Mediated Tuning of Electronic Properties of Isostructural Metal–Organic Frameworks, Inorg. Chem. 57 (2018) 13246–13251. https://doi.org/10.1021/acs.inorgchem.8b01748.

[240] S.L. Hanna, X. Zhang, K.I. Otake, R.J. Drout, P. Li, T. Islamoglu, O.K. Farha, Guest-Dependent Single-Crystal-to-Single-Crystal Phase Transitions in a Two-Dimensional Uranyl-Based Metal-Organic Framework, Cryst. Growth

Des. 19 (2019) 506–512. https://doi.org/10.1021/acs.cgd.8b01689.

[241] D.D. Liu, Y.L. Wang, F. Luo, Q.Y. Liu, Rare Three-Dimensional Uranyl-Biphenyl-3,3′-disulfonyl-4,4′-dicarboxylate Frameworks: Crystal Structures, Proton Conductivity, and Luminescence, Inorg. Chem. 59 (2020) 2952–2960. https://doi.org/10.1021/acs.inorgchem.9b03323.

[242] X. Hou, S.-F. Tang, Variability of Uranyl Carboxylates from Rigid Terophenyldicarboxylic Acid Ligands, Inorg. Chem. 59 (2020) 15824–15831. https://doi.org/10.1021/acs.inorgchem.0c02278.

[243] X. Gao, C. Wang, Z.F. Shi, J. Song, F.Y. Bai, J.X. Wang, Y.H. Xing, A family of uranyl-aromatic dicarboxylate (pht-, ipa-, tpa-) framework hybrid materials: photoluminescence, surface photovoltage and dye adsorption, Dalt. Trans. 44 (2015) 11562–11571. https://doi.org/10.1039/c5dt01470k.

[244] L. Wang, W. Xu, W. Li, M. Xie, Y. Zheng, A Water-Stable Uranyl Organic Framework as a Highly Selective and Sensitive Bifunctional Luminescent Probe for Fe3+ and Tetracycline Hydrochloride, Chem. – An Asian J. 14 (2019) 4246–4254. https://doi.org/10.1002/asia.201901124.

[245] W. Liu, X. Dai, J. Xie, M.A. Silver, D. Zhang, Y. Wang, Y. Cai, J. Diwu, J. Wang, R. Zhou, Z. Chai, S. Wang, Highly sensitive detection of UV radiation using a uranium coordination polymer, ACS Appl. Mater. Interfaces. 10 (2018) 4844–4850. https://doi.org/10.1021/acsami.7b17954.

[246] Y. Wang, X. Yin, W. Liu, J. Xie, J. Chen, M.A. Silver, D. Sheng, L. Chen, J. Diwu, N. Liu, Z. Chai, T.E. Albrecht-Schmitt, S. Wang, Emergence of Uranium as a Distinct Metal Center for Building Intrinsic X-ray Scintillators, Angew. Chemie - Int. Ed. 57 (2018) 7883–7887. https://doi.org/10.1002/anie.201802865.

[247] Y. Wang, Z. Liu, Y. Li, Z. Bai, W. Liu, Y. Wang, X. Xu, C. Xiao, D. Sheng, J. Diwu, J. Su, Z. Chai, T.E. Albrecht-Schmitt, S. Wang, Umbellate distortions of the uranyl coordination environment result in a stable and porous polycatenated framework that can effectively remove cesium from aqueous solutions, J. Am. Chem. Soc. 137 (2015) 6144–6147. https://doi.org/10.1021/jacs.5b02480.

[248] P. Li, N.A. Vermeulen, C.D. Malliakas, D.A. Gómez-Gualdrón, A.J. Howarth, B.L. Mehdi, A. Dohnalkova, N.D. Browning, M. O'Keeffe, O.K. Farha, Bottom-up construction of a superstructure in a porous uranium-organic crystal, Science. 356 (2017) 624–627. https://doi.org/10.1126/science.aam7851.

[249] X. Wang, X. Zhang, P. Li, K.I. Otake, Y. Cui, J. Lyu, M.D. Krzyaniak, Y. Zhang, Z. Li, J. Liu, C.T. Buru, T. Islamoglu, M.R. Wasielewski, Z. Li, O.K. Farha, Vanadium Catalyst on Isostructural Transition Metal, Lanthanide, and Actinide Based Metal-Organic Frameworks for Alcohol Oxidation, J. Am. Chem. Soc. 141 (2020) 8306–8314. https://doi.org/10.1021/jacs.9b02603.

[250] X. Wang, Y. Wang, X. Dai, M.A. Silver, W. Liu, Y. Li, Z. Bai, D. Gui, L. Chen, J. Diwu, R. Zhou, Z. Chai, S. Wang, Phase transition triggered aggregation-

induced emission in a photoluminescent uranyl-organic framework, Chem. Commun. 54 (2018) 627–630. https://doi.org/10.1039/c7cc09594e.

[251] S. Wang, L. Mei, J.P. Yu, K.Q. Hu, Z.R. Liu, Z.F. Chai, W.Q. Shi, Large-Pore Layered Networks, Polycatenated Frameworks, and Three-Dimensional Frameworks of Uranyl Tri(biphenyl)amine/Tri(phenyl)amine Tricarboxylate: Solvent-/Ligand-Dependent Dual Regulation, Cryst. Growth Des. 18 (2018) 4347–4356. https://doi.org/10.1021/acs.cgd.8b00246.

[252] N. Zhang, Y.H. Xing, F.Y. Bai, A Uranyl-Organic Framework Featuring Two-Dimensional Graphene-like Layered Topology for Efficient Iodine and Dyes Capture, Inorg. Chem. 58 (2019) 6866–6876. https://doi.org/10.1021/acs.inorgchem.9b00317.

[253] L. Cheng, C. Liang, W. Liu, Y. Wang, B. Chen, H. Zhang, Y. Wang, Z. Chai, S. Wang, Three-Dimensional Polycatenation of a Uranium-Based Metal–Organic Cage: Structural Complexity and Radiation Detection, J. Am. Chem. Soc. 142 (2020) 16218–16222. https://doi.org/10.1021/jacs.0c08117.

[254] C. Liu, C.Y. Gao, W. Yang, F.Y. Chen, Q.J. Pan, J. Li, Z.M. Sun, Entangled Uranyl Organic Frameworks with (10,3)-b Topology and Polythreading Network: Structure, Luminescence, and Computational Investigation, Inorg. Chem. 55 (2016) 5540–5548. https://doi.org/10.1021/acs.inorgchem.6b00582.

[255] C. Liu, C. Wang, Z.-M. Sun, Conformational 2-Fold Interpenetrated Uranyl Supramolecular Isomers Based on (6,3) Sheet Topology: Structure, Luminescence, and Ion Exchange, Inorg. Chem. 57 (2018) 15370–15378. https://doi.org/10.1021/acs.inorgchem.8b02696.

[256] L. Shao, F. Zhai, Y. Wang, G. Yue, Y. Li, M. Chu, S. Wang, Assembly of porphyrin-based uranium organic frameworks with (3,4)-connected: Pto and tbo topologies, Dalt. Trans. 48 (2019) 1595–1598. https://doi.org/10.1039/c8dt04585b.

[257] F. Hu, Z. Di, P. Lin, P. Huang, M. Wu, F. Jiang, M. Hong, An Anionic Uranium-Based Metal-Organic Framework with Ultralarge Nanocages for Selective Dye Adsorption, Cryst. Growth Des. 18 (2018) 576–580. https://doi.org/10.1021/acs.cgd.7b01525.

[258] P. Li, N.A. Vermeulen, X. Gong, C.D. Malliakas, J.F. Stoddart, J.T. Hupp, O.K. Farha, Design and Synthesis of a Water-Stable Anionic Uranium-Based Metal–Organic Framework (MOF) with Ultra Large Pores, Angew. Chemie - Int. Ed. 55 (2016) 10358–10362. https://doi.org/10.1002/anie.201605547.

[259] J. Ai, F.-Y. Chen, C.-Y. Gao, H.-R. Tian, Q.-J. Pan, Z.-M. Sun, Porous Anionic Uranyl–Organic Networks for Highly Efficient Cs+ Adsorption and Investigation of the Mechanism, Inorg. Chem. 57 (2018) 4419–4426. https://doi.org/10.1021/acs.inorgchem.8b00099.

[260] K.Q. Hu, X. Jiang, C.Z. Wang, L. Mei, Z.N. Xie, W.Q. Tao, X.L. Zhang, Z.F. Chai, W.Q. Shi, Solvent-Dependent Synthesis of Porous Anionic Uranyl–Organic Frameworks Featuring a Highly Symmetrical (3,4)-Connected ctn or bor

Topology for Selective Dye Adsorption, Chem. - A Eur. J. 23 (2017) 529–532. https://doi.org/10.1002/chem.201604225.

[261] R. Christoffels, U. Ruschewitz, Two New Coordination Polymers with UO22+ Units and Fluorinated Aromatic Carboxylate Linkers, Zeitschrift Fur Anorg. Und Allg. Chemie. (2019) 156–161. https://doi.org/10.1002/zaac.201900302.

[262] D. Gu, W. Yang, G. Ning, F. Wang, S. Wu, X. Shi, Y. Wang, Q. Pan, In Situ Ligand Formation-Driven Synthesis of a Uranyl Organic Framework as a Turn-on Fluorescent pH Sensor, Inorg. Chem. 59 (2020) 1778–1784. https://doi.org/10.1021/acs.inorgchem.9b02999.

[263] L. Mei, K. Liu, S. Wu, X.H. Kong, K.Q. Hu, J.P. Yu, C.M. Nie, Z.F. Chai, W.Q. Shi, Metal-Carboxyl Helical Chain Secondary Units Supported Ion-Exchangeable Anionic Uranyl–Organic Framework, Chem. - A Eur. J. 25 (2019) 10309–10313. https://doi.org/10.1002/chem.201902180.

[264] J. Song, X. Gao, Z.N. Wang, C.R. Li, Q. Xu, F.Y. Bai, Z.F. Shi, Y.H. Xing, Multifunctional Uranyl Hybrid Materials: Structural Diversities as a Function of pH, Luminescence with Potential Nitrobenzene Sensing, and Photoelectric Behavior as p-type Semiconductors, Inorg. Chem. 54 (2015) 9046–9059. https://doi.org/10.1021/acs.inorgchem.5b01364.

[265] N. Zhang, Y.H. Xing, F.Y. Bai, Triazine Functionalized Porous Three-Dimensional Uranyl-Organic Framework: Extraction of Uranium(VI) and Adsorption of Cationic Dyes in Aqueous Solution, Cryst. Growth Des. 20 (2020) 1838–1848. https://doi.org/10.1021/acs.cgd.9b01553.

[266] Z. Chen, P. Li, X. Zhang, M.R. Mian, X. Wang, P. Li, Z. Liu, M. O'Keeffe, J.F. Stoddart, O.K. Farha, Reticular exploration of uranium-based metal-organic frameworks with hexacarboxylate building units, Nano Res. 12 (2020) 1–5. https://doi.org/10.1007/s12274-020-2690-3.

[267] H. Ghasempour, K.-Y. Wang, J.A. Powell, F. ZareKarizi, X.-L. Lv, A. Morsali, H.-C. Zhou, Metal-organic frameworks based on multicarboxylate linkers, Coord. Chem. Rev. 426 (2021) 213542. https://doi.org/10.1016/j.ccr.2020.213542.

[268] J. Xie, Y. Wang, D. Zhang, C. Liang, W. Liu, Y. Chong, X. Yin, Y. Zhang, D. Gui, L. Chen, W. Tong, Z. Liu, J. Diwu, Z. Chai, S. Wang, Photo-exfoliation of a highly photo-responsive two-dimensional metal-organic framework, Chem. Commun. 55 (2019) 11715–11718. https://doi.org/10.1039/c9cc05455c.

[269] J. Xie, Y. Wang, W. Liu, C. Liang, Y. Zhang, L. Chen, D. Sheng, Z. Chai, S. Wang, A uranyl based coordination polymer showing response to low-dosage ionizing radiations down to 10−5 Gy, Sci. China Chem. 63 (2020) 1608–1612. https://doi.org/10.1007/s11426-020-9817-9.

[270] P. Thuéry, Y. Atoini, J. Harrowfield, Counterion-Controlled Formation of an Octanuclear Uranyl Cage with cis-1,2-Cyclohexanedicarboxylate Ligands, Inorg. Chem. 57 (2018) 6283–6288. https://doi.org/10.1021/acs.inorgchem.8b00147.

[271] J. Harrowfield, P. Thuéry, Dipodal, Tripodal, and Discoidal Coordination Modes of Kemp's Triacid Anions, Eur. J. Inorg. Chem. 2020 (2020) 749–756. https://doi.org/10.1002/ejic.201901249.

[272] F. Abraham, B. Arab-Chapelet, M. Rivenet, C. Tamain, S. Grandjean, Actinide oxalates, solid state structures and applications, Coord. Chem. Rev. 266–267 (2014) 28–68. https://doi.org/10.1016/j.ccr.2013.08.036.

[273] S. Wang, N. Xhaferaj, M. Wahiduzzaman, K. Oyekan, X. Li, K. Wei, B. Zheng, A. Tissot, J. Marrot, W. Shepard, C. Martineau-Corcos, Y. Filinchuk, K. Tan, G. Maurin, C. Serre, Engineering Structural Dynamics of Zirconium Metal–Organic Frameworks Based on Natural C4 Linkers, J. Am. Chem. Soc. 141 (2019) 17207–17216. https://doi.org/10.1021/jacs.9b07816.

[274] R. Bai, L. Chen, Y. Zhang, L. Chen, J. Diwu, X.F. Wang, The presence of mixed-valent silver in the uranyl phenylenediphosphonate framework, New J. Chem. 44 (2020) 6037–6041. https://doi.org/10.1039/d0nj00573h.

[275] X. Hou, S.F. Tang, A new uranyl triphosphonate constructed from semi-rigid triphosphonate ligand: New method for the construction of higher dimensional uranyl phosponates, J. Mol. Struct. 1146 (2017) 39–42. https://doi.org/10.1016/j.molstruc.2017.05.125.

[276] E.C. Spencer, N.L. Ross, R.G. Surbella, C.L. Cahill, The influence of pressure on the structure of a 2D uranium(VI) carboxyphosphonoate compound, J. Solid State Chem. 218 (2014) 1–5. https://doi.org/10.1016/j.jssc.2014.05.026.

[277] X. Hou, S.F. Tang, Construction of uranyl phosphonates from multifunctional zwitterionic ligands, Inorganica Chim. Acta. 474 (2018) 11–15. https://doi.org/10.1016/j.ica.2018.01.019.

[278] Y. Wang, Y. Li, Z. Bai, C. Xiao, Z. Liu, W. Liu, L. Chen, W. He, J. Diwu, Z. Chai, T.E. Albrecht-Schmitt, S. Wang, Design and synthesis of a chiral uranium-based microporous metal organic framework with high SHG efficiency and sequestration potential for low-valent actinides, Dalt. Trans. 44 (2015) 18810–18814. https://doi.org/10.1039/c5dt02337h.

[279] F.Z. Li, L. Mei, K.Q. Hu, J.P. Yu, S.W. An, K. Liu, Z.F. Chai, N. Liu, W.Q. Shi, Releasing Metal-Coordination Capacity of Cucurbit[6]uril Macrocycle in Pseudorotaxane Ligands for the Construction of Interwoven Uranyl-Rotaxane Coordination Polymers, Inorg. Chem. 57 (2018) 13513–13523. https://doi.org/10.1021/acs.inorgchem.8b02126.

[280] K.P. Carter, M. Kalaj, A. Kerridge, C.L. Cahill, Probing hydrogen and halogen-oxo interactions in uranyl coordination polymers: A combined crystallographic and computational study, CrystEngComm. 20 (2018) 4916–4925. https://doi.org/10.1039/c8ce00682b.

[281] M.B. Andrews, C.L. Cahill, Uranyl Bearing Hybrid Materials: Synthesis, Speciation, and Solid-State Structures, Chem. Rev. 113 (2013) 1121–1136. https://doi.org/10.1021/cr300202a.

[282] L. Mei, W.Q. Shi, Z.F. Chai, Ordered entanglement in actinide-organic

coordination polymers, Bull. Chem. Soc. Jpn. 91 (2018) 554–562. https://doi.org/10.1246/bcsj.20170418.

[283] L. Feng, G.S. Day, K.-Y. Wang, S. Yuan, H.-C. Zhou, Strategies for Pore Engineering in Zirconium Metal-Organic Frameworks, Chem. 6 (2020) 2902–2923. https://doi.org/10.1016/j.chempr.2020.09.010.

[284] N.M. Padial, B. Lerma-Berlanga, N. Almora-Barrios, J. Castells-Gil, I. Da Silva, M. De La Mata, S.I. Molina, J. Hernández-Saz, A.E. Platero-Prats, S. Tatay, C. MartÍ-Gastaldo, Heterometallic Titanium-Organic Frameworks by Metal-Induced Dynamic Topological Transformations, J. Am. Chem. Soc. 142 (2020) 6638–6648. https://doi.org/10.1021/jacs.0c00117.

[285] A.P. Shevchenko, E. V. Alexandrov, A.A. Golov, O.A. Blatova, A.S. Duyunova, V.A. Blatov, Topology versus porosity: what can reticular chemistry tell us about free space in metal–organic frameworks?, Chem. Commun. 56 (2020) 9616–9619. https://doi.org/10.1039/D0CC04004E.

[286] J. Calbo, M.J. Golomb, A. Walsh, Redox-active metal–organic frameworks for energy conversion and storage, J. Mater. Chem. A. 7 (2019) 16571–16597. https://doi.org/10.1039/C9TA04680A.

[287] P.F. Muldoon, C. Liu, C.C. Miller, S.B. Koby, A. Gamble Jarvi, T.-Y. Luo, S. Saxena, M. O'Keeffe, N.L. Rosi, Programmable Topology in New Families of Heterobimetallic Metal–Organic Frameworks, J. Am. Chem. Soc. 140 (2018) 6194–6198. https://doi.org/10.1021/jacs.8b02192.

[288] A.M. Rice, G.A. Leith, O.A. Ejegbavwo, E.A. Dolgopolova, N.B. Shustova, Heterometallic Metal–Organic Frameworks (MOFs): The Advent of Improving the Energy Landscape, ACS Energy Lett. 4 (2019) 1938–1946. https://doi.org/10.1021/acsenergylett.9b00874.

[289] Y.-P. He, Y.-X. Tan, J. Zhang, Functional metal–organic frameworks constructed from triphenylamine-based polycarboxylate ligands, Coord. Chem. Rev. 420 (2020) 213354. https://doi.org/10.1016/j.ccr.2020.213354.

[290] M.J. Kalmutzki, N. Hanikel, O.M. Yaghi, Secondary building units as the turning point in the development of the reticular chemistry of MOFs, Sci. Adv. 4 (2018). https://doi.org/10.1126/sciadv.aat9180.

[291] Z. Chen, S.L. Hanna, L.R. Redfern, D. Alezi, T. Islamoglu, O.K. Farha, Reticular chemistry in the rational synthesis of functional zirconium cluster-based MOFs, Coord. Chem. Rev. 386 (2019) 32–49. https://doi.org/10.1016/j.ccr.2019.01.017.

[292] P.M. Bhatt, V. Guillerm, S.J. Datta, A. Shkurenko, M. Eddaoudi, Topology Meets Reticular Chemistry for Chemical Separations: MOFs as a Case Study, Chem. 6 (2020) 1613–1633. https://doi.org/10.1016/j.chempr.2020.06.018.

[293] Z. Chen, Ł.J. Weseliński, K. Adil, Y. Belmabkhout, A. Shkurenko, H. Jiang, P.M. Bhatt, V. Guillerm, E. Dauzon, D.X. Xue, M. O'Keeffe, M. Eddaoudi, Applying the Power of Reticular Chemistry to Finding the Missing alb-MOF Platform Based on the (6,12)-Coordinated Edge-Transitive Net, J. Am.

Chem. Soc. 139 (2017) 3265–3274.
https://doi.org/10.1021/jacs.7b00219.

[294] C. Gropp, S. Canossa, S. Wuttke, F. Gándara, Q. Li, L. Gagliardi, O.M. Yaghi, Standard Practices of Reticular Chemistry, ACS Cent. Sci. 6 (2020) 1255–1273. https://doi.org/10.1021/acscentsci.0c00592.

[295] D. Sun, P.R. Adiyala, S.J. Yim, D.P. Kim, Pore-Surface Engineering by Decorating Metal-Oxo Nodes with Phenylsilane to Give Versatile Super-Hydrophobic Metal–Organic Frameworks (MOFs), Angew. Chemie - Int. Ed. 58 (2019) 7405–7409. https://doi.org/10.1002/anie.201902961.

[296] L. Feng, K.-Y. Wang, G.S. Day, M.R. Ryder, H.-C. Zhou, Destruction of Metal–Organic Frameworks: Positive and Negative Aspects of Stability and Lability, Chem. Rev. 120 (2020) 13087–13133. https://doi.org/10.1021/acs.chemrev.0c00722.

[297] X. Liu, X. Wang, F. Kapteijn, Water and Metal–Organic Frameworks: From Interaction toward Utilization, Chem. Rev. 120 (2020) 8303–8377. https://doi.org/10.1021/acs.chemrev.9b00746.

[298] B. Li, X. Dong, H. Wang, D. Ma, K. Tan, Z. Shi, Y.J. Chabal, Y. Han, J. Li, Functionalized metal organic frameworks for effective capture of radioactive organic iodides, Faraday Discuss. 201 (2017) 47–61. https://doi.org/10.1039/c7fd00013h.

[299] C. Falaise, C. Volkringer, J. Facqueur, T. Bousquet, L. Gasnot, T. Loiseau, Capture of iodine in highly stable metal-organic frameworks: A systematic study, Chem. Commun. 49 (2013) 10320–10322. https://doi.org/10.1039/c3cc43728k.

[300] T. Assaad, B. Assfour, Metal organic framework MIL-101 for radioiodine capture and storage, J. Nucl. Mater. 493 (2017) 6–11. https://doi.org/10.1016/j.jnucmat.2017.05.036.

[301] D. Banerjee, X. Chen, S.S. Lobanov, A.M. Plonka, X. Chan, J.A. Daly, T. Kim, P.K. Thallapally, J.B. Parise, Iodine Adsorption in Metal Organic Frameworks in the Presence of Humidity, ACS Appl. Mater. Interfaces. 10 (2018) 10622–10626. https://doi.org/10.1021/acsami.8b02651.

[302] L.J. Small, R.C. Hill, J.L. Krumhansl, M.E. Schindelholz, Z. Chen, K.W. Chapman, X. Zhang, S. Yang, M. Schröder, T.M. Nenoff, Reversible MOF-Based Sensors for the Electrical Detection of Iodine Gas, ACS Appl. Mater. Interfaces. 11 (2019) 27982–27988. https://doi.org/10.1021/acsami.9b09938.

[303] Z. Wang, Y. Huang, J. Yang, Y. Li, Q. Zhuang, J. Gu, The water-based synthesis of chemically stable Zr-based MOFs using pyridine-containing ligands and their exceptionally high adsorption capacity for iodine, Dalt. Trans. 46 (2017) 7412–7420. https://doi.org/10.1039/c7dt01084b.

[304] Y. Tang, H. Huang, J. Li, W. Xue, C. Zhong, IL-induced formation of dynamic complex iodide anions in IL@MOF composites for efficient iodine capture, J. Mater. Chem. A. 7 (2019) 18324–18329. https://doi.org/10.1039/c9ta04408f.

[305] Y. Feng, P. Yang, Y. Li, J. Gu, AgNPs-Containing Metal-Organic Frameworks for the Effective Adsorption and Immobilization of Radioactive Iodine, J. Chem. Eng. Data. 65 (2020) 1986–1992. https://doi.org/10.1021/acs.jced.9b01146.

[306] M. Feng, P. Zhang, H.C. Zhou, V.K. Sharma, Water-stable metal-organic frameworks for aqueous removal of heavy metals and radionuclides: A review, Chemosphere. 209 (2018) 783–800. https://doi.org/10.1016/j.chemosphere.2018.06.114.

[307] P. Kumar, A. Pournara, K.-H. Kim, V. Bansal, S. Rapti, M.J. Manos, Metal-organic frameworks: Challenges and opportunities for ion-exchange/sorption applications, Prog. Mater. Sci. 86 (2017) 25–74. https://doi.org/10.1016/j.pmatsci.2017.01.002.

[308] M. Mon, R. Bruno, J. Ferrando-Soria, D. Armentano, E. Pardo, Metal-organic framework technologies for water remediation: Towards a sustainable ecosystem, J. Mater. Chem. A. 6 (2018) 4912–4947. https://doi.org/10.1039/c8ta00264a.

[309] J. Li, X. Wang, G. Zhao, C. Chen, Z. Chai, A. Alsaedi, T. Hayat, X. Wang, Metal-organic framework-based materials: Superior adsorbents for the capture of toxic and radioactive metal ions, Chem. Soc. Rev. 47 (2018) 2322–2356. https://doi.org/10.1039/c7cs00543a.

[310] Q. Gao, J. Xu, X.H. Bu, Recent advances about metal–organic frameworks in the removal of pollutants from wastewater, Coord. Chem. Rev. 378 (2019) 17–31. https://doi.org/10.1016/j.ccr.2018.03.015.

[311] L. Mei, L. Wang, L.Y. Yuan, S.W. An, Y.L. Zhao, Z.F. Chai, P.C. Burns, W.Q. Shi, Supramolecular inclusion-based molecular integral rigidity: a feasible strategy for controlling the structural connectivity of uranyl polyrotaxane networks, Chem. Commun. 51 (2015) 11990–11993. https://doi.org/10.1039/c5cc04409j.

[312] L. Mei, P. Ren, Q. Wu, Y. Ke, J. Geng, K. Liu, X. Xing, Z. Huang, K. Hu, Y. Liu, L. Yuan, G. Mo, Z. Wu, J.K. Gibson, Z. Chai, W. Shi, Actinide Separation Inspired by Self-Assembled Metal–Polyphenolic Nanocages, J. Am. Chem. Soc. 142 (2020) 16538–16545. https://doi.org/10.1021/jacs.0c08048.

[313] A.A. Berseneva, C.R. Martin, V.A. Galitskiy, O.A. Ejegbavwo, G.A. Leith, R.T. Ly, A.M. Rice, E.A. Dolgopolova, M.D. Smith, H.C. Zur Loye, D.P. Diprete, J.W. Amoroso, N.B. Shustova, "boarding-Up": Radiation Damage and Radionuclide Leaching Kinetics in Linker-Capped Metal-Organic Frameworks, Inorg. Chem. 59 (2020) 179–183. https://doi.org/10.1021/acs.inorgchem.9b01310.

[314] S. Dhaka, R. Kumar, A. Deep, M.B. Kurade, S.-W. Ji, B.-H. Jeon, Metal–organic frameworks (MOFs) for the removal of emerging contaminants from aquatic environments, Coord. Chem. Rev. 380 (2019) 330–352. https://doi.org/10.1016/j.ccr.2018.10.003.

[315] S. Rojas, P. Horcajada, Metal-Organic Frameworks for the Removal of Emerging Organic Contaminants in Water, Chem. Rev. (2020).

https://doi.org/10.1021/acs.chemrev.9b00797.

[316] J. Leduc, M. Frank, L. Jürgensen, D. Graf, A. Raauf, S. Mathur, Chemistry of Actinide Centers in Heterogeneous Catalytic Transformations of Small Molecules, ACS Catal. 9 (2019) 4719–4741. https://doi.org/10.1021/acscatal.8b04924.

[317] J. Yu, C. Zhao, R. Zhou, W. Gao, S. Wang, K. Liu, S. Chen, K. Hu, L. Mei, L. Yuan, Z. Chai, H. Hu, W.-Q. Shi, Visible-Light-Enabled C−H Functionalization by a Direct Hydrogen Atom Transfer Uranyl Photocatalyst, Chem. – A Eur. J. 26 (2020) 16521–16529. https://doi.org/10.1002/chem.202003431.

[318] Y. Li, S.A. e. A. Rizvi, D. Hu, D. Sun, A. Gao, Y. Zhou, J. Li, X. Jiang, Selective Late-Stage Oxygenation of Sulfides with Ground-State Oxygen by Uranyl Photocatalysis, Angew. Chemie - Int. Ed. 58 (2019) 13499–13506. https://doi.org/10.1002/anie.201906080.

[319] L. Monsigny, P. Thuéry, J.C. Berthet, T. Cantat, Breaking C-O Bonds with Uranium: Uranyl Complexes as Selective Catalysts in the Hydrosilylation of Aldehydes, ACS Catal. 9 (2019) 9025–9033. https://doi.org/10.1021/acscatal.9b01408.

[320] X. Zhang, P. Li, M. Krzyaniak, J. Knapp, M.R. Wasielewski, O.K. Farha, Stabilization of Photocatalytically Active Uranyl Species in a Uranyl–Organic Framework for Heterogeneous Alkane Fluorination Driven by Visible Light, Inorg. Chem. 59 (2020) 16795–16798. https://doi.org/10.1021/acs.inorgchem.0c00850.

[321] Z.H. Syed, F. Sha, X. Zhang, D.M. Kaphan, M. Delferro, O.K. Farha, Metal–Organic Framework Nodes as a Supporting Platform for Tailoring the Activity of Metal Catalysts, ACS Catal. 10 (2020) 11556–11566. https://doi.org/10.1021/acscatal.0c03056.

[322] J. Lyu, X. Zhang, P. Li, X. Wang, C.T. Buru, P. Bai, X. Guo, O.K. Farha, Exploring the Role of Hexanuclear Clusters as Lewis Acidic Sites in Isostructural Metal-Organic Frameworks, Chem. Mater. 31 (2019) 4166–4172. https://doi.org/10.1021/acs.chemmater.9b00960.

[323] J.G. Knapp, X. Zhang, T. Elkin, L.E. Wolfsberg, S.L. Hanna, F.A. Son, B.L. Scott, O.K. Farha, Single crystal structure and photocatalytic behavior of grafted uranyl on the Zr-node of a pyrene-based metal–organic framework, CrystEngComm. 22 (2020) 2097–2102. https://doi.org/10.1039/C9CE02034A.

[324] L.S. Natrajan, Developments in the photophysics and photochemistry of actinide ions and their coordination compounds, Coord. Chem. Rev. 256 (2012) 1583–1603. https://doi.org/10.1016/j.ccr.2012.03.029.

[325] J. Heine, K. Müller-Buschbaum, Engineering metal-based luminescence in coordination polymers and metal–organic frameworks, Chem. Soc. Rev. 42 (2013) 9232. https://doi.org/10.1039/c3cs60232j.

[326] D.-W. Lim, H. Kitagawa, Proton Transport in Metal–Organic Frameworks, Chem. Rev. 120 (2020) 8416–8467. https://doi.org/10.1021/acs.chemrev.9b00842.

[327] J.M. Dorhout, M.P. Wilkerson, K.R. Czerwinski, Irradiation and isolation of fission products from uranium metal–organic frameworks, J. Radioanal. Nucl. Chem. 320 (2019) 415–424. https://doi.org/10.1007/s10967-019-06478-w.

[328] N.A. Conroy, E.M. Wylie, B.A. Powell, A Novel Method for Tracer Concentration Plutonium(V) Solution Preparation, Anal. Chem. 88 (2016) 4196–4199. https://doi.org/10.1021/acs.analchem.6b00229.

[329] B. Burger, P.M. Maffettone, V. V. Gusev, C.M. Aitchison, Y. Bai, X. Wang, X. Li, B.M. Alston, B. Li, R. Clowes, N. Rankin, B. Harris, R.S. Sprick, A.I. Cooper, A mobile robotic chemist, Nature. 583 (2020) 237–241. https://doi.org/10.1038/s41586-020-2442-2.

[330] X. Gong, K. Gnanasekaran, Z. Chen, L. Robison, M.C. Wasson, K.C. Bentz, S.M. Cohen, O.K. Farha, N.C. Gianneschi, Insights into the Structure and Dynamics of Metal–Organic Frameworks via Transmission Electron Microscopy, J. Am. Chem. Soc. 142 (2020) 17224–17235. https://doi.org/10.1021/jacs.0c08773.

[331] J. Lyu, X. Gong, S.J. Lee, K. Gnanasekaran, X. Zhang, M.C. Wasson, X. Wang, P. Bai, X. Guo, N.C. Gianneschi, O.K. Farha, Phase Transitions in Metal-Organic Frameworks Directly Monitored through in Situ Variable Temperature Liquid-Cell Transmission Electron Microscopy and in Situ X-ray Diffraction, J. Am. Chem. Soc. 142 (2020) 4609–4615. https://doi.org/10.1021/jacs.0c00542.

[332] S. Sabale, D. Barpaga, J. Yao, L. Kovarik, Z. Zhu, S. Chatterjee, B.P. McGrail, R.K. Motkuri, X.Y. Yu, Understanding Time Dependence on Zinc Metal-Organic Framework Growth Using in Situ Liquid Secondary Ion Mass Spectrometry, ACS Appl. Mater. Interfaces. 12 (2020) 5090–5098. https://doi.org/10.1021/acsami.9b19991.

[333] M.J. Van Vleet, T. Weng, X. Li, J.R. Schmidt, In Situ, Time-Resolved, and Mechanistic Studies of Metal-Organic Framework Nucleation and Growth, Chem. Rev. 118 (2018) 3681–3721. https://doi.org/10.1021/acs.chemrev.7b00582.

[334] W.-Q. Shi, L.-Y. Yuan, C.-Z. Wang, L. Wang, L. Mei, C.-L. Xiao, L. Zhang, Z.-J. Li, Y.-L. Zhao, Z.-F. Chai, Exploring Actinide Materials Through Synchrotron Radiation Techniques, Adv. Mater. 26 (2014) 7807–7848. https://doi.org/10.1002/adma.201304323.

[335] V. Bon, E. Brunner, A. Pöppl, S. Kaskel, Unraveling Structure and Dynamics in Porous Frameworks via Advanced In Situ Characterization Techniques, Adv. Funct. Mater. 30 (2020) 1907847. https://doi.org/10.1002/adfm.201907847.